

**A MODEL BASED FLIGHT CONTROL SYSTEM DESIGN APPROACH
FOR MICRO AERIAL VEHICLES USING INTEGRATED FLIGHT TESTING
AND HIL SIMULATIONS**

Ph.D. THESIS

Burak YÜKSEK

Mechatronics Engineering Department

Mechatronics Engineering Programme

NOVEMBER 2019

**A MODEL BASED FLIGHT CONTROL SYSTEM DESIGN APPROACH
FOR MICRO AERIAL VEHICLES USING INTEGRATED FLIGHT TESTING
AND HIL SIMULATIONS**

Ph.D. THESIS

Burak YÜKSEK
(518132003)

Mechatronics Engineering Department

Mechatronics Engineering Programme

Thesis Advisor: Prof. Dr. Gökhan İNALHAN

NOVEMBER 2019

**KÜÇÜK BOYUTLU İNSANSIZ HAVA ARAÇLARI ÜZERİNDE
SİSTEM TANILAMA, UÇUŞ KONTROL SİSTEMİ TASARIMI VE
DONANIM İLE BENZETİM UYGULAMALARI**

DOKTORA TEZİ

**Burak YÜKSEK
(518132003)**

Mekatronik Mühendisliği Anabilim Dalı

Mekatronik Mühendisliği Programı

Tez Danışmanı: Prof. Dr. Gökhan İNALHAN

KASIM 2019

Burak YÜKSEK, a Ph.D. student of ITU Graduate School of Science Engineering and Technology 518132003 successfully defended the thesis entitled “A MODEL BASED FLIGHT CONTROL SYSTEM DESIGN APPROACH FOR MICRO AERIAL VEHICLES USING INTEGRATED FLIGHT TESTING AND HIL SIMULATIONS”, which he/she prepared after fulfilling the requirements specified in the associated legislations, before the jury whose signatures are below.

Thesis Advisor : **Prof. Dr. Gökhan İNALHAN**
Istanbul Technical University

Jury Members : **Prof. Dr. Muammer KALYON**
Istanbul Commerce University

Prof. Dr. Fikret ÇALIŞKAN
Istanbul Technical University

Assoc. Prof. Dr. Tayfun ÇİMEN
Turkish Aerospace Industries (TAI)

Assist. Prof. Dr. Ramazan YENİÇERİ
Istanbul Technical University

Date of Submission : **14 October 2019**
Date of Defense : **19 November 2019**

To Yağmur and my family,

FOREWORD

First of all, I would like to express my sincere gratitude to Prof. Dr. Gökhan İnalhan for his support and understanding in each phase of my studies. It is an invaluable experience and a milestone to work with him during my PhD progress in ITU Aerospace Research Center.

I would like to thank Prof. Dr. Muammer Kalyon and Assist. Prof. Dr. Ramazan Yeniçeri for being members of the steering commit. Their supports in theoretical and practical fields speed up the test period and increase the maturity of my studies.

I would like to thank Prof. Dr. Fikret Çalışkan for being member of the defense jury, his guidance and encouragement about writing several publications.

I would like to express my appreciation to Dr. Tayfun Çimen for being member of the defense jury, his guidance and advice about my professional career.

I would like to thank Dr. Umut Demirezen for his support especially in the last part of my thesis.

I would like to express my special thanks to Assist. Prof. Dr. Uğur Özdemir and Aslıhan Vuruşkan for their support and cooperation in Turaç UAV project.

I would like to thank Assist. Prof. Dr. Emre Koyuncu, Assist. Prof. Dr. N. Kemal Üre and all my colleagues in ITU Aerospace Research Center for their support, advice, guidance and time.

I am grateful to my colleagues Aykut Çetin and Emre Saldıran for their precious supports. They helped me to complete the flight tests in all weather conditions even in winter. I will never forget the breakfasts that we had on the way of the test facility.

Also, I would like to thank Scientific and Technological Research Council of Turkey (TÜBİTAK) for financial support during my PhD progress. It could have been so hard to start my doctoral studies without this scholarship.

Lastly, I would like to express my deep appreciation to my fiancée Yağmur and my family for their limitless support. I am feeling lucky to have them.

November 2019

Burak YÜKSEK

TABLE OF CONTENTS

	<u>Page</u>
FOREWORD.....	ix
TABLE OF CONTENTS.....	xi
ABBREVIATIONS	xv
SYMBOLS.....	xvii
LIST OF TABLES	xix
LIST OF FIGURES	xxi
SUMMARY	xxv
ÖZET	xxvii
1. INTRODUCTION	1
1.1 Purpose of Thesis	10
1.2 Literature Survey	11
2. THEORETICAL BACKGROUND.....	19
2.1 Frequency Domain System Identification Method.....	19
2.1.1 Test input design.....	20
2.1.2 Data consistency	22
2.1.3 Single-input / single-output frequency response identification theory ...	23
2.1.3.1 Frequency response definition	24
2.1.3.2 Relation between the Fourier transform and frequency response....	24
2.1.3.3 General observations.....	26
2.1.4 Coherence function.....	26
2.1.5 Transfer function modeling	28
2.1.6 State-space modeling.....	29
Accuracy analysis	34
2.1.7 Time-domain verification	35
2.2 Model Stitching: Developing a Full Flight Envelope Simulation Environment	36
2.2.1 Basics of model stitching.....	37
2.2.2 Key elements of a stitched model.....	39
2.3 Multi-Objective Optimization Based Control System Design Approach	41
2.3.1 Overall road map	42
2.3.2 Quantitative design requirements	46
2.3.2.1 Stability and stability margins	47
2.3.2.2 Damping ratio	48
2.3.2.3 Minimum crossover frequency	48
2.3.2.4 Pilot-induced oscillation specifications	49
2.3.2.5 Disturbance rejection requirements	49
2.3.2.6 Performance metrics	51

2.3.3 Design optimization.....	51
2.4 Closed-loop Reference Model Based Adaptive Control	53
2.5 Continuous-time Control in Reinforcement Learning.....	55
3. TRANSITION FLIGHT MODELING OF A FIXED-WING VTOL UAV: A FIRST PRINCIPLE MODELING APPROACH.....	57
3.1 Mathematical Modeling.....	61
3.1.1 General equations of motion	61
3.1.2 Modeling of transition flight.....	63
3.1.3 Propeller-induced airflow effects.....	64
3.1.4 Free airflow effects	67
3.1.5 Total airflow effects	68
3.1.6 Modeling the thrust-airspeed relationship for the tilt-rotor propeller	70
3.2 Computational Fluid Dynamics Analysis.....	70
3.2.1 2D analysis	71
3.2.2 3D analysis	71
3.3 Transition Scenario.....	77
3.4 Complete Mathematical Model Structure and Simulations.....	79
3.4.1 Forward and back-transition algorithms.....	80
3.4.2 Simulation results	81
4. SYSTEM IDENTIFICATION AND CONTROL SYSTEM DESIGN FOR RANGER-EX UAV	87
4.1 Experimental Platform.....	92
4.2 Mathematical Modeling.....	94
4.3 Identification of Longitudinal and Lateral Dynamics	96
4.3.1 Identification of servo actuator dynamics.....	96
4.3.2 Design of flight experiments	97
4.3.3 Identification of longitudinal dynamics.....	99
4.3.4 Identification of lateral dynamics	100
4.4 Time-Domain Verification	104
4.5 Autopilot System	107
4.5.1 Control system design requirements	108
4.5.1.1 First tier specifications.....	109
4.5.1.2 Second tier specifications	109
4.5.2 Determining the DRB and DRP values	110
4.5.3 Control system structures	111
4.5.4 Optimization process of the controller parameters.....	111
4.5.5 Uncertainty analysis	113
4.6 Hardware-in-the-loop Simulation System.....	114
4.7 Flight Test Results	116
5. SYSTEM IDENTIFICATION AND CONTROL SYSTEM DESIGN FOR AN AGILE QUADROTOR PLATFORM.....	119
5.1 Experimental Platform.....	122
5.2 Mathematical Model Structure	124
5.3 System Identification and Verification.....	126
5.3.1 Frequency response generation	127

5.3.2 Obtaining the speed derivatives for hover flight Conditions	128
Estimation of longitudinal speed stability derivative M_u	130
5.3.3 System identification results for hover and forward flight conditions....	131
5.3.4 Identification of the propulsion system dynamics	133
5.3.5 Model verification	136
5.4 Model Stitching	139
5.4.1 Anchor point data	140
5.5 Control System Design.....	141
5.5.1 ArduCopter controller structure	142
5.5.2 ArduCopter inner-loop attitude controller performance Evaluation	142
5.5.3 Dynamic scaling	145
5.5.4 Trajectory tracking control system design.....	146
Minimum crossover frequency	147
Disturbance rejection requirements	148
5.5.5 Robustness analysis of the attitude controllers.....	149
5.6 Simulation and Flight Test Results.....	150
5.6.1 Kinematic scaling	151
5.6.2 Position-hold performance evaluation in hover flight	151
5.6.3 Trajectory tracking and aggressiveness analysis	153
6. IMPROVEMENT OF CRM-ADAPTIVE SYSTEM PERFORMANCE BY UTILIZING REINFORCEMENT LEARNING	157
6.1 Background and Problem Definition.....	160
6.1.1 Helicopter pitch dynamics in hover.....	161
6.2 Adaptive Control System Design	162
6.2.1 Model reference adaptive control system design.....	162
6.2.2 CRM-adaptive control system	163
6.2.3 Transient response characteristics	164
6.2.3.1 Water-bed effect.....	164
6.2.3.2 Optimal design of observer gain (l) in CRM	164
6.2.4 RL-CRM adaptive system	166
6.3 Simulation Results.....	169
6.3.1 Uncertainty analysis	171
7. CONCLUSIONS AND RECOMMENDATIONS.....	175
REFERENCES.....	181
CURRICULUM VITAE	193

ABBREVIATIONS

ACAH	: Attitude Command - Attitude Hold
BL	: Broken-Loop
BLDC	: Brushless Direct Current
CR	: Cramer-Rao
CFD	: Computational Fluid Mechanics
CL	: Closed-Loop
CMRAC	: Combined/Composite Model Reference Adaptive Control
COTS	: Commercially off the Shelf
CRM	: Closed-loop Reference Model
DDPG	: Deep Deterministic Policy Gradient
DM	: Design Margin
DRB	: Disturbance Rejection Bandwidth
DRP	: Disturbance Rejection Peak
DVE	: Degraded Visual Environment
ESC	: Electronic Speed Controller
FCS	: Flight Control System
GM	: Gain Margin
GVE	: Good Visual Environment
HIL	: Hardware-in-the-loop
HQ	: Handling Qualities
IMU	: Inertial Measurement Unit
LTI	: Linear-time-invariant
LOES	: Low-order Equivalent System
MAV	: Micro Aerial Vehicle
MIMO	: Multi-input-multi-output
MRAC	: Model Reference Adaptive Control
MTE	: Mission Task Element
NED	: North-East-Down
PM	: Phase Margin
RL	: Reinforcement Learning
RMSE	: Root-Mean-Square Error
RTOS	: Real-time Operating System
SIL	: Software-in-the-loop
SISO	: Single-input-single-output
SNR	: Signal-to-Noise Ratio
TIC	: Theil-Inequality Constant
TTA	: Trajectory Tracking and Aggressiveness
UAV	: Unmanned Aerial Vehicle
VLM	: Vortex Lattice Method
VTOL	: Vertical Takeoff and Landing

SYMBOLS

f	: Frequency in Hz
ω	: Frequency in rad/s
T	: Period
F	: Force
U, V, W	: Velocity components on X_b, Y_b, Z_b Axes
P, Q, R	: Angular Rates on X_b, Y_b, Z_b Axes
ϕ, θ, ψ	: Roll, Pitch and Yaw Euler Angles
H	: Frequency Response Function
ϕ	: Phase Shift
J	: Cost Function
W	: Weighting Function
ε	: Error Function
\mathbf{x}	: System States
\mathbf{y}	: System Outputs
\mathbf{A}	: System Matrix
\mathbf{B}	: Control Input Matrix
\mathbf{C}	: Output Matrix
\mathbf{D}	: Feedforward Matrix
σ	: Standard Deviation
e	: Tracking Error
L	: Luenberger Gain
θ	: Parameter Vector
Γ	: Adaptation Rate
ω_n	: Natural Frequency
ζ	: Damping Ratio
τ	: Time Constant
ϕ_{TTA}	: Trajectory Tracking and Aggressiveness Score

LIST OF TABLES

	<u>Page</u>
Table 1.1 : 500-Run Monte-Carlo analysis results of the MRAC, CRM and RL-CRM adaptive systems.	8
Table 1.2 : Comparison of the state-of-the-art and thesis contributions.	16
Table 3.1 : The force and moment coefficient for transition scenario.....	74
Table 3.2 : The moment coefficient and force components for the forward-transition scenario.	77
Table 3.3 : The force and moment coefficient for back transition scenario.	78
Table 4.1 : Ranger EX MAV specifications.	93
Table 4.2 : Dynamical characteristics of the Ranger EX MAV baseline model. ..	95
Table 4.3 : System identification test input parameters.....	98
Table 4.4 : Identified longitudinal stability and control derivatives.	101
Table 4.5 : Cost values for the identified longitudinal model.	102
Table 4.6 : Identified lateral stability and control derivatives.	105
Table 4.7 : Cost values for the identified lateral model.....	105
Table 4.8 : Time-domain verification results.....	106
Table 4.9 : Identified dynamical characteristics of the Ranger EX MAV.....	107
Table 4.10 : Design specifications for longitudinal and lateral attitude control systems.....	110
Table 4.11 : Rotor diameter and disturbance rejection bandwidth of the UH-60. ..	110
Table 4.12 : Froude scaling for the Ranger EX MAV.	111
Table 4.13 : Longitudinal and lateral attitude control system parameters.	112
Table 4.14 : Performance comparison of the proposed and the legacy controllers.	118
Table 5.1 : Identification costs for each input-output pairs.	134
Table 5.2 : Identified parameters for hover and forward flight conditions.....	135
Table 5.3 : Test signal parameters for propulsion system identification in high frequency range.....	135
Table 5.4 : Verification TIC and cost (J_{vrf}) values for hover and forward flight conditions.....	139
Table 5.5 : Frequency sweep signal parameters for Arducopter performance evaluation tests.....	143
Table 5.6 : Performance evaluation of the legacy control systems.	145
Table 5.7 : Froude scaling analysis of the agile maneuvering drone roll mode in hover flight.....	146
Table 5.8 : Summary of the selected design specifications in control system design process.	149
Table 5.9 : Position and velocity RMSE for hover flight test.....	153
Table 5.10 : Weights used in the TTA analysis.	155

Table 5.11 :	TTA score guideline for scaled lateral reposition and depart/abort MTEs [1].	155
Table 6.1 :	Comparison of performance metrics in the transient phase.	159
Table 6.2 :	Hyperparameters of Actor-Critic agent.	168
Table 6.3 :	Training parameters for DDPG algorithm.	168
Table 6.4 :	500-Run Monte-Carlo analysis results of the MRAC, CRM and RL-CRM adaptive systems.	172
Table 6.5 :	Robustness analysis results of the MRAC, CRM and RL-CRM adaptive systems in the worst case scenario.	172
Table 7.1 :	Comparison of the state-of-the-art and thesis contributions.	179

LIST OF FIGURES

	<u>Page</u>
Figure 1.1 : Turac VTOL UAV in flight test.	2
Figure 1.2 : Transition flight simulation of the Turac VTOL UAV.	3
Figure 1.3 : General view of a) fixed-wing and b) rotary-wing UAV platforms used in this thesis.	4
Figure 1.4 : General view of the desktop-to-flight design workflow [2].	5
Figure 1.5 : Attitude reference tracking performance tests of the optimized and legacy controllers on the fixed-wing MAV, a) Roll attitude control system responses, b) Pitch attitude control system responses.	6
Figure 1.6 : Depart-Abort maneuver test results for different aggressiveness levels (a) ($a = 1, 1.5, 2$).	7
Figure 1.7 : General overview of the key aspects of urban air mobility concept..	9
Figure 2.1 : Frequency-domain system identification workflow [3].	21
Figure 2.2 : Attitude and body rate measurement error model.	23
Figure 2.3 : General view of the stitch model structure (Adapted from [4]).	39
Figure 2.4 : General view of the multi-objective optimization based flight control system design road map [2].	43
Figure 2.5 : Calspan total in-flight simulator [5].	46
Figure 3.1 : General view of the Turac VTOL concept.	59
Figure 3.2 : General view of the tilt mechanism.	60
Figure 3.3 : General view of the 1/3 scale prototype of the Turac.	61
Figure 3.4 : Earth and body fixed axis systems.	62
Figure 3.5 : Force, moment, and geometrical dimensions of the UAV propulsion system.	63
Figure 3.6 : Forces and moments on the Turac in transition flight.	64
Figure 3.7 : Propeller induced airflow effects on the UAV body.	65
Figure 3.8 : Change of effectiveness coefficient with the tilt angle.	66
Figure 3.9 : Total airspeed vector on the UAV.	69
Figure 3.10 : Thrust - propeller intake airflow speed characteristics of the 12x6 fixed-pitch propeller.	71
Figure 3.11 : Lift coefficient C_{L_s} of the 2D wing airfoil for different Reynolds numbers.	72
Figure 3.12 : Drag coefficient C_{D_s} of the 2D wing airfoil for different Reynolds numbers.	72
Figure 3.13 : Pitching moment coefficient C_{M_s} of the 2D wing airfoil for different Reynolds numbers.	73
Figure 3.14 : The half of Turac model for forward flight regime in CFD analysis.	73
Figure 3.15 : The static pressure distribution of Turac.	74
Figure 3.16 : Angle of attack - C_L graph of the Turac.	75

Figure 3.17: Angle of attack - C_D graph of the Turac.	75
Figure 3.18: Angle of attack - C_M graph of the Turac.	75
Figure 3.19: The path lines of Turac in transition regime.	76
Figure 3.20: The static pressure distribution of Turac in transition regime.	76
Figure 3.21: General block diagram of the nonlinear mathematical model of the complete flight regimes.	79
Figure 3.22: Transition and back transition algorithms.	81
Figure 3.23: Airspeed time history during the simulation.	82
Figure 3.24: Altitude time history during the simulation.	82
Figure 3.25: Pitch angle time history during the simulation.	83
Figure 3.26: Tilt angle time history during the simulation.	83
Figure 3.27: Experimental transition maneuver demonstration.	85
Figure 4.1 : Surveillance mission concept.	88
Figure 4.2 : Ranger EX MAV platform.	89
Figure 4.3 : Desktop-to-flight design workflow (adapted from [2]).	90
Figure 4.4 : Sample autonomous flight trajectory.	91
Figure 4.5 : Ranger EX MAV flight platform and the autopilot system.	92
Figure 4.6 : Nonlinear model structure.	94
Figure 4.7 : HS-85MG servo actuator system identification results.	97
Figure 4.8 : Elevator test input and aircraft response.	99
Figure 4.9 : Frequency responses of the MAV and identified longitudinal model for elevator input.	101
Figure 4.10: Aileron and rudder test inputs and aircraft responses.	102
Figure 4.11: Frequency responses of the MAV and identified lateral model for aileron input.	103
Figure 4.12: Frequency responses of the MAV and identified lateral model for rudder input.	104
Figure 4.13: Comparison of the MAV and longitudinal model responses for 1-1 elevator doublet input.	106
Figure 4.14: Comparison of the MAV and lateral model responses for 1-1 (a) aileron and (b) rudder doublet inputs.	107
Figure 4.15: General scheme of the avionics architecture.	108
Figure 4.16: Proposed pitch attitude control structure.	111
Figure 4.17: Proposed roll attitude control structure.	112
Figure 4.18: Family of designs for pitch autopilot.	113
Figure 4.19: Family of designs for lateral autopilot - (a) Roll axis, (b) Yaw axis.	114
Figure 4.21: Robustness analysis of the lateral autopilot.	114
Figure 4.20: Robustness analysis of the longitudinal autopilot.	115
Figure 4.22: HIL test system structure.	116
Figure 4.23: Attitude error and actuator usage RMS in level flight.	117
Figure 4.24: Doublet reference input tracking test results on roll and pitch axes.	117
Figure 5.1 : General view of the desktop-to-flight design workflow [2].	121
Figure 5.2 : Moderate agility lateral reposition maneuver. a) A footage from actual flight tests, b) Recorded North and East position.	122
Figure 5.3 : General view of the high performance agile maneuvering drone platform.	123

Figure 5.4 :	General scheme of the Racer drone avionics architecture.....	124
Figure 5.5 :	Block diagram and input/output definitions for frequency sweep tests.	127
Figure 5.6 :	Roll axis frequency sweep test.	128
Figure 5.7 :	Frequency responses of the $\dot{v}(s)/\phi(s)$ and $\dot{u}(s)/\theta(s)$	130
Figure 5.8 :	LSS flight test in near hover conditions.....	131
Figure 5.9 :	On-Axis $p/\delta_a, r/\delta_r$ frequency responses of the actual system and identified model in hover flight conditions.	132
Figure 5.10:	On-Axis $q/\delta_e, a_z/\delta_T$ frequency responses of the actual system and identified model in hover flight conditions.	132
Figure 5.11:	On-Axis frequency responses of the actual system and identified model in forward flight conditions.....	133
Figure 5.12:	Identification of high frequency dynamics on longitudinal and lateral axes.	136
Figure 5.13:	Schematics of the bare-airframe model verification process.....	136
Figure 5.14:	Sample doublet reference input tests on pitch and roll axes.....	137
Figure 5.15:	Roll axis verification test results in hover flight.	137
Figure 5.16:	Pitch axis verification test results.	138
Figure 5.17:	Yaw axis verification test results.	138
Figure 5.18:	General view of the stitch model structure [4].	140
Figure 5.19:	Anchor point models and trim data obtained from the forward flight tests in trim conditions.	141
Figure 5.20:	Block diagram of the ArduCopter Position control system.....	142
Figure 5.21:	Schematic of the closed-loop, broken-loop and disturbance rejection test input-output pairs.	143
Figure 5.22:	Performance evaluation of ArduCopter roll attitude controller in CONDUIT for hover/low speed conditions.	144
Figure 5.23:	Block diagram of the proposed trajectory tracking system.	146
Figure 5.24:	3σ robustness analysis of optimized roll attitude controller in CONDUIT for hover/low speed conditions.	150
Figure 5.25:	Position-hold flight test results with the legacy and optimized controllers.	152
Figure 5.26:	Position and velocity time histories in hover flight test with the legacy and optimized controllers.	152
Figure 5.27:	Lateral reposition simulation and flight test results.....	153
Figure 5.28:	Longitudinal depart/abort simulation and flight test results.	154
Figure 5.29:	TTA Scoring of the depart/abort and lateral reposition maneuvers with optimized controllers.	155
Figure 6.1 :	Comparison of $ e^o(t) $ and $ \dot{u}(t) $ time history of the dynamic system with MRAC, CRM and RL-CRM.....	158
Figure 6.2 :	Transient response analysis for CRM-adaptive system.....	165
Figure 6.3 :	General structure of the CRM-RL.	166
Figure 6.4 :	Actor-Critic agent structure.	167
Figure 6.5 :	Transient Response of the dynamic system with MRAC, CRM and RL-CRM.	170

Figure 6.6 : Time history of the agent response (scaling factor, k) in the transient phase.....	170
Figure 6.7 : Comparison of $ e^o(t) $ and $ \dot{u}(t) $ time history of the CRM and RL-CRM systems in the presence of -35% parametric uncertainty..	173
Figure 6.8 : Step responses of the CRM and RL-CRM systems in the presence of -35% parametric uncertainty.....	173
Figure 7.1 : General overview of the key aspects of urban air mobility concept..	176

A MODEL BASED FLIGHT CONTROL SYSTEM DESIGN APPROACH FOR MICRO AERIAL VEHICLES USING INTEGRATED FLIGHT TESTING AND HIL SIMULATIONS

SUMMARY

In recent decade, urban air mobility has an increasing demand in passenger and cargo transportation in the urban airspace. One of the most critical factors in urban air mobility concept is operation safety which requires reliable flight control and guidance system and predictable mathematical model of the aerial platform. To provide these requirements, developing and using a verified design workflow becomes quite crucial. In this thesis, mathematical modeling, flight control system design and test workflow is applied on tilt-rotor, fixed-wing and rotary-wing aerial platforms.

In the first part of this thesis, nonlinear mathematical model of a fixed-wing tilt-rotor unmanned aerial vehicle (UAV) is developed which covers hover, transition and forward flight phases. The model includes propeller-induced airstream effects on the UAV body which are directly related to flight speed, rotor nacelle angle and angle-of-attack. Momentum theory is used to calculate the propeller-induced airstream characteristics such as output cross-section area and velocity. 2D aerodynamic analysis is performed on the area that is affected by the propeller-induced airstream because of the lack of finite-wing effects on this region. The obtained aerodynamic parameters are embedded into look-up tables and used in the mathematical model. 3D aerodynamic analysis is also performed on the complete airframe geometry and calculated parameters are used in the nonlinear model. Especially in the transition flight phase, thrust and aerodynamic effects are acted together on the airframe and UAV dynamics become quite complex. To provide the flight safety in the transition phase, forward- and back-transition scenarios are developed by performing trim analysis for each flight condition and required airspeed, angle-of-attack, nacelle angle and thrust level are calculated. Then, a command-schedule is generated by using these vehicle states which can be utilized as a reference signal set for the flight control system or pilot cue. We evaluated the proposed closed-loop system in the developed nonlinear simulation environment and flight tests.

In the second part of the thesis, system identification and model-based flight control system design approach, in which flight testing and hardware-in-the-loop (HIL) simulation are integrated into the design workflow, is applied on a fixed-wing micro aerial vehicle (MAV). This approach relies on adaptation of system identification and control system design methodologies from the manned aircraft domain. The MAV is specifically designed for a surveillance mission in which a moving ground or seaborne target, such as a track or a boat, is tracked fully autonomously from a specified altitude by using a downward-facing body-fixed camera. We utilize a design process in which the longitudinal and lateral mathematical models are identified through open-loop system identification flight testing. These models are later used in a multi-objective controller optimization scheme in which a control system is designed

inline with the high performance tracking requirements. We have utilized a HIL simulation system allowing comprehensive simulation and testing of designed control and guidance algorithms before fully autonomous flight tests as to minimize cost and crash risk. Both the proposed and legacy flight control systems are evaluated in actual flight tests. The results demonstrate that the proposed design methodology and the resulting control system provides superior reference tracking performance and robust disturbance rejection in face of real-world conditions such as turbulence and winds.

In the third part of the thesis, we utilize a system identification, model stitching and model-based flight control system design methodology for an agile maneuvering quadrotor MAV technology demonstrator platform. The proposed MAV is designed to perform agile maneuvers in hover/low-speed and fast forward flight conditions in which significant changes in system dynamics are observed. As such, these significant changes may result in considerable loss of performance in terms of reference signal tracking and disturbance rejection. To capture the changing dynamics, we consider an approach which is adapted from the full-scale manned aircraft and rotorcraft domain. Specifically, linear mathematical models of the MAV in hover and forward flight are obtained by using the frequency-domain system identification method and they are validated in time domain. These point models are stitched by utilizing the trim data and quasi-nonlinear mathematical model is generated for simulation purposes. Identified linear models are used in a multi-objective optimization based flight control system design approach in which several handling quality specifications are used to optimize the controller parameters. Lateral reposition and longitudinal depart/abort mission task elements from ADS-33E-PRF are scaled-down by using kinematic scaling to evaluate the proposed flight control systems. Position hold, trajectory tracking and aggressiveness analysis are performed, Monte-Carlo simulations and actual flight test results are compared. It is shown that the proposed methodology provides high precision and predictable maneuvering control capability over an extensive speed envelope in comparison to classical controller design techniques.

In the fourth part of the thesis, closed-loop reference model (CRM) based adaptive control algorithm is improved by using reinforcement learning (RL) method. In the proposed system, an actor-critic agent is utilized to increase or decrease the observer gain scaling factor by using tracking error observations from the environment. Several simulation studies are performed on simplified longitudinal linear model of a transport helicopter. For a quantitative comparison of the transient response performance, key signal norms are calculated and results are evaluated. Monte-Carlo and the worst-case analyses are performed to compare the transient response performance of the adaptive systems in the presence of parametric uncertainties. It is shown that the proposed RL-CRM method has superior transient response performance when compared to the model reference adaptive control (MRAC) and optimized fixed-gain CRM-adaptive systems. In addition, the control structure provides the possibility to learn numerous adaptation strategies across various flight conditions rather this be driven by high-fidelity simulators or through flight testing.

KÜÇÜK BOYUTLU İNSANSIZ HAVA ARAÇLARI ÜZERİNDE SİSTEM TANILAMA, UÇUŞ KONTROL SİSTEMİ TASARIMI VE DONANIM İLE BENZETİM UYGULAMALARI

ÖZET

İnsansız hava araçları, uzun yıllardır askeri amaçlı operasyonlarda oldukça yoğun olarak kullanılmaktadırlar ve gelecekte de bu uygulamaların hızlı bir şekilde artması beklenmektedir. Operasyonel riskleri ve maliyetleri oldukça düşük seviyelere çektikleri için son yıllarda sivil alanlarda da kullanımları oldukça yaygınlaşmıştır. Hatta, hava trafik yönetimi çalışmalarındaki hızlı gelişmelere paralel olarak, insansız hava araçlarının şehir hava sahasına entegrasyonu çalışmaları da başlamış, birçok teknoloji firması yatırımlarını bu yönde yoğunlaştırma kararı almışlardır. Günümüzde kargo ve yolcu taşımacılığı için geliştirilen çok başarılı konseptleri görmek mümkündür. Hava araçlarının özellikle şehir içi taşıma uygulamalarında kullanılması ile birlikte bu sistemlerin uçuş güvenliğinin sağlanması daha da kritik bir konu haline gelmiştir.

Şehir hava sahasını yöneten hava trafik yönetimi sistemini ve araç üzerinde bulunan güdüm ve kontrol sistemlerini hiyerarşik bir yapıda incelemek, genel sistemi daha anlaşılır bir hale getirecektir. Hiyerarşik olarak en üst kademede bulunan hava trafik yönetimi sistemi, hava araçlarının koordinasyonunu sağlayarak havada oluşabilecek bir çarpışmayı veya hava araçlarının şehirde bulunan sabit engellere (binalar, yer şekilleri, vs.) çarpmasını engellemektedir. Ancak, hava trafik yönetim sistemi ne kadar uygulanabilir ve etkin uçuş yörüngeleri üretirse üretsin, araç üzerindeki güdüm ve kontrol sistemleri bu komutları istenen başarımla takip edemez ise bu durum bütün sistemin güvenilirliğini oldukça yüksek seviyede tehlikeye sokacaktır. Bu nedenle, orta ve alt seviye sistemler olan güdüm ve kontrol sistemlerinin, belirli kararlılık ve performans gereksinimlerine göre tasarımı ve doğrulanması oldukça önem arz etmektedir. Bu tez kapsamında, sivil hava sahası içerisinde farklı amaçlar için kullanılacak olan sabit kanatlı dikey iniş ve kalkış yapabilen, sabit kanatlı ve döner kanatlı insansız hava araçlarının matematiksel modelleme ve kontrol sistem tasarımı çalışmaları yapılmıştır.

Tezin ilk bölümünde, sabit kanatlı ve tilt-rotor konseptine sahip bir insansız hava aracı olan Turaç'ın altı serbestlik dereceli doğrusal olmayan matematiksel modeli oluşturulmuştur. Buradaki temel amaç, askı uçuşundan yatay uçuşa ve yatay uçuştan askı uçuşuna geçiş için uygun bir senaryo geliştirmektir. Elde edilen matematiksel model pervane tarafından hızlandırılan hava akımının gövde üzerindeki etkilerini de içermektedir. Bu etkiler seyir hızının, rotor tilt açısının ve hücum açısının bir fonksiyonudur. Pervane tarafından hızlandırılan hava akımının, pervane çıkışındaki kesit alanı ve akış hızı momentum teorisi kullanılarak elde edilmiştir. Gövde ve kanat üzerinde pervane hava akımı tarafından etkilenen alan üzerinde iki boyutlu aerodinamik analizler yapılmış ve pervane hava akımının etkileri modellenmiş, elde edilen aerodinamik katsayılar tablolar içerisinde entegre edilip benzetim ortamına aktarılmıştır. İnsansız hava aracının gövde ve kanatlarının aerodinamik analizi

hesaplamalı akışkanlar dinamiği araçları ile analiz edilmiş ve bu katsayılar da tablolar ile benzetim ortamına aktarılmıştır.

Fazlar arası geçiş durumlarında (askı uçuşundan yatay uçuşa veya yatay uçuştan askı uçuşuna) insansız hava aracı üzerindeki aerodinamik ve itki kuvvet ve momentleri, hava aracı tilt mekanizmasına sahip olduğundan dolayı çok daha karmaşık bir şekilde etki etmektedirler ve aracın dinamiği oldukça karmaşık hale gelmektedir. Bu nedenle geçiş fazlarındaki uçuş güvenliğini sağlamak ve performansı belirli bir seviyede korumak için etkili bir faz geçiş metodunun tanımlanması gerekmektedir. Bu amaçla, uçuş hızı, tilt açısı, hücum açısı ve itki seviyesi için, dinamik sistemin durum değişkenlerine bağlı olarak, denge uçuşunu sağlayacak şekilde uçuş fazları arasında geçiş senaryoları oluşturulmuştur. Bu senaryolarda elde edilen kontrol girişleri, uçuş kontrol sistemine komut olarak beslenebilmekte veya pilota uçuş sırasında kullanabileceği bir tablo olarak verilebilmektedir. Oluşturulan senaryolar kullanılarak geçiş fazı üzerinde benzetim çalışmaları yapılmış ve uçuş testleri gerçekleştirilmiştir.

Tezin ikinci bölümünde, sabit kanatlı bir insansız hava aracı için, döngüde donanımsal benzetim (hardware-in-the-loop) ve uçuş testlerini içeren, model tabanlı uçuş kontrol sistem tasarımı gerçekleştirilmiştir. Bu uygulamada, insanlı hava araçları için geliştirilen sistem tanılama ve uçuş kontrol sistem tasarımı metodolojisi, sabit kanatlı insansız bir hava platformuna uyarlanmıştır. Kullanılan insansız hava aracı platformu, hareketli kara ve deniz araçlarını, belirli bir irtifadan, gövdeye sabit ve aşağı bakan bir kamera ile, otonom bir şekilde takip etmek için geliştirilmiştir. Hava aracının boylamasına ve yanlamasına doğrusal matematiksel modelleri, frekans bölgesinde açık-çevrim sistem tanılama metodolojisi ile elde edilmiş ve zaman bölgesinde doğrulanmışlardır. Tanımlanan doğrusal modeller, yüksek hedef takip başarımı için gerekli olan uçuş kontrol sistemlerinin, birden fazla amaç fonksiyonlu parametre optimizasyonu metodu ile geliştirilmesi amacıyla kullanılmışlardır. Ayrıca, bu süreçte kestirimi yapılan aerodinamik katsayılar, altı serbestlik dereceli doğrusal olmayan modelin oluşturulmasında da kullanılmıştır. Oluşturulan doğrusal olmayan model, döngüde donanımsal benzetim sisteminin ana bileşenini oluşturmaktadır. Test süreci maliyetlerini ve kaza/kırım riskini en aza indirmek için, tasarlanan kontrol sistemleri gerçek uçuş testlerinden önce, döngüde donanımsal benzetim ortamında test edilmişlerdir. Donanım içerisine gömülen kontrol sistemi algoritmalarında herhangi bir mantıksal ve algoritmik hata olup olmadığı incelenmiştir. Tasarlanan ve donanım içerisinde hazır olarak gelen uçuş kontrol sistemlerinin başarımları testleri de gerçekleştirilmiş ve karşılaştırmaları yapılmıştır. Yapılan uçuş testleri, tasarlanan kontrol sisteminin, rüzgar ve türbülanslı uçuş şartlarında, referans takip ve bozucu sönümleme performansının, hazır kontrol sisteminden çok daha iyi olduğunu göstermiştir.

Tezin üçüncü bölümünde, sistem tanılama, model birleştirme (stitching) ve model tabanlı uçuş kontrol sistem tasarımı çalışmaları, agresif manevra kabiliyetine sahip, insansız, dört rotorlu hava aracı üzerinde uygulanmıştır. Üzerinde çalışılan insansız hava aracı, askı uçuşuna yakın şartlarda ve sistem dinamiğinin oldukça değiştiği hızlı ileri uçuş şartlarında agresif manevra kabiliyetine sahip olması için tasarlanmıştır. Bu tür bir sistem üzerinde klasik bir denetleyici tasarım süreci, referans takibinde performans kaybına ve hataların artmasına neden olacaktır. İnsansız hava aracının askı ve hızlı ileri uçuş dinamikleri arasındaki farkı yakalayabilmek için, insanlı hava araçları için geliştirilen uygulamalar esas alınmıştır. Askı ve yüksek hızlı

ileri uçuş fazlarındaki doğrusal matematiksel modeller frekans bölgesinde sistem tanılama çalışmaları ile elde edilmişlerdir. Elde edilen matematiksel modellerin doğrulaması zaman bölgesinde analizler yapılarak gerçekleştirilmiştir. Farklı uçuş hızları için elde edilen uçuş denge koşulları ve tanılanan doğrusal modeller kullanılarak sistemin yaklaşık doğrusal olmayan (quasi-nonlinear) matematiksel modeli elde edilmiştir. Kapsamlı benzetim çalışmaları oluşturulan doğrusal olmayan model üzerinde gerçekleştirilmiştir. Tanılaması yapılan doğrusal matematiksel modeller, farklı dinamik gereksinimleri kısıt olarak içeren, birden fazla amaç fonksiyonu bulunduran optimizasyon tabanlı uçuş kontrol sistem tasarımı sürecinde, en iyi kontrol parametrelerini elde etmek için kullanılacaktır. ADS-33E-PRF içerisinde yer alan ve tam ölçekli helikopterler için kullanılan yanlamasına yeniden konumlandırma ve boylamasına ileri yönde hızlanma ve durma manevraları, kinematik ölçekleme yöntemi ile insansız hava aracı için uygun hale getirilmişlerdir. Tasarlanan denetleyiciler kullanılarak pozisyon koruma, yörünge takibi ve agresif manevra kabiliyeti uçuş testleri yapılmıştır. Ardından, Monte-Carlo benzetim çalışmaları ve uçuş test sonuçları karşılaştırılarak sonuçların ne kadar yakın olduğu incelenmiştir. Test ve analiz sonuçları göstermiştir ki, uygulanan kontrol sistem tasarımı metodolojisi, klasik yöntemler ile karşılaştırıldığında, yüksek hassasiyette ve tahmin edilebilir manevra kontrol kabiliyeti sağlamaktadır.

Tezin dördüncü bölümünde, model referans uyarlamalı kontrol sisteminin bir iyileştirmesi sayılabilecek olan ve kapalı çevrim referans model içeren uyarlamalı kontrol sistemi, takviyeli öğrenme (reinforcement learning) metodu ile geliştirilmiştir. Referans model ile sistemin verdiği cevap arasındaki hata kullanılarak, uygulayıcı-değerlendirici (actor-critic) yapısında ve yapay sinir ağı ile oluşturulan ajan (agent, öğrenen sistem) eğitilmiş, geçici hal cevabını iyileştirmek için kapalı çevrim referans model içerisinde bulunan geribesleme kazancını artırıp azaltması sağlanmıştır. Sistemin benzetim çalışmaları, bir nakliye helikopterinin basitleştirilmiş ve doğrusal boylamasına modeli üzerinde yapılmıştır. Geliştirilen uyarlamalı kontrol sisteminin geçici hal cevabı başarımının, diğer uyarlamalı kontrol sistemlerinin başarımları ile nicel olarak karşılaştırılabilmesi için, sistemin geçici hal performansı ile doğrudan ilişkili olan sinyallerin L_2 ve L_∞ normları hesaplanmıştır. Monte-Carlo benzetim çalışmaları ile incelenen sistemlerin, aerodinamik parametrelerdeki belirsizliklere karşı ne kadar dayanıklı oldukları incelenmiş ve sonuçlar karşılaştırılmıştır. Bu analizler sonucunda, değişken geribesleme kazancına sahip kapalı çevrim referans model kullanan uyarlamalı kontrol sisteminin, açık çevrim referans modele sahip uyarlamalı kontrol sistemine ve sabit geribesleme kazançlı kapalı çevrim referans modele sahip uyarlamalı kontrol sistemine göre çok daha iyi bir geçici hal cevabı performansına sahip olduğu, salınımları önemli ölçüde bastırdığı gösterilmiştir. Ayrıca, geliştirilen sistem üzerinde farklı adaptasyon ve öğrenme stratejileri kullanılarak, geniş bir uçuş zarfı içerisinde sistemin adapte olma kabiliyetini artırma olanağı da sağlanmaktadır. Bir diğer deyişle, geliştirilen uyarlamalı kontrol sistemi daha kapsamlı bir şekilde eğitildiği takdirde, farklı uçuş şartlarında da sistemin geçici hal cevabının iyileştirilmesi mümkün olmaktadır.

1. INTRODUCTION

Urban air mobility has an increasing demand as a result of developments in battery, electric propulsion systems and autonomy technologies. These fundamental subjects provide a solid background to increase mobility, sustainability, capacity, functionality and, above all, safety of the transportation process. These requirements are met by designing novel manned and unmanned aerial platforms in passenger and cargo transportation applications such as Vahana, Volocopter, Prime Air and Zipline projects.

Importance of the aerial vehicles in military applications is an unquestionable fact. However, using the aerial vehicles in the urban airspace is a relatively new research field which is called as urban air mobility concept. In these applications, manned and unmanned aerial vehicles are both used in passenger and cargo transportation in urban airspace. It is an efficient solution in terms of operating and maintenance costs when compared to conventional aerial transportation. However, integration of these vehicles into the urban airspace requires inter-disciplinary studies that include various research fields such as air traffic management, flight control systems (FCS), aerodynamics, flight mechanics, electric propulsion and battery technologies. The main objective to integrate these research fields is providing safety, reliability and connectivity of the urban air space.

Fixed-wing vertical-takeoff-and-landing (VTOL) concept is quite popular in the urban airspace applications due to its forward flight and hovering capabilities. It combines advantages of the rotary-wing and fixed-wing aircraft platforms in one airframe. Also, it is possible to operate these systems with minimal infrastructure requirements. In literature, there are several examples for the fixed-wing VTOL aircraft concepts with tilt-wing and tilt-rotor mechanisms. In both systems, thrust direction is controlled to complete the transition between hover and forward flight phases. However, in the transition phase, dramatic changes occur in dynamical characteristics due to the variations in the aircraft configuration and it is important to investigate the dynamics of the aircraft to design a suitable flight control system.



Figure 1.1 : Turac VTOL UAV in flight test.

The first part of this thesis includes mathematical modeling of a tilt-rotor VTOL unmanned aerial vehicle (UAV), Turac, which is designed and developed in ITU Control and Avionics Laboratory. Turac is designed based on flying wing concept and it has a blended wing profile that provides longitudinal stability of the airframe. By using the blended wing profile, aerodynamic efficiency of the system is enhanced up to 20% when compared to the conventional design. A capture from flight test of the Turac VTOL UAV is given in Figure 1.1.

Turac VTOL UAV has two tilt-rotor mechanism on the leading edge of the wings and one main coaxial lifting fan embedded into the body. In hover and near-hover flight phases, there is no aerodynamic force and moments acting on the airframe. However, in the transition flight phase, aerodynamic forces and moments occur as a result of increased dynamic pressure. In addition to the free airstream effects, propeller induced airflow also creates extra aerodynamic forces and moments on the airframe as a function of flight speed and tilt angle. These effects on the UAV are modeled and 6-degree-of-freedom (DoF) nonlinear mathematical model is developed. Required aerodynamic coefficients are calculated by using computational fluid dynamics (CFD) analysis and empirical tools. Also, to perform a safe transition between the hover and forward flight phases, trim conditions are calculated for different flight speed and tilt angle values. This data can be used as a reference for the FCS or as a transition aid for the pilot. A sample transition flight simulation result is given in Figure 1.2.

After the first flight test of the autopilot, called as Sperry's gyroscopic stabilizer, in 1912, flight control systems have become one of the fundamental subsystems

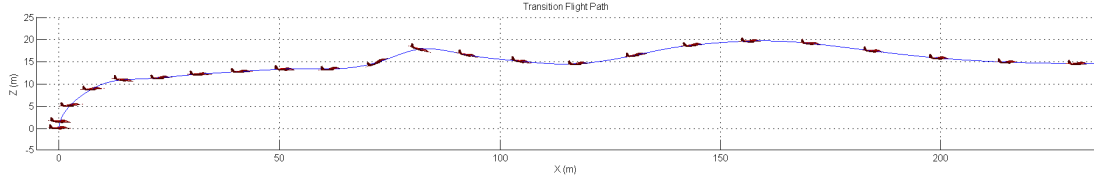


Figure 1.2 : Transition flight simulation of the Turac VTOL UAV.

of the aircraft and rotorcraft platforms. Technological developments, especially in electronics, have led compact, lightweight and cost-effective flight control system solutions. Such that, it is possible to find a flight control system for a conventional UAV at \$150 price. These systems provide very effective solutions for ordinary and non-critical missions. However, the airspace integration process of an aerial vehicle requires a verified and certified flight control system which can be obtained by using a reliable design workflow.

In this workflow, there are four main steps that must be applied. These are 1) obtaining verified mathematical model of the aerial platform, 2) flight control system design and analysis based on selected performance requirements, 3) software-in-the-loop (SIL) and hardware-in-the-loop (HIL) tests and 4) performing validation flight tests of the embedded controller. After two or three iterations, a reliable flight control system can be obtained with desired performance specifications.

Obtaining a verified mathematical model of the aerial vehicle is the first and most important step of the flight control system design workflow. High/mid-fidelity mathematical model provides an insight about the dynamical characteristics of the aerial platform, shortens the design period and reduces development costs. In addition, it is used in SIL-HIL simulation step of the design workflow which reduces crash risk in the flight tests. After obtaining the verified high/mid-fidelity mathematical model of the aerial vehicle, flight control system can be designed to improve the dynamical characteristics of the vehicle by using feedback and feedforward loops. At this point, it is important to define and determine the dynamical requirements to complete the mission successfully. By utilizing the selected requirements, a multi-objective optimization is applied to obtain the optimal control parameter set by using selected handling and flight quality specifications as optimization constraints. In this step, a pareto-optimal solution is required which satisfies the selected dynamical characteristics while minimizing the actuator usage. After initial evaluations of the

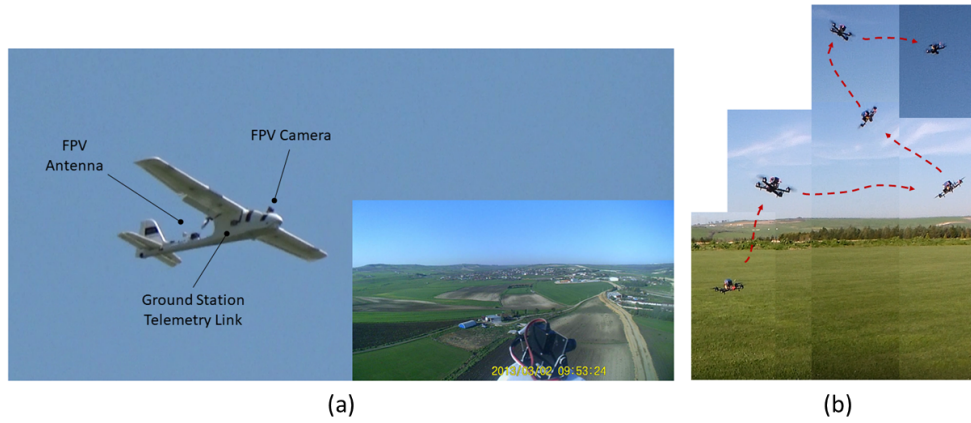


Figure 1.3 : General view of a) fixed-wing and b) rotary-wing UAV platforms used in this thesis.

closed-loop performance, the proposed flight control system algorithm is embedded into the main flight control computer (FCC) software and hardware and then SIL and HIL tests are performed. This is a critical step in which FCC software is evaluated and tested against algorithmic and logic errors that may cause catastrophic accidents. After the debugging process of the FCC software and hardware, initial flight test procedure is applied and closed-loop system performance is evaluated in terms of selected design requirements. Optimized and validated FCS can be obtained after two or three iterations based on this design cycle with minimal cost and crash risk. In the second and third part of the thesis, this design workflow is applied on fixed-wing and rotary-wing UAVs given in Figure 1.3. Linear mathematical models are obtained by using frequency-domain system identification process and they are verified in time-domain. 6-DoF nonlinear mathematical models are created by using the identified aerodynamic parameters. Flight control system architectures are determined as classical nested-loop proportional-integral-derivative (PID) structure. Optimal control system parameters are obtained by using multi-objective parameter optimization method in which selected handling quality requirements are used as optimization problem constraints. Then, designed controllers are tested and verified in the real flight tests after SIL-HIL simulations.

Methodological design process and a verified mathematical model are key elements in flight control system design applications. Hence, in this work, an iterative design pathway, which is called as desktop-to-flight control system design workflow [2], is utilized. This methodology is developed and validated by several applications on the manned and unmanned aerial platforms. In this workflow, system identification,

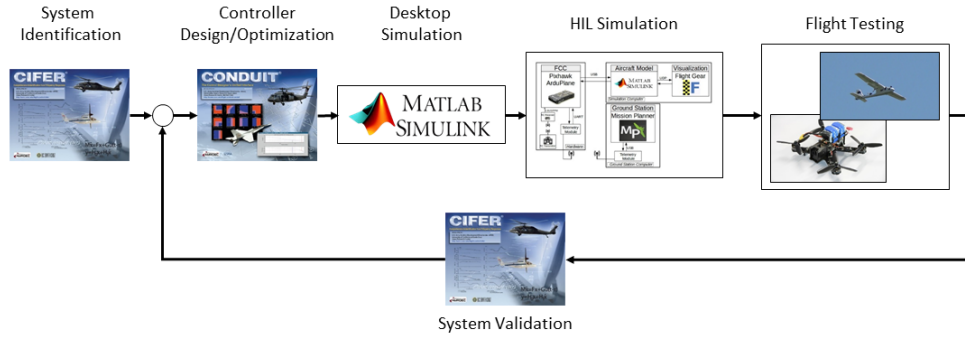


Figure 1.4 : General view of the desktop-to-flight design workflow [2].

multi-objective optimization based flight control system design, desktop simulations, HIL tests and validation/verification steps are tightly connected in an iterative way. The general scheme of the desktop-to-flight design workflow is given in Figure 1.4.

Originally, this workflow is developed for full-scale manned aerial vehicles. Especially in the *Controller Design/Optimization* step, all of the performance specifications are originated from manned aircraft and rotorcraft domain. In recent years, several studies are focused on applying this workflow on UAVs and MAVs by scaling-down the design requirements and they have promising results. Hence, one of the main purposes of this thesis is to demonstrate the desktop-to-flight control system design workflow on fixed-wing and rotary-wing MAVs such as Ranger-EX and Racer quadrotor platforms given in Figure 1.3. It is observed that the desktop-to-flight design workflow is also quite effective on unmanned and scaled platforms. To complete the general view and brevity, flight test results for fixed-wing and rotary-wing platforms are given in Figure 1.5 and Figure 1.6, respectively.

Doublet reference tracking flight test results of the optimized and legacy (Ardupilot) attitude control systems are given in Figure 1.5.a. It is obvious that the rise time and settling time of the optimized controller are shorter than the legacy one. In addition, pitch attitude reference tracking test results are given in Figure 1.5.b. Steady-state error and overshoot is observed in the closed-loop system response with the legacy controller. This situation results in deterioration of the mission success. On the other hand, optimized pitch attitude controller has better reference performance and it is suitable for missions in which precise reference signal tracking is necessary.

The explained desktop-to-flight design workflow is also applied on the agile quadrotor platform. System identification is performed for hover and forward flight phases and

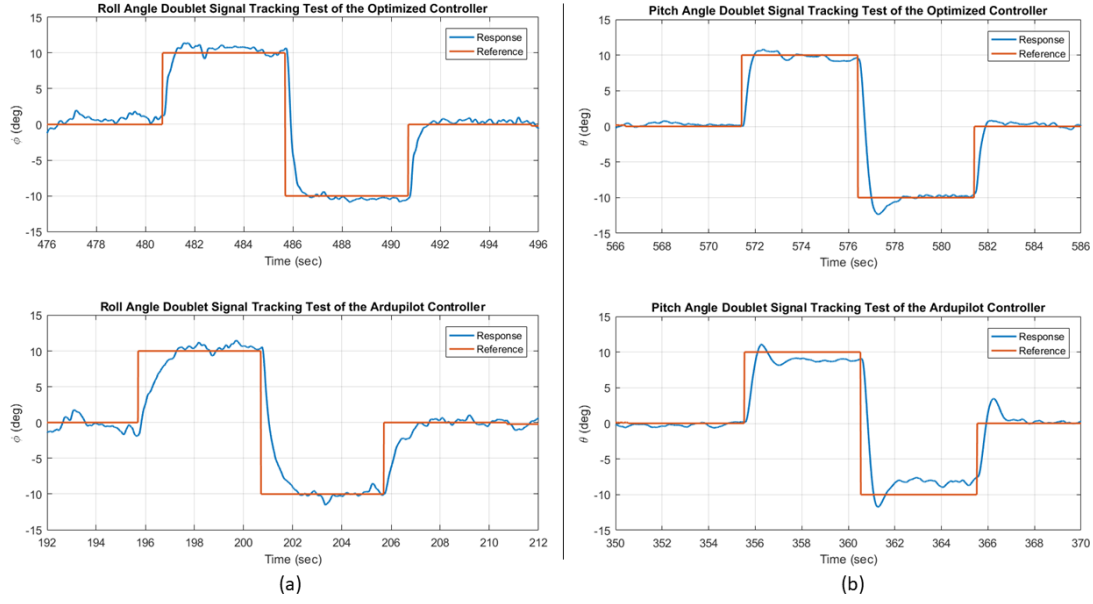


Figure 1.5 : Attitude reference tracking performance tests of the optimized and legacy controllers on the fixed-wing MAV, a) Roll attitude control system responses, b) Pitch attitude control system responses.

a stitched quasi-nonlinear model is developed for simulation purposes. Trajectory tracking is not possible by using the legacy control system Ardupilot. Hence, a modification is performed and controller parameters are optimized. Then, system performance is evaluated in several flight maneuvers such as depart-abort and lateral reposition. Depart-Abort maneuver sequence is designed for full-scale rotorcrafts to evaluate their longitudinal reposition capability for various aggressiveness levels. However, it cannot be used directly for the MAV platforms and it should be scaled-down based on several geometric specifications such as rotor diameter and rotor-to-rotor diagonal distance. Simulation and flight tests results are given in Figure 1.6 for scaled-down depart-abort maneuver with different aggressiveness levels. As seen in these plots, the proposed trajectory tracking system is quite successful for various aggressiveness levels. Also, closed-loop system responses that obtained from the simulation environment and actual flight tests are quite similar to each other which indicates adequate fidelity of the mathematical model.

One of the most important issues in flight control system design for an aerial vehicle in the urban airspace is to provide the safety of the operation in the presence of variations in the system parameters and/or component faults and failures. Aerodynamic parameters of the aerial vehicle change as a function of airspeed and aerodynamic angles. Also, mass properties of the aerial vehicle are directly affected by flight

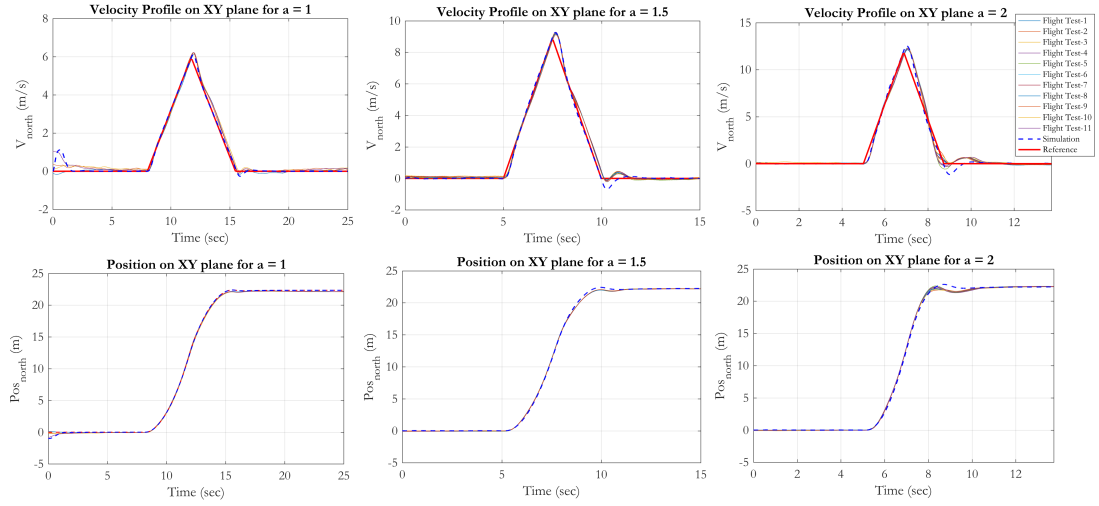


Figure 1.6 : Depart-Abort maneuver test results for different aggressiveness levels ($a = 1, 1.5, 2$).

weight (i.e. payload and/or passenger weight). These variations in the dynamical characteristics of the aerial vehicle are observed frequently in urban operations. Hence, FCS should compensate these changes and provide the flight stability and safety.

Adaptive control theory is a promising tool which has been developed to handle with the parameter variations and uncertainties in a dynamical system. It is also quite suitable for aerial platforms that have wide range of flight envelope in which dynamical characteristics change dramatically. The first application of the adaptive controller on an aircraft was NASA X-15 program in which three hypersonic X-15 aircrafts were flown. The first and second aircrafts are called as X-15-1 and X-15-2 and they were equipped with classical stability augmentation systems in which look-up tables are utilized to obtain the controller gains. The third aircraft, X-15-3, was equipped with a Honeywell MH-96 self-adaptive controller in which control parameters were adjusted throughout the flight envelope to increase the performance of the aircraft. As a part of the X-15 program, nearly 200 flight tests were performed between 1959 and 1968. This time period is called as *brave era* in [6] because of quite short development path from idea to flight test without performing comprehensive theoretical analysis in between. Grievously, on November 15 in 1967, a fatal accident occurred with the X-15-3 because of the limit cycle oscillation which was led by the adaptive controller [7].

After the X-15-3 accident, several studies have been performed on design and analysis methods of the adaptive controllers for the systems with parametric uncertainties.

Table 1.1 : 500-Run Monte-Carlo analysis results of the MRAC, CRM and RL-CRM adaptive systems.

Performance Metrics	MRAC ($l = 0$)	CRM ($l = l_{opt}$)	Improvement (%)	RL-CRM	Improvement (%)
$\ \hat{\dot{k}}_q\ $	15.2114	3.7341	75.4520	2.4489	83.9008
$\ \hat{\dot{k}}_{qcmd}\ $	18.4647	7.8298	57.5958	5.5146	70.1344
$\ \hat{\dot{\theta}}\ $	0.0888	0.0338	61.9369	0.0207	76.6892
$\ q_m\ _\infty$	0.2	0.2064	-3.2	0.2	-
$\ e\ $	0.4616	0.1957	57.6039	0.1379	70.1256
$\ e^o\ $	0.4616	0.3928	14.9047	0.3886	15.8145
$\ \dot{u}\ $	6.5704	2.0811	68.3262	1.4163	78.4290

Today, the adaptive control theory is a powerful tool for aerial vehicles with large flight envelopes and parametric uncertainties.

Model reference adaptive control (MRAC) system is one of the fundamental applications of the adaptive control theory. It has been applied on several aerial platforms and munitions. Also, modifications are developed to increase the robustness characteristics of the MRAC algorithm. However, the most problematic issue in the MRAC is high-frequency oscillations observed in the control signal at the beginning of the adaptation. This oscillatory behavior may result in catastrophic accidents in the aerial missions. Hence, transient response of the MRAC has to be modified and improved to provide safety of the closed-loop system. For this purpose, modifications are performed on the MRAC and several adaptive control systems are developed such as combined-composite model reference adaptive control (CMRAC) and closed-loop reference model (CRM) adaptive control systems.

In CMRAC system, indirect and direct adaptive control algorithms are combined and estimated system parameters are used in the adaptation laws. It offers increased robustness against parametric uncertainties. Although the stability proof of the CMRAC system is given in the literature, no guarantees were provided for improved transient response performance and it has remained as a conjecture. In CRM-adaptive systems, an observer gain is used in the closed-loop reference model to increase the transient performance of the system. It is shown that by using an optimal value of the observer gain, it is possible to damp oscillatory transient responses in adaptive parameters and control signals. In the last part of this thesis, we proposed further improvement in the transient performance of the CRM-adaptive system by introducing

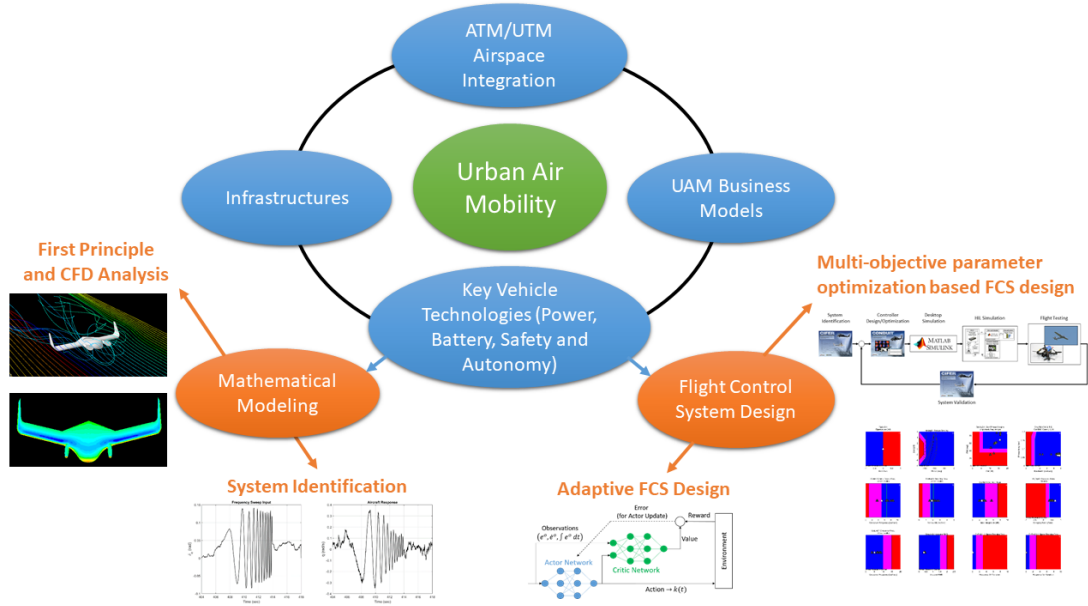


Figure 1.7 : General overview of the key aspects of urban air mobility concept.

a time-varying scaling factor for the optimized observer gain. A reinforcement learning (RL) agent is utilized for this purpose and it is trained by using deep deterministic policy gradient (DDPG) algorithm according to the error between original reference model and system responses. After the training process, it is shown that the proposed RL-CRM adaptive control algorithm has superior performance than the MRAC and optimized fixed-gain CRM-adaptive systems in terms of selected key signal norms. Monte-Carlo simulations are performed to evaluate the system robustness in the presence of parametric uncertainties and results are introduced in Table 1.1 for brevity.

In the urban air mobility (UAM) concept, there are four key aspects that should be considered. These are air traffic management (ATM) / UAV traffic management (UTM) integration, UAM business models, infrastructures and key vehicle technologies such as power, battery, safety and autonomy. As it is understood from the above mentioned explanations, this thesis mainly focuses on mathematical modeling and flight control system design subjects which are included in the key vehicle technologies. To clarify the focus point of the studies that are covered in the thesis, Figure 1.7 is given in which general overview of the urban airspace concept is summarized. In this figure, key aspects are pointed out as orange ellipses which are in the scope of this thesis.

The remaining of this thesis is organized as following; in Chapter 2, theoretical background about the system identification, multi-objective parameter optimization based flight control system design, CRM-adaptive systems and DDPG reinforcement

learning method is given briefly. In Chapter 3, nonlinear model of the Turac VTOL UAV, which covers hover, transition and forward flight phases, is developed. In Chapter 4 and Chapter 5, desktop-to-flight control system design workflow is utilized on the fixed-wing Ranger-EX UAV and Racer highly agile quadrotor MAV. The proposed control systems are evaluated in actual flight tests. In Chapter 6, CRM-adaptive system is augmented by using reinforcement learning method to improve the transient response performance of the dynamical system. Proposed algorithm is demonstrated on a simplified pitch dynamics of a transport helicopter. In Chapter 7, concluding remarks and possible future works are discussed.

1.1 Purpose of Thesis

There are three main purposes of this thesis. The first one is developing a 6 degree-of-freedom nonlinear mathematical model of the Turac fixed-wing VTOL UAV by utilizing physics-based modeling approach. In this study, aerodynamic parameters of the UAV are determined by utilizing CFD analysis. Propeller-induced airstream effects are modeled separately and summed into the aerodynamic forces and moments. Trim analysis is performed for the transition phase to provide a reference trajectory for the flight control system and pilot. System performance is evaluated by utilizing soft-real-time transition flight simulations.

The second purpose is to demonstrate the flight control system design workflow step-by-step which includes system identification, verification, nonlinear modeling, control system design and analysis, SIL and HIL simulations and real flight tests. This workflow is applied on fixed-wing and rotary-wing unmanned aerial platforms and test results are given.

The third purpose of this thesis is improving the transient performance of the CRM-adaptive system by using reinforcement learning method. An agent is created in the form of a neural network and it is trained to increase or decrease the feedback gain of the reference model in the CRM-adaptive system. The proposed RL-CRM adaptive system is analyzed against parametric uncertainties and its performance is compared with MRAC and optimized fixed-gain CRM-adaptive systems.

1.2 Literature Survey

Aerodynamic analysis of VTOL fixed-wing air vehicles can be divided up as aerodynamic analyses of hover, transition, and forward flight regimes. For the hover regime, numerous studies have been performed experimentally and numerically. In [8], a quad tilt-rotor in hover mode is modeled and analyzed by using the CFD method. The pressure distribution on the wing, flow-field around the vehicle, and spanwise loading is investigated in and out of ground effect. Another study [9], which includes CFD analyses of a full and half span V-22 tilt-rotor configuration in hover mode, has been done in order to observe flow-field around the vehicle. Rotor performance differences between two different models are evaluated. In [10], rotor/wing interaction, aircraft aerodynamics, pressure distribution, and force loading along wingspan are experimentally investigated on a quarter-scale V-22 tilt-rotor aircraft in hover mode.

For forward flight regime, performance and design of conventional tilt-rotors and quad tilt-rotors have been investigated in [11]. In these concepts, lift-to-drag ratio is directly related to interference, reduction in rotor tip speed and the change in rotational direction of the rotor. Wind tunnel tests and CFD analysis are utilized to evaluate the flow field around the airframe and to determine the aerodynamic parameters [12, 13]. The propeller is modeled as an actuator disc in [14] to investigate the propeller/wing interaction on a transport class aircraft. Furthermore, aerodynamic stability and control coefficients of TR-E2S1 tilt-rotor aircraft are calculated by using the CFD method and the wind tunnel tests. The results from both methods are evaluated and compared at the end of the study [15]. The same methods are applied to V-22 Osprey tilt-rotor aircraft in forward flight regime [16]. In [17], Yak-54 is analyzed aerodynamically and results from Vorstab, Fluent, and Aircraft Advanced Analysis (AAA) are compared. In these studies, the area on the wing affected by propeller cannot be specified exactly by using CFD methods or wind tunnel tests. The area affected by the propeller is defined with mathematical formula, so this brings freedom about in which angle of attack and tilt angle should be set to use the advantage of the propeller effect.

In the transition flight regime, the dynamics of the vehicle includes the effects that are observed in both the hover and the forward-flight regimes. Thus, studies about

dynamic modeling of the transition regime mainly focuses on the two fundamental flight regimes (namely hover and forward flight) and blending of these two models through parameterization. In [18], modeling, control and simulation of a tilt-duct UAV are presented. Two – loop state-dependent Ricatti Equations (SDRE) control algorithm is applied. Allocating of the controllers during the transition flight is achieved by using blended inverse control allocation algorithm. Specifically, equations of motion of the tilt-duct UAV are described in two flight regimes and the stability analysis is performed based on the linearized equations of motion for trim flight condition. In [19], authors describe modeling, control and test results of a four tilt-rotor micro aerial vehicle. For hover flight mode, a nonlinear control algorithm is proposed which consists of feedback linearization and hierarchical control scheme. A Lyapunov-based backstepping control algorithm is developed for horizontal flight mode. In the follow-up work [20], the authors model the aerodynamic forces in two primary flight regimes and the transition strategy for a control algorithm is defined. Thus in general, studies on the aerodynamic analysis of aircraft are mostly about hover and forward flight regime. However, transitional flight is the most complex case due to the flow-field around the airframe, rotor/wing interaction, pressure and force loading throughout the wingspan. In some experimental work [21,22], different flap deflections were tested to develop rotor/wing interactions, pressure, force loading, and velocity distribution along wingspan. However, in the literature, there is no work on flow-field around aircraft in transition mode using CFD or other numerical methods.

In our approach, we focus on modeling of the aerodynamic effects in the transition phase as a standalone analysis instead of blending the hover and forward flight aerodynamics. Propeller-induced and free airstream effects are modeled separately by using the CFD analysis method and aerodynamic database is embedded into the nonlinear model. Thrust – airspeed test results of the propeller that are used in tilt-rotor assembly is obtained from the manufacturer’s database, a lookup-table is generated for this relationship and embedded into the nonlinear model.

In literature, there are several studies about the system identification and control system design applications for manned aerial platforms. In [23], closed-loop handling qualities of the AH-64D Apache helicopter are evaluated and higher-order linear model is obtained at hover flight condition. Then, the identified model is integrated with the

baseline control algorithm of the AH-64D and the performance of the closed-loop system is evaluated. In [24], flight control system is designed for AH-64D helicopter to provide Level-1 handling qualities in the day and degraded visual environments by using ADS-33E design specifications. In [25], lateral/directional mathematical model of a large wide-body transport aircraft is obtained by using the frequency domain system identification method and the obtained model is verified in the time domain. In [26] and [27], longitudinal and lateral/directional flight control systems are designed for a business jet by using multi-objective parametric optimization approach for different flight conditions.

Several studies have shown that the system identification and flight control system design procedure can be completely scaled-down for the MAVs and this design workflow promises successful results. The identification process is a bit more complicated for the unmanned rotorcrafts than the fixed-wing platforms because of their inherent instability. [28] describes the frequency domain system identification, characterization and control design for the unmanned rotorcrafts. In [29], state-space models of the Yamaha R-MAX unmanned helicopter are identified and verified for both hover and forward flight conditions. In [30], system identification, inner- and outer-loop control system development processes are described for MQ-8B Fire Scout autonomous helicopter platform. Closed-loop dynamical model of a quadrotor is identified by using the frequency-domain system identification process in [31]. Bare-airframe dynamics of a quadrotor MAV is identified and control system is designed in [32] and [33]. Also, as another example, identification of the bare-airframe dynamics of the quadrotor MAV is studied in [34]. Most of the fixed-wing unmanned aerial platforms have stable open-loop dynamics which is required for open-loop system identification process. In this method, control systems are disengaged and pilot command is applied into the control surfaces, directly. In [35], identification of the system dynamics of the Dynam HawkSky model airplane is performed. The goal of this study is to develop a classroom flight dynamics demonstrator. In [36], state-space model of a 12% scale Cessna 182 UAV is identified by using the frequency-domain system identification process. Then, closed-loop performance requirements are defined for a surveillance-type mission and longitudinal attitude control system is designed by using selected design specifications. In [37], system identification procedure is

described and applied on Ultra Stick 25e MAV. Sensitivity and residual analyses are performed to improve the verification of model accuracy. As a complementary study of the reference [37], an overview of the airborne experimental test platform is provided in [38]. Subsystems of the test platform such as simulation models, controllers and synthetic air data system, are described. In [39], flight dynamics model of a tail-sitter MAV is identified and verified from flight data. Both inner and outer control loops are optimized for turbulence rejection and performance comparisons are performed for the proposed and legacy controllers.

Model fidelity level of a UAV platform plays a crucial role in formulating the efficiency airspace integration. Specifically, accurate mathematical models, covering the flight envelope of the aerial vehicle as much as possible, ensures capability to provide high-performance navigation capabilities. This specific issue becomes more critical for the aerial platforms with wide flight envelope because of significant deviations in the system dynamics in different flight conditions. To increase the model fidelity of a rotorcraft in the forward flight phase, model stitching technique is developed by Zivan and Tischler in [40] and applied to obtain the continuous full flight-envelope model of the Bell 206 helicopter. In [41], full flight-envelope mathematical model of the Calspan NF-16D Variable-stability In-flight Simulator Test Aircraft (VISTA) is developed by utilizing the stitching method and verified by using the recorded flight data. In addition to the manned aircrafts, model stitching is also applied for the UAVs and MAVs. In [42], full flight-envelope mathematical model of the unmanned K-MAX rotorcraft platform is obtained and flight control systems are optimized. In [43], model stitching method is applied for a quadrotor platform and developed STITCH software is introduced. In [44], stitched model of an octocopter platform, which performs package delivery missions with the varying size of payloads, is generated and verified.

Extensive researches were performed in the early 1950s about adaptive control systems in related with the design of autopilots for high-performance aerial vehicles which had a wide flight envelope. However, the interest in adaptive control applications diminished day by day because of the limited technological developments at that time. After the 1960s, several studies were performed about state-space models, stability theory, stochastic control theory and dynamic programming which provided theoretical background and increased the understanding of the adaptive control theory.

The original approach of the model reference adaptive control is called as *MIT rule* which was developed at the Instrumentation Laboratory at MIT in the late 1950s and early 1960s to improve the flight performance of aircrafts and spacecrafts [45]. In the late 1970s and early 1980s, stability proofs of the adaptive control theory appeared. Also, in the late 1980s and early 1990s, robustness of the adaptive controllers was studied which gave a new insight to the adaptive controllers. Several improvements were applied on classical model reference adaptive control algorithms such as σ , e and dead-zone modifications in [46], [47] and [48].

Transient response of the model reference adaptive control (MRAC) system is the most important phase that should be considered. Because of the initial errors in the adaptation parameters and high adaptation rates, high-frequency oscillation may occur in the transient response phase which is not desired especially in aerial platforms. Hence, to improve the transient response of the MRAC, several studies were performed. In [49, 50], combined/composite MRAC (CMRAC) structure is developed in which direct and indirect adaptive control algorithms are utilized together. Although CMRAC provides a better transient performance, rigorous guarantees are not provided and it remains as a conjecture. In addition to the CMRAC, the MRAC structure is modified and a feedback gain is included in the reference model [51–53]. This structure is called as closed-loop reference model (CRM) adaptive system. In this system, tracking error is also included in the reference model and an additional design freedom is provided for tuning of the controller parameters. However, there is a trade-off between improved transient response and convergence speed of the adaptation parameters. Hence, CRM-adaptive control system parameters should be selected by utilizing an optimization process. Otherwise, water-bed effect may occur in the tracking error and time derivative of the control signal [52].

To sum up all of the above mentioned thesis proposal and literature survey, a brief and concise comparison of the state-of-the-art and contribution of this thesis are summarized and listed in Table 1.2.

Table 1.2 : Comparison of the state-of-the-art and thesis contributions.

	State-of-Art	Thesis Contribution
Turac VTOL UAV	Aerodynamics effects in the transition phase are studied based on several simplifications and assumptions. In most of the studies, propeller-induced airflow effects in the transition phase are either neglected or modeled in a simple way such as a linear function of the tilt angle.	A detailed and new aerodynamics and trim methodology is developed including free airstream and propeller-induced airstream effects on the UAV airframe. Propeller-induced airstream effects are modeled by using 2D Vortex Lattice Method (VLM) and momentum theory. The new mathematical model and the methodology that was developed has been referenced and applied in numerous follow up studies.
Applications of Desktop-to-Flight Control System Design Workflow	Desktop-to-flight control system design workflow has been developed by US Army, Universities Space Research Association and NASA. There are lots of successfully applications on manned aerial vehicles.	Up to authors' knowledge, several local defense companies have started to use this design workflow, however the full cycle has not been demonstrated and it has not been applied on academic research realm. This thesis is the first full cycle (system identification, control system design, verification,) application of the workflow in a research laboratory in Turkey. This work has increased the maturity of the theoretical research and provided a much needed baseline controller design process to which every new is benchmarked against. Both the process and the results have provided a breakthrough in local micro UAV control system design and implementation methodology extending it beyond empiric gain tuning.
	The design workflow has also been used for unmanned aerial vehicles such as fixed-wing and non-agile rotary-wing platforms in recent years with promising results.	In this thesis, the design workflow is applied on a fixed-wing and agile quadrotor platforms. To the authors' knowledge, it is the first time that the design workflow is applied on a highly-agile multi-copter platform which has a significantly wider flight envelope and thus providing modeling challenges that need to be addressed. The model as developed has been used in designing agile flight control systems which demonstrate significant agility metrics in performance not demonstrated in previous autonomous flight designs.

Table 1.2 (continued): Comparison of the state-of-the-art and thesis contributions.

	State-of-Art	Thesis Contribution
RL-CRM Adaptive System	Closed-loop reference model (CRM) adaptive control system has been developed to increase the transient response performance of the system. Fixed feedback gain of the reference model is determined by utilizing an optimization process.	In this thesis, we introduced a new reinforcement learning (RL) based CRM-adaptive control methodology which utilizes time-varying feedback gain of the closed-loop reference model. The variation policy of this gain is determined by an RL agent which is trained by utilizing the deep deterministic policy gradient algorithm. This modification provides almost 10% improvement in the transient response performance in terms of key signal norms when compared to the optimized fixed-gain CRM-adaptive system.

2. THEORETICAL BACKGROUND

As it is seen from the Introduction chapter, this thesis covers and integrates several applications from different domains such as system identification, control system design optimization, adaptive control theory and reinforcement learning. Hence, it is useful to review some of the basic subjects of these research areas as a brief introductory to define and complete the connections between them.

This chapter is organized as follows; in Section 2.1, basic definitions for test input design and frequency-domain system identification theory is given. In Section 2.2, model stitching technique is described and quasi-nonlinear simulation environment is introduced. In Section 2.3, multi-objective parameter optimization based control system design process is summarized and several requirements are described. In Section 2.4, general scheme of the closed-loop reference model (CRM) adaptive control system is reviewed. In Section 2.5, deep deterministic policy gradient (DDPG) algorithm is summarized which constitutes a basis for training a reinforcement learning agent for continuous-time control applications.

2.1 Frequency Domain System Identification Method

Frequency-domain system identification method was developed to characterize the dynamical behavior of a system such as fixed-wing and rotary-wing aerial vehicles. Identified linear models are used in control system design process, evaluation of handling qualities and validation of nonlinear simulation models. General structure of the system identification process is given in Figure 2.1. In this method, pilot- or computer-generated test input signal which has good spectral content is applied to the control effectors to excite the interested dynamical mode of the aircraft. Then, system responses are measured by an inertial measurement unit (IMU) and logged onboard. Before starting the system identification process, it is important to check the data consistency against several error sources on the measurement system such as drift, bias and scale factors. In practical applications, it is not possible to obtain all of the states

as measurements. So, after checking the data consistency, required but unmeasured states can be reconstructed from the measured data by using dynamical and kinematical relationships. Then, spectral analysis of the prepared database is performed and non-parametric model of the system is obtained which characterizes the dynamical behavior of the system without the need for a model structure. Non-parametric models are useful for preliminary analysis and applications such as control system design, evaluation of the handling qualities, stability margin determination (phase and gain margins) and validation of the simulation environments. After obtaining the non-parametric model, parametric model is fitted on the frequency responses. The first step for parametric modeling is to determine a transfer function model structure in which gain, pole and zero locations are obtained for a best match to the frequency response data. The transfer function model can be described as a low-order equivalent system (LOES) approximation of the nonlinear dynamics. So, it is useful especially for handling quality analysis and control system design process. Transfer function models are final products for most of the system identification studies in the aeronautics field. The next step of the system identification process is obtaining the state-space model of the dynamical system. The state-space model structure is developed based on the linearized equations of motion and it provides more insight into the dynamics of the system. Hence, transfer function models can be used as initial guesses of the dynamical characteristics for the state-space models.

2.1.1 Test input design

The frequency sweep input design is crucial for the frequency-domain system identification applications. The input signal should cover a broad range of frequency to excite the interested dynamical modes. If the mode is not excited, its characteristics could not be identified. Hence, test signal should be designed according to Equations (2.1) to (2.3) to collect data which represents the dynamical characteristics of the system.

$$f_{min} = \frac{\omega_{min}}{2\pi} \quad (2.1)$$

$$f_{max} = \frac{\omega_{max}}{2\pi} \quad (2.2)$$

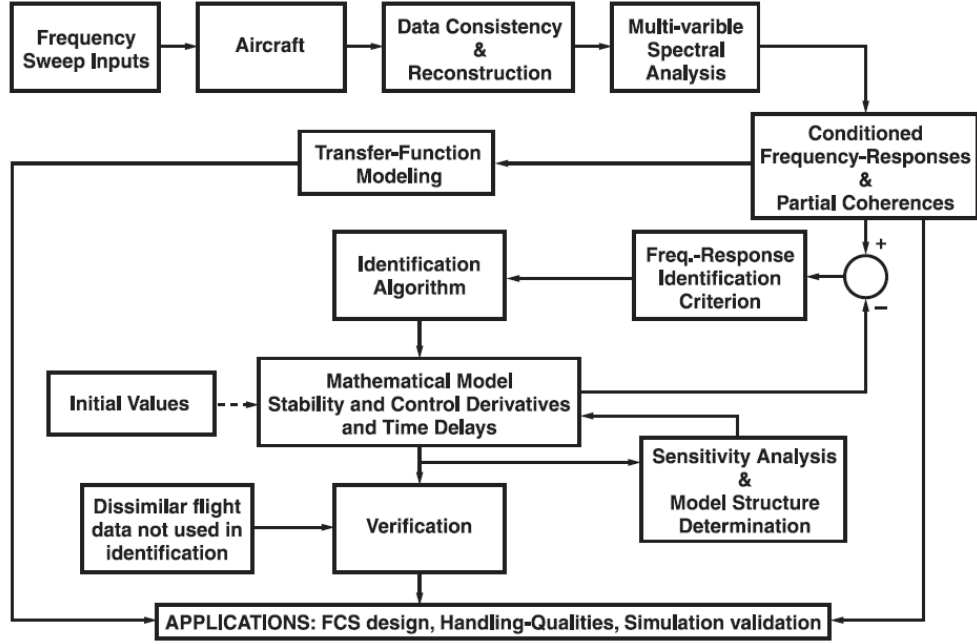


Figure 2.1 : Frequency-domain system identification workflow [3].

$$T_{rec} \geq (4 \text{ to } 5) \times T_{max} \quad (2.3)$$

where, f_{min} , ω_{min} , f_{max} , ω_{max} are defined as minimum and maximum frequency bounds of the interested frequency range, T_{max} is maximum time period which is determined by using f_{min} and T_{rec} is total sweep record length.

The desired maximum frequency of model applicability ω_{max} is an important factor to determine the filter cutoff frequency and sampling rate of the sensors. Theoretically, sampling rate can be set as $2\omega_{max}$ which puts the Nyquist frequency ($\omega_{Nyq} = 0.5\omega_s$) at the maximum frequency of interest. However, due to the atmospheric disturbance and sensor noise, an accurate system identification cannot be obtained with low sampling rate. As a rule of thumb, the filter cutoff frequency (ω_f) and sampling rate (ω_s) are determined by using equations 2.4 and 2.5 [3].

$$\omega_f \geq 5\omega_{max} \quad (2.4)$$

$$\omega_s \geq 5\omega_f \quad (2.5)$$

2.1.2 Data consistency

Before the system identification process, it is important to perform a data consistency analysis for measured and estimated variables. There are two general groups of error sources that lead to data inconsistency. The first group is deterministic sources and it consists of sign convention, instrument calibration error, unknown bias and drift in attitude and body rate measurements. The second group is non-deterministic or random sources which consist of data loss, signal noise and disturbances. The whole dataset is evaluated by using consistency analysis against the above mentioned potential error sources. Especially for off-the-shelf autopilots and data logging systems, such as Pixhawk, it is crucial to check the consistency of the measured and estimated data.

If it is assumed that the system identification test flight is performed in the trim flight conditions, the Euler angle and body rate relationships can be given as shown in equation 2.6.

$$\begin{aligned} p &= \dot{\phi} \\ q &= \dot{\theta} \\ r &= \dot{\psi} \end{aligned} \tag{2.6}$$

The Laplace transformation is applied to the equation 2.6 and the results are given in equation 2.7.

$$\begin{aligned} p &= s\phi \\ q &= s\theta \\ r &= s\psi \end{aligned} \tag{2.7}$$

An error model is developed for the measurements and estimations as shown in Figure 2.2. Here, $\lambda_{rate}(\lambda_p, \lambda_q, \lambda_r)$ is a scale factor of the body rate measurements and $\lambda_{Att}(\lambda_\phi, \lambda_\theta, \lambda_\psi)$ is a scale factor of the attitude measurements. By using these definitions, attitude and body rate measurements are represented as shown in equation 2.8.

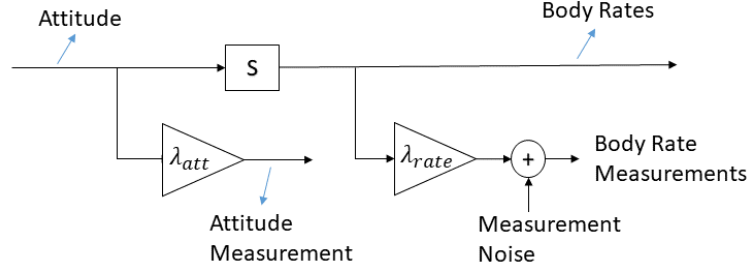


Figure 2.2 : Attitude and body rate measurement error model.

$$\begin{aligned}
 \phi_m &= \lambda_\phi \phi \\
 \theta_m &= \lambda_\theta \theta \\
 \psi_m &= \lambda_\psi \psi \\
 p_m &= \lambda_p p + n_p \\
 q_m &= \lambda_q q + n_q \\
 r_m &= \lambda_r r + n_r
 \end{aligned} \tag{2.8}$$

where, subscript ' m ' is used to defined the measurement. If the attitude and body rate data is set as input and output, respectively, the relationship between measured body rate and attitude is represented by using the transfer functions. For example, transfer function from measured pitch attitude to measured pitch rate is given in equation 2.9.

$$\frac{q_m(s)}{\theta_m(s)} = K s e^{-\tau s} \tag{2.9}$$

where, K is the ratio of the error factors $K = \frac{\lambda_q}{\lambda_\theta}$ and τ is effective time delay caused by filtering. The error model parameters are determined by using transfer function fitting procedure for the obtained $\frac{q_m(s)}{\theta_m(s)}$ frequency response analysis results. If the measured data is consistent, the K and τ parameters will be nearly 1 and 0, respectively [3].

2.1.3 Single-input / single-output frequency response identification theory

In this subsection, basic definitions about the single-input / single-output (SISO) frequency-domain system identification theory, which is an important requirement to perform a successful identification of the dynamical system, are summarized. Analysis of the input-output relationship of a dynamical system in the frequency domain is referred as spectral analysis. Here, several parameters should be selected by the user and hence, it is considered as *more art than science* [3].

2.1.3.1 Frequency response definition

Lets assume that a SISO system is excited by a periodic sine wave input signal given in equation 2.10 with magnitude A and frequency f in hertz.

$$u(t) = A \sin(2\pi ft) \quad (2.10)$$

After the transient phase, steady-state response of the system will also be in sine-wave form with the same frequency f but different amplitude B and phase shift φ . Mathematical definition of the system response is given in equation 2.11.

$$y(t) = B \sin(2\pi ft + \varphi) \quad (2.11)$$

This means that when sine-wave input is applied into the time-invariant linear system, it results in a sine-wave output with the same frequency which is called as first harmonic frequency.

The frequency response function $H(f)$ is a complex function which is defined by magnification factor and phase shift at each frequency, f , which are given in equations 2.12 and 2.13.

$$|H(f)| = \text{Magnification Factor} = \frac{B(f)}{A(f)} \quad (2.12)$$

$$\angle H(f) = \text{Phase Shift} = \varphi(f) \quad (2.13)$$

The behavior of the dynamical system can be characterized by using the frequency response $H(f)$ without any requirement of prior knowledge about the system structure. However, to simplify the problem, several assumptions are made in the above equations such that the system is linear, SISO, stable and time-invariant.

2.1.3.2 Relation between the Fourier transform and frequency response

The Fourier Transform method transforms non-periodic, time-domain, input $u(t)$ and output $y(t)$ signals into equivalent frequency domain signals, $U(f)$ and $Y(f)$ which are given in equation 2.14.

$$\begin{aligned} U(f) &= \int_{-\infty}^{\infty} u(t) e^{-j2\pi ft} dt \\ Y(f) &= \int_{-\infty}^{\infty} y(t) e^{-j2\pi ft} dt \end{aligned} \quad (2.14)$$

where, $U(f), Y(f)$ are called as Fourier coefficients. The frequency response $H(f)$ is defined as a complex function by using the Fourier coefficient as given in equation 2.15.

$$H(f) = \frac{Y(f)}{U(f)} = H_R(f) + j H_I(f) \quad (2.15)$$

where sign convention should be considered for the phase angle (ϕ) calculation. By using this definition in equation 2.15, magnification factor and phase shift are calculated by using equations 2.16 and 2.17.

$$|H(f)| = \sqrt{H_R^2(f) + H_I^2(f)} \quad (2.16)$$

$$\phi(f) = \angle H(f) = \tan^{-1} \left[\frac{H_I(f)}{H_R(f)} \right] \quad (2.17)$$

where H_R, H_I define real and imaginary parts of the frequency response, respectively.

According to the Dirichlet Condition in [3], integral of the input-output signals in time-domain should be bounded as expressed in equation 2.18.

$$\begin{aligned} \int_{-\infty}^{\infty} |u(t)| dt &< \infty \\ \int_{-\infty}^{\infty} |y(t)| dt &< \infty \end{aligned} \quad (2.18)$$

This condition does not let open-loop frequency sweep test of the systems with unstable dynamics. When the bounded input signal is applied into an unstable system, its response will be unbounded which violates equation 2.18.

According to the flight test guidelines, frequency sweep test requires a) trim conditions at the beginning and end of the test maneuver, b) aircraft response should be roughly symmetric about the trim flight conditions. In the frequency sweep flight test, pilot or control system provides the regulation to obtain bounded system response even if the

bare-airframe has inherent unstable dynamics. Hence, the Dirichlet Condition can be satisfied for systems with unstable and stable bare-airframe dynamics.

Performing the system identification procedure under the closed-loop conditions (FCS-active situations) is quite suitable for the systems with unstable bare-airframe dynamics such as rotorcrafts. However, it will result in bias error in the estimated frequency response. In practice, the bias error level is not significant if the noise level is quite low when compared to the forced excitation magnitude [3].

2.1.3.3 General observations

As a summary about the frequency response of a dynamical system, several observations are made as listed below [3];

- Frequency response is used to characterize the system dynamics.
- Non-parametric model is obtained based on the frequency response dataset.
- There is no assumption about the structure and order of the system in the non-parametric modeling approach.
- System linearity and time-invariance assumptions are necessary.
- Frequency response can be obtained for stable and unstable systems (with utilizing the feedback compensation).
- Aircraft and rotorcraft platforms include dynamic and aerodynamic nonlinearities. However, these nonlinearities can most often be characterized by using the identified frequency responses.

2.1.4 Coherence function

Coherence function ($\hat{\gamma}_{xy}^2$) is an important product of smooth spectral functions defined in [3] and its mathematical description is given in equation 2.19.

$$\hat{\gamma}_{xy}^2 = \frac{|\hat{G}_{xy}(f)|^2}{|\hat{G}_{xx}(f)||\hat{G}_{yy}(f)|} \quad (2.19)$$

where $|\hat{G}_{xy}(f)|$, $|\hat{G}_{xx}(f)|$, $|\hat{G}_{yy}(f)|$ are smooth spectral estimates of cross-spectrum, input auto-spectrum and output auto-spectrum, respectively [3, p. 155,156]. The

physical interpretation of the coherence function is given as the fraction of the output power of the system that is linearly related with the input power. The value range of the coherence function is in $[0, 1]$ interval. For a perfectly linear system, in which the output spectrum is attributable to the input spectrum, the coherence is obtained as 1. However, there are several effects that decreases the coherence value below 1 and they are listed below;

- Noise contamination on the measured system output.
- Nonlinearity in the system input-to-output.
- Process noise as a result of unknown and uncorrelated inputs.

The coherence function can be used to evaluate the accuracy of the identified frequency response. As a rule of thumb, it is desired to have a coherence value higher than 0.6 as given in equation 2.20.

$$\hat{\gamma}_{xy}^2 \geq 0.6 \quad (2.20)$$

If this condition is satisfied and is not oscillating, it means that the obtained frequency response has adequate accuracy and represents the linear dynamics of the related system.

As mentioned before, measurement noise directly affects the coherence function value. The relation between the coherence value and noise-to-signal ratio is given in equation 2.21.

$$\hat{\gamma}_{xy}^2 = \frac{1}{1 + \varepsilon} \quad (2.21)$$

where ε is noise-to-signal ratio. It is obvious that to obtain the coherence function value higher than 0.77, it is required to get signal-to-noise ratio (SNR) higher than 3. However, $SNR > 5$ is more suitable for the practical applications to obtain a high coherence value.

For more theoretical information about obtaining the frequency response of a dynamical system and coherence function, readers may refer to [3].

2.1.5 Transfer function modeling

Transfer functions are the simplest form of parametric models which represent the dynamical behavior of the system by using gain, poles and zeros. Basically, the transfer function modeling approach is utilized to find a suitable transfer function whose frequency response is fitted on the Bode plot of the test data over a defined frequency range. The transfer function models are used for preliminary analysis of handling qualities, actuator dynamics, aeroelastic modes and classical control system design process. This approach is based on low-order equivalent system (LOES) assumption which is put forth by Hodgkinson et al. [54].

Transfer function models include numerator and denominator elements. They can also contain, an equivalent time delay τ_{eq} which is utilized for unmodeled, high-frequency dynamics and transport delays. General form of the transfer function model is given in equation 2.22. Also, it can be given in the factored form as shown in equation 2.23.

$$T(s) = \frac{(b_0 s^m + b_1 s^{m-1} + \dots + b_m) e^{\tau_{eq} s}}{s^n + a_1 s^{n-1} + \dots + a_n} \quad (2.22)$$

$$T(s) = \frac{k(1/T_{z_1})(1/T_{z_1})\dots(1/T_{z_m}) e^{\tau_{eq} s}}{(1/T_{p_1})(1/T_{p_2})\dots(1/T_{p_n})} \quad (2.23)$$

Here, k is high-frequency gain, $1/T_{z_i}$ is shorthand notation for the i^{th} zero $(s + 1/T_{z_i})$, $1/T_{p_i}$ is shorthand notation for the i^{th} pole $(s + 1/T_{p_i})$ and τ_{eq} is equivalent time delay of the system.

If the system includes complex poles, they are given in terms of damping ratio and natural frequency as shown in equation 2.24.

$$[\zeta, \omega] = (s^2 + 2\zeta\omega s + \omega^2) \quad (2.24)$$

The set of unknown parameters in equation 2.22 is determined by a numerical optimization method to minimize the error between the desired transfer function (T) and frequency response estimate \hat{T}_c . A quadratic cost function in equation 2.25 is used in the optimization process.

$$J = \frac{20}{n_\omega} \sum_{\omega_1}^{\omega_{n_\omega}} W_\gamma [W_g (|\hat{T}_c| - |T|)^2 + W_p (\angle \hat{T}_c - \angle T)^2] \quad (2.25)$$

Here, $|\cdot|$ describes magnitude (dB) at each frequency, \angle describes phase angle (deg) at each frequency, n_ω is number of frequency points, $\omega_1, \omega_{n_\omega}$ are starting and ending frequencies to fit, respectively. W_γ is weighting function which is dependent on the coherence function and it is given in equation 2.26.

$$W_\gamma = [1.58(1 - e^{-\gamma_{xy}^2})]^2 \quad (2.26)$$

W_g and W_p are relative weights used in magnitude and phase squared-error calculation and they are given in equations 2.27 and 2.28, respectively.

$$W_g = 1.0 \quad (2.27)$$

$$W_p = 0.01745 \quad (2.28)$$

In the transfer function identification process, $J \leq 100$ reflects an acceptable accuracy of the linear model for flight dynamics applications.

Accuracy of the identified linear model can be evaluated by using error response function. In terms of magnitude (dB) and phase (deg) responses, the error response function is defined as shown in equation 2.29.

$$\begin{aligned} Mag_{err}(f) &= (|T| - |\hat{T}_c|) \\ Phase_{err}(f) &= (\angle T - \angle \hat{T}_c) \end{aligned} \quad (2.29)$$

For more theoretical information about transfer function structure and model fitting algorithm, readers may refer to [3].

2.1.6 State-space modeling

Preliminary analysis of flight dynamics is performed by using the transfer function identification method. It provides key features about the system such as model structure, dynamic modes and parameters. However, transfer function models are not suitable for modeling of the complex systems with higher-order modes and coupled

dynamics. Also, it is hard to model multi-input / multi-output (MIMO) systems by using the transfer function models.

In many aeronautical applications, mathematical model of the system should be defined in the state-space form which includes stability and control derivatives of the aerial platform. In the state-space modeling approach, system dynamics is represented by using the first-order differential equations of motion. For aerospace applications, unknown parameters are stability and control derivatives of the aerial vehicle. Initial guesses of these parameters can be obtained by using the transfer function modeling approach and first-principle analysis such as CFD method.

Perturbation equations of motion for a linear-time-invariant (LTI) MIMO system are represented as first-order differential equations as given in equation 2.30.

$$\begin{aligned}
m_{11}\dot{x}_1 + m_{12}\dot{x}_2 + \dots + m_{1n}\dot{x}_n &= (f_{11}x_1 + f_{12}x_2 + \dots + f_{1n}x_n) + \\
& (g_{11}u_1 + g_{12}u_2 + \dots + g_{1n_c}u_{n_c}) \\
m_{21}\dot{x}_1 + m_{22}\dot{x}_2 + \dots + m_{2n}\dot{x}_n &= (f_{21}x_1 + f_{22}x_2 + \dots + f_{2n}x_n) + \\
& (g_{21}u_1 + g_{22}u_2 + \dots + g_{2n_c}u_{n_c}) \\
& \dots \\
m_{n1}\dot{x}_1 + m_{n2}\dot{x}_2 + \dots + m_{nn}\dot{x}_n &= (f_{n1}x_1 + f_{n2}x_2 + \dots + f_{nn}x_n) + \\
& (g_{n1}u_1 + g_{n2}u_2 + \dots + g_{nn_c}u_{n_c})
\end{aligned} \tag{2.30}$$

Here, x_1, x_2, \dots, x_n are states, u_1, u_2, \dots, u_{n_c} are control inputs, m_{ij} are mass terms and they are used for inclusion of the forces and moments which depends on state derivatives such as $N_{\dot{v}}$. In the equations of motion of an aerial platform, the mass matrix is usually unity. The f_{ij} are stability derivatives and g_{ij} are control derivatives. In the state-space system identification applications, m_{ij} , f_{ij} and g_{ij} are the system parameters to be identified.

The equation 2.30 can be rewritten in the matrix form as shown in equation 2.31.

$$\mathbf{M}\dot{\mathbf{x}} = \mathbf{F}\mathbf{x} + \mathbf{G}\mathbf{u}(t - \tau) \tag{2.31}$$

where, \mathbf{M} , \mathbf{F} and \mathbf{G} matrices include system parameters to be identified. Also, the time delays due to the unmodeled dynamics are included as τ . Measurement vector \mathbf{y} is obtained by using the states and state derivatives as given in equation 2.32.

$$\mathbf{y} = \mathbf{H}_0 \mathbf{x} + \mathbf{H}_1 \dot{\mathbf{x}} \quad (2.32)$$

where, \mathbf{H}_0 and \mathbf{H}_1 matrices are determined from measurement equations which includes unit conversions, gravity acceleration and kinematic relationships. equations 2.31 and 2.32 are converted into the classical state-space representation as shown in equation 2.33.

$$\begin{aligned} \dot{\mathbf{x}} &= \mathbf{A}\mathbf{x} + \mathbf{B}\mathbf{u}(t - \tau) \\ \mathbf{y} &= \mathbf{C}\mathbf{x} + \mathbf{D}\mathbf{u}(t - \tau) \end{aligned} \quad (2.33)$$

where, \mathbf{A} , \mathbf{B} , \mathbf{C} , \mathbf{D} are defined as given in equation 2.34.

$$\begin{aligned} \mathbf{A} &= \mathbf{M}^{-1}\mathbf{F} \\ \mathbf{B} &= \mathbf{M}^{-1}\mathbf{G} \\ \mathbf{C} &= \mathbf{H}_0 + \mathbf{H}_1\mathbf{M}^{-1}\mathbf{F} \\ \mathbf{D} &= \mathbf{H}_1\mathbf{M}^{-1}\mathbf{G} \end{aligned} \quad (2.34)$$

The cost function that is used in the identification of the MIMO system is an extended version used in the transfer function identification algorithm. Simply, the total cost function value is sum of the individual cost functions of the identified SISO system models.

The frequency response matrix of the identified model $\mathbf{T}(s)$ is calculated by using the Laplace transform of the input vector \mathbf{u} and output vector \mathbf{y} as shown in equation 2.35.

$$\mathbf{y}(s) = \mathbf{T}(s)\mathbf{u}(s) \quad (2.35)$$

The expanded form of the equation 2.35 is shown in equation 2.36.

$$\begin{bmatrix} y_1(s) \\ y_2(s) \\ \vdots \\ y_{n_o}(s) \end{bmatrix} = \begin{bmatrix} T_{11}(s) & T_{12}(s) & \cdots & T_{1n_c}(s) \\ T_{21}(s) & T_{22}(s) & \cdots & T_{2n_c}(s) \\ \vdots & \vdots & \ddots & \vdots \\ T_{n_o1}(s) & T_{n_o2}(s) & \cdots & T_{n_on_c}(s) \end{bmatrix} \begin{bmatrix} u_1(s) \\ u_2(s) \\ \vdots \\ u_{n_c}(s) \end{bmatrix} \quad (2.36)$$

The frequency response matrix can be defined by using state-space system matrices $\mathbf{M}, \mathbf{F}, \mathbf{G}, \mathbf{H}_0$ and \mathbf{H}_1 as shown in equation 2.37. In this equation, the time delays are ignored.

$$\mathbf{T}(s) = [\mathbf{H}_0 + s\mathbf{H}_1][(\mathbf{sI} - \mathbf{M}^{-1}\mathbf{M})^{-1}\mathbf{M}^{-1}\mathbf{G}] \quad (2.37)$$

The time-delays for each individual frequency response can be written in the matrix form as given in equation 2.38.

$$\boldsymbol{\tau}(s) = \begin{bmatrix} e^{-\tau_{11}s} & e^{-\tau_{12}s} & \dots & e^{-\tau_{1n_c}s} \\ e^{-\tau_{21}s} & e^{-\tau_{22}s} & \dots & e^{-\tau_{2n_c}s} \\ \vdots & \vdots & \vdots & \vdots \\ e^{-\tau_{n_o1}s} & e^{-\tau_{n_o2}s} & \dots & e^{-\tau_{n_on_c}s} \end{bmatrix} \quad (2.38)$$

If a common time delay is used for each output response, the time delay matrix reduced to the time delay vector and the frequency-response of the model to be identified is given in equation 2.39.

$$\mathbf{T}(s) = [\mathbf{H}_0 + s\mathbf{H}_1][(\mathbf{sI} - \mathbf{M}^{-1}\mathbf{M})^{-1}\mathbf{M}^{-1}\mathbf{G}] \circ \boldsymbol{\tau}(s) \quad (2.39)$$

Here, ' \circ ' defines the *Schur product* which performs element-by-element multiplication.

The aim of the system identification process is to obtain the linear system matrices $\mathbf{M}, \mathbf{F}, \mathbf{G}$ and time delay τ that closely matches the frequency response obtained from the flight test data. For this purpose, linear model is fitted on the actual frequency response by using an optimization process in which it is desired to minimize the cost function given in equation 2.40.

$$J = \sum_{l=1}^{n_{TF}} \left\{ \frac{20}{n_\omega} \sum_{\omega_l}^{\omega_{n_\omega}} W_\gamma [W_g(|\hat{T}_c| - |T|)^2 + W_p(\angle \hat{T}_c - \angle T)^2] \right\} \quad (2.40)$$

Where, l is the number of the frequency response pairs, $l = 1, 2, 3, \dots, n_{TF}$ and n_ω is the number of frequency points which is used by all transfer functions. Although each transfer function has the same number of frequency points, each transfer function is evaluated in the corresponded frequency range in which the coherence value is above

the assigned threshold. It is obtained from the experience that the coherence cutoff parameter should be $(\gamma_{xy_{cut}}^2) = 0.4$.

The accuracy of the identified state-space model is evaluated by using average cost function as shown in equation 2.41.

$$J_{ave} = \frac{J}{n_{TF}} \quad (2.41)$$

The weighting functions W_γ, W_g, W_p have the same definitions that are given in the transfer function identification subsection. Identified parameters are collected in an identification vector Θ and it is shown in equation 2.42.

$$\Theta = [\theta_1 \quad \theta_2 \quad \cdots \quad \theta_{n_p}] \quad (2.42)$$

In the optimization algorithm, the identification vector parameters are varied until a minimum cost function value J_{ave} is obtained. In this process, the secant method is used which is a type of pattern search algorithm. The secant method is a robust and powerful tool against sudden changes and discontinuities in the optimization parameters. Estimated values cannot be far away from the best estimate of the previous step. So, the estimated parameters are obtained in a smooth and reliable manner. A guideline for overall average cost function of the MIMO system identification process is given in equation 2.43.

$$J_{ave} \leq 100 \quad (2.43)$$

Some of the cost functions, especially off-axis response cost functions, may be between 150 and 200 as given in equation 2.44

$$J_{off-axis} = 150 - 200 \quad (2.44)$$

For more theoretical information about the state-space structure and model fitting algorithm, readers may refer to [3].

Accuracy analysis

After obtaining the state-space model of the system, it is required to evaluate the accuracy of the identified parameters because of several reasons. The first reason is the possible model reduction requirements. If an identified parameter is not reliable due to the lack of information content, it is better to eliminate this parameter or to replace it with a reasonable value which is obtained by using analytical or numerical methods. The second reason for using the accuracy analysis is the robustness requirements of the control systems. In many control system design process, especially in robust control system design, parameter uncertainties are used to evaluate the robustness of the closed-loop system. By using the parameter uncertainties, the designer can predict the system performance in the off-nominal operation conditions. The third reason for using the accuracy analysis is to evaluate the differences between the simulation and flight test results which requires the level of confidence of each identified parameter [3].

In the frequency-domain system identification method, theoretical accuracy analysis is used to evaluate the variability of the estimated parameters [55]. In this analysis, Cramer-Rao (CR_i) inequality is used as a principal metric which provides the minimum expected standard deviation in the estimated parameter value θ_i . It should be less than or equal to the standard deviation of the identified parameter as given in equation 2.45.

$$\sigma_i \geq CR_i \quad (2.45)$$

The Cramer-Rao bound is used in model structure refining. Large values of the Cramer-Rao bound indicate poor identifiability and it is better to eliminate or fix the related parameters in the model structure. In general, scale factors of 5 to 10 are adequate to obtain a reasonable estimate of the scatter.

$$\sigma_i \approx (5 - 10)CR_i \quad (2.46)$$

When measurement noise is modeled or eliminated, a scale factor of 2 can be suitable. In CIFER software, the factor of 2 is used to calculate the Cramer-Rao bounds of the estimated parameters as given in equation 2.47.

$$(CR)_{CIFER} \approx \sigma_i \approx 2CR_i \quad (2.47)$$

The Cramer-Rao bounds are expressed as a percentage of the estimated value of the related parameter as shown in equation 2.48.

$$\bar{CR}_i = \left| \frac{CR_i}{\theta_i} \right| \times 100\% \quad (2.48)$$

Experience suggests that a reasonable guideline for the Cramer-Rao bound can be used as shown in equation 2.49.

$$\bar{CR}_i \leq 25\% \quad (2.49)$$

It reflects reliability of the state-space model together with an average identification cost function of $J_{ave} \leq 100$. Here, it is noted that the largest Cramer-Rao bound might be in the range of 25% – 40% to obtain a reliable mathematical model [3].

For more theoretical information about the accuracy analysis, readers may refer to [3].

2.1.7 Time-domain verification

After obtaining the identified model from the frequency-domain system identification process, it is important to evaluate the fidelity, robustness and limitations of the model. For this aim, time-domain test signals in the form of step or doublet can be used which are dissimilar from the identification test signal.

In the time-domain verification analysis, same input signal is applied into both the actual system and the estimated model. Then, the model responses are compared with the test flight measurements to evaluate the fidelity of the model. In this process, bias and reference-shift corrections should be determined due to the several error sources such as untrimmed flight conditions, sensor noise, disturbances, integration errors and off-axis input signals applied into the system [3].

Perturbation control input is defined as shown in equation 2.50.

$$\mathbf{u} = \mathbf{U}_{data} - \mathbf{U}_0 \quad (2.50)$$

where, \mathbf{U}_{data} is the time history of the measured control signal, \mathbf{U}_0 is the trim value of the control signal which is obtained from the initial few seconds at the start of the test flight.

The perturbation time history of the test flight is obtained by using equation 2.51.

$$\mathbf{y}_{data} = \mathbf{Y}_{data} - \mathbf{Y}_0 \quad (2.51)$$

where, \mathbf{Y}_0 is trim output time history, \mathbf{Y}_{data} is recorded output time history.

A normalized criterion, called as Theil Inequality Coefficient (TIC), is adopted by Jategaonkar et al. [56] as shown in equation 2.52 and it is used to evaluate the prediction accuracy of the identified mathematical model.

$$TIC = \frac{\sqrt{[1/(n_t \cdot n_0)] \sum_{i=1}^{n_t} [(\mathbf{y}_{data} - \mathbf{y})^T \mathbf{W} (\mathbf{y}_{data} - \mathbf{y})]}}{\sqrt{[1/(n_t \cdot n_0)] \sum_{i=1}^{n_t} [\mathbf{y}^T \mathbf{W} \mathbf{y}] + [1/(n_t \cdot n_0)] \sum_{i=1}^{n_t} [\mathbf{y}_{data}^T \mathbf{W} \mathbf{y}_{data}]}} \quad (2.52)$$

The TIC value is determined in the range of $[0, 1]$. A value of $TIC = 1$ means that model response is predicted perfectly. A value of $TIC = 0$ means that obtained model has no predictive capability. Jategaonkar suggests a guideline as shown in equation 2.53 for an adequate prediction performance [3].

$$TIC \leq 0.25 - 0.30 \quad (2.53)$$

For more information about the system identification and verification theory, readers may refer to [3].

2.2 Model Stitching: Developing a Full Flight Envelope Simulation Environment

By using the frequency-domain and time-domain system identification methods, individual linear mathematical models are obtained for the related flight conditions. The complexity and fidelity of the proposed mathematical model are defined by the intended applications. Then, flight control system design process is applied for each flight condition according to design specifications such as ADS-33E-PRF and MIL-STD-1797B. In a classical FCS design process, this procedure is performed for each flight condition and a gain schedule is generated for the controller parameters.

The developed flight control system should be tested in non-real-time and real-time simulation environments to evaluate its performance in the nominal and off-nominal flight conditions. Also, it is important to observe the closed-loop system behavior in several situations such as subsystem failure and flight phase transitions. For this purpose, it is crucial to generate a high-fidelity mathematical model which is valid in the full-flight envelope.

In literature, there are two types of methods for generating a full-flight envelope simulation environment. The first method is called as first principle modeling approach in which each subsystem is modeled by using physical relationships. For example, aerodynamic forces and moments are calculated by using the aerodynamic database which is generated by CFD analysis or wind tunnel tests. This approach requires extensive calculation, development cost and time. The second approach to generate the full-flight envelope simulation environment is called as model stitching method. In this application, identified linear mathematical models of each flight condition are combined by using trim data (state and control signal) of the aerial vehicle to obtain a continuous full-flight envelope simulation environment.

Stitched models can be used for performance evaluation of the control systems, pilot training and hardware-in-the-loop simulations in the flight envelope of the aerial vehicle. Depending on the specific mission requirements, the stitched model may include additional dynamical effects of external load pick up/delivery and takeoff/landing phases. In this section, a general overview of the model stitching is introduced. For more information, readers may refer to [3] and [4].

2.2.1 Basics of model stitching

The key elements of the stitched model are identified linear models and state/control data of the related trim flight conditions. These point models and trim dataset are obtained by using the system identification process and trim flight tests on the actual system or non-real-time simulation environment, if available.

The linear state-space mathematical model is utilized to represent the perturbation dynamics of the system in the reference flight condition. Generalized form of the state-space model as a function of trim X_b axis velocity U_0 is given in equation 2.54.

$$\begin{aligned}\dot{\mathbf{x}} &= \mathbf{A}_{|U_0} \mathbf{x} + \mathbf{B}_{|U_0} \mathbf{u} \\ \mathbf{y} &= \mathbf{C}_{|U_0} \mathbf{x} + \mathbf{D}_{|U_0} \mathbf{u}\end{aligned}\tag{2.54}$$

where, $\mathbf{A}, \mathbf{B}, \mathbf{C}, \mathbf{D}$ are linear model matrices identified in the reference flight conditions, \mathbf{x}, \mathbf{y} are perturbed state and measurement vectors, \mathbf{u} is control signal vector. Subscript U_0 indicates the total airspeed in trim flight conditions.

The state-space representation of the aerial vehicle dynamics is rewritten by using total values of the state, measurement and control signal vector as shown in equation 2.55. Here, instantaneous X_b axis airspeed component U is used instead of the trim value U_0 .

$$\begin{aligned}\dot{\mathbf{X}} &= \mathbf{A}_{|U} (\mathbf{X} - \mathbf{X}_{0|U}) + \mathbf{B}_{|U} (U - U_{0|U}) \\ \mathbf{Y} &= \mathbf{C}_{|U} (\mathbf{X} - \mathbf{X}_{0|U}) + \mathbf{D}_{|U} (U - U_{0|U}) + \mathbf{Y}_{0|U}\end{aligned}\tag{2.55}$$

where, subscript $0|U$ indicates the trim conditions for instantaneous total airspeed U .

Trim data and aerodynamic parameters are interpolated by using X_b axis airspeed component. At the anchor point flight, trim conditions are satisfied ($\dot{\mathbf{X}} = 0$) and equation 2.56 is obtained.

$$\begin{aligned}\mathbf{X} &= \mathbf{X}_{0|U} \\ U &= U_{0|U} \\ \mathbf{Y} &= \mathbf{Y}_{0|U}\end{aligned}\tag{2.56}$$

In the model stitching method, all stability derivatives, which are related to the X_b axis airspeed, such as X_u, M_u and Z_u , are nulled-out. Instead, they are modeled implicitly by using the partial derivatives of the trim state and control values as shown in equation 2.57.

$$\begin{aligned}X_u &= g \cos(\Theta_{0|U}) \left(\frac{\partial \Theta_{0|U}}{\partial u} \right) - X_{w|U} \left(\frac{\partial W_{0|U}}{\partial u} \right) - X_{\delta_{lon}|U} \left(\frac{\partial \delta_{lon0|U}}{\partial u} \right) - X_{\delta_{col}|U} \left(\frac{\partial \delta_{col0|U}}{\partial u} \right) \\ Z_u &= g \sin(\Theta_{0|U}) \left(\frac{\partial \Theta_{0|U}}{\partial u} \right) - Z_{w|U} \left(\frac{\partial W_{0|U}}{\partial u} \right) - Z_{\delta_{lon}|U} \left(\frac{\partial \delta_{lon0|U}}{\partial u} \right) - Z_{\delta_{col}|U} \left(\frac{\partial \delta_{col0|U}}{\partial u} \right) \\ M_u &= -M_{w|U} \left(\frac{\partial W_{0|U}}{\partial u} \right) - M_{\delta_{lon}|U} \left(\frac{\partial \delta_{lon0|U}}{\partial u} \right) - M_{\delta_{col}|U} \left(\frac{\partial \delta_{col0|U}}{\partial u} \right)\end{aligned}\tag{2.57}$$

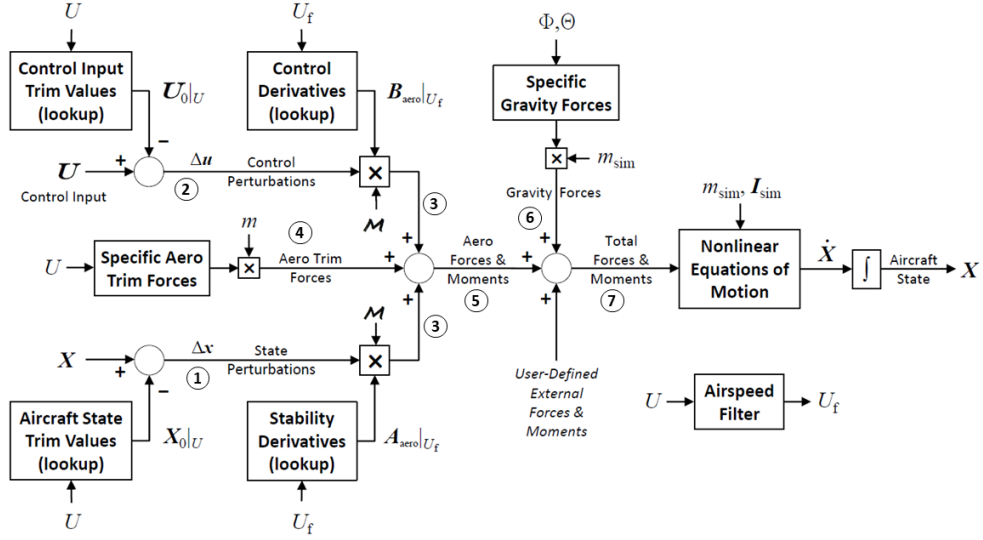


Figure 2.3 : General view of the stitch model structure (Adapted from [4]).

2.2.2 Key elements of a stitched model

In general view, the stitched model consists of state and control perturbations, aerodynamic perturbation forces and moments, aerodynamic trim forces, nonlinear gravitational forces and nonlinear equations of motion as shown in Figure 2.3. Each component of the stitch structure is described in the following.

State and control perturbations ($\Delta \mathbf{x}$, $\Delta \mathbf{u}$) are used to obtain the perturbed aerodynamic forces and moments. Instantaneous state vector and trim state vector are provided by the nonlinear EoMs and look-up tables, respectively. In a similar way, control perturbation is calculated by using actual controller signal and look-up table of the trim flight control vector. Mathematical description of the $\Delta \mathbf{x}$ and $\Delta \mathbf{u}$ are given in equation 2.58 and they are given in Figure 2.3 as Signal-1 and Signal-2 labels.

$$\begin{aligned}\Delta \mathbf{x} &= \mathbf{X} - \mathbf{X}_{0|U} \\ \Delta \mathbf{u} &= \mathbf{U} - \mathbf{U}_{0|U}\end{aligned}\tag{2.58}$$

Aerodynamic force and moment perturbations are calculated by using the state and control perturbations ($\Delta \mathbf{x}$, $\Delta \mathbf{u}$) and identified linear state-space matrices (\mathbf{A}_{aero} , \mathbf{B}_{aero}). Here, state-space matrices include only stability and control derivatives. Gravity, Coriolis and Euler angle terms are not included in these matrices.

To obtain the dimensional perturbation aerodynamic forces and moments, a dimensional mass matrix \mathbf{M} is multiplied with \mathbf{A}_{aero} , \mathbf{B}_{aero} matrices. Mass matrix contains mass properties of the aerial vehicle and it is given in equation 2.59 for the state vector $[u, v, w, p, q, r]$. Aerodynamic dimensional perturbation forces and moments are given in Figure 2.3 as Signal-3.

$$\mathbf{M} = \begin{bmatrix} m & 0 & 0 & 0 & 0 & 0 & 0 \\ 0 & m & 0 & 0 & 0 & 0 & 0 \\ 0 & 0 & m & 0 & 0 & 0 & 0 \\ 0 & 0 & 0 & I_{xx} & 0 & -I_{xz} & 0 \\ 0 & 0 & 0 & 0 & I_{yy} & 0 & 0 \\ 0 & 0 & 0 & -I_{xz} & 0 & I_{zz} & 0 \end{bmatrix} \quad (2.59)$$

Aerodynamic trim forces are obtained by utilizing several flight tests. Airspeed and Euler angles are recorded in trim conditions to generate look-up tables as a function of X_b axis total airspeed. The specific aerodynamic trim forces are given in equation 2.60.

$$\begin{aligned} \bar{X}_{aero_0} &= g \sin(\Theta_{0|U}) \\ \bar{Y}_{aero_0} &= g, \cos(\Theta_{0|U}) \sin(\Phi_{0|U}) \\ \bar{Z}_{aero_0} &= g, \cos(\Theta_{0|U}) \cos(\Phi_{0|U}) \end{aligned} \quad (2.60)$$

To obtain the dimensional aerodynamic trim forces, the specific aerodynamic trim forces are multiplied by aerial vehicle mass, m . Dimensional aerodynamic trim forces are shown in Figure 2.3 as Signal-4.

Total aerodynamic forces and moments (Signal-5) are obtained by summing the trim aerodynamic forces/moments (Signal-4) and perturbed aerodynamic forces/moments (Signal-3).

Stitch model structure includes **nonlinear gravitational forces** acting on the center of gravity of the aerial vehicle. Here, instantaneous roll and pitch angles are used instead of trim Euler angles. Specific gravitational forces are given in equation 2.61.

$$\begin{aligned} \bar{X}_{grav} &= -g \sin(\Theta) \\ \bar{Y}_{grav} &= g \cos(\Theta) \sin(\Phi) \\ \bar{Z}_{grav} &= g \cos(\Theta) \cos(\Phi) \end{aligned} \quad (2.61)$$

The specific gravitational forces are multiplied by simulation mass value m_{sim} to obtain the dimensional gravity forces. m_{sim} may be different from the mass value of the identified linear model. Hence, it is possible to evaluate the off-nominal flight performance of the aerial vehicle with different weight configurations. The dimensional gravity forces are shown as Signal-6 in Figure 2.3.

Total forces and moments (Signal-7) for the nonlinear EoMs are obtained by summing the aerodynamic, gravitational and external force/moment components as shown in Figure 2.3. Here, external forces and moments are used to simulate additional components such as landing gears, tail hooks and tether systems.

Nonlinear equations of motion are derived based on Newton's Second Law and are used to obtain the state derivatives ($\dot{\mathbf{X}}$). The nonlinear EoMs include cross-coupling dynamics and Coriolis terms. Also, by using the simulation values of the mass (m_{sim}) and inertia (\mathbf{I}_{sim}), it is possible to evaluate the system performance in off-nominal flight conditions with different mass characteristics.

In the look-up table interpolation process of the stability and control derivatives, a first-order low-pass **airspeed filter** is used to avoid any jumps in the short-term motions. Especially at the anchor points, accurate dynamical responses are obtained by using the airspeed filter. Break frequency can be selected as $\omega_f = 0.2 \text{ rad/s}$ which is suitable for moderate/aggressive maneuvers of the aerial vehicles. Also, for more agile vehicles, it is possible to utilize a higher value of break frequency [3,43].

2.3 Multi-Objective Optimization Based Control System Design Approach

In practical applications, the main problem of the flight control system design process is to obtain a suitable and optimized controller parameters that satisfies several stability and performance requirements. In addition, safety of the flight crew and platform is a crucial factor, especially in the test period. As a result of these inherent characteristics of the flight control system design process, cost of the testing and evaluating of a new control system is around $75K/hr$ [2]. Hence, it is necessary to develop a systematic approach in designing an optimal solution for the control problem.

In literature, there are two fundamental examples for optimized flight control system design procedures in which direct parameter optimization methods are utilized [2].

In Group for Aeronautical Research and Technology in Europe (GARTEUR) case study, 30% of improvements in controller performance is achieved by using the multi-objective parameter synthesis (MOPS) method when compared to manual tuning process of the control system parameter [57]. MOPS has been used successfully in the flight control system design and development process of the Euro Fighter program [58].

In [59], a systematic approach based on multi-objective parametric optimization method is introduced to increase the efficiency and safety of the flight control system design process. As a result of the collaborative research between the US Army Aeroflightdynamics Directorate (AFDD), University of Maryland and University of California, a comprehensive tool is developed which is called as Control Designer's Unified Interface (CONDUIT). The effectiveness of the proposed design method has been proven and demonstrated in UH-60 [60], Armed Reconnaissance Helicopter (ARH-70A) program by Bell Helicopter [61], V-22 and RAH-66 programs by Boeing Helicopter [62]. Brief description about this design process is given in following subsections. For more information about the multi-objective parameter optimization based flight control system design, readers may refer to [2].

2.3.1 Overall road map

In the proposed road map given in [2], there are several sub-process to evaluate and optimize the design parameters as shown in Figure 2.4. It would be useful to describe the road map step-by-step before using the multi-objective parametric optimization process.

At the beginning of the optimization process, it is required to define **program requirements** such as operational environment (i.e. visual and weather conditions, etc.), mission category (search and rescue, cargo transportation, etc.), aircraft class (fixed-wing or rotary-wing), vision aids (sensors and displays) and autonomy level of the aircraft. The proposed control system performance is evaluated according to the selected program requirements.

System architecture determines the capability of closed-loop structure and it is selected based on the program requirements, desired response type (such as Attitude-Control / Attitude-hold (ACAH) or Rate-Control / Attitude-Hold (RCAH)) and authority level (partial or full). After determining these high-level requirements,

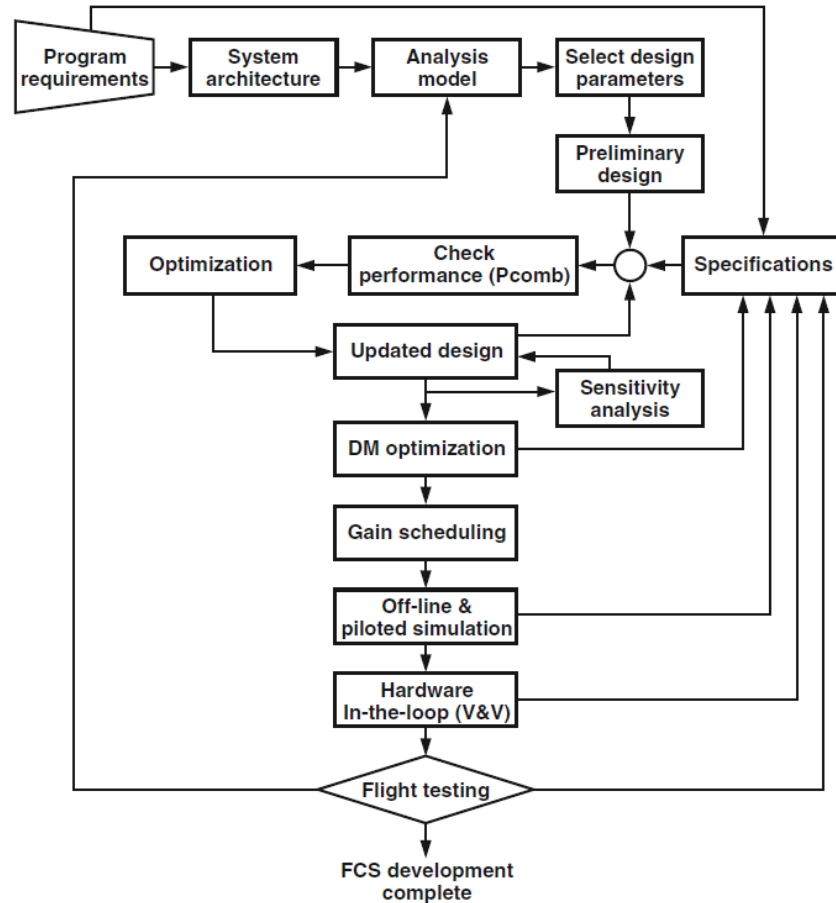


Figure 2.4 : General view of the multi-objective optimization based flight control system design road map [2].

detailed control system architecture should be selected based on various methodologies such as PID, model following, linear quadratic regulator (LQR), dynamic inversion, adaptive and robust control.

After determining the program requirements and control system architecture, **design specifications** are selected based on several standards such as SAE AS94900, ADS-33 (for rotorcrafts), MIL-STD-1797 (for fixed-wing platforms), FAR Part 25 and several company specifications. These regulations include quantitative requirements for the flight control system such as stability margins, time delay, bandwidth, actuator activity and disturbance rejection characteristics of the controller.

Accurate **analysis model** is an important element in the control design process. It represents critical open-loop system dynamics such as natural frequency and damping ratio of the dominant poles and zeros. Besides of the bare-airframe dynamics, the analysis model may contain higher-order rotor and actuator dynamics, structural modes, control allocation algorithm (mixer) and logic elements.

Design parameters are used to tune the dynamical characteristics of the closed-loop system. For example, in a PID controller structure, proportional, derivative and integral gains are utilized as design parameters and control system engineer should select these coefficients to meet the predefined dynamical requirements. Similarly, in LQR architecture, the feedback gain matrix is selected to minimize the predefined cost function. If the control system contains lead-lag compensation, filter pole and zero frequencies are selected as design parameters to meet these requirements.

To reduce computation time and obtain global optimal design parameter value, it is required to perform a **preliminary design process** in which a near-optimal solution is determined. It provides an adequate starting point about the controller parameters even though they are sub-optimal. Classical PID design rules or LQR algorithm can be used for this initial design step. In addition, the minimum crossover frequency of the broken-loop system is estimated in this step which is a crucial dynamical characteristics for adequate reference tracking and robustness. Then, in **performance checking process**, raw score of the proposed closed-loop system is calculated and handling quality level of the preliminary design is evaluated for each specification.

Optimization process is performed by using normalized score of the selected specifications. Feasible Sequential Quadratic Programming (FSQP) algorithm determines the search direction for the selected specifications, individually. In this step, it is also important to minimize the over-design which may result in sub-optimal solution. There are three phases that are used to obtain the optimized value of the design parameters. In Phase-1, design parameters are selected to meet all hard constraints such as stability requirements. Then, soft constraints (i.e. handling quality requirements) are met in Phase-2. Summed objectives are used in Phase-3 and the cost of feedback is minimized.

As a result of the optimization process, **updated parameters** are obtained and evaluated in the performance checking step. Then, if an improper controller parameter set is obtained, optimization-update and design-check performance loop is repeated until an appropriate controller parameter value is calculated. In result, all design specifications should be met with a minimum over-design.

The sensitivity of the closed-loop system to initial conditions and uncertain model parameters are evaluated in the **sensitivity analysis**. This process is performed based on 1-dimensional search topology. It gives insight about the quality of convergence and accuracy of the final design parameters.

In the controller design process, there are trade-offs between several specifications such as crossover frequency and disturbance rejection requirements. Hence, the Level-1 boundaries of the selected specifications are tightened progressively and design trade-offs are explored in **design margin optimization (DMO) process**. As a result of the DMO analysis, pareto-optimum design solution is obtained which satisfies the design requirements with minimum actuator activity.

If the aircraft has a wide flight envelope, it is required to re-design the controller parameters for each operation point. This step is called as **gain-scheduling process**. Then, a look-up table is generated and controller parameters are interpolated in real-time as a function of airspeed, Mach number or dynamic pressure. Here, it is important to obtain a smooth variation of the design parameters to avoid control signal jumps.

Off-line and piloted simulations are performed to evaluate the robustness and performance of the proposed controller. In the off-line simulations, nonlinear higher-order mathematical models are used. Real-time piloted simulations are performed in fixed-based, motion-based and in-flight simulation environments.

Fixed and motion-based flight simulators are safe and effective solutions to evaluate the closed-loop system performance. However, synthetic visual cues are used in these simulation platforms and motion is limited with the mechanical and electromechanical elements such as actuators. In-flight simulators provide real motion and vision cues though they are limited by the dynamical response and flight envelope of the host aircraft. Calspan total in-flight simulator (TIFS) may be given as an example which is shown in Figure 2.5. This simulator was used in several projects such as landing control system design for the space shuttle, evaluation of the flying qualities of the Concord and B-1. The TIFS was retired in 2008 and today Learjet LJ-25 variable stability system (VSS) aircrafts are used as in-flight simulators [2].



Figure 2.5 : Calspan total in-flight simulator [5].

The in-flight simulators are also used in rotorcraft platforms. Sikorsky was developed Helicopter Advanced Demonstrator of Operator Workload (SHADOW) platform based on a modified S-76 helicopter. SHADOW was used in development process of RAH-66 Comanche control system. Now, it is not in operation but several in-flight simulators are used such as JUH-60A RASCAL, EC-135 and Bell 412 [2].

Hardware-in-the-loop (HIL) simulation environment includes a high/mid-fidelity nonlinear mathematical model, flight control system hardware and actuators. In this process, the proposed control algorithm, hardware, software and actuators are tested under realistic flight conditions. Also, mode switching logic, redundancy management and failure modes are evaluated in this step.

After performing HIL simulations, the proposed control system is evaluated in **actual flight tests**. In this step, predicted and actual system performance are compared. Also, pilot comments are used to re-design the controller structure and parameters. All of the previous steps in the design methodology should be performed clearly before the test flights because of the safety considerations and its high cost which is about \$75K / *flight hour* [2].

2.3.2 Quantitative design requirements

To ensure that the proposed flight control system satisfies adequate handling qualities for a specified type of mission, it is crucial to define a complete set of design requirements and specifications which are drivers to obtain the optimal design solution.

In this section, quantitative design requirements are reviewed and explained briefly. For more information, readers may refer to Chapter-5 in [2].

2.3.2.1 Stability and stability margins

Eigenvalues: Eigenvalues of the dynamical system are important parameters to evaluate the system stability. For stable dynamical characteristics, all of the eigenvalues should be on the left-hand plane in the s-domain. In other words, eigenvalues should have negative real parts. In manned aerial vehicles, low-frequency unstable modes, such as phugoid and spiral modes, can be compensated by the pilot. However, in the unmanned aerial vehicles, all of the poles should be on the left-hand side to ensure absolute asymptotic stability of the system.

Stability Margins: Stability margin requirements provide gain margin (GM) and phase margin (PM) of the broken-loop responses in which the loop is broken at the actuator or mixer input. The stability margin requirements should be maintained for the off-nominal center of gravity (cg) location, mass distribution and external store configuration in the flight envelope of the aircraft.

For the rigid body dynamics, stability margin requirements can be defined as $\pm 45^\circ$ of phase margin and $\pm 6dB$ gain margin for the standard operational flight envelope. According to the SAE-AS94900, uncertainty analysis should be performed for the key stability derivatives with 20% uncertainty. It is required that the stability margins should not degrade by more than 50% of the requirements. For the frequencies below the structural modes in nominal flight conditions, this requirement indicates $\pm 22.5^\circ$ phase margin and $\pm 3dB$ gain margin should be maintained in the uncertainty analysis.

Nichols Margin is evaluated by using the broken-loop gain-phase response of the dynamical system and it used to define robust stability margins in terms of an exclusion zone. Nichols margin boundaries were introduced by Magni et. al. to ensure that simultaneous changes in gain and phase of the broken-loop response do not cause dynamical characteristics with low stability margin. The Nichols margin requirements are commonly used in the European flight control system design projects [2].

2.3.2.2 Damping ratio

The damping ratio (ζ) describes how fast the oscillation on the system response decays after the external disturbance is applied to the system. In other words, it is a measure of the oscillation decay rate. If the damping ratio is smaller than 1, ($\zeta < 1$), the system is called as *underdamped* and the magnitude of the oscillatory response decays with a rate of $a = \zeta \omega_n$. If the damping ratio equals to zero, ($\zeta = 0$), the system oscillates with a constant magnitude. If the damping ratio is 1, ($\zeta = 1$), it is called as *critically damped system* and it exhibits no oscillatory motion. In the control system and filter design process, a damping ratio of $\zeta = 0.707$ is desired which results a flat frequency response magnitude.

2.3.2.3 Minimum crossover frequency

The main benefit of the feedback signal in a control system is its suppression behavior against the deviations and uncertainties in the bare-airframe parameters such as aerodynamic coefficients, mass and cg location. So, high feedback gain results in high magnitude control signal and actuator activity. The crossover frequency is a measure of the level of the feedback in a closed-loop system. A higher crossover frequency better suppresses the system variations at the cost of increased actuator activity, decreased stability margin and increased noise susceptibility. So, it is important to find an optimal solution for balancing the benefits and costs. In the optimization procedure, the crossover specification is used as both soft constraint and performance objective. Because of the minimization of the performance objectives, the optimal solution is obtained when the crossover frequency is equal to the minimum required value. This is the minimum crossover frequency which still meets the Level 1 requirements.

Typically, the minimum crossover frequency is a user-defined parameter which is defined for different aircrafts. There are several requirements to set the minimum crossover frequency such as stabilization of the unstable low-frequency modes, disturbance rejection, model following and performance robustness under parametric uncertainty situations.

To provide the closed-loop stability of the system, minimum crossover frequency should be defined as 2 or 3 times greater than the natural frequency of the unstable

modes. X-29A highly-maneuverable aircraft could be given as an example. This aircraft has an unstable static margin (-35%) to obtain enhanced maneuvering capability. However, it is necessary to stabilize the unstable modes. For high-subsonic flight conditions ($M=0.9$), it has a real unstable pole at $\lambda = 5.1$. So, to provide the closed-loop stability, minimum crossover frequency is selected as $\omega_c \geq 10\text{rad/s}$ and it is verified as $\omega = 12\text{rad/s}$ by using flight test data [2].

2.3.2.4 Pilot-induced oscillation specifications

The control system design process is performed by using linear analysis methods. Generally, nonlinear effects of position and rate limitations of the actuators are ignored. However, these effects can degrade the system performance and safety in nonlinear simulations and flight tests and they should be considered in the design phase.

Rate limit of the actuator is particularly important for a dynamical system. It increases the phase-lag and it is directly related to the pilot-induced oscillation (PIO) events. Open-loop-onset-point criteria is developed by Duda in [63] for fixed-wing aircrafts to predict the possible PIO situations and it can also be used for the rotorcraft platforms.

2.3.2.5 Disturbance rejection requirements

The crossover frequency is directly related to the disturbance rejection bandwidth (DRB) and stability margin requirements. It can be stated that the lower bound of the crossover frequency is determined by using the disturbance rejection bandwidth and the upper bound is determined by using the stability margin requirement. Also, it is important to note that the primary dependency of the ω_{DRB} is on the attitude gain. From the point of view of the controller parameters, the attitude gain is lower-bounded by the minimum DRB requirements and upper-bounded by the stability margin requirements [2].

Some of the specifications for the fixed-wing platforms are obtained from ADS-33E-PRF which contains a set of quantitative requirements for military helicopters. The selected requirements are disturbance rejection peak (DRP), disturbance rejection bandwidth (DRB) and Bandwidth/Phase delay specifications which are described in the following.

DRB and DRP specifications are developed by US Army Aviation Development Directorate (ADD) in 2005. These specifications are used to quantify the ability of an aircraft to reject the disturbance and return the commanded state such as attitude and position.

DRB and DRP specifications are defined in the frequency domain and they are calculated by using sensitivity transfer function, $S(s)$, which is given in equation 2.62. The DRB is defined as -3 dB crossover frequency of the sensitivity function as shown in equation 2.63.

$$S(s) = \frac{1}{1 + G(s)H(s)} \quad (2.62)$$

where, $G(s)$ is the process model and $H(s)$ is the feedback compensation element on the feedback path.

$$\omega \left(\left| \frac{y'(s)}{y_d(s)} \right|_{s=j\omega} = -3\text{dB} \right) \equiv \omega_{DRB} = DRB (\text{rad/s}) \quad (2.63)$$

where, y_d is disturbance input and y' is measured signal after the disturbance input is applied into the closed-loop system.

DRP is the peak amplitude of the frequency response of the sensitivity function and it is defined in equation 2.64.

$$\max \left(\left| \frac{y'(s)}{y_d(s)} \right|_{s=j\omega} \right) \equiv DRP (\text{dB}) \quad (2.64)$$

Bandwidth (BW) is defined as the highest input signal frequency that can be tracked by the closed-loop system. It characterizes the aircraft response for the pilot inputs. Phase delay τ is defined as the effective time delay in the control system. Low bandwidth and high phase delay results in a poor handling quality and sluggish response, especially for tasks which require high precision tracking and aggressive maneuvers.

In ADS-33E-PRF, there are two types of bandwidth called as gain and phase margin bandwidths. The gain margin bandwidth is defined as the frequency where the closed-loop system has 6 dB gain margin. Similarly, the phase margin bandwidth defines the frequency where the closed-loop system has 45 deg phase margin.

It is important to note that, for the rate command response types, the bandwidth is defined as the minimum of the gain and phase margin bandwidth frequencies. For the attitude response types, the bandwidth is defined as the phase margin bandwidth. The gain margin bandwidth is an important parameter for the attitude control systems. If it is significantly smaller than the phase margin bandwidth, it may be an indicator of pilot-induced oscillation and it must be evaluated during the design process [2].

2.3.2.6 Performance metrics

The control system optimization process aims to obtain a desired performance level with a minimum control effort. So, performance metrics are used to achieve the Pareto-optimum solution which indicates maximum performance with the most efficient usage of the controls. Use of these specifications in the summed objective means that the optimization algorithm forces the design into Level-1 and as far as possible from the Level-1 boundary. This results in the minimum summed objective costs while still meeting the Level-1 conditions for all other specifications [2].

The first performance metric is *actuator root mean square (RMS)* which improves the stability margin in the presence of parametric uncertainty in the aircraft dynamics. It minimizes noise sensitivity of the closed-loop system, actuator saturation and PIO susceptibility. It also prevents the excitation of the high-frequency modes such as structural dynamics. The actuator RMS specification is applied from the commanded signal to the actuator response in the aircraft platforms.

The second performance metric used as the summed objective is *crossover frequency* which is defined as the frequency at which the magnitude curve of the open-loop response crosses $0dB$. This specification is used as a summed objective to minimize the crossover frequency while maintaining the Level-1 conditions in all other criteria. The crossover frequency specification is applied for the broken-loop response at the input of the actuator or mixer.

2.3.3 Design optimization

The flight control system design process requires consideration of several specifications, complex control architecture and numerous design parameters. The design space is highly constrained and constitutes a non-convex optimization problem. Hence, a

three-phase optimization scheme is developed in [2] which is combined with feasible sequential quadratic programming (FSQP) solver. FSQP is used to solve the min-max optimization problem of the multiple objective functions. Here, the optimization problem is divided into three phases such as *Phase-1*, *Phase-2* and *Phase-3*. Hard constraints, such as eigenvalue, PM and GM requirements, are satisfied in *Phase-1*. In *Phase-2*, soft constraints are satisfied without violating the hard constraints. In the last phase, *Phase-3*, the best solution is selected among the solution space that satisfies hard and soft constraints. *Pareto-optimum* solution is obtained in *Phase-3* which meets all of the requirements with minimum control usage.

The main purpose of the numerical optimization step is to tune the design parameter vector (**dp**) until all of the specifications are in Level-1 region with minimum actuator usage, in other words, minimum over-design. In the worst-case scenarios, such as edge of the flight envelope and faulty conditions, design solution might be in Level-2 or Level-3 which is acceptable for degraded conditions.

One of the several approaches to solve the multi-objective parameter optimization problem is FSQP which is able to solve the non-convex, nonlinear programming problems with large design variable set. These are the main characteristics of the flight control system design problems and FSQP algorithm is well suited for them. It is a fast and effective solver for many complex flight control system design problems. Hence, the FSQP is integrated into the CONDUIT software.

In the FSQP algorithm, a vector search direction (**d**) and correction direction (**d^c**) are determined at each iteration to update the parameter vector **dp** given in equation 2.65.

$$\mathbf{dp}_{k+1} = \mathbf{dp}_k + t_k \mathbf{d}_k + t_k^2 \mathbf{d}_k^c \quad (2.65)$$

where, k is iteration number and t is step size.

Quadratic programming search algorithm [64], which is based on [65], is the core of the FSQP solver. For more information about application of the FSQP solver in CONDUIT software, readers may refer to [2].

2.4 Closed-loop Reference Model Based Adaptive Control

In this section, closed-loop reference model (CRM) adaptive system is introduced and its stability and convergence properties are established in the absence of any perturbations. This analysis is performed based on a linear system with scalar input as given in equation 2.66.

$$\dot{x}(t) = A_p x(t) + b u(t) \quad (2.66)$$

where, $x(t) \in \mathbb{R}^n$, $u(t) \in \mathbb{R}$ are state vector and control signal, respectively. Also, it is assumed that, $A_p \in \mathbb{R}^{n \times n}$ is unknown and $b \in \mathbb{R}^n$ is known. The main goal is designing an adaptive controller such that system states $x(t)$ tracks the reference model states $x_m(t)$ which is defined in equation 2.67.

$$\dot{x}_m(t) = A_m x_m(t) + b r(t) - L(x(t) - x_m(t)) \quad (2.67)$$

where, reference model $A_m \in \mathbb{R}^{n \times n}$ is Hurwitz and command signal $r(t) \in \mathbb{R}$ is bounded. $L \in \mathbb{R}^{n \times n}$ is *Luenberger-gain* and it is chosen such that;

$$\bar{A}_m \triangleq A_m + L \quad (2.68)$$

is Hurwitz. If L is set to zero, classical model reference adaptive control (MRAC) structure is obtained.

It is assumed that a parameter vector $\theta^* \in \mathbb{R}^n$ exists which satisfies the matching condition as given in equation 2.69. Superscript (*) indicates the desired value of the θ .

$$A_m = A_p + b \theta^{*T} \quad (2.69)$$

Adaptive control signal is defined as given in equation 2.70.

$$u(t) = \theta^T(t) x(t) + r(t) \quad (2.70)$$

where, $\theta(t) \in \mathbb{R}^n$ is adaptive control gain. Update law of the adaptive gain vector is given in equation 2.71.

$$\dot{\theta}(t) = -\Gamma x(t)e(t)^T P b \quad (2.71)$$

where, $\Gamma = \Gamma^T > 0$ is defined as adaptation rate, $e(t)$ is model following error (pseudo tracking error) given in equation 2.72 and $P = P^T > 0$ is the solution of the algebraic Lyapunov equation given in equation 2.73.

$$e(t) = x(t) - x_m(t) \quad (2.72)$$

$$\bar{A}_m^T P + P \bar{A}_m = -I_{n \times n} \quad (2.73)$$

Time derivation of the error is obtained as given in equation 2.74.

$$\dot{e}(t) = \bar{A}_m e(t) + b \tilde{\theta}(t)x(t) \quad (2.74)$$

where $\tilde{\theta}(t) = \theta(t) - \theta^*$ is defined as estimation error in the adaptive parameters. More information about stability and convergence properties of the CRM-adaptive system can be found in [66].

Standard open-loop reference model (ORM), which is used in MRAC, is given in equation 2.75.

$$\dot{x}_m^o(t) = A_m x_m^o(t) + b r(t) \quad (2.75)$$

For this model, tracking error is defined as given in equation 2.76.

$$e^o(t) = x(t) - x_m^o(t) \quad (2.76)$$

Here, e^o is called as true tracking error. It is important to note that the convergence properties of the ORM-adaptive systems, in which $e^o(t)$ tends to zero, is guaranteed for the CRM-adaptive systems [66].

The main advantage of the CRM-adaptive system when compared to the ORM-adaptive one is its improved transient response characteristics. The characterization of the transient response is performed based on L_2 and L_∞ norms of several key signals such as $\dot{\theta}$, x_m , e , e^o and \dot{u} . More information about the transient response characterization is given in Chapter 6 and in references [52] and [67].

2.5 Continuous-time Control in Reinforcement Learning

Artificial intelligence is a popular and powerful tool to solve complex problems by using observations, such as sensor data. Several successful studies have been performed in which deep learning and reinforcement learning algorithms are combined. In result, Deep Q-Network (DQN) algorithm is developed in 2015 by Mnih et. al. [68] which is able to provide human-level performance on Atari games by using pixel data. In this study, a deep neural network is utilized as a function approximator which is used to estimate the action-value function.

However, DQN algorithm is able to handle discrete and low-dimensional action space while many physical control tasks require high-dimensional action space. Also, continuous-valued cases require an optimization process which should be performed iteratively at every step. Simply, DQN algorithm can be applied to the continuous case by discretizing the action space. However, this situation results in curse of dimensionality which is a common problem in machine learning applications.

In [69], a model-free, off-policy and actor-critic based algorithm is proposed in which deep neural network agent structure is used as a function approximator. They combined actor-critic approach with the DQN structure developed in [70] and [68]. Training of the system is performed by using deterministic policy gradient (DPG) algorithm given in [71]. The developed system is called as deep deterministic policy gradient (DDPG) and it is able to learn the policy by using low-dimensional observations and generated network structure with predefined hyper-parameters.

The most important feature of the DDPG algorithm is its simplicity. It uses an actor-critic structure and a proper learning algorithm which makes it easy to use, implementable and scalable for difficult problems.

In this algorithm, a standard reinforcement learning setup is utilized which consists of an agent interacting with the environment (E) in each time step (t). At each step, the agent receives observation (x_t), action ($a_t \in \mathbb{R}^N$) and scalar reward (r_t). The agent response is defined as policy (π) and it maps observations states to a probability distribution of the actions. Observation state is given as s_t and it is assumed that the environment is fully observable, $s_t = x_t$.

Finding the greedy policy in continuous-time systems requires optimization of the action a_t in every time step. This is not a practical solution for complex action spaces and large, unconstrained function approximators. Hence, in [69], actor-critic structure based on DPG algorithm is utilized to obtain continuous-time actions. Application of this reinforcement learning structure on CRM-adaptive control system is described in Chapter 6. For a detailed explanation about the continuous control with deep reinforcement learning method, readers may refer to [69].

3. TRANSITION FLIGHT MODELING OF A FIXED-WING VTOL UAV: A FIRST PRINCIPLE MODELING APPROACH

In recent years, civil UAVs have been used widely in areas such as agricultural observation, wildlife protection, and traffic monitoring. There are various types of UAVs such as quadrotor, tilt-rotor/tilt-wing and vertical take-off and landing UAV, etc. which are each designed for different operational aims. Each of these airframe concepts has advantages and disadvantages depending on the design.

Unmanned rotorcrafts are able to take-off and land vertically on both flat and rugged surfaces. They do not need a helipad because of their low weight and small dimensions. Observation and reconnaissance missions of a specified area can be performed for several minutes while hovering, which is the most important capability of the unmanned rotorcrafts.

Despite the advantages of the hover flight regime, unmanned rotorcrafts cannot be used for operations which require higher speeds, longer flight ranges or larger payload capacities. Compared to the rotorcrafts, fixed-wing UAVs have remarkable payload capacities for different types of operations such as logistics and high altitude observation.

Especially in military applications, it is important to be able to operate UAVs in variable conditions. Depending on the combat area, it may be necessary to land and take off from difficult terrain such as steep slopes and uneven surfaces. In addition, UAVs may operate in multiple flight regimes during a surveillance operation that requires tracking static and moving targets.

These requirements are relevant not only for military operations but also for civilian applications such as detecting cracks or leakages in pipelines, performing surveillance of a moving or static target in urban traffic, or transporting emergency medical supplies between medical storage facilities, hospitals, and clinics in both cities and the countryside. Runways may not be available in these areas. Especially in urban areas, it may be necessary to landing and takeoff in a limited area such as the roof of a building.

If operation time is an important factor, aircraft design should combine the high-speed cruising capability of fixed-wing UAVs and the hovering and vertical take-off/landing capability of rotary-wing UAVs. To combine the advantages of hover and forward flight capabilities, fixed-wing vertical takeoff and landing (VTOL) concept has been developed and studied in recent years.

For this reason, recent studies have focused on fixed-wing VTOL concepts that combine the advantages of fixed-wing and rotary-wing UAVs.

There are several VTOL UAV concepts with tilt-wing, tail-sitter, and tilt-rotor designs [72]. Tilt-wing UAVs take off and land vertically with a tilted-wing propulsion system. Initially, they start to climb vertically and altitude increases. During the transition flight regime, the tilt angle of the wing gradually decrease toward the horizontal position before the UAV starts to accelerate. After reaching stall speed, the wing-propulsion system is oriented horizontally and transition flight regime is completed. Tail-sitter UAVs do not have wing or propulsion system with tilt mechanisms but instead have pusher or tractor propellers. At the beginning of the flight, the UAV accelerates vertically to increase altitude. Then it performs the transition from hover to horizontal flight, which is the most critical point. In practice, the transition is achieved by a crucial stall-and-tumble maneuver. For this reason, controlled transition scenarios and maneuvers are developed to minimize crash probability.

In tilt-rotor models, the propulsion system can be positioned vertically or horizontally depending on the flight regime. Tilt-rotor UAVs behave like helicopters during hover flight and operations can be performed in this flight regime. As tilt angle decreases toward the horizontal position, the UAV starts to accelerate. After the UAV's velocity is about 1.2 times faster than the stall speed, the tilt-rotors are positioned horizontally and the transition flight regime is completed. During the transition flight, it is important to follow a transition schedule to reach the trim point. To accomplish this reliably, transition scenarios are developed that supply the required flight velocity and angle of attack data to the flight control system.

Driven by the below design requirements [73];

- 1 hr cruise flight +10 min hover flight +15 min takeoff and landing 70 km operation flight range.

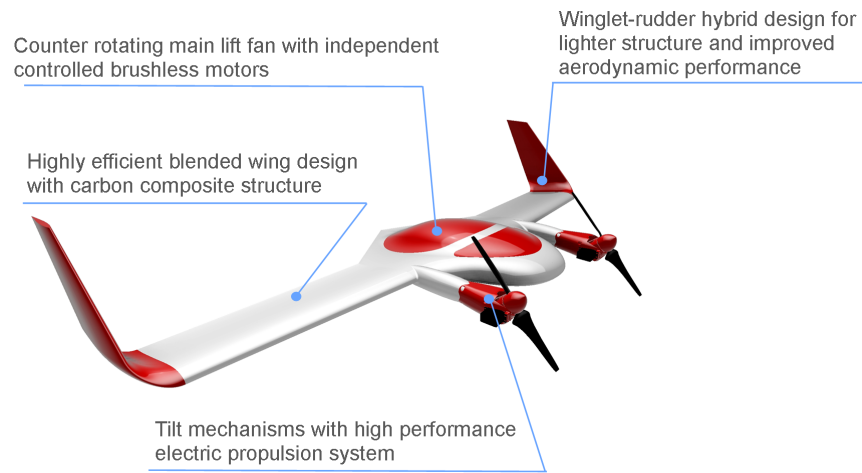


Figure 3.1 : General view of the Turac VTOL concept.

- 20 m/s cruise speed
- 8 kg payload
- Automatic takeoff/landing flight control system

following the above-mentioned advantages associated with tilt-rotor VTOL UAVs, “Turac” is designed and prototyped by the Control and Avionics Laboratory of the Istanbul Technical University [74]. General view of the Turac is given in Figure 3.1.

It is important to note that, besides various academic researchers, several companies are also working on tilt-rotor UAV designs. Commercial fixed-wing tilt-rotor UAVs include the Panther (Israel Aerospace Industries), Eagle Eye (Bell Helicopter), AD-150 (American Dynamics Flight System), and Phantom Swift (Boeing), which were all developed for military applications. In that respect, Turac is tailored towards civilian applications and the design embeds various distinct and novel concepts.

Turac design has a blended-wing airframe that generates lift with both the body (in the closed coaxial fan configuration) and the wings. For longitudinal static stability, reflex airfoil profiles are used instead of a tail group. In this way, the lift force capacity is increased while the drag force remains at an acceptable level. The wings and winglets are detachable, an advantage for easy transportation and adjusting the wingspan according to mission requirements. The all-electrical propulsion system includes brushless direct-current motors and Lithium Polymer batteries that provide high performance.

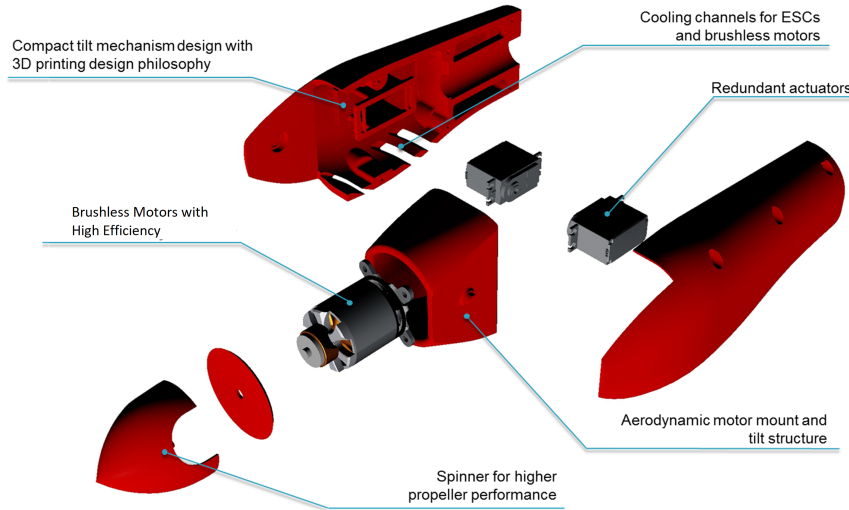


Figure 3.2 : General view of the tilt mechanism.

Turac has two tilt-rotors which are mounted on the port- and starboard-front of the body. Each tilt-rotor group provides the 15% (and up to maximum 30%) of the total weight of the UAV and they are active during the hover, transition and cruise flight regimes. General view of the tilt-rotor mechanism is given in Figure 3.2.

A co-axial lifting fan group is mounted on the rear part of the body and it is embedded into the airframe. In hover and transition flight regimes, the co-axial fan group becomes active and provides the vertical thrust force about 70% of the total UAV weight.

In hover flight regime, tilt-rotors are positioned upward and the co-axial fan group is activated. Then the UAV increases its altitude to a predefined safety level before the transition. In the transition flight regime, tilting mechanisms start to rotate toward the horizontal position to generate horizontal thrust force and this acceleration phase is kept until the forward flight speed reaches about 1.2 times of the stall speed. When the UAV exceeds the stall speed, the rotations of the tilt rotors are completed and the UAV enters the horizontal flight regime.

For hover, forward flight and transition flight tests, several scaled prototypes of Turac are manufactured by using rapid-prototyping techniques. Flight test are performed on various 1/2 - 1/3 scale models of Turac due to the limited flight test area on the university campus. So, mathematical modeling studies are performed on this prototype to verify flight tests and simulations. 1/3 scale prototype is shown in Figure 3.3. We refer the reader to [74] for an extensive treatment of not only the design but also the prototype manufacturing process of Turac.

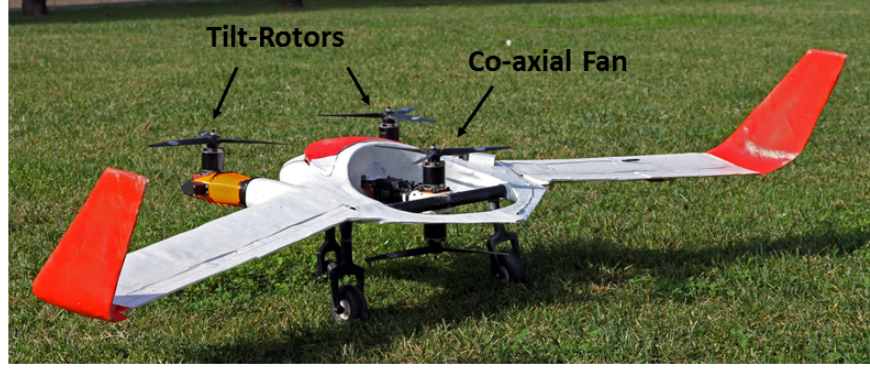


Figure 3.3 : General view of the 1/3 scale prototype of the Turac.

In [75] we focus on the dynamic modeling of the Turac fixed-wing VTOL. Specifically, we introduce a complete six-degree-of-freedom nonlinear mathematical model which is developed for the design of a forward- and back-transition control system. During the transition flight phase, UAV dynamics become quite complex due to the propeller-induced airflow effects on the airframe. Hence, it is critical to define a transition corridor for hover-to cruise and cruise-to-hover flights. To this end, forward- and back-transition scenarios are described based on the balance of forces and moments on the UAV. A state schedule is generated for flight velocity, angle of attack, and thrust levels of each propeller and is used as a feed-forward data set for the flight control system.

3.1 Mathematical Modeling

In this section, we focus on the deriving 6 degree-of-freedom (DoF) nonlinear mathematical model of the Turac which includes hover, transition and cruise flight regimes.

3.1.1 General equations of motion

The general equations of motion for the UAV are obtained based on Newton's Second Law. According to the law of motion, summing all external forces acting on a body is equal to the time derivative of its momentum with respect to inertial space. The total moment on a body is defined as the time derivative of its moment of momentum (angular momentum) with respect to the inertial space.

Before deriving the nonlinear equations of motion, it is necessary to make following assumptions [76]:

- The UAV body is symmetric on the body-XY plane.
- Total mass remains constant during the flight.
- The UAV has a rigid body.
- Inertial reference is the Earth.

Defining the axis system as shown from the Figure 3.4, body axis system (B) is fixed to the aircraft center of gravity (CG) and inertial axis system (or Earth axis system) (E) is fixed to the Earth.

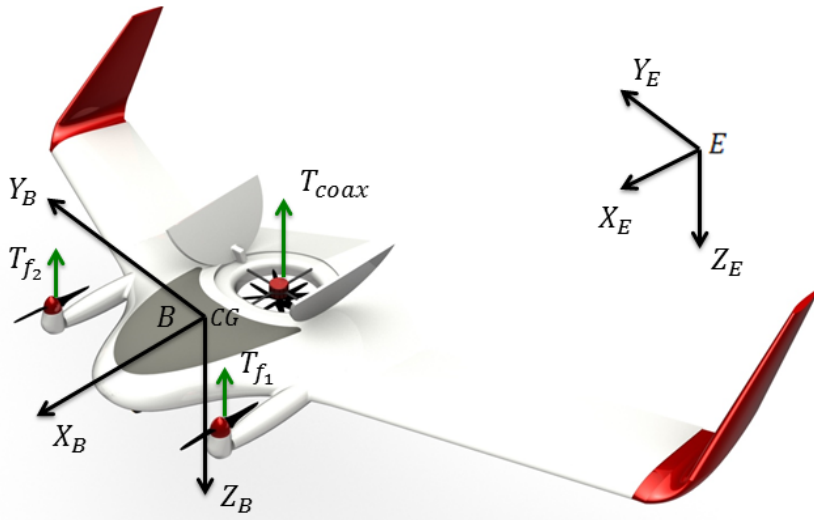


Figure 3.4 : Earth and body fixed axis systems.

Using Newton's second law of motion and the above-mentioned assumptions, force and moment equations are derived, as shown in equations 3.1 and 3.2. External forces which are placed on the right hand side of the equations, consist of gravity, aerodynamic and thrust forces. Similarly, external moments are defined as aerodynamic and thrust moments [77].

$$\begin{aligned}
 m(\dot{U} + QW - RV) &= F_{G_x} + F_{A_x} + F_{T_x} \\
 m(\dot{V} + RU - PW) &= F_{G_y} + F_{A_y} + F_{T_y} \\
 m(\dot{W} + PV - QU) &= F_{G_z} + F_{A_z} + F_{T_z}
 \end{aligned} \tag{3.1}$$

$$\begin{aligned}
 \dot{P}I_{xx} + QR(I_{zz} - I_{yy}) - (\dot{R} + PQ)I_{xz} &= L_A + L_T \\
 \dot{Q}I_{yy} - PR(I_{zz} - I_{xx}) + (P^2 + R^2)I_{xz} &= M_A + M_T \\
 \dot{R}I_{zz} + PQ(I_{yy} - I_{xx}) + (QR - \dot{P})I_{xz} &= N_A + N_T
 \end{aligned} \tag{3.2}$$

where, m is mass, I_{xx} , I_{yy} , I_{zz} , I_{xz} are inertia moments, U , V , W are body axis velocity components, P , Q , R are body rates, F is force and L , M , N are moments acting on the UAV body. Subscripts A , T , G are used for aerodynamic, thrust and gravity effects, respectively.

3.1.2 Modeling of transition flight

Transition flight is a complex regime between hover and horizontal flight. Forces and moments acting on the UAV body change continuously according to the tilt angle of the front propellers. Before deriving the dynamical equations of the transition flight, it is useful to define some geometrical dimensions, thrust and drag forces that affect the airframe.

In Figure 3.5, T_{f1} , T_{f2} , D_{f1} and D_{f2} are thrust forces and drag moments of the tilt-rotor group. T_{c1} , T_{c2} , D_{c1} and D_{c2} are thrust forces and drag moments of the coaxial fan group. l_1 and l_2 are moment arms, ζ is the angle between l_1 and X_B axis. In [73, 74], a detailed description of motor-propeller configuration and performance test results are given.

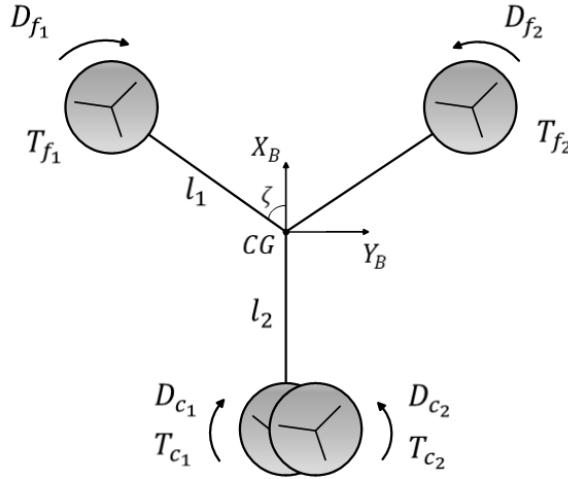


Figure 3.5 : Force, moment, and geometrical dimensions of the UAV propulsion system.

In the near hover regime, there is no aerodynamic force or moment acting on the UAV body because of the low forward airspeed. When the front motors start to rotate about the tilt axis, horizontal force is created proportional to the tilting angle. So, aerodynamic lift force, drag force, and pitching moment affect the airframe, as shown in Figure 3.6.

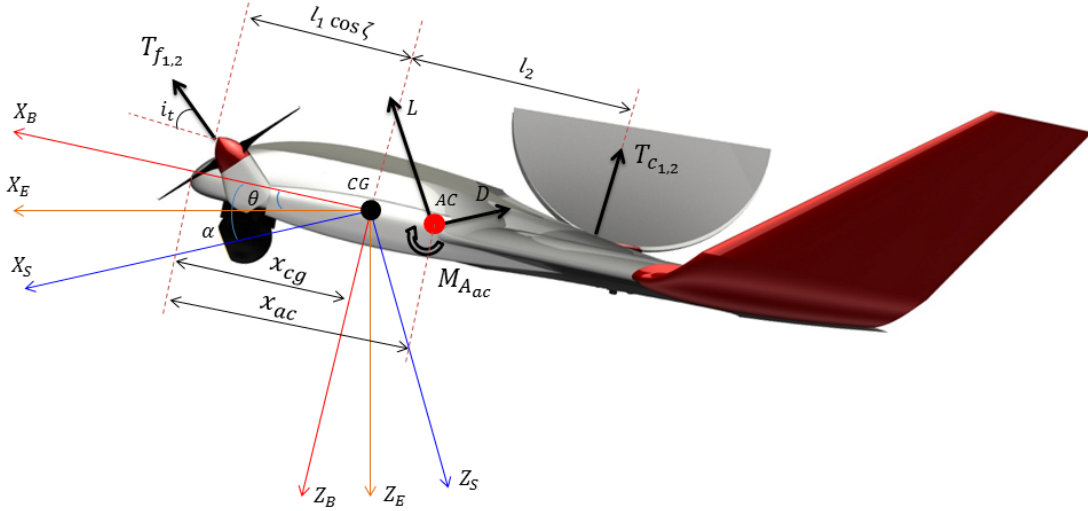


Figure 3.6 : Forces and moments on the Turac in transition flight.

Six-degree-of-freedom equations of motion can be rewritten as shown in equations 3.3 and 3.4.

$$\begin{aligned}
 m(\dot{U} + QW - RV) &= -mg\sin(\theta) + (-D\cos(\alpha) + L\sin(\alpha)) + (T_{f1} + T_{f2})\cos(i_t) \\
 m(\dot{V} + RU - PW) &= F_{G_y} + F_{A_y} + F_{T_y} \\
 m(\dot{W} + PV - QU) &= mg\cos(\phi)\cos(\theta) + (-D\sin(\alpha) - L\cos(\alpha)) - \\
 &\quad ((T_{f1} + T_{f2})\sin(i_t) + T_c)
 \end{aligned} \tag{3.3}$$

$$\begin{aligned}
 \dot{P}I_{xx} + QR(I_{zz} - I_{yy}) - (\dot{R} + PQ)I_{xz} &= L_A + (T_{f1} + T_{f2})l_1\sin(\zeta) \\
 \dot{Q}I_{yy} - PR(I_{zz} - I_{xx}) + (P^2 + R^2)I_{xz} &= (M_{A_{fs}} + M_{A_p}) - (L\cos(\alpha) + D\sin(\alpha))(x_{ac} - x_{cg}) + \\
 &\quad ((T_{f1} + T_{f2})l_1\sin(i_t)\cos(\zeta) - T_cl_2) \\
 \dot{R}I_{zz} + PQ(I_{yy} - I_{xx}) + (QR - \dot{P})I_{xz} &= N_A + (D_{f1} + D_{f2} + D_{f3} + D_{f4})
 \end{aligned} \tag{3.4}$$

3.1.3 Propeller-induced airflow effects

In the previous subsection, it is explained that, the forces and moments on the UAV are created by the thrust system and the airflow that passes through the body. Aerodynamic forces and moments exerted on the UAV are functions of total airflow vector, V_T . So, it is important to determine the magnitude and direction of the total airflow.

As shown in Figure 3.7, there are two separate airflow vectors acting on the UAV. The first one is V_∞ which is defined as free airstream velocity and it is generated by

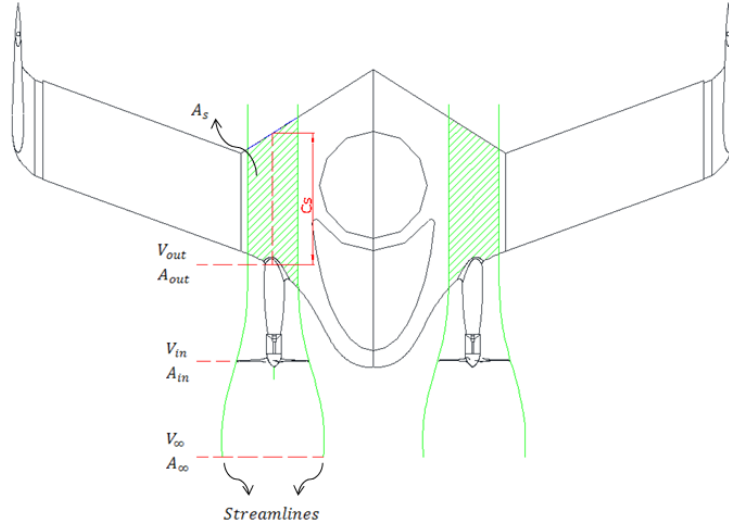


Figure 3.7 : Propeller induced airflow effects on the UAV body.

translational motion. The first one is V_{∞} and it is generated by translational motion. The components of V_{∞} are body axis velocity vectors U and W . The second airflow vector acting on the body is propeller induced airflow V_{out} which is a function of front propeller thrust $T_{f1,2}$, air density ρ , propeller area A and intake airflow velocity of the propeller V_{in} .

Input and output velocities of the propeller are shown in Figure 3.7. These velocities are calculated using classical momentum theory as shown in equation 3.5 and 3.6.

$$V_{in} = \frac{V_{\infty} \cos(\alpha) \cos(i_t) + V_{out}}{2} \quad (3.5)$$

$$V_{out} = \sqrt{\frac{2T_f}{\rho \pi R_p^2} + (V_{\infty} \cos(\alpha) \cos(i_t))^2} \quad (3.6)$$

In equation 3.5, intake airflow velocity V_{in} is defined in the term of tilt angle and angle of attack which is an important detail for transition scenario calculations. Note that equation 3.5 and 3.6, appear differently than their form in momentum theory, and these are due to angle of attack and tilt angle.

According to the continuity equation, output cross section area of the propeller induced airflow changes as a function of V_{in} and V_{out} and given in equation 3.7.

$$A_{out} = \frac{\pi R_p^2 V_{in}}{V_{out}} \quad (3.7)$$

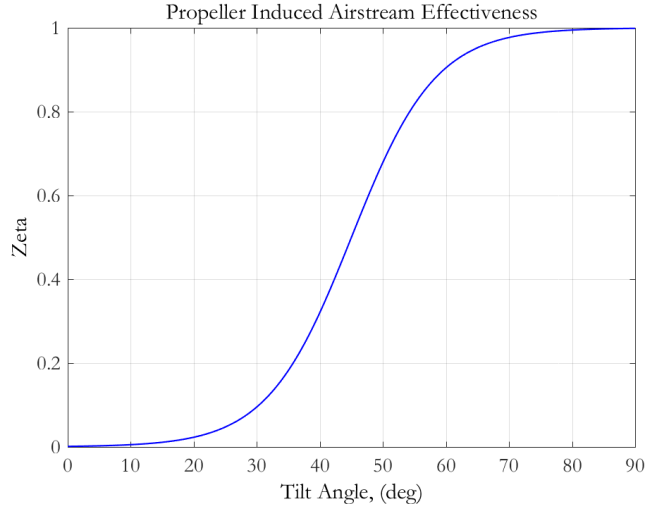


Figure 3.8 : Change of effectiveness coefficient with the tilt angle.

In transitional and horizontal flight, the total airflow vector flows over in a specific area (A_s) on the UAV body as shown in Figure 3.7 and it is calculated geometrically as given in equation 3.8.

$$A_s = 2R_s c_s \quad (3.8)$$

where c_s is mean aerodynamic chord of the specified region that shown in Figure 3.7.

In hover flight, the thrust axis of the tilt rotors is perpendicular to the X_B axis, so any propeller induced aerodynamic effects are not observed on the body. When the tilt angle starts to decrease, additional forces and moments are generated due to the propeller airstream. However, this effect does not occur suddenly. It changes step-by-step as a function of tilt angle. For this type of change, an effectiveness coefficient ξ is defined as an assumption in modeling the tilt-rotor aerodynamic effect on the UAV body. We model it as a sigmoid function as shown in equation 3.9. In Figure 3.8, the change of effectiveness coefficient is shown. as a function of tilt angle. The effectiveness coefficient ξ is used to calculate the total effective velocity on the body profile while the tilt angle value is between 0 and 90 degrees.

$$\xi = 1 - \frac{1}{1 + e^{-0.15(i_t - 45)}} \quad \text{for } i_t \in [0^\circ, 90^\circ] \quad (3.9)$$

3.1.4 Free airflow effects

The free airflow passes through from the area which is not affected by the propeller-induced airflow. In the beginning of transition flight regime, the effect of the free airflow is dominant on the UAV because of the almost-vertical tilt-rotors. So, it is important to represent the aerodynamic effect of this airflow vector.

The aerodynamic forces L_w, D_w, Y_w and moments m_w, l_w, n_w of the UAV without propeller effect are calculated in equation 3.10. In the following equations, the region which is not affected by the propeller-induced airflow is specified as $(A - 2A_s)$.

$$\begin{aligned}
 L_w &= \bar{q}(A - 2A_s)C_{L_w} \\
 D_w &= \bar{q}(A - 2A_s)C_{D_w} \\
 Y_w &= \bar{q}(A - 2A_s)C_{D_w} \\
 m_w &= \bar{q}\bar{c}(A - 2A_s)C_{m_w} \\
 l_w &= \bar{q}b(A - 2A_s)C_{l_w} \\
 n_w &= \bar{q}b(A - 2A_s)C_{n_w}
 \end{aligned} \tag{3.10}$$

where A is the planform area of the UAV and \bar{q} is dynamic pressure. Here, w subscript is used to represent the free airflow forces and moments. Aerodynamic coefficients in equation 3.10 are derived as shown in equation 3.11.

$$\begin{aligned}
 C_{L_w} &= C_{L_{w,b}} + C_{L_{w,\delta_e}} \delta_e + C_{L_{\dot{\alpha}}} \frac{\dot{\alpha}\bar{c}}{2U_1} + C_{L_q} \frac{q\bar{c}}{2U_1} \\
 C_{D_w} &= C_{D_{w,b}} + C_{D_{w,\delta_e}} \delta_e + C_{D_{\dot{\alpha}}} \frac{\dot{\alpha}\bar{c}}{2U_1} + C_{D_q} \frac{q\bar{c}}{2U_1} \\
 C_Y &= C_{Y_{w,b}} + C_{Y_{w,\delta_a}} \delta_a + C_{Y_{w,\delta_r}} \delta_r + C_{Y_p} \frac{pb}{2U_1} + C_{Y_r} \frac{rb}{2U_1} \\
 C_{l_w} &= C_{l_{w,b}} + C_{l_{\delta_a}} \delta_a + C_{l_{\delta_r}} \delta_r + C_{l_p} \frac{pb}{2U_1} + C_{l_r} \frac{rb}{2U_1} \\
 C_{m_w} &= C_{m_{w,b}} + C_{m_{w,\delta_e}} \delta_e + C_{m_{\dot{\alpha}}} \frac{\dot{\alpha}\bar{c}}{2U_1} + C_{m_q} \frac{q\bar{c}}{2U_1} \\
 C_{n_w} &= C_{n_{w,b}} + C_{n_{w,\delta_a}} \delta_a + C_{n_{\delta_r}} \delta_r + C_{n_p} \frac{pb}{2U_1} + C_{n_r} \frac{rb}{2U_1}
 \end{aligned} \tag{3.11}$$

where;

$$\begin{aligned}
C_{L_{w,b}} &= C_{L_0} + C_{L_\alpha} \alpha \\
C_{D_{w,b}} &= C_{D_0} + C_{D_\alpha} \alpha \\
C_{m_{w,b}} &= C_{m_0} + C_{m_\alpha} \alpha \\
C_{Y_{w,b}} &= C_{Y_0} + C_{Y_\beta} \beta \\
C_{l_{w,b}} &= C_{l_0} + C_{l_\beta} \beta \\
C_{n_{w,b}} &= C_{n_0} + C_{n_\beta} \beta
\end{aligned} \tag{3.12}$$

Here, the aerodynamic coefficients with (wb) subscript represents the wing-body geometry effects on each coefficient.

In transition flight, longitudinal aerodynamic coefficients of the wing-body geometry identify the dynamic characteristics of the UAV. So, $C_{L_{w,b}}$, $C_{D_{w,b}}$ and $C_{m_{w,b}}$ are obtained by using 3D CFD analysis. They are used to generate lookup-tables which is embedded into the nonlinear mathematical model. Remaining aerodynamic coefficients, including lateral directional coefficients, are obtained by using Advanced Aircraft Analysis (AAA) software which is developed by DAR corporation [78]. During our analysis, we assume that the aerodynamic coefficients of the UAV body (i.e. the part which is carrying the payload and the avionics) are not affected by coaxial fan airstream. Thus in this sense, we are assuming the lift and drag coefficients to be constant for the body part. This is indeed a valid approach as the wing is the preliminary force generation mechanism. This is further illustrated and verified by the CFD analysis.

3.1.5 Total airflow effects

In transition flight, there are very complex and nonlinear aerodynamic effects on the UAV which are created by the free airflow and propeller induced airflow. So, it is very hard to represent these nonlinear aerodynamic effects mathematically without making any assumptions.

In this study, free and propeller-induced airflow effects are modeled linearly by using superposition rule. Hence, these two aerodynamic effects are examined separately. This assumption essentially simplifies the derivation of the mathematical representations. For this purpose, the lift force, drag force and pitching moment are calculated for two situations as with propeller effect L_s, D_s, M_s and without propeller

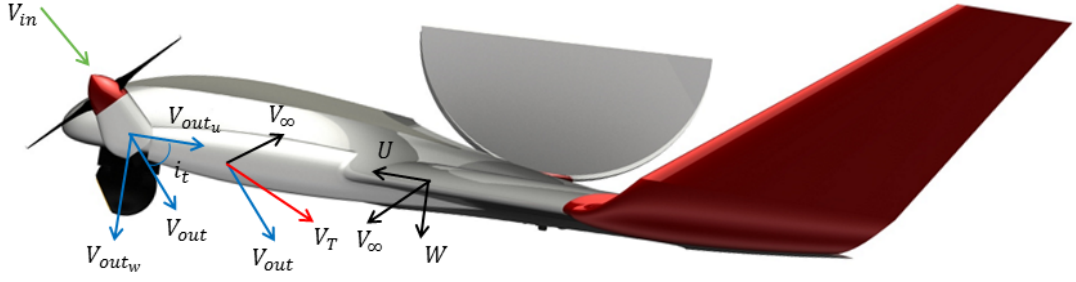


Figure 3.9 : Total airspeed vector on the UAV.

effect L_w, D_w, M_w . Then, the values of aerodynamic forces and moments with and without propeller effect are summed up to obtain the total aerodynamic effects on the UAV body. Both the free airstream and the propeller-induced airstream are effective on A_s . Therefore, the total airspeed V_T is used to calculate the lift force, drag force and pitching moment that generated on A_s as shown in equation 3.13.

$$\begin{aligned} L_s &= \frac{1}{2} \rho V_T^2 A_s C_{L_s} \\ D_s &= \frac{1}{2} \rho V_T^2 A_s C_{D_s} \\ M_s &= \frac{1}{2} \rho V_T^2 A_s c_s C_{M_s} \end{aligned} \quad (3.13)$$

As shown from the Figure 3.7, there is no downwash effect on the section that the propeller induced airstream passes through. So, this region can be assumed as infinite wing. Hence, the aerodynamic coefficients in equation 3.13 are obtained from 2D analysis of the wing airfoil and lookup-tables are generated. The detail information about this subject is given in the CFD analysis section.

The total airspeed that affects the above-mentioned area A_s is defined in vector form as shown in Figure 3.9 and it is calculated by using equation 3.14.

$$V_T = \sqrt{(V_{out} \xi \sin(\alpha + i_t))^2 + (V_{out} \xi \cos(\alpha + i_t) + V_\infty)^2} \quad (3.14)$$

The airflow over the wing is affected by free-stream velocity and output velocity of the propeller. Propeller-induced airstream velocity is separated into its x and y components, because of inserting free-stream velocity as shown in equation 3.14. Tilt effect is also shown in calculation as tilt angle i_t in this equation.

As mentioned before, the total airflow vector V_T passes through the specified area A_s on the UAV body. Magnitude of the V_T is a function of free-stream airflow speed, angle of attack and tilt angle. For modeling of aerodynamic effects of the total airflow vector, it is important to define effective angle of attack α_{eff} on the A_s which is produced by propeller-induced airstream and free airstream vectors. Geometrically, α_{eff} is calculated by using equation 3.15.

$$\alpha_{eff} = \arctan \left(\frac{V_{\infty} \sin(\alpha) - V_{out} \sin(i_t)}{V_{\infty} \cos(\alpha) + V_{out} \cos(i_t)} \right) \quad (3.15)$$

Unlike propeller effect on a conventional airplane wing, tilt angle is inserted into the tilt-rotor calculations of effective angle of attack in VTOL concept.

3.1.6 Modeling the thrust-airspeed relationship for the tilt-rotor propeller

Propeller intake airflow speed V_{in} is the free-stream velocity which is in the same direction as propeller rotation axis. The value of V_{in} and thrust relate to the angle of attack and the tilt angle. In other words, the angle of attack on the propeller blades decreases as the intake airflow speed increases. So, the thrust decreases because of the low angle of attack on the blades.

In Figure 3.10, propeller intake airflow speed—generated thrust characteristics of the 12x6 inch fixed pitch propeller are shown for various RPM. The test data for different airspeed and RPM are available at producer's database. This dataset is used to generate thrust functions and lookup-tables with respect to airspeed for each RPM. A surface function is used to find out thrust forces at different airspeed which is not available at the test data.

3.2 Computational Fluid Dynamics Analysis

Computational Fluid Dynamics (CFD) is used to generate aerodynamic coefficients and create transition and back-transition scenarios. The 2D-analysis of the wing airfoil is used to develop the transition scenario. In this section, 2D analysis, forward flight, and transition flight are explained.

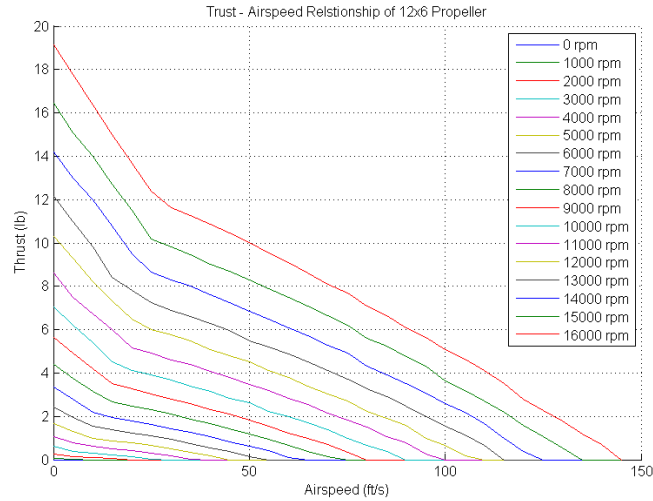


Figure 3.10 : Thrust - propeller intake airspeed speed characteristics of the 12x6 fixed-pitch propeller.

3.2.1 2D analysis

As mentioned before, the propeller induced airflow passes through the wing profile and there is no finite wing effects (See Figure 3.7). So, this region is assumed as infinite wing and 2D aerodynamic analysis can be used to calculate the aerodynamic coefficients of this region.

The wing airfoil of Turac is selected as MH-78 and its aerodynamic coefficients are calculated by using 2D analysis for different Reynold numbers in XFLR5 which applies Vortex Lattice Method (VLM). The lift coefficient C_{L_s} of wing profile at 2D analysis versus Reynolds number and elevator angle is shown in Figure 3.11. Similarly, in Figs. 3.12 and 3.13, the drag coefficient C_{D_s} and the pitching moment coefficient C_{M_s} of wing profile versus Reynolds number and elevator angle is shown.

3.2.2 3D analysis

The CFD analysis for forward and transition flights is done in four steps: creating model and control volume, meshing whole geometry, building up boundary layer and setting up the analysis. In this study, the cases are prepared for forward and transition flight step by step to solve the problem accurately. One of the important issues in the analysis is generating boundary layers with respect to the value of y^+ which is 1 for the first cell height of the boundary layer. The value of y^+ changes due to viscous, transition and turbulence regime. It is a vital issue for the quality of the analysis in

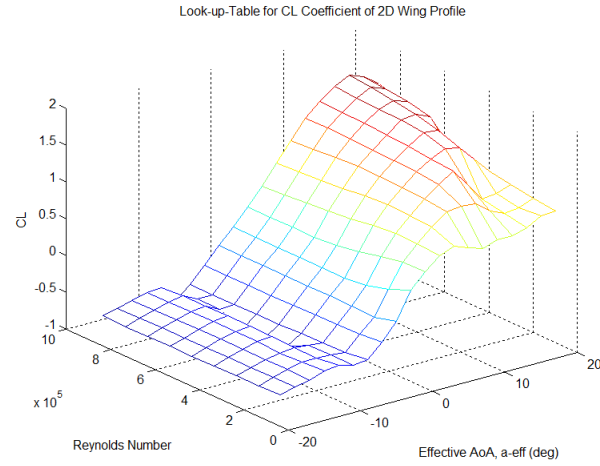


Figure 3.11 : Lift coefficient C_{L_s} of the 2D wing airfoil for different Reynolds numbers.

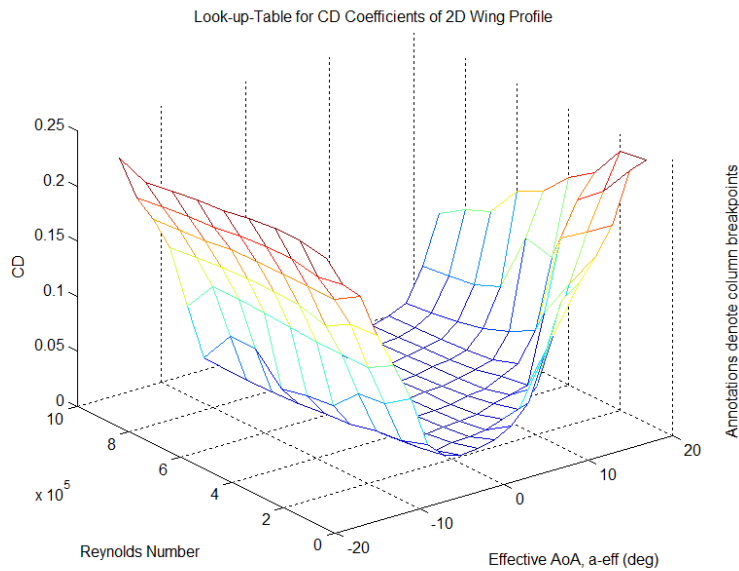


Figure 3.12 : Drag coefficient C_{D_s} of the 2D wing airfoil for different Reynolds numbers.

which Fluent is used as a solver software. The K-epsilon Realizable Enhanced Wall Treatment turbulent model is obtained for all CFD cases.

In developing part of the transition and back transition scenarios, aerodynamic coefficients are provided from the CFD analysis. In these analysis, half of Turac is modeled because of symmetry to decrease solving time memory use. For the analysis, the coaxial fan door is closed as in forward flight. The model of the half Turac can be seen in Figure 3.14. It is lied on one of the control volume wall which is set as symmetry.

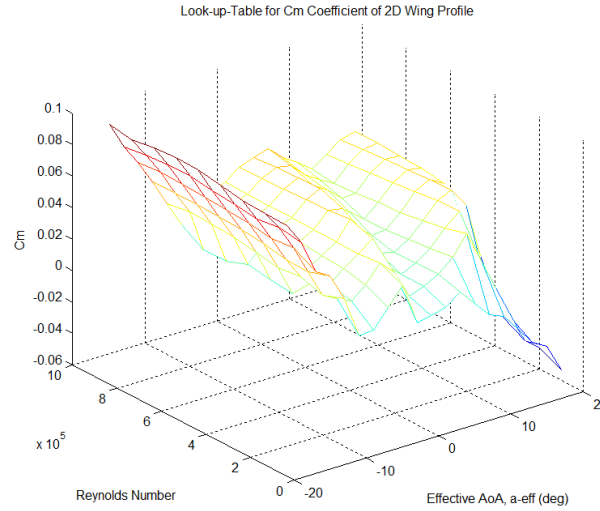


Figure 3.13 : Pitching moment coefficient C_{M_s} of the 2D wing airfoil for different Reynolds numbers.

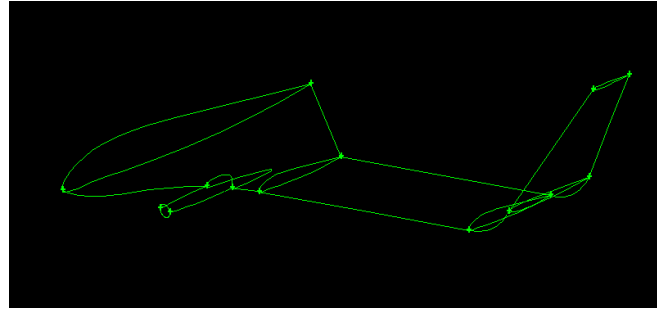


Figure 3.14 : The half of Turac model for forward flight regime in CFD analysis.

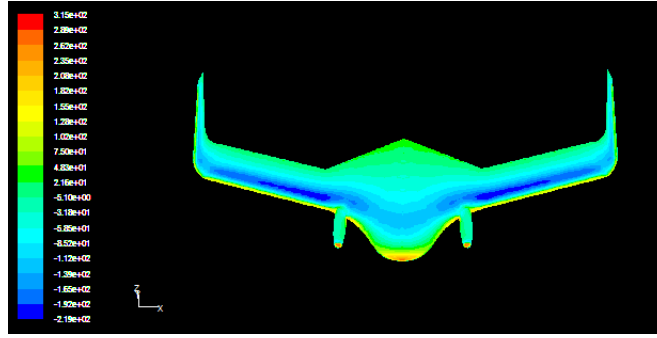
The half of Turac geometry at forward flight concept is analyzed from 0° to 15° angle of attack at forward flight speed. The aerodynamic coefficients are calculated from the mentioned analysis. Moreover, the same analysis for different forward flight speed at the constant angle of attack are repeated to search the change of aerodynamic coefficients. The analysis are applied for -3° , 0° and 3° angle of attack values at 5 m/s, 10 m/s, 15 m/s and 20 m/s forward flight velocities. Table 3.1 shows the aerodynamic coefficients of Turac due to different forward flight speed at constant angle of attack. In that sense, we assume that the aerodynamic coefficients of the Turac prototype do not change with respect to airspeed.

In Table 3.1, as the angle of attack increases, lift and drag coefficients increase and pitching moment coefficient decreases. It can be seen obviously in the table that the aerodynamic coefficients do not change with the Reynolds number at constant angle of attack.

Table 3.1 : The force and moment coefficient for transition scenario.

α (deg)	V (m/s)	C_L	C_D	C_m
-3	15	-0.08601	0.04092	0.01516
	20	-0.08699	0.03964	0.01589
0	5	0.12406	0.03836	-0.09538
	10	0.12376	0.03489	-0.09486
	15	0.12496	0.03321	-0.09521
	20	0.12494	0.03209	-0.09499
3	5	0.34476	0.04104	-0.20825
	10	0.34680	0.03745	-0.20864
	15	0.34844	0.03567	-0.20921
	20	0.34927	0.03450	-0.20926

In Figure 3.15, the change of pressure on the Turac can be seen. The values of static pressure on the colorbar are Pascal. The highest value of pressure is at the nose and tilt component. The lowest pressure on Turac is at the quad-chord of the wings.

**Figure 3.15** : The static pressure distribution of Turac.

In the nonlinear mathematical model of the Turac, it is necessary to generate the lookup-tables represent the aerodynamic effects of the wing-body geometry. For this purpose, the 3D CFD dataset is obtained for forward flight in $0^\circ - 15^\circ$ angle of attack region which includes stall effects as shown in Figures 3.16, 3.17 and 3.18.

The same aerodynamic coefficients were used at different forward flight velocities for calculations of transition and back-transition scenarios, as per the description and Table 3.1.

A part of the transition scenario is also modeled and analyzed by using CFD method. Further information on the the transition-flight analysis can be found in [72]. In this model complete Turac is used and two tilt propellers and coaxial propellers are modeled as fan boundary condition. In this analysis, coaxial part of the Turac is open because of the transition concept. As boundary conditions for propeller, a pressure

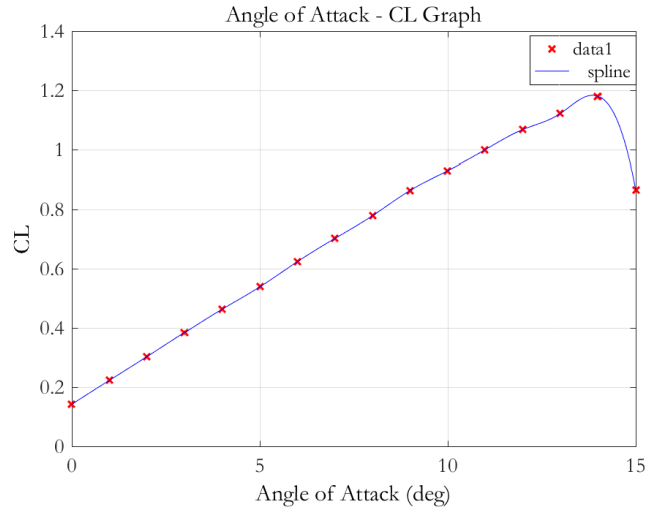


Figure 3.16 : Angle of attack - C_L graph of the Turac.

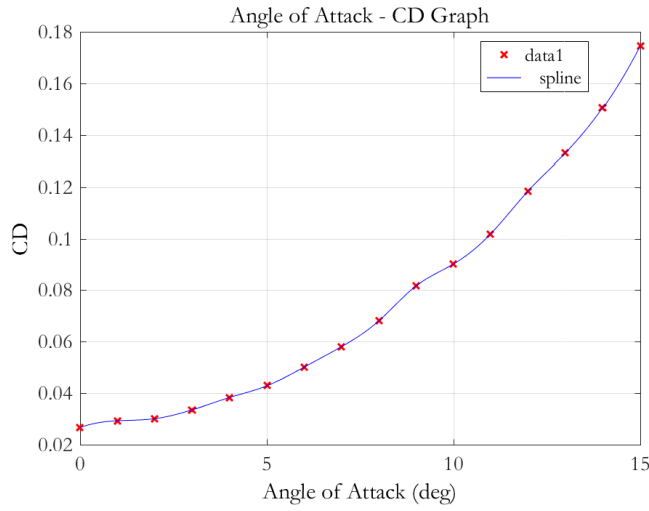


Figure 3.17 : Angle of attack - C_D graph of the Turac.

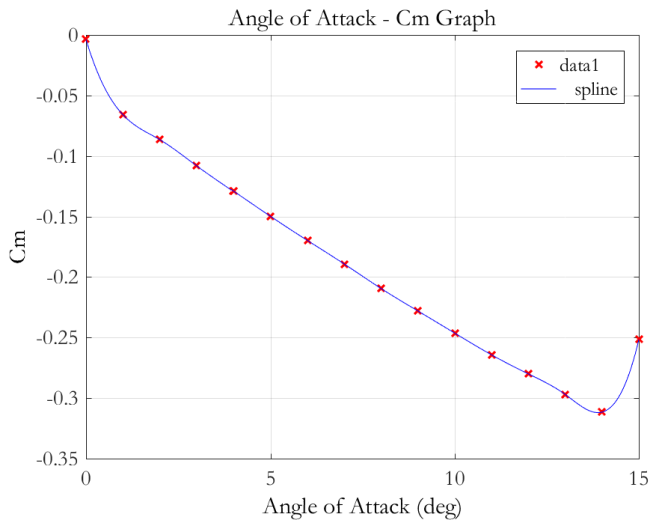


Figure 3.18 : Angle of attack - C_M graph of the Turac.

jump is inserted in order to properly define the thrust produced by each propeller. The pressure jump of the propeller is calculated from momentum theory. Figure 3.19 shows

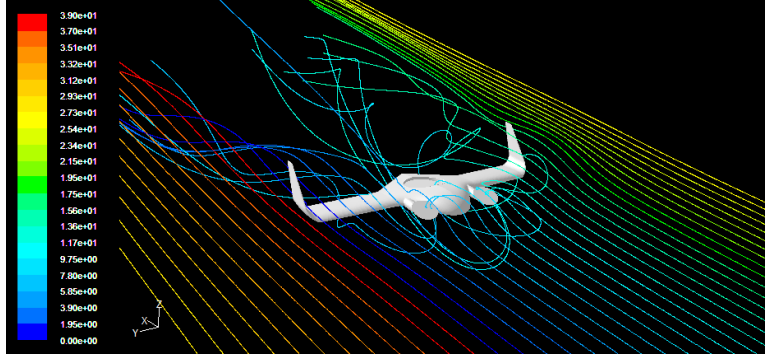


Figure 3.19 : The path lines of Turac in transition regime.

the streamlines of the Turac at 70° tilt angle and -1° angle of attack at 10 m/s forward flight speed.

In Figure 3.19, the flow is inserted into the propeller disc for tilt and for coaxial rotors. The swirl of the flow can also be seen in the figure behind the propellers. The streamlines on the wings are smooth compared to those on the body. The body of Turac has airfoil profile which produces lift during forward flight. However, in transition flight, the contribution of body in producing lift is very poor because of the complex flow on the body and the opened fan doors. For this reason, we assume the lift and drag contribution of the body to be independent of the coaxial fan operation during the hover and the transition.

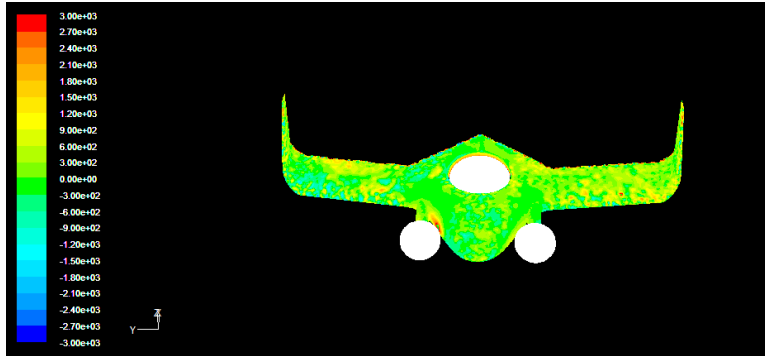


Figure 3.20 : The static pressure distribution of Turac in transition regime.

In Figure 3.20, the static distribution on Turac body can be seen. According to these results, the aerodynamics of the transition regime is extremely complex. However it is apparent that the forces and moments generated by the tilt and the coaxial propellers and the net force effects are extremely important in defining the transition regime and maneuver. In the next subsection, we calculate the necessary thrust forces to achieve a balanced flight (both in forces and moments) for a designed transition scenario.

Table 3.2 : The moment coefficient and force components for the forward-transition scenario.

$V(m/s)$	$i_t(deg)$	$\delta_e(deg)$	$\alpha(deg)$	$T_f(N)$	$T_c(N)$	ΣF_x	ΣF_z	C_m
2	70	0	-1	8.58	39.29	7.44	-0.086	-0.0015
5	70	0	-1	8.59	39.38	7.5	-0.005	-0.002
10	70	0	-1	8.55	39.2	7.44	0.066	-0.001
15	70	0	-1	8.55	38.68	7.28	-0.001	0.002
20	70	0	-1	8.7	37.76	7.13	0	0.006
25	70	6.45	-1	10.2	29.86	7.82	0.006	-0.001
29	70	17	-1	19.8	0	14.9	0.002	0.049
32	0	-1	0.5	24.9	0	44.5	0	-0.005
35	0	-5.55	0.5	3	0	-0.005	0.005	0.021
40	0	-15	0.5	3.9	0	-0.043	-0.061	0.075

3.3 Transition Scenario

As to achieve a trimmed flight in the forward- and back-transition phases, it would be necessary to drive the magnitude of forces for both the tilt-rotors and lifting fan. Through the application of these forces during the transition, one would ensure a trimmed transition into the forward flight (or hover). The total force in the x and z directions and moment around aerodynamic center can be calculated using equation 3.16.

$$\begin{aligned}
 F_z &= L_w \cos(\alpha) + 2T \sin(i_t) \cos(\alpha) + L_s \cos(\alpha_w) - D_s \sin(\alpha_w) + T_c \cos(\alpha) - mg \\
 F_x &= 2T \cos(i_t) \cos(\alpha) - D_w - L_s \sin(\alpha_w) - D_s \cos(\alpha_w) - T_c \sin(\alpha) \\
 M_{ac} &= 2T \sin(i_t)(x_{ac} - x_T) + T_c(x_{ac} - x_{T_c}) + mg(x_{ac} - x_w) \cos(\alpha)
 \end{aligned} \tag{3.16}$$

Here positive direction is lift direction ΣF_z and thrust direction at ΣF_x [79]. The pitching moment coefficient is obtained using equation 3.17.

$$C_M = \frac{M_{ac}}{0.5\rho V^2 c S} + C_{m_{\delta_e}} \delta_e \tag{3.17}$$

Using the force descriptions, a transition scenario is developed for the 1/3 scale Turac prototype. In the designed transition scenario, which is shown in Table 3.2, excess thrusts are produced at each step of the transition as to accelerate the UAV. In this scenario, the speed of the UAV increases almost uniformly during the transition flight regime. At the last step of transition, all aerodynamic forces and moment equal to zero to achieve forward flight trim equilibrium point.

Table 3.3 : The force and moment coefficient for back transition scenario.

$V(m/s)$	$i_t(deg)$	$\delta_e(deg)$	$\alpha(deg)$	$T_f(N)$	$T_c(N)$	$\Sigma F_x(N)$	$\Sigma F_z(N)$	C_m
40	90	-7.42	0.5	0.8	0.47	-10.1	-0.019	0.0377
35	90	-7.42	0.5	1.2	1.5	-7.84	-0.009	-0.0044
32	90	-7.42	0.5	3.21	5.85	-6.9	0.006	0.0012
29	90	-7.42	0.5	4.2	11.5	-5.88	0.019	0.0004
25	90	-7.42	0	7	22	-3.56	-0.01	0.0071
20	90	-7.42	0	7.44	28	-2.26	-0.002	0
15	90	-7.42	0	8.1	32	-1.26	-0.009	-0.0034
10	90	-1.6	0	8.6	35	-0.55	0.002	-0.0048
5	90	-6.0	0	9	36.5	-0.12	0.059	0.0003
2	90	-2.8	0	9.15	36.7	0.003	-0.004	-0.0037

At the transition flight regime first, the front tilt-rotor propeller angle is set as 70° and angle of attack at -1° until 29 m/s forward flight speed. The scenario continues until 40 m/s in order to establish stable forward flight after the transition flight regime. The aerodynamic forces and pitching moment are calculated for each flight speed by using the above-mentioned equations.

Here the coaxial fan force and the tilt rotor forces are calculated to achieve almost perfect balanced flight in z force direction and around y moment direction. In addition, the elevator angle δ_e was also used in order to have balanced and stable flight throughout the complete transition regime. Elevator angle δ_e is set as 0° until 20 m/s, then it equals 6.45° at 25 m/s, 17° at 29 m/s, -1° at 32 m/s, -5.548° at 35 m/s and -15° at 40 m/s. In the scenario, excess thrust occurs until 32 m/s to accelerate the UAV in x direction, then the balance situation is provided after that speed. Thrust produced by the coaxial engine starts from a high value and decreases to zero. In complete scenario, moment coefficient and ΣF_z almost equals to zero and thus in perfect z -force and y -moment balance. Also note that in the last two steps of the scenario, all aerodynamic forces and pitching moment are zero which means the UAV is at equilibrium at cruise speed.

The back-transition scenario is also developed from forward flight regime to hover flight as shown in Table 3.3. In back transition regime, the thrust of the tilt and coaxial engines are increased as the forward flight velocity decreases. At the last step, lift and drag forces and pitching moment equal to zero to make the UAV in trim flight conditions.

In this scenario, the tilt angle is set at 90° during whole scenario. The back-transition scenario is the inverse of the transition scenario. It starts at 40 m/s forward flight with

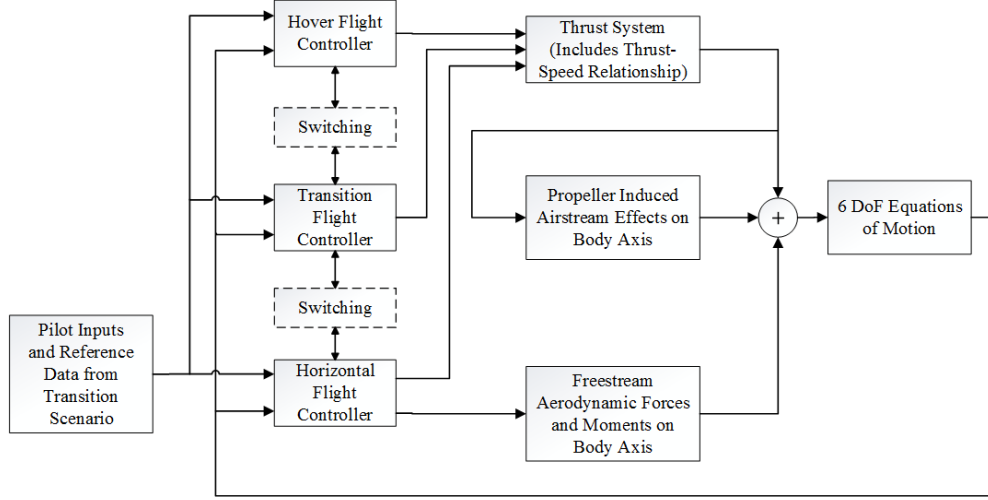


Figure 3.21 : General block diagram of the nonlinear mathematical model of the complete flight regimes.

90° tilt angle, then the UAV slows down by changing the thrust of tilt and coaxial angle, angle of attack and elevator deflection δ_e .

In this scenario, elevator angle δ_e is not set to 0° from start. It is set to -7.42° at 40 m/s, -1.6° at 10 m/s, -6° at 5 m/s and -2.8° at 2 m/s. The thrust of the tilt and coaxial engines start from almost zero and increase until reaching the values of hover-flight thrust. At 2 m/s airspeed, aerodynamic forces and moment are at zero which means the UAV is at equilibrium and in full hover regime.

In the next section, we show the design of a transition control system which uses the provided forward- and back-transition scenarios as reference signals. In addition we provide the details of a complete flight which involves hover-forward flight-hover regimes demonstrating fully controlled flight envelope.

3.4 Complete Mathematical Model Structure and Simulations

In Section 3.1, we had presented the thrust and aerodynamic effects and showed the highly nonlinear relations that govern not only the hover, forward flight but also the transition flight regime. Combining the dynamics associated with hover, transition and forward flight in Figure 3.21, we obtain the general block diagram of the nonlinear mathematical model of the complete flight envelope. Here the flight controls for each of the regimes are also represented with switching functions between each of these regimes.

To demonstrate the effectiveness and feasibility of the transition control scheme in experiment, we designed a control system which has readily (and easily) implementable cascaded PID structure. The cascade control system consists of a three-loop PID controller. In this control system, rate feedback is performed in the first loop to increase the stability. Then, attitude data is fed back into the second loop to generate reference attitude commands. In the third loop, linear velocity is fed back into the controller. Beside the hover and transition control systems, horizontal flight control system contains classical attitude controllers such as roll, pitch and yaw control systems which are also designed based on PID control.

3.4.1 Forward and back-transition algorithms

In this subsection, detailed transition and back-transition scenarios are obtained by using basic force and moment equations. Before applying these scenario dataset into the nonlinear mathematical model as a reference signal, it is important to sequence the algorithm that is used for switching between low level controllers. Transition and back-transition algorithms are shown in Figure 3.22. High-level flight control system is programmed according to these algorithms.

Following Figure 3.22, step-by-step transition algorithm is described as following.

1. Turac is in hover flight regime. Tilt-rotors are positioned vertically and three-loop hover controller runs to track linear velocity commands $V_{ref_{hover}} \leq 3 \text{ m/s}$ in hover flight.
2. Acceleration in hover regime up to 3 m/s flight speed. Step 1 and Step 2 are coded as Phase-1.
3. If the flight speed V_∞ reaches to 2 m/s, the transition controller is activated and the tilt-rotors are positioned at 80° .
4. Acceleration in transition regime up to 25 m/s flight speed. Step-3 and Step-4 are coded as Phase-2.
5. If the flight speed V_∞ reaches to 25 m/s, the horizontal flight controllers are activated and the tilt-rotors are positioned at 0° . Horizontal flight regime is coded as Phase-3.

Step-by-step back-transition algorithm is described as following;

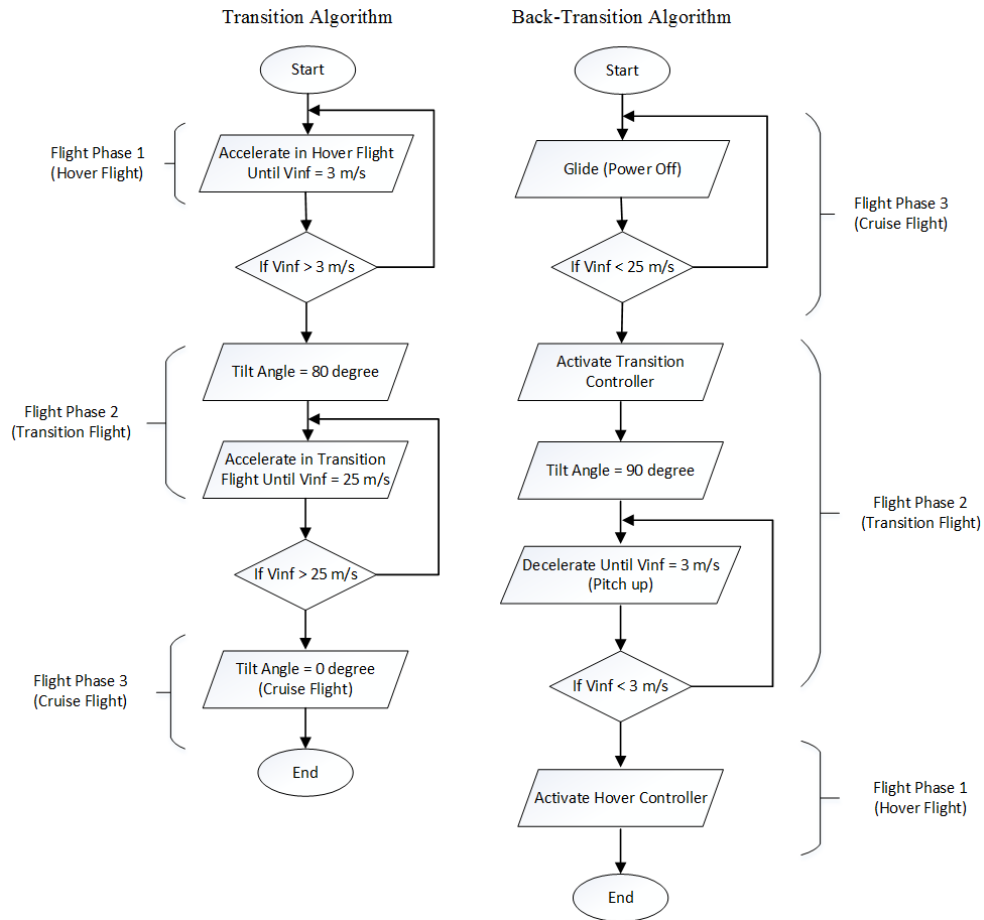


Figure 3.22 : Transition and back transition algorithms.

1. It is important to reduce the flight speed before transition regime. To do this, the front propellers are stopped and the aircraft starts to glide.
2. If the flight velocity is lower than 25 m/s, the transition controller is activated.
3. Tilt angle is positioned at 90°
4. Pitch up command is send to the system to decelerate until the 3 m/s flight speed.
5. Hover controller is activated and Turac flies in hover regime.

3.4.2 Simulation results

In this part of study, simulations are performed on 6-DoF nonlinear mathematical model and a complete flight (hover – transition – cruise - back transition–hover) of the Turac is simulated for about 120 sec. The above-mentioned algorithms are used in flight phase switching system. Simulation results are shown in Figures 3.23, 3.24,

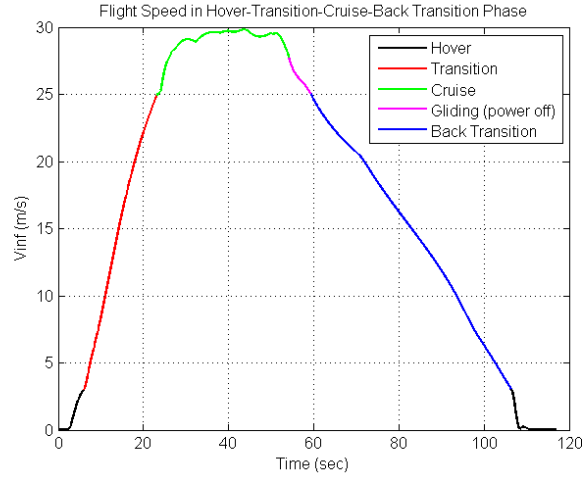


Figure 3.23 : Airspeed time history during the simulation.

3.26 and 3.25. Each flight regime is represented in different colors and labeled on the graphs.

In Figure 3.23, hover flight is performed until the flight speed reaches to 3m/s (black region). Then transition flight regime starts, tilt-rotors are positioned at 90° and Turac accelerates until 25 m/s (red region). After that, horizontal flight controllers are activated and the UAV performs horizontal flight about 29 – 30 m/s (green region). Before the back-transition regime, power of the tilt-rotor group is cutoff, the UAV starts to glide and flight speed decreases to 25 m/s (magenta region). The back-transition flight regime starts when the flight speed goes down below 25 m/s and continue until the hover flight speed limit, 3 m/s (blue region). Finally, hover flight controllers are activated by the algorithm and flight speed decreases to 0 m/s in hover flight (black region at the end of the flight).

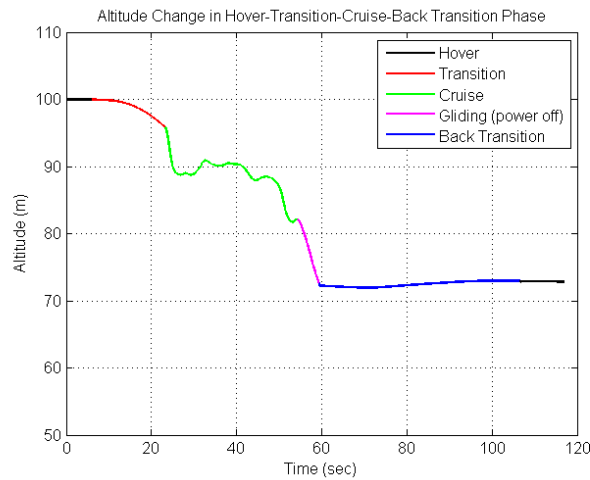


Figure 3.24 : Altitude time history during the simulation.

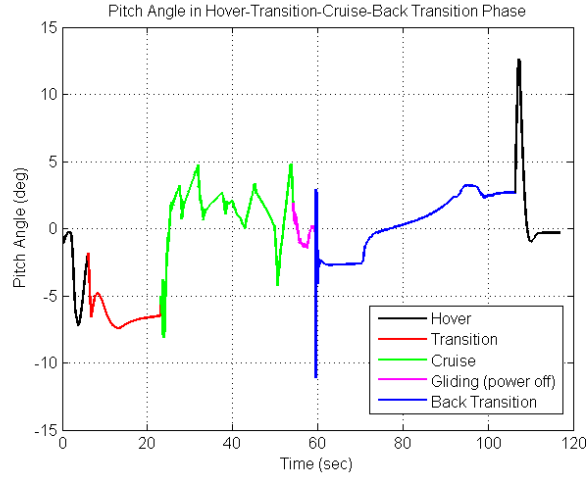


Figure 3.25 : Pitch angle time history during the simulation.

Altitude change is shown in Figure 3.24. In hover flight, altitude remains constant for several seconds at 100 m. Then, the transition flight starts and the altitude decreases about 5 m because of the transition maneuver. After the transition regime, the horizontal flight starts and performed around 90 m altitude. Before the back-transition, gliding flight is performed around 82 – 72 m altitude and then transition controller is activated around 72 m altitude. The tilt angle is set to 90° and the flight speed of the UAV is decreased at almost constant altitude with pitch-up motion. Finally, when the flight speed decreases below 3 m/s, hover control system is activated by the algorithm and the UAV completes the back-transition maneuver.

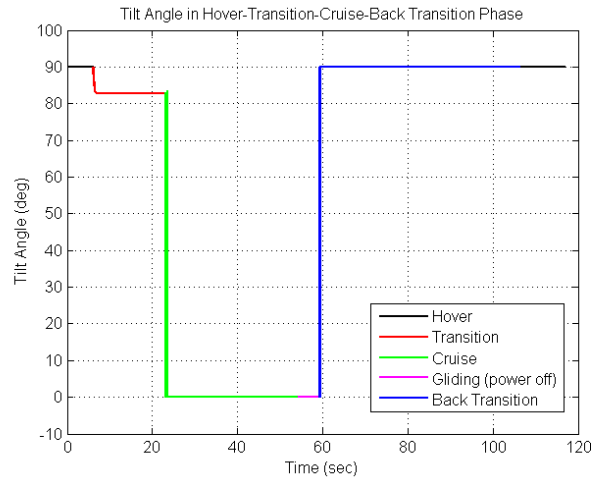


Figure 3.26 : Tilt angle time history during the simulation.

Tilt angle of the front propellers is shown in Figure 3.26. In hover flight, tilt-rotors are positioned at 90° . In transition, they are positioned at 82° and the UAV starts to

accelerate. Then, the tilt angle is set to 0° and the UAV performs the cruise flight. After the gliding flight, tilt angle is set to 90° by the back-transition algorithm.

Pitch angle of the UAV during the flight is shown in Figure 3.25. The pitch angle is used for accelerating and decelerating in hover and back-transition flight regimes. In hover flight, the flight speed of the UAV is increased by pitch-down motion (black range). At the end of the flight, in back-transition and hover flights, the speed of the UAV is decreased by giving a pitch-up command as shown in Figure 3.25 between 70 – 90 seconds.

Using the described control system methodology, we have demonstrated the hover to transition maneuver with Turac. Figure 3.27 shows the step by step forward flight transition of Turac.



Figure 3.27 : Experimental transition maneuver demonstration.

4. SYSTEM IDENTIFICATION AND CONTROL SYSTEM DESIGN FOR RANGER-EX UAV

Micro aerial vehicles provide an effective and cost-efficient solution for low altitude surveillance and tracking missions in both civilian and military settings. However, one of the key challenges of MAV platforms is the lack of methodical control system design processes which can provide high performance and robust autonomous flight in face of modeling uncertainties and environmental conditions such as turbulence and winds. In this paper, we propose a model-based flight control system (FCS) design approach for a MAV using integrated flight testing and hardware-in-the-loop simulation. Specifically, the MAV is designed for a surveillance mission in which it is required to track a moving ground target such as a ship or a boat from a specified altitude by using a downward facing camera fully autonomously. The concept of the mission is illustrated in Figure 4.1.

The MAV used is a commercial off-the-shelf (COTS) Ranger EX radio controlled model (shown in Figure 4.2) fitted with an in-house customized Pixhawk autopilot and an indigenous Linux based single board payload/flight management computer. This solution is envisioned to be a cheap but effective alternative to manned aircraft or tactical unmanned aerial vehicles. For this mission, it is necessary to design a tracking and attitude control system which should not only provide precise position and attitude control and but also be robust against environmental disturbances. However, there are two significant challenges associated with this goal. First is the lack of mathematical model which is necessary for the design of such high precision control system. Second is the limited capability of standard Pixhawk loop structures for embedding and achieving mission tracking requirements. We handle these challenges by introducing and adapting system-identification and control system design methodologies from the manned aircraft domain towards the MAV domain. These design methodologies are embedded into a model based FCS design approach as illustrated in Figure 4.3.

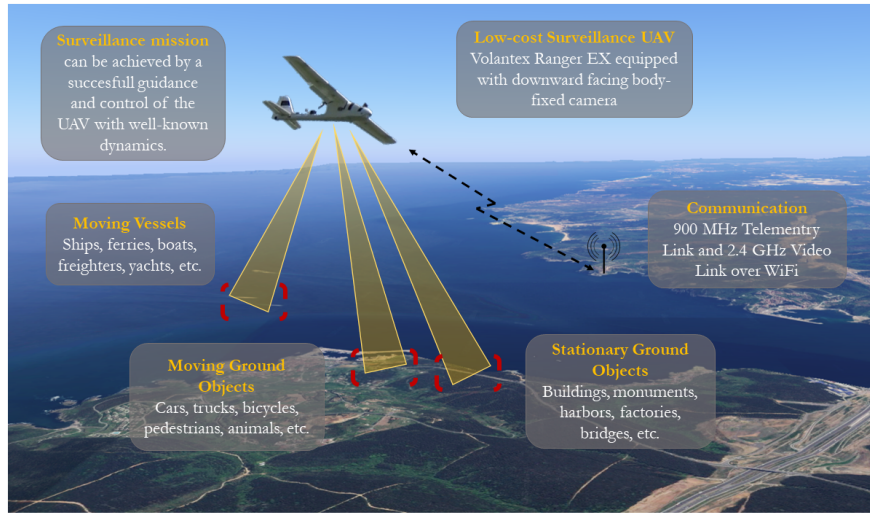


Figure 4.1 : Surveillance mission concept.

Specifically, we utilize a design process in which we perform open-loop system identification flight testing where the longitudinal and lateral mathematical models are identified by Comprehensive Identification from Frequency Response (CIFER®) [3]. These models are later used to design control system using Control Designer's Unified Interface (CONDUIT®) [2], in which tracking, disturbance rejection and robustness requirements are translated into loop objectives.

Operational concepts, such as transition [75], fast forward and agile maneuvering flights [80] brings distinct challenges associated with each flight regime with significant variations in the underlying aerodynamics (and thus the mathematical models) of the flight vehicle. As such, from flight control design perspective, flying in turbulence, gusts and winds requires a certain level of disturbance rejection capability to complete the mission. For example, in high altitude flights, icing effect is an uncertainty source which changes the aerodynamics characteristics of the wing thus resulting in degradation of the flight control performance as a result of unmodeled aerodynamic effects acting as disturbances. Thus, an ideal flight control system design would indeed need to handle the effects of dynamical parameter variations, uncertainties and external disturbances to provide adequate system performance for the defined mission. However, one of the main issues in designing a model-based flight control system is obtaining the aerodynamic control and stability coefficients of the MAV platform. There are several ways to obtain these coefficients such as empirical analysis tools, aerodynamic analysis tools, computational fluid dynamics analysis tools, wind tunnel tests and system identification testing.

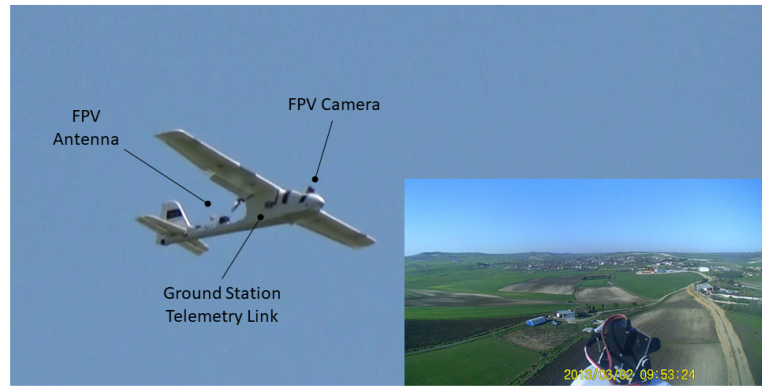


Figure 4.2 : Ranger EX MAV platform.

In the empirical analysis tools, physical properties of the aircraft and flight conditions are used to obtain aerodynamic coefficients. For example, Digital DATCOM software is a widely used analysis tool which is based on the USAF Stability and Control Data Compendium (DATCOM). The Digital DATCOM calculates static stability, high-lift device effects and dynamic derivatives by using semi-empirical data. However, DATCOM is tailored more towards aerial vehicles flying in higher Reynolds numbers (starting on the order of a few millions) and the flow regime for MAV is marked with low Reynolds number (on the order of hundred thousands). In such regimes, DATCOM is known to produce erroneous stability and control derivatives [81]. In addition, aerodynamic analysis tools such as XFLR5, which is based on lifting line theory, fail to correctly capture viscous effects again providing only approximate values on stability and control derivatives [82]. In addition, for all these methods and tools, it is important to define the required geometric data such as wing profile, chord, span and incidence angles accurately. For an off-the-shelf MAV platform, it is easy to determine some of the geometric properties such as wing span and chord. However, it is hard to obtain the wing and tail profile, and incidence angles precisely. The aforementioned design features are crucial for aerodynamic analysis of the aircraft.

In CFD analysis, it is also important to have detailed geometric data which is hard to know for an off-the-shelf MAV. In addition, computational cost and requirement of actual data for absolute value validation makes CFD analysis a last resort alternative for MAV modelling. As such, in the wind tunnel analysis, it is possible to obtain accurate aerodynamic characteristics of the aircraft by using full-scale or sub-scale models of the airframe according to test section dimensions. However, it may not be possible to use a wind tunnel because of the availability of such a tunnel or the extensive cost

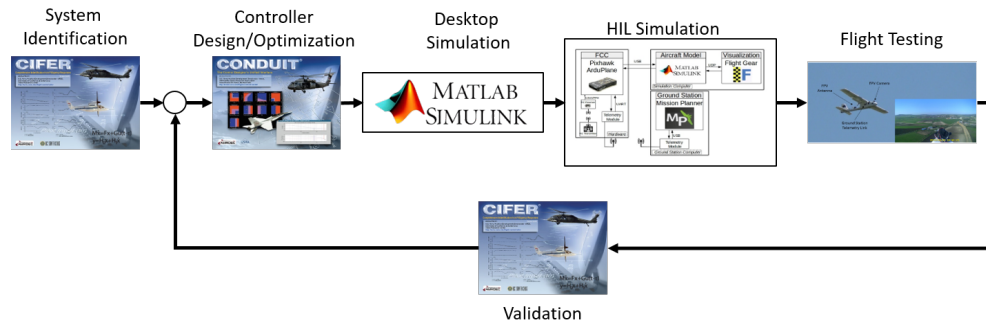


Figure 4.3 : Desktop-to-flight design workflow (adapted from [2]).

of such testing. In addition, measurement of dynamic stability derivatives requires expensive testing equipment which provide only approximate values.

In comparison, system identification provides an efficient and cost-effective approach to obtain the aerodynamic stability and control derivatives of a MAV. In this approach, input and output signals of the open-loop or closed-loop system are logged. Then, the system dynamics are determined by using online or offline identification process. One of the key features of this approach is the fact that it is not necessary to know all of the geometric and aerodynamic data such as wing profile and incidence angle to obtain the control and stability coefficients. In that sense, system identification can provides a powerful capability especially for modeling of the commercially off-the-shelf aerial platforms.

Essentially, by using flight testing and system identification, flight control system design challenges can be handled by using a desktop-to-flight workflow which consists of system identification, controller design, hardware-in-the-loop simulations and controller verification steps [2]. The system identification process is a fundamental step in which an adequate system model is identified to represent the dynamics of the aerial platform. A reliable mathematical model provides an insight about the dynamical characteristics of the system and decreases the uncertainties which is a critical factor in the controller design step. In addition, it is important to define the mission-specific flying qualities which provide design requirements for to the predefined mission. Although there are several sources about the design requirements for the manned aerial vehicles, there is limited information about the unmanned aerial systems. At this point, design requirements for the manned aerial platforms are scaled-down for the unmanned ones by using scaling techniques such as Froude scaling [36]. After developing the control and guidance algorithm, it is critical to test the performance of the closed-loop

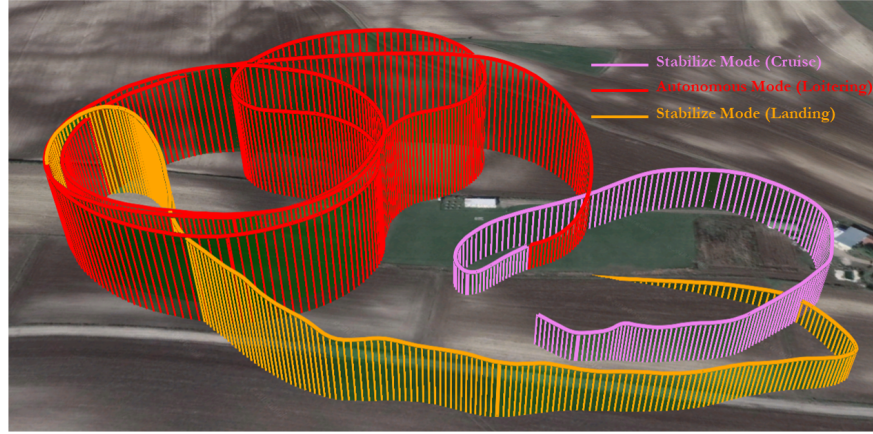


Figure 4.4 : Sample autonomous flight trajectory.

system with minimum crash risk. Hence, a simulation environment is crucial to test the proposed algorithms. These types of systems are called as X-in-the-loop test environments where "X" refers the system under test and it can be software, hardware or processor. The last step of the desktop-to-flight control system design workflow is performing verification tests of the closed-loop system. In these flight tests, variable frequency sinusoidal input signals are applied into the developed system. Closed-loop, broken-loop and disturbance rejection characteristics are obtained from the frequency response analysis. Then, flight test results are compared with the theoretical ones. Required revisions are performed on the system identification and control system design steps, if necessary.

In this chapter, frequency-domain system identification is performed to obtain lateral and longitudinal mathematical models of a MAV platform. The prediction accuracy of the models are evaluated through time-domain verification process. Baseline aerodynamic model is updated by using the identified parameters. The obtained linear models are used in a model-based flight control system (FCS) design approach in which longitudinal and lateral attitude-command/attitude-hold (ACAH) control systems are designed. HIL tests are performed before the actual flight tests and embedded control algorithms are verified. Then, both the designed control system and also the legacy flight control system of the autopilot are flight tested. The results demonstrate that the proposed methodology and the resulting control system provides higher performance and robust disturbance rejection in face of real-world conditions such as turbulence and winds. In that respect, this work provides a unique and successful application of the manned flight control system methodology

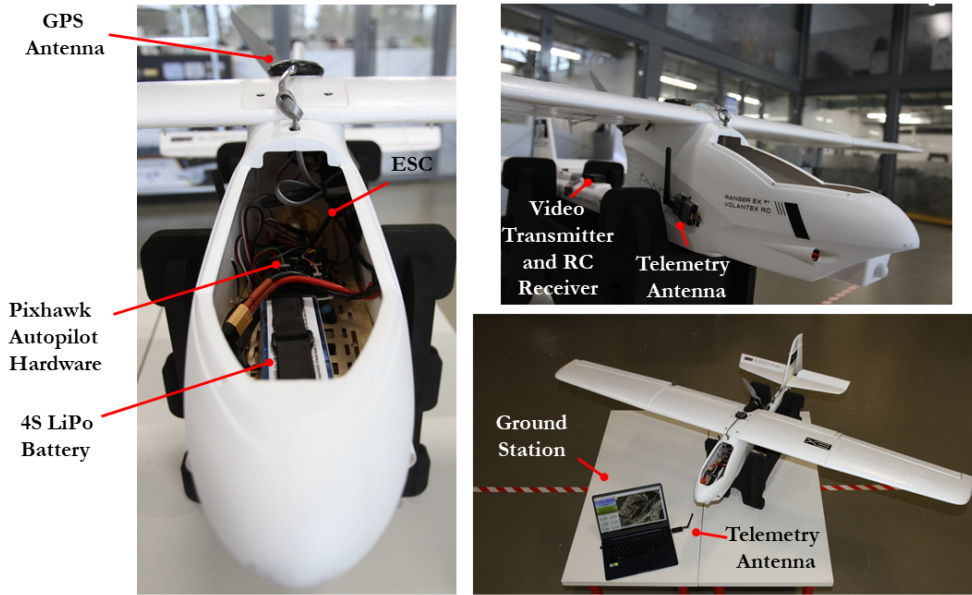


Figure 4.5 : Ranger EX MAV flight platform and the autopilot system.

to this particular flight platform. This is illustrated in Figure 4.4 in which an actual autonomous surveillance flight is shown.

The remaining of the chapter is organized as follows; problem and system definitions are given in Section 4.1. In Section 4.2, nonlinear mathematical model structure is given and sub-models are explained. In Section 4.3, longitudinal and lateral system identification studies are explained and results are given. In Section 4.4, the identified mathematical models are verified in the time-domain by using doublet-inputs and results are given. In Section 4.5, multi-objective parametric optimization based flight control system design procedure is explained and uncertainty analysis is performed to evaluate the parameter uncertainty effects on the closed-loop system stability and performance. In Section 4.6, HIL simulation structure is given and software specifications and interfaces are described. In Section 4.7, attitude-hold and doublet reference tracking flight test results are evaluated and performance comparison is performed between the proposed and the legacy controller.

4.1 Experimental Platform

The MAV platform that we have used for the surveillance mission is a commercial off-the-shelf (COTS) Ranger EX radio controlled model fitted with an in-house customized Pixhawk autopilot and an indigenous Linux based single board payload/ flight management computer. This solution is envisioned to be a cheap but effective

Table 4.1 : Ranger EX MAV specifications.

Property	
Chord	0.24 m
Span	2 m
Takeoff Weight	2.4 kg
ESC	EMAX 80A
Motor	1000KV BLDC
Propeller	APC 10x7E
Battery	4S LiPo
Endurance	≈ 12 min
Cruise Speed	≈ 13 m/s

alternative to manned aircraft and tactical unmanned aerial vehicles. Mechanical properties and performance specifications of the Ranger EX MAV are given in Table 4.1 and the underlying flight test platform from the flight test preparation phase in hangar is shown in Figure 4.5.

For this mission, in which it is required to track a moving target fully autonomously from a specified altitude by using a downward facing camera, it is necessary to design an ACAH control system which should not only provide a precise attitude control but also robustness against environmental disturbances and parametric uncertainties. However, there are two significant challenges associated with these goals. The first challenge is the absence of the mathematical model of the platform which is necessary for developing a high-performance control system. The second one is the limited capability of the standard Pixhawk control loop structures for achieving the mission requirements.

These challenges are handled by introducing and adapting the system identification and control system design methodologies from the manned aircraft domain towards the MAV domain. These design methodologies are embedded into a model-based FCS design approach as illustrated in Figure 4.3 [2]. In the next section we provide the mathematical modeling approach for our flight platform.

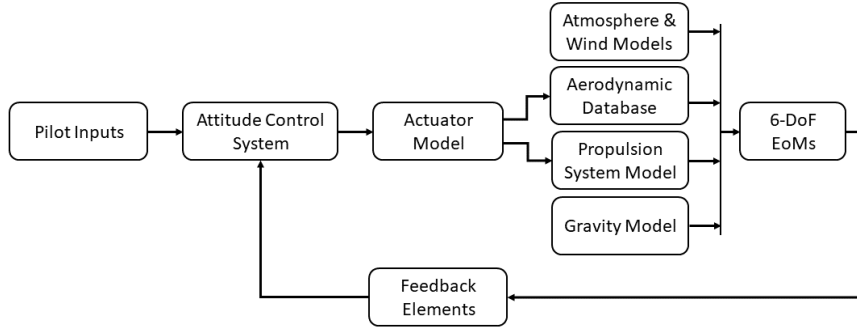


Figure 4.6 : Nonlinear model structure.

4.2 Mathematical Modeling

A high-fidelity mathematical model of the dynamical system provides accurate preliminary insight about the performance of the closed-loop system. General structure of the nonlinear mathematical model of the simulation environment is given in Figure 4.6. It is shown that there are 9 basic sub-models that constructs the nonlinear model.

The motion of a rigid body in the inertial frame is represented by using Newton's 2nd law. It states that the total external forces acting on the body is equal to the time rate of change of the linear momentum. Similarly, the total external moments are equal to the time rate of change of the moment of momentum, in other words, angular momentum [83].

Actually, electromechanical servo actuators have electrical and mechanical subsystems which defines the dynamical characteristics. In the simulation environment, for simplification, the electromechanical actuator is modeled as a second-order system with rate and deflection constraints. In the propulsion system of the MAV, APC 10x7E propeller is used and the thrust map is obtained by using the manufacturer database [84]. If a wind tunnel is available, the thrust map of the propeller can be obtained from the wind tunnel tests for a range of airspeed. Also, blade element theory can be used which requires aerodynamical parameters of the propeller [85].

Aerodynamic forces and moments are generated by using the aerodynamic coefficients C_D, C_L, C_Y, C_l, C_m and C_n . Actually, these coefficients are nonlinear functions of several parameters such as Mach number, angle of attack, angle of sideslip, body rates and control surface deflections. However, for simplification, linear approximations of the

Table 4.2 : Dynamical characteristics of the Ranger EX MAV baseline model.

Property	Short-period Mode	Roll Mode	Dutch-Roll Mode
ζ	0.76	-	0.203
ω_n (rad/s)	10.9	22.4	3.09

aerodynamic force and moment coefficients, which consist of stability and control derivatives, are used in the simulation environment [86]. The baseline values of the stability and control derivatives are obtained from XFLR5 software which uses the lifting line theory. To improve the nonlinear model fidelity, the aerodynamic database will be updated by using the identified model parameters.

The required atmospheric data in the simulation environment is determined from standard atmosphere model, which provides air density, speed of sound, temperature, pressure and viscosity as a function of altitude [87]. External disturbance effects such as gust and turbulence are also integrated into the simulation environment. The gust has "1-cosine" shape and implemented from [88]. For turbulence effects, Dryden form of the spectra for turbulence speed components is used [88]. Because of the low altitude and restricted operating area of the proposed MAV, constant gravity acceleration approximation is used and the gravitational acceleration is applied into the NED frame on positive Z axis. If it is required to use a more complicated gravity model, readers can refer to Earth gravitational model 1996 (EGM-96) [89] or World Geodetic System 1984 (WGS-84) [90] which provide the gravity vector for a given coordinates on the Earth. Sensors are used as feedback elements to obtain the required measurements for the control systems and state estimators such as Kalman filters. Primary onboard measurement system on a MAV platform consists of accelerometer, rate gyro, barometric altitude sensor, pitot tube, compass and global positioning system (GPS). In this study, it is assumed that the sensor information is processed in a fusion filter and filtered data is provided into the control algorithm via feedback path.

After generating the mathematical model of these sub-systems and combining them in a simulation environment, trim and linearization steps are performed at the level flight conditions. As a result, dynamical characteristics of the MAV baseline model are given in Table 4.2. In the next section, we provide insight on the system identification of the longitudinal and the lateral dynamics.

4.3 Identification of Longitudinal and Lateral Dynamics

Unlike other methods that are used to obtain aerodynamic parameters of the aircraft, such as CFD analysis and wind tunnel tests, the system identification method is more suitable for modeling of the off-the-shelf MAV platforms. In this approach, it is not necessary to know all of the geometric data to obtain the control and stability coefficients. Frequency sweep input signals for the control surfaces are designed for each mode of the aircraft. The control surface inputs and aircraft responses are recorded on a data logger. By using the collected input/output data, linear longitudinal and lateral models are identified. Then, the obtained mathematical models are validated in the time-domain by using the doublet inputs. After the validation of the identified models, baseline aerodynamic database of the MAV is updated according to the obtained stability and control derivatives. In this study, frequency domain system identification method is applied by using the Comprehensive Identification from Frequency Response (CIFER®) software [3].

4.3.1 Identification of servo actuator dynamics

Aerodynamic control surfaces of the MAV are directly controlled by the servo actuators. Hence, it is important to evaluate the dynamics of the servo actuator before the system identification process. For a successful airframe identification, the bandwidth of the servo actuator should cover the fastest mode of the airframe. So, a frequency-domain system identification test is designed and applied for the HS-85MG servo actuator to evaluate the suitability of the servo dynamics for the airframe system identification process. The frequency sweep test signal is designed between $1 - 70 \text{ rad/s}$ frequency range to cover the servo dynamics. Total sweep duration is 160 sec and data is collected at 200 Hz sampling rate. By using the CIFER, the second-order servo dynamics is identified as shown in equation 4.1 which represents the transfer function from reference position input to actual position output. Bode plots of the actual system and identified model are given in Figure 4.7. As seen in the figure, coherence value is above 0.6 for the frequency range $1 - 42 \text{ rad/s}$. Cost of the identified model is 2.831 which implies that an accurate model is obtained for this frequency range. Also, it is shown that the bandwidth of the servo actuator is about

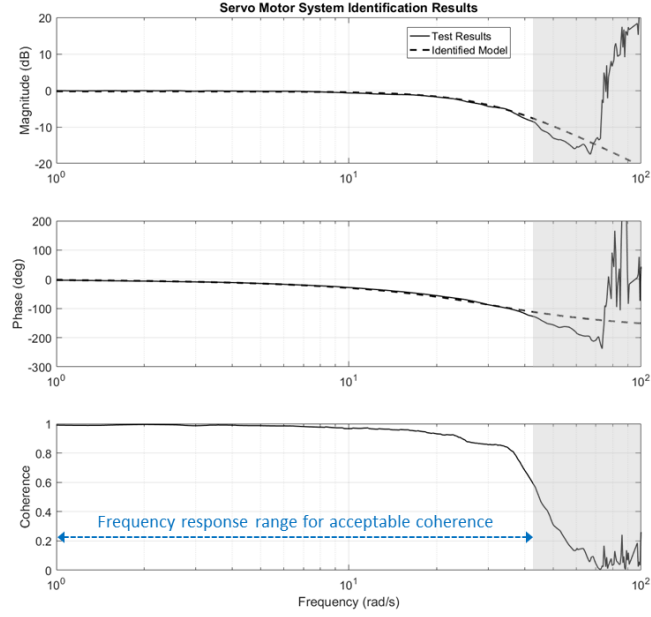


Figure 4.7 : HS-85MG servo actuator system identification results.

27 rad/s which covers the natural frequency of the fastest mode ($\omega_{roll} = 22.4 \text{ rad/s}$) in the baseline model. So, it is determined that the proposed servo actuator is suitable for the system identification process of the MAV platform.

$$\frac{\mu_{act}(s)}{\mu_{cmd}(s)} = \frac{K}{[\zeta_n, \omega_n]} = \frac{947.615}{[0.7967, 31.203]} \quad (4.1)$$

4.3.2 Design of flight experiments

The MAV platform is remotely controlled by using RC transmitter/receiver system within about 1000 m range. So, it is important to design a flight experiment in this range to avoid possible signal disconnection which may cause a crash. Also, pilot's visual contact is a critical factor for tracking of the orientation of the MAV. In clear weather conditions, the visual range is about 500-700 m for an experienced pilot.

The flight tests can be divided into two groups to identify the fast and slow dynamics of the MAV. The fast dynamics are observed in short-period, roll and dutch-roll modes which require relatively short test duration about 10-15 seconds. The slow dynamics are observed in phugoid and spiral modes and these modes require relatively long frequency sweep test duration about 60-70 seconds. In this study, it is proposed to identify the fast dynamics which is important for the control system design.

Table 4.3 : System identification test input parameters.

Test Parameter	Value
ω_{min}	1.2 rad/s
ω_{max}	30 rad/s
T_{sweep}	10.47 sec
$T_{win_{min}}$	6.28 sec
$T_{win_{max}}$	10.47 sec
ω_f	25 Hz
ω_s	150 Hz
$T_{rec_{total}}$	52 sec

The sinusoidal frequency sweep input signal should cover a broad range of frequency to excite the interested dynamical modes. If the mode is not excited, its characteristics could not be identified. The fastest mode in the baseline model is roll mode and it is located at about $22.4 rad/s$. So, maximum frequency of the sinusoidal signal is set to $\omega_{max} = 30 rad/s$. Because of the receiver/transmitter and the pilot's visual range constraints, minimum frequency of the sinusoidal signal is determined as $\omega_{min} = 1.2 rad/s$ which results in a 10.47 seconds of the frequency sweep flight test.

The desired maximum frequency of model applicability (ω_{max}) is an important factor to determine the filter cutoff frequency and data sampling rate. Theoretically, sampling rate can be set as $2 \omega_{max}$ which puts the Nyquist frequency ($\omega_{nyq} = 0.5 \omega_s$) at the maximum frequency of interest. However, due to the atmospheric disturbance and sensor noise, low sample rate may result in inaccurate identification of the system dynamics. As a rule of thumb, the filter cutoff frequency (ω_f) and sampling rate (ω_s) are determined as shown in equations 4.2 and 4.3. By using these requirements and a practical guideline in [3], the flight test input signal parameters are given in Table 4.3.

$$\omega_f \geq 5 \omega_{max} \quad (4.2)$$

$$\omega_s \geq 5 \omega_f \quad (4.3)$$

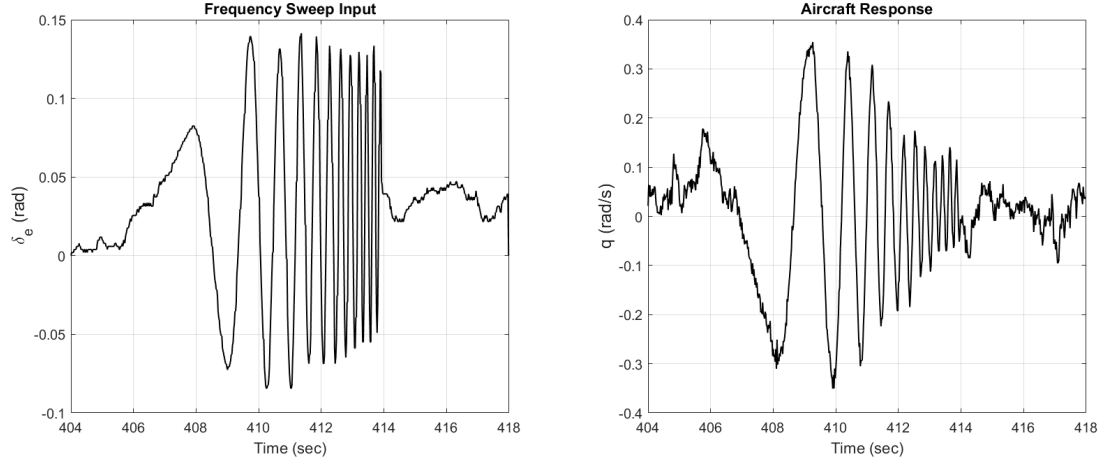


Figure 4.8 : Elevator test input and aircraft response.

4.3.3 Identification of longitudinal dynamics

Linearized longitudinal dynamics of the MAV can be represented by using complex phugoid-mode and short-period mode poles. The phugoid mode poles of the MAV have low-frequency and low-damping dynamical characteristics. So, they can be neglected in the control system design process. Unlike the phugoid mode poles, the short-period mode poles have higher frequency and damping ratio. The short-period mode response of the MAV is observed in a few seconds after the control input is applied to the control surface. Because of its fast dynamical characteristics, the short-period mode approximation model is used in the pitch attitude control system design. So, in this study, the short-period mode of the MAV will be identified. A sample short-period mode system identification test input and airframe response in pitch axis are shown in Figure 4.8.

The linearized equations of motion for the longitudinal dynamics are given in equation 4.4.

$$\begin{aligned}
 \dot{q} &= M_q q + M_w w + M_{\delta_e} \delta_e \\
 \dot{\theta} &= q \\
 \dot{w} &= (U_0 + Z_q) q + Z_w w + Z_{\delta_e} \delta_e
 \end{aligned} \tag{4.4}$$

The measurements are defined as shown in equation 4.5.

$$\begin{aligned}
q &= q \\
a_z &= \dot{w} - U_0 q + (g \sin \Theta_0) \theta \\
\dot{w} &= a_z + U_0 q - (g \sin \Theta_0) \theta
\end{aligned} \tag{4.5}$$

where, 0 indicates the trim flight conditions. \dot{w} is generated by using data reconstruction to improve the identification quality [3].

The short-period longitudinal mathematical model and measurements are represented in the state-space form as shown in equations 4.6, 4.7 and 4.8. Here, subscript "ln" indicates the longitudinal dynamics.

$$\mathbf{M}_{ln} \dot{\mathbf{x}}_{ln} = \mathbf{A}_{ln} \mathbf{x}_{ln} + \mathbf{B}_{ln} \mathbf{u}_{ln} \tag{4.6}$$

$$\mathbf{y}_{ln} = \mathbf{H}_{0_{ln}} \mathbf{x}_{ln} + \mathbf{H}_{1_{ln}} \dot{\mathbf{x}}_{ln} \tag{4.7}$$

$$\begin{bmatrix} 1 & 0 & 0 \\ 0 & 1 & 0 \\ 0 & 0 & 1 \end{bmatrix} \begin{bmatrix} \dot{q} \\ \dot{\theta} \\ \dot{w} \end{bmatrix} = \begin{bmatrix} M_q & 0 & M_w \\ 1 & 0 & 0 \\ U_0 + Z_q & 0 & Z_w \end{bmatrix} \begin{bmatrix} q \\ \theta \\ w \end{bmatrix} + \begin{bmatrix} M_{\delta_e} \\ 0 \\ Z_{\delta_e} \end{bmatrix} [\delta_e](t - \tau_{ln}) \tag{4.8}$$

where, q, θ, w are body pitch rate, pitch Euler angle and velocity vector on z_b axis.

Longitudinal axis frequency response of the actual system and identified model are compared in Figure 4.9. As seen from the figure, an adequate agreement is achieved between the actual MAV and identified model responses.

The identified short-period model parameters are given in Table 4.4. Insensitivities of these parameters are below the 10%. However, M_q and M_w stability derivatives are above the defined Cramer-Rao boundary ($CR \leq 20\%$). So, in the pitch attitude control system design process, the importance of the uncertainty analysis increases especially for these derivatives. The cost values for the identified model are given in Table 4.5. It is shown that each of the cost values are satisfies the ($J \leq 100$) condition which means that an appropriate longitudinal mathematical model is fitted on the frequency responses of the MAV.

4.3.4 Identification of lateral dynamics

Linearized lateral dynamics of the MAV is represented by three separate modes, namely, spiral mode, dutch-roll mode and roll mode. The spiral dynamics has the

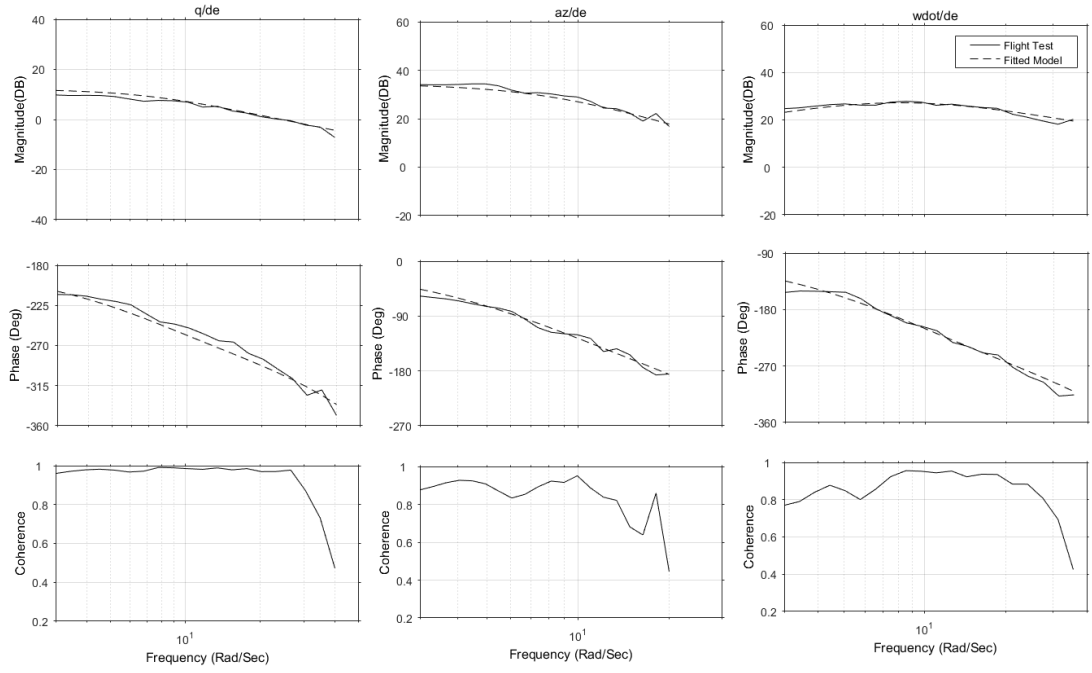


Figure 4.9 : Frequency responses of the MAV and identified longitudinal model for elevator input.

Table 4.4 : Identified longitudinal stability and control derivatives.

Parameter	Value	CR Bound	CR Bound (%)	Insensitivity (%)
M_q	-4.213	1.123	26.66	2.642
M_w	-1.323	0.7305	55.21	7.662
Z_w	-11.04	0.5701	5.163	2.327
M_{δ_e}	-24.17	1.424	5.892	1.140
δ_e	0.03154	2.529E-9	8.018	2.917

lowest frequency among these modes and it is not so critical for the control system design. Hence, the study is focused on the identification of the roll mode and dutch-roll mode dynamics. To obtain the dynamical characteristics of the roll and dutch-roll mode, variable frequency sinusoidal test input is applied into the aileron and rudder channels separately and sensor measurements are logged as shown in Figure 4.10.

The linearized lateral equations of motion are given in equation 4.9.

$$\begin{aligned}
 \dot{v} &= -U_0 r + W_0 p + (g \cos \Theta_0) \phi + Y_v v + Y_p p + Y_r r + Y_{\delta_a} \delta_a + Y_{\delta_r} \delta_r \\
 \dot{p} &= L_v v + L_p p + L_r r + L_{\delta_a} \delta_a + L_{\delta_r} \delta_r \\
 \dot{r} &= N_v v + N_p p + N_r r + N_{\delta_a} \delta_a + N_{\delta_r} \delta_r \\
 \dot{\phi} &= p + r \tan \Theta_0
 \end{aligned} \tag{4.9}$$

Table 4.5 : Cost values for the identified longitudinal model.

Response	Cost (J)
q/δ_e	43.23
a_z/δ_e	43.35
\dot{w}/δ_e	30.56
J_{avg}	39.05

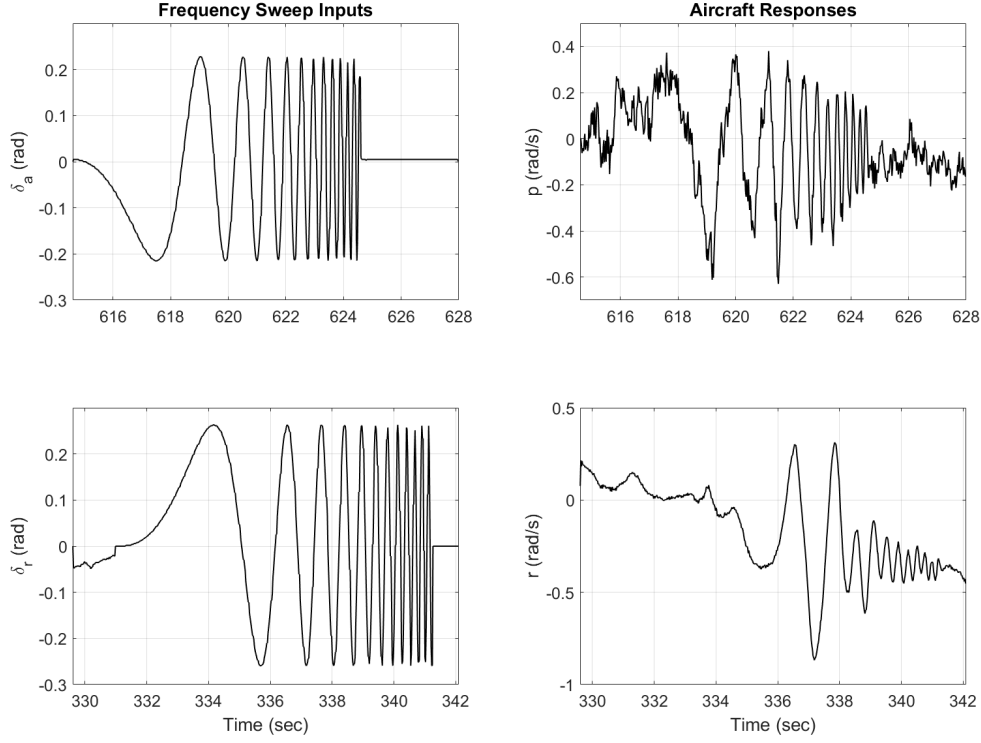


Figure 4.10 : Aileron and rudder test inputs and aircraft responses.

where, v is linear velocity on y_b axis, p is roll rate, r is yaw rate, ϕ is roll angle. Primed derivatives ($'$) are defined in [91]. Measurement equations for the lateral motion are given in equation 4.10.

$$\begin{aligned} p &= p \\ r &= r \end{aligned} \tag{4.10}$$

$$a_y = \dot{v} + U_0 r - W_0 p - (g \cos \Theta_0) \phi$$

where, ' 0 ' indicates the trim conditions and a_y is acceleration on y_b axis.

By using the linearized lateral equations of motion and the measurements, state-space model structure of the lateral dynamics is generated as given in equations 4.11, 4.12 and 4.13. Here, subscript " lt " indicates the lateral dynamics.

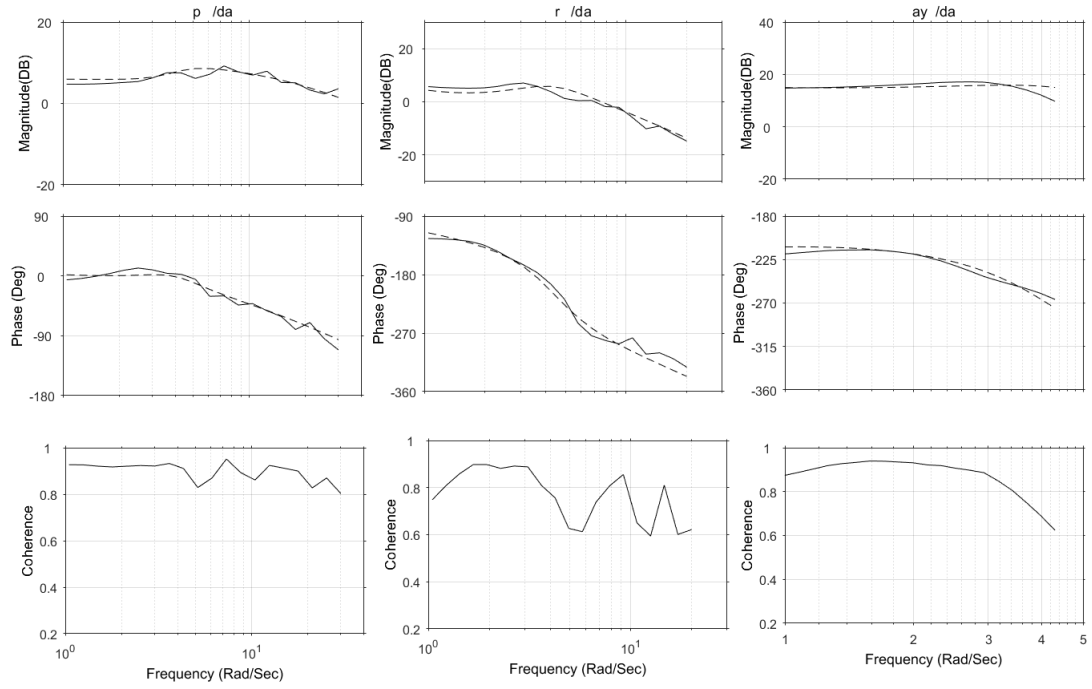


Figure 4.11 : Frequency responses of the MAV and identified lateral model for aileron input.

$$\mathbf{M}_{lt}\dot{\mathbf{x}}_{lt} = \mathbf{A}_{lt}\mathbf{x}_{lt} + \mathbf{B}_{lt}\mathbf{u}_{lt} \quad (4.11)$$

$$\mathbf{y}_{lt} = \mathbf{H}_{0lt}\mathbf{x}_{lt} + \mathbf{H}_{1lt}\dot{\mathbf{x}}_{lt} \quad (4.12)$$

$$\begin{bmatrix} 1 & 0 & 0 & 0 \\ 0 & 1 & -I_{xz}/I_{xx} & 0 \\ 0 & -I_{xz}/I_{zz} & 1 & 0 \\ 0 & 0 & 0 & 1 \end{bmatrix} \begin{bmatrix} \dot{v} \\ \dot{p} \\ \dot{r} \\ \dot{\phi} \end{bmatrix} = \begin{bmatrix} Y_v & Y_p + W_0 & Y_r - U_0 & g \cdot \cos(\Theta_0) \\ L_{v'} & L_{p'} & L_{r'} & 0 \\ N_{v'} & N_{p'} & N_{r'} & 0 \\ 0 & 1 & \tan(\Theta_0) & 0 \end{bmatrix} \begin{bmatrix} v \\ p \\ r \\ \phi \end{bmatrix} + \begin{bmatrix} Y_{\delta_a} & Y_{\delta_r} \\ L_{\delta_a'} & L_{\delta_r'} \\ N_{\delta_a'} & N_{\delta_r'} \\ 0 & 0 \end{bmatrix} \begin{bmatrix} \delta_a \\ \delta_r \end{bmatrix} (t - \boldsymbol{\tau}_{lt}) \quad (4.13)$$

where, $\boldsymbol{\tau}_{lt}$ is time-delay matrix.

Frequency response of the actual system and identified lateral model are compared in Figure 4.11 and Figure 4.12 for aileron and rudder inputs. As shown from the figures, an appropriate agreement is achieved between the actual system and the identified model responses.

The identified lateral aerodynamic parameters are given in Table 4.6. Most of the insensitivity values of these parameters are below 10% boundary. The parameters

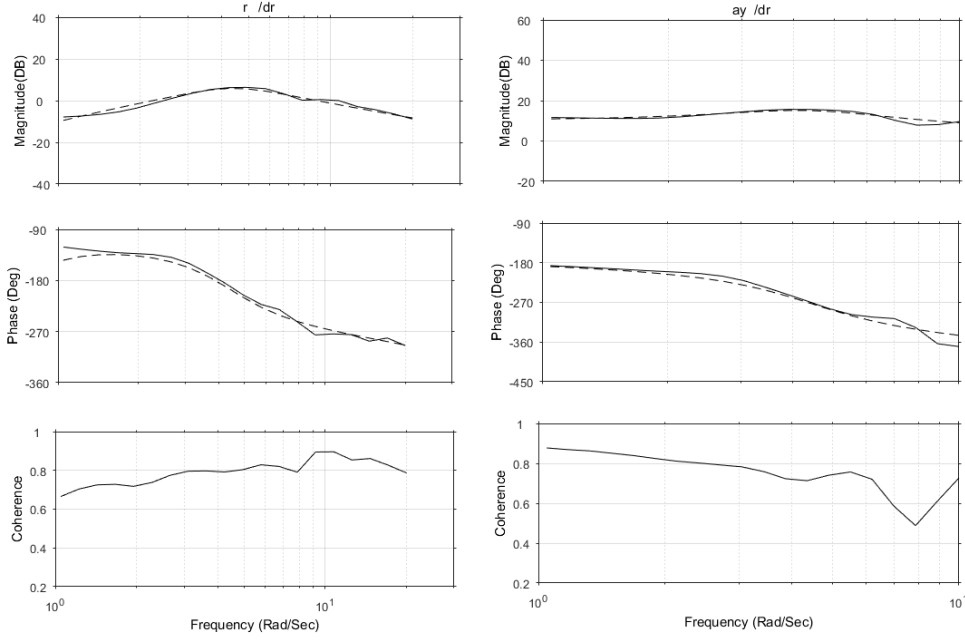


Figure 4.12 : Frequency responses of the MAV and identified lateral model for rudder input.

which have *insensitivity* $\geq 10\%$ are neglected in the optimization algorithm. Still, Cramer-Rao bounds of some of the off-axis stability and control derivatives such as L_r and L_{δ_r} are quite above of the 20% bound. So, a robustness analysis will be performed in the control system design step. The cost values, which indicate the matching quality of the frequency responses of the actual system and identified model, are given in Table 4.7. As seen from the table, individual cost values are sufficient, ($J \leq 100$) and average cost value is below 50, ($J_{ave} = 42.15$) which means that an adequate mathematical model of the MAV is identified. In the next section, we provide time domain verification of the identified dynamic models.

4.4 Time-Domain Verification

To evaluate the prediction accuracy and reliability of the identified models, 1-1 form doublet inputs are applied into the control surfaces of the actual system and mathematical models. Then, the model responses are compared with the flight test measurements.

A normalized criterion called as The Theil Inequality Coefficient (TIC), adopted by Jategaonkar et al. [56], is used to evaluate the model prediction accuracy. The TIC value is between 0 and 1 in the verification process. A value of $TIC = 1$ means that

Table 4.6 : Identified lateral stability and control derivatives.

Derivative	Value	CR Bound	CR Bound (%)	Insensitiviy (%)
Y_v	-0.8168	0.09201	11.26	1.358
Y_p	-1.645	0.6651	40.44	2.930
Y_r	1.224	0.3166	25.87	4.181
L_v	-1.626	0.2578	15.86	3.005
L_p	-13.51	1.723	12.76	1.295
L_r	5.058	1.243	24.57	4.508
N_v	0.858	0.0663	7.729	1.683
N_p	-1.596	0.3118	19.54	2.892
N_r	-2.778	0.2361	8.498	2.249
Y_{δ_a}	3.313	1.851	55.88	4.174
Y_{δ_r}	2.247	0.7329	32.61	7.555
L_{δ_a}	38.31	3.629	9.473	1.103
L_{δ_r}	-14.83	8.756	59.04	6.931
N_{δ_a}	-1.917	0.6731	35.10	6.130
N_{δ_r}	-19.440	1.193	6.135	1.290
δ_a	0.02167	4.571E-03	21.09	7.298
δ_r	0.03258	3.775E-03	11.59	5.121

Table 4.7 : Cost values for the identified lateral model.

Response	Cost (J)
p/δ_a	29.849
r/δ_a	48.103
a_y/δ_a	34.178
r/δ_r	24.439
a_y/δ_r	32.587
J_{avg}	33.831

model response is predicted perfectly. On the other hand, a value of $TIC = 0$ means that the obtained model has no prediction capability. Jategaonkar suggests a guideline as shown in equation 4.14 for an adequate prediction performance.

$$TIC \leq 0.25 - 0.30 \quad (4.14)$$

In the time-domain verification process, bias and reference shift corrections are also determined to account for several error sources such as disturbance, untrimmed flight conditions and measurement noise. The calculation of the shift parameter vector Θ reduces to a least-squares solution which minimizes the $J(\Theta)$ weighted least-squares error function. The RMS fit error (J_{rms}) provides insight about the time-domain

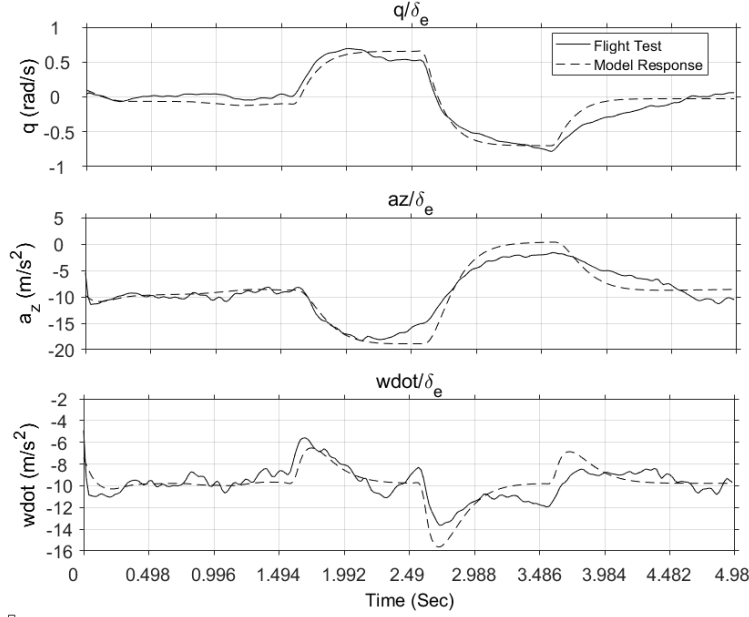


Figure 4.13 : Comparison of the MAV and longitudinal model responses for 1-1 elevator doublet input.

Table 4.8 : Time-domain verification results.

Input Channel	TIC	J_{rms}
Elevator	0.107	1.110
Aileron	0.209	0.189
Rudder	0.161	0.170

accuracy of the identified model. For the fixed-wing platforms, a guideline is given in equation 4.15 for the J_{rms} to obtain acceptable level of the model accuracy [3].

$$J_{rms} \leq 0.5 - 1.0 \quad (4.15)$$

For the longitudinal and lateral model verification, 1-1 doublet signal is applied to the elevator, aileron and rudder control surfaces in different test flights and responses are recorded. The comparison of the state-space model and flight test data are compared in Figure 4.13 and 4.14.

The TIC and J_{rms} cost values for the identified longitudinal and lateral models are given in Table 4.8. As seen from the table, TIC value meets the requirements, $TIC < 0.25$, for all axis. Although the J_{rms} exceeds 1.0 for the longitudinal model, it is close to the defined limit value.

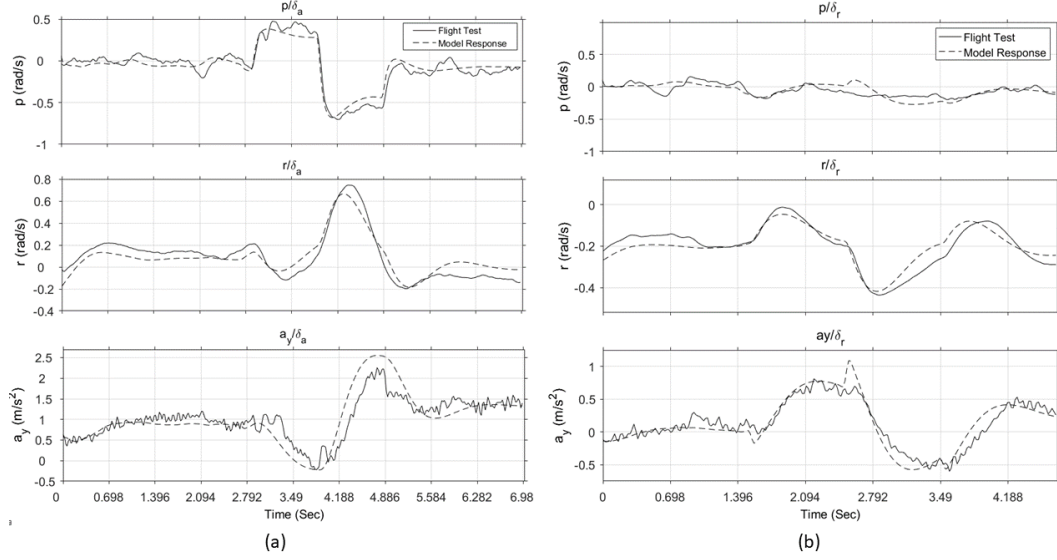


Figure 4.14 : Comparison of the MAV and lateral model responses for 1-1 (a) aileron and (b) rudder doublet inputs.

As a result of the frequency domain system identification and time-domain verification processes, dynamical characteristics of the Ranger-EX MAV in cruise flight conditions are given in Table 4.9. In the next section we provide insight on the autopilot system and demonstrate the flight control system design methodology.

Table 4.9 : Identified dynamical characteristics of the Ranger EX MAV.

Property	Short-period Mode	Roll Mode	Dutch-Roll Mode
ζ	0.941	-	0.443
ω_n (rad/s)	8.108	13.388	4.176

4.5 Autopilot System

To perform the surveillance mission, Pixhawk autopilot system is used for guidance and control of the MAV platform [92]. The Pixhawk autopilot system is a low-cost, off-the-shelf solution and has a wide application area in MAV community. It has 32-bit ARM Cortex M4 micro-controller and runs NuttX Real-Time Operating System (RTOS). There are 14 PWM outputs, and I2C, SPI, Serial, CAN interfaces on the hardware. Sensor set contains two accelerometers, two gyroscopes, one magnetometer, one barometer and one GPS module. The autopilot software on the Pixhawk is ArduPlane, which is the fixed-wing aerial vehicles implementation of the ArduPilot Project [93]. The ArduPlane is a popular open-source modular autopilot system with neat flight stack architecture which allows easy implementation of new control laws

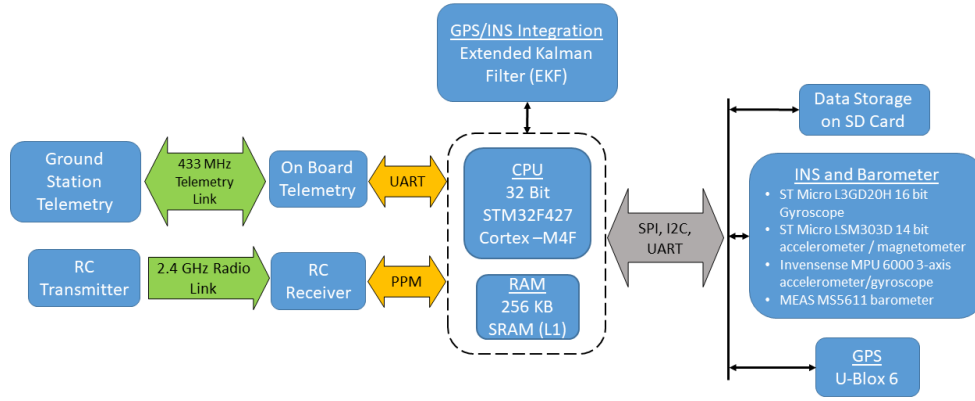


Figure 4.15 : General scheme of the avionics architecture.

or customization. General structure of the Pixhawk avionics architecture is given in Figure 4.15.

For general purpose applications such as waypoint tracking, it is a reliable and cost-effective system. However, it may not be suitable for missions which requires strict performance constraints defined by the proposed operation. Hence, for a surveillance mission by using a body-fixed camera, it is not possible to track the moving ground-target with the default controller structure and parameters of the Ardupilot. So, we propose a control system design for the roll and pitch axes which is suitable for target tracking applications with a downward-facing body-fixed camera. In the first step of the control system design, required flying qualities and the control system structure are defined. Then, the control system parameters are obtained in CONtrol Designer's Unified InTerface (CONDUIT®) software by using the design requirements. After that, the developed control system is implemented into the ArduPilot software.

4.5.1 Control system design requirements

In the proposed system, classical proportional+integral+derivative (PID) control structure is used in both longitudinal and lateral control systems which provides adequate flying performance for linear aerodynamic regimes. It is critical to select the design specifications to optimize the control parameters for obtaining the Level-1 handling qualities. However, there is limited information about the small-scale MAV control system design specifications. So, some of the full scale aircraft and rotorcraft specification boundaries need to be adjusted for the small-scale MAVs by using

dynamic scaling. The selected and modified specifications are used in the CONDUIT to drive the control system parameter optimization process.

4.5.1.1 First tier specifications

The first tier specifications composed of hard and soft constraints. Eigenvalue location, stability margins and Nichols margin are used as hard constraints in the first phase of the optimization routine. After obtaining the Level 1 conditions for the hard constraints, the optimization routine will not allow them to pass the Level 1 / Level 2 boundary to ensure the stability in the second and third phase.

In the second phase, the soft constraints are used to drive the optimization process which ensures handling-qualities and performance specifications. Eigenvalue damping specification is used as handling-quality requirement. For the performance specifications, disturbance rejection peak (DRP), disturbance rejection bandwidth (DRB), closed-loop bandwidth and broken-loop minimum crossover frequency specifications are used to obtain steadiness of the on-board downward-facing camera in the turbulence and to ensure adequate bandwidth while obtaining the minimum crossover frequency.

In the third phase of the optimization routine, the summed objectives are used to reach Pareto-Optimum solution which ensures the maximum performance with minimum control effort. The crossover frequency and actuator root-mean-square (RMS) for disturbance input are used as the summed objective.

4.5.1.2 Second tier specifications

Second tier specifications are included as check-only specifications and they are not used to drive the optimization process. In this study, three-sigma tracking error specifications in time and frequency domains are used to check the transient response of the aircraft in the turbulence flight conditions.

Summary of the design specifications are given in Table 4.10. As shown in the table, all of the selected design requirements are originated from full scale aircraft and rotorcraft specifications. As mentioned in [36], DRP, damping ratio and stability margin specifications for full-scale aircrafts and rotorcrafts can be used for the small-scale

Table 4.10 : Design specifications for longitudinal and lateral attitude control systems.

Constraint	Spec. Name	Description	Axis	Source
First Tier Specifications				
Hard	EigLcG1	Eigenvalues in LHP (Stability)	All	Generic
	StbMgG1	Gain and phase margin for loop broken at elevator input (Stability)	All	MIL-DTL-9490E, SAE-AS94900
	NicMgG1	Nichols Margin for loop broken at elevator input (Stability)	All	GARTEUR
Soft	CrsMnG2	Minimum crossover frequency for loop broken at elevator input. (Needed for 2-DOF architectures)	All	Generic
	BnwPil4	Pitch attitude bandwidth and phase delay	Pitch	MIL-STD-1797B
	BnwRoD1	Roll attitude bandwidth and phase delay	Roll	WL-TR-94-3162
	EigDpG1	Eigenvalue damping ratio	All	Generic
	DstPkG1	Disturbance rejection peak (Loads, ride quality)	All	[94]
	DstBwG1	Disturbance rejection bandwidth (Hold characteristics)	All	[94]
Summed Objectives	CrsLnG1	Minimize crossover frequency for loop broken at elevator input (Actuator activity)	All	Generic
	RmsAcG1	Minimize elevator input RMS for disturbance input (Actuator activity)	All	Generic
Second Tier Specifications				
Check-Only Objectives	ErrTmG1	3-Sigma Tracking Error in Time Domain	All	Generic
	ErrFqG2	3-Sigma Tracking Error in Frequency Domain	All	Generic

UAVs. However, DRB specification should be updated by using Froude scaling analysis.

4.5.2 Determining the DRB and DRP values

There is limited data about the DRB values of the full scale platforms. Hence, DRB of the UH-60 Blackhawk rotorcraft is used for the Froude scaling application. Mechanical dimensions, scale factors and DRB values for full-scale UH-60 are given in Table 4.11 [36]. Scaled DRB value for the Ranger MAV is calculated by using the Froude Scaling as shown in Table 4.12.

Table 4.11 : Rotor diameter and disturbance rejection bandwidth of the UH-60.

	Rotor Diameter (m)	Roll Axis DRB (rad/s)	Pitch Axis DRB (rad/s)
UH-60	16.46	0.96	0.56

To obtain the steadiness of the downward-facing camera, DRP specification should be considered beside of the DRB. In [36], an analysis is performed about the DRP value for a surveillance-type mission of a MAV equipped with downward-facing and forward-facing cameras. According to the above mentioned reference, $DRP = 3.1dB$ is determined as an adequate value for the image quality of the downward-facing camera and, in this study, it is used in the optimization process.

Table 4.12 : Froude scaling for the Ranger EX MAV.

	Wing Span (m)	Scale Factor (N)	Froude Scaling (\sqrt{N})	Roll Axis DRB (rad/s)	Pitch Axis DRB (rad/s)
Ranger MAV	1.98	8.31	2.8827	2.77	1.6143

4.5.3 Control system structures

The pitch attitude control system structure is given in Figure 4.16. Here, the controller parameters are K_q and K_{θ_p} . In the outer-loop, $\frac{K_{\theta_i}}{K_{\theta_p}}$ is set to 0.2 to limit the peak overshoot percentage of the response.

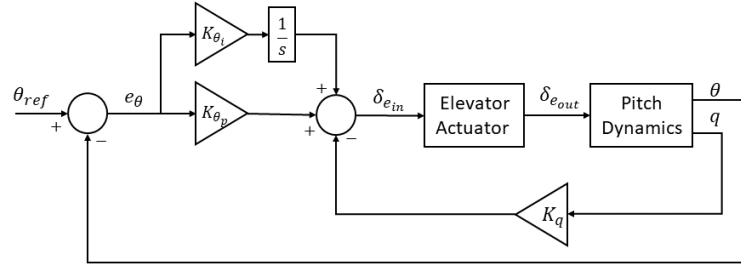


Figure 4.16 : Proposed pitch attitude control structure.

The roll attitude control system structure, which includes a dutch-roll damper, is given in Figure 4.17. The controller parameters are K_{ϕ_p} , K_{ϕ_i} , K_p and K_r . In the outer-loop, $\frac{K_{\theta_i}}{K_{\theta_p}}$ is equal to 0.2 to limit the peak overshoot percentage of the response, as mentioned in the longitudinal control system parameters. In the dutch-roll damper, a washout filter is used to suppress the low frequency feedback signal and it is shown in equation 4.16.

$$G_{wo}(s) = \frac{s}{s+2} \quad (4.16)$$

4.5.4 Optimization process of the controller parameters

After determining the control system structures and design specifications, the next step is to obtain the initial optimal values of the control system parameters. For this process, it is assumed that there is no uncertainty in the identified mathematical models of the MAV and design margin is equal to zero.

A family of the controller design parameters is obtained by using the design margin optimization (DMO) tool in CONDUIT. In the DMO analysis, Level-1 / Level-2

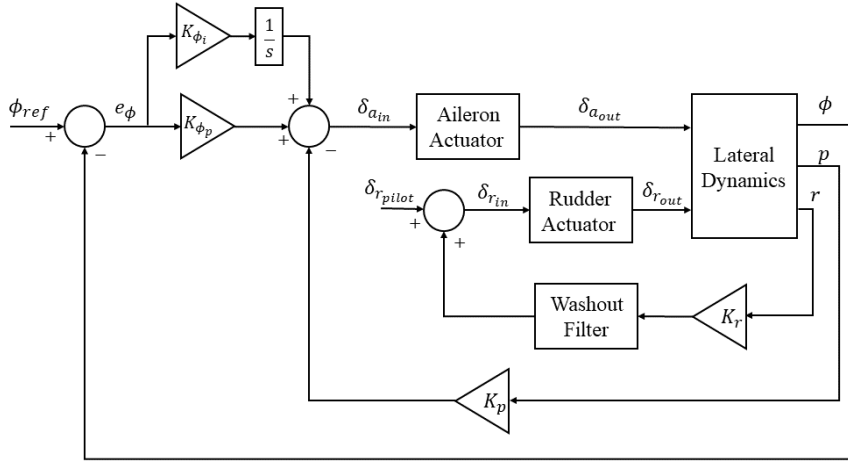


Figure 4.17 : Proposed roll attitude control structure.

bounds of the selected specifications are shifted with a user-defined percentage. DMO analysis results are used to evaluate the design margin (DM) effects on the system performance. In this study, design margin is set on the CrsMnG2 (Minimum crossover frequency) and DstBwG1 (Disturbance rejection bandwidth) specifications. In the pitch and roll attitude control design steps, the design margin evaluation is performed within the range of $[-20\%, 60\%]$ and $[-20\%, 42\%]$, respectively. Variations of the disturbance rejection bandwidth, disturbance rejection peak, crossover frequency, closed-loop damping ratio, phase margin and actuator root-mean-square (RMS) with the design margin percentage are given in Figure 4.18 and 4.19 for longitudinal and lateral attitude control systems. After evaluating these specifications, 40% DM for the longitudinal attitude control system and 22% DM for the lateral attitude control system are selected which provide adequate closed-loop dynamical characteristics. Optimized control system parameters for the pitch and roll attitude controllers are given in Table 4.13 for the selected design margins.

Table 4.13 : Longitudinal and lateral attitude control system parameters.

Parameter	Value
K_{θ_p}	1.4624720
K_{θ_i}	0.2924944
K_q	0.2840031
$K_{\theta_i}/K_{\theta_p}$	0.2
K_{ϕ_p}	2.3068940
K_{ϕ_i}	0.4613788
K_p	0.2297885
K_r	0.3803796
K_{ϕ_i}/K_{ϕ_p}	0.2

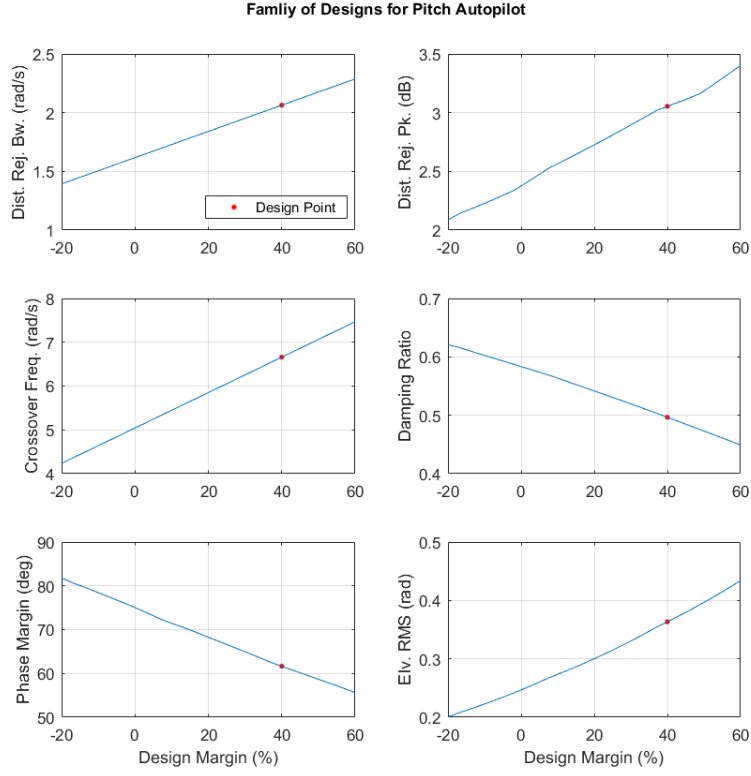


Figure 4.18 : Family of designs for pitch autopilot.

4.5.5 Uncertainty analysis

Robustness analysis is a key step to evaluate the sensitivity of the control system against the parametric uncertainties in the MAV dynamics. The robustness analysis is performed by randomly perturbing the identified stability and control derivatives and evaluating the effects of these uncertainties on the dynamical characteristics of the closed-loop system. The uncertainty level of the model parameters are obtained in CIPHER by using the Cramer-Rao bounds which defines the theoretical accuracy metrics of the identified parameters.

In Figure 4.20 and Figure 4.21, it is shown the uncertainty analysis results of the longitudinal and lateral attitude control systems. These analysis are performed for 100 random perturbations at 2σ standard deviations. Although, some of the case shift into the Level-3 region, the closed-loop systems remain stable. In the next section, we provide HIL system used as a part of the design process.

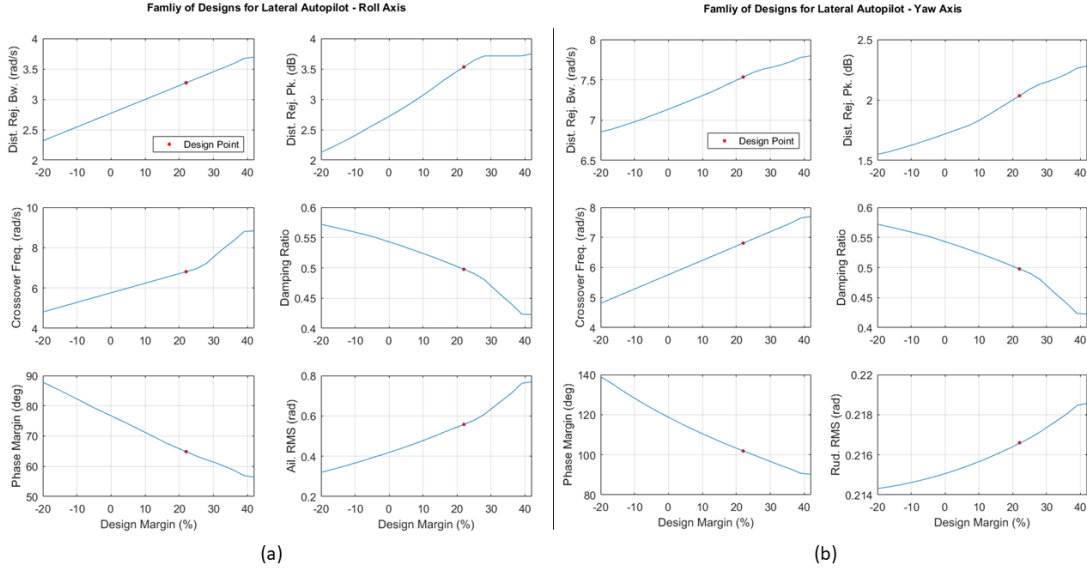


Figure 4.19 : Family of designs for lateral autopilot - (a) Roll axis, (b) Yaw axis.

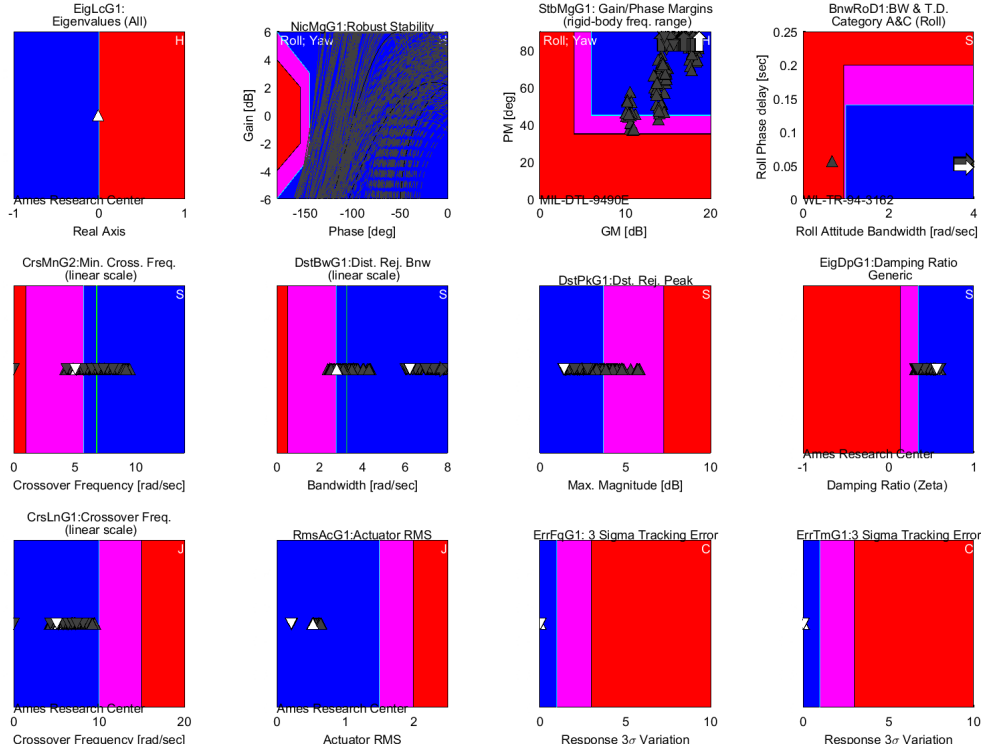


Figure 4.21 : Robustness analysis of the lateral autopilot.

4.6 Hardware-in-the-loop Simulation System

HIL simulation allows comprehensive simulation and testing of designed control and guidance algorithms before performing the flight tests while minimizing development cost and crash risk. The HIL system incorporates with a modified version of the ArduPlane running on the Pixhawk hardware and the aircraft nonlinear mathematical model on Simulink. Block diagram of the HIL architecture is given in Figure 4.22. The

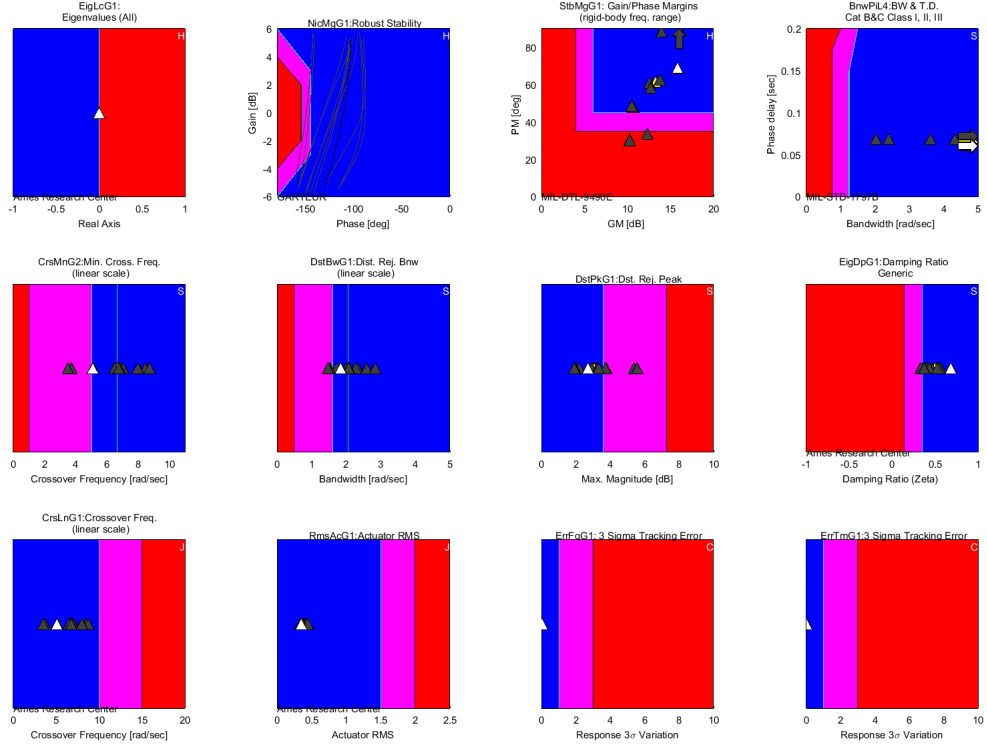


Figure 4.20 : Robustness analysis of the longitudinal autopilot.

data exchange between the ArduPlane and the Simulink is performed via MAVLink protocol over the serial port [95]. The MAVLink is a lightweight communication protocol that is used in source and time critical system such as embedded systems. The ArduPlane receives the sensor and actuator data from the Simulink. The data transfer rate between two system is 50 Hz which is the ArduPlane main loop frequency. The size of the received sensor and actuator messages including overhead bytes due to MAVLink 2.0 is 68 bytes and 34 bytes, respectively. The data rate of these two packages are 3400 bytes/sec and 1700 bytes/sec at 50 Hz frequency. The theoretical maximum speed of the serial port for the baud-rate is 92160 bytes/sec. This speed is far above the required transfer speed over the serial port.

The Simulink runs in normal mode in the desktop PC with Ubuntu 14.04 operating system. The desktop PC has Intel I7 4700HQ 2.4GHZ as a processor and 12GB DDR3 1600 MHz random access memory. The MAV model operates in soft real-time mode provided by the Aerospace Toolbox [96]. High data rate over the serial port allows low latency during transmission of the data. Time jitters due to Simulation Pace Block sleep method is smaller than the main loop frequency of ArduPlane. The highest pace error observed during HIL simulation is below 10 millisecond which allows running the simulation in soft real-time without needing any complex structure.

RC receiver is connected to the Pixhawk in order to incorporate the pilot into the HIL environment. Manual control capability using the RC equipment gives a close-to-real flight sense to the pilot while performing the HIL test flights. Hence, the open-loop or closed-loop performance of the MAV can be evaluated by the pilot qualitatively.

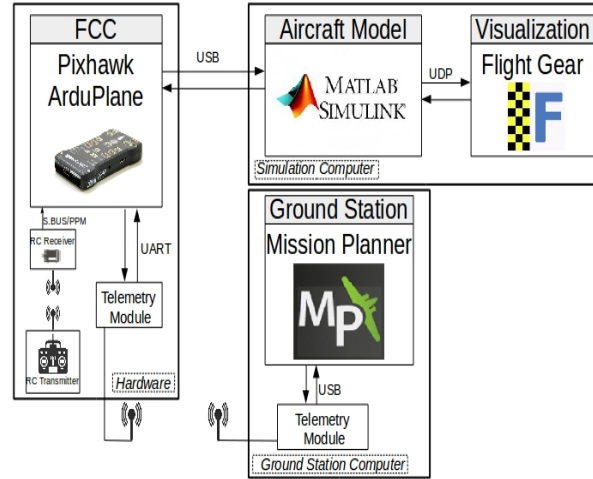


Figure 4.22 : HIL test system structure.

The HIL simulations are performed before each flight test to be sure the control system integration is completed without any bug and coding errors. In the HIL simulations, the test pilot performs several maneuvers to evaluate the closed-loop system responses and express his/her opinions to the flight test crew. For example, several simple sign errors, which cause a certain crash, are detected and the autopilot code is updated before the flight tests. So, the importance of the HIL system is proven directly. In the next section we provide the results of our flight tests comparing our designs with legacy controllers from the autopilot.

4.7 Flight Test Results

The next step of the desktop-to-flight control system design workflow is evaluating the control system performance by performing predefined flight tests. Root-mean-square (RMS) analysis is used for this purpose. Error is calculated by using the actual and trim values of the attitude and control surface deflections.

Level flight and doublet input reference tracking test cases are designed for the proposed and legacy ArduPilot controllers, separately. Each level flight test carries on about 30 sec and the reference pitch and roll angles are set to zero during the

test. In Figure 4.23a, attitude error RMS analysis results are given for the pitch and roll axes autopilots. Here, it is shown that the attitude error RMS values of the proposed controller (red cross) are lower than the ArduPilot controller and naturally more actuator usage is required for the proposed system as shown in Figure 4.23b to achieve high precision controls.

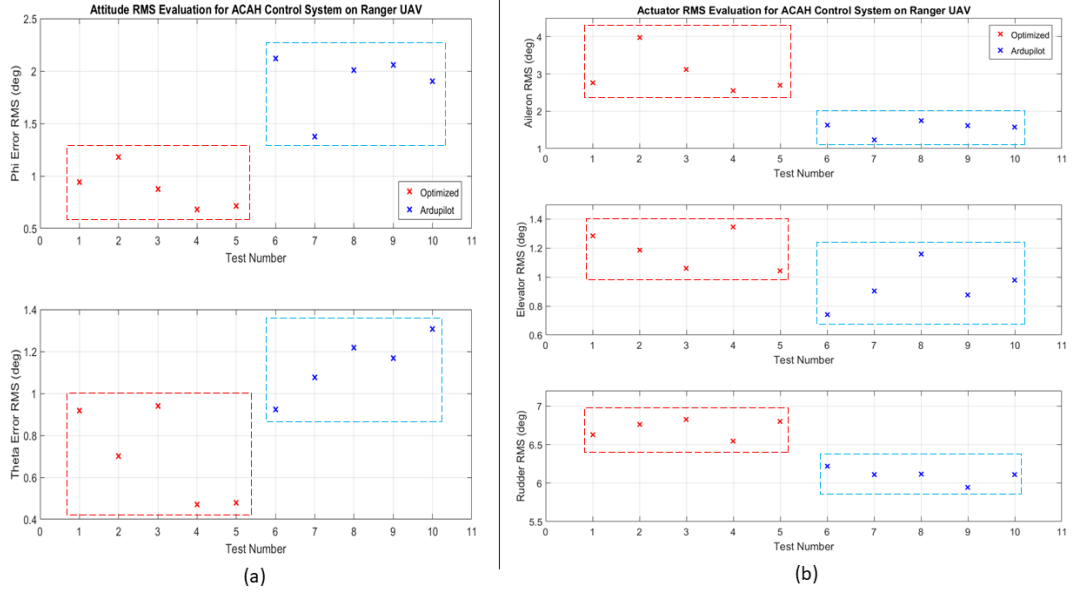


Figure 4.23 : Attitude error and actuator usage RMS in level flight.

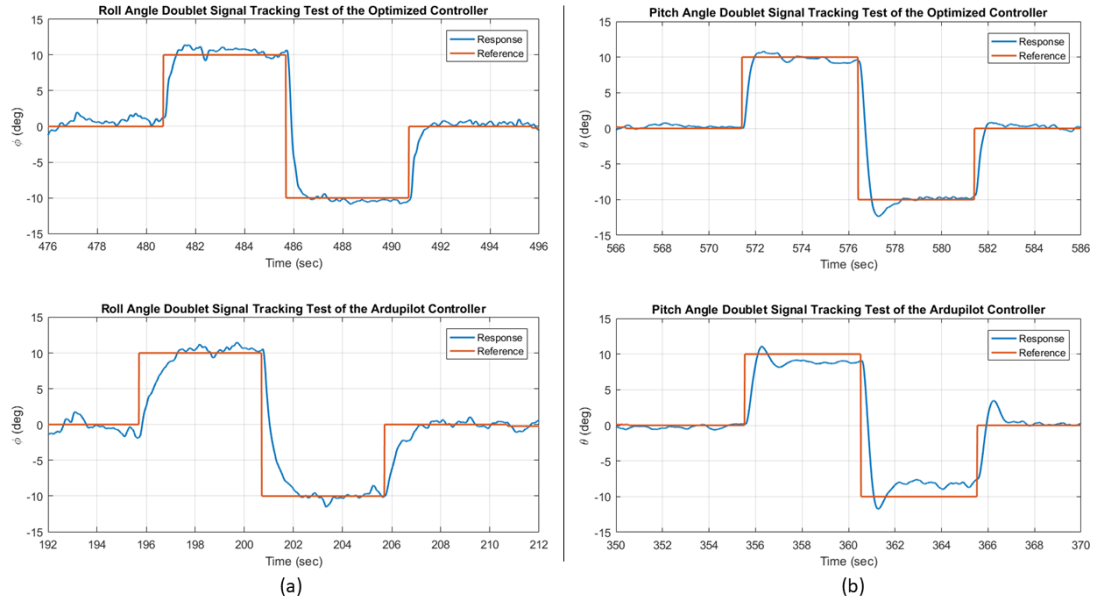


Figure 4.24 : Doublet reference input tracking test results on roll and pitch axes.

The closed-loop roll and pitch axis doublet input reference tracking test case results are given in Figure 4.24. Here, it is shown that the rise time of the roll attitude response of the proposed controller is shorter than the response of the ArduPilot as shown in Figure 4.24a. Also, the proposed pitch attitude controller is superior to the ArduPilot about

the steady-state error in the doublet reference tracking test case as shown in Figure 4.24b.

Table 4.14 : Performance comparison of the proposed and the legacy controllers.

Axis	Controller	ω_{180} (rad/s)	$\omega_{BW_{phase}}$ (rad/s)	$\omega_{BW_{gain}}$ (rad/s)	ω_c (rad/s)	PM (deg)	GM (dB)	DRB (rad/s)	DRP (dB)	ω_{DRP} (rad/s)
Roll ACAH	Proposed	14.247	10.150	11.802	6.805	64.848	14.179	3.271	3.53	10.04
	Ardupilot	19.413	11.591	11.157	1.418	82.421	19.888	1.703	0.970	13.895
Pitch ACAH	Proposed	11.490	8.338	8.622	6.665	61.636	13.252	2.064	3.054	8.377
	Ardupilot	13.459	9.543	9.482	4.067	21.466	13.676	2.978	2.7633	8.926

For a quantitative comparison of the system performances, it is required to obtain the frequency responses of the legacy controller. So, the frequency sweep input signal is designed and applied into the closed-loop system with the legacy controller. Then, by using the CIFER, the closed-loop, broken-loop and disturbance rejection characteristics of the legacy controller are determined in the frequency domain. The performance comparison of the proposed and the legacy controller is given in Table 4.14. In this table, it is shown that the crossover frequencies and phase margins of the roll and pitch attitude control systems are shifted into an adequate region. Also, for the roll attitude control system, DRB is increased at the cost of the DRP increment which is still in the acceptable region.

5. SYSTEM IDENTIFICATION AND CONTROL SYSTEM DESIGN FOR AN AGILE QUADROTOR PLATFORM

In recent years, urban mobility has an increasing demand especially for people and cargo transportation in the urban environment in which strict requirements should be defined because of its dense structure. Agents in this environment should be operated with effective coordination to ensure the airspace safety with increased versatility, speed, and minimum environmental impact. In this work, we provide a system identification, model stitching and model-based flight control system design methodology for an agile maneuvering technology demonstrator quadrotor platform. The proposed methodology is to ensure high precision maneuvering control capability over an extensive speed envelope in comparison to classical control techniques.

Novel manned and unmanned aerial vehicles (such as CityAirbus, Vahana, and Volocopter) have a promising role in the future of the urban air mobility and cargo services (Skyways, Uber Air and Prime Air) which are aimed to provide sustainable solutions with minimum infrastructure requirements. However, integration of the manned/unmanned vehicles into the urban airspace is a key challenge in the urban air mobility concept. Specifically, predictability of the dynamic behaviour of these vehicles is crucial in ensuring Unmanned Aircraft System Traffic Management (UTM) solutions which is capable of accommodating all of these vehicles in the same airspace safely and efficiently.

Blending with the general Air Traffic Management (ATM), it is obvious that the aerial vehicles integrated into the airspace should have mid/high fidelity mathematical model and adequate control system performance for hover, low speed, and fast forward flight phases. At this point, accurate/verified mathematical modeling and proper/transparent control system design process is crucial to obtain a certifiable flight control/autonomy system.

In literature, there are two fundamental methods for modeling an aerial vehicle. The first method is called as physics-based modeling approach in which it is required to

calculate the aerodynamic, inertial and structural parameters by using analytical and empirical tools. This approach can be used before the aircraft has been built and it is useful to gain preliminary insights about the dynamics of the designed aircraft. However, it can be time intensive to obtain these parameters by using several test setups and analytical/empirical tools. The second approach for modeling of the aerial platform is system identification method which can be applied in time-domain and frequency-domain. In this process, several pre-designed flight tests are performed and aerodynamic parameters are obtained by using the recorded responses of the aircraft. The system identification process can also be utilized to quantify the difference in the actual and predicted responses which is useful to improve the mathematical model fidelity of the aerial vehicle. In other words, physics-based modeling and system identification tools can be used in a complementary way.

Control system design process for the aerial vehicles requires to consider lots of handling quality specifications to provide mission safety and reliability. The importance of these requirements is increased significantly for the missions performed in the urban airspace. One of the first issue to maintain the flight safety is designing a control system which has adequate stability characteristics and reference signal tracking performance. Hence, several handling quality requirements are developed to design and evaluate the flight control systems. For manned fixed-wing and rotary-wing aircrafts, these requirements are collected in several handbooks such as MIL-STD-1797B [97] and ADS-33E-PRF [98], respectively.

Methodological design process and a verified mathematical model are key elements in flight control system design applications. Hence, in this work an iterative design pathway, which is called as desktop-to-flight control system design workflow [2], is utilized. This methodology is developed and validated by several applications on the manned aerial systems [2]. In this workflow, system identification, multi-objective optimization based flight control system design, desktop simulations, hardware-in-the-loop tests and validation/verification steps are tightly connected in an iterative way. The general scheme of the desktop-to-flight design workflow is given in Figure 5.1.

In previous studies, system identification and controller design processes are applied for several non-agile quadrotor platforms such as 3DR Iris+. Due to the narrow flight

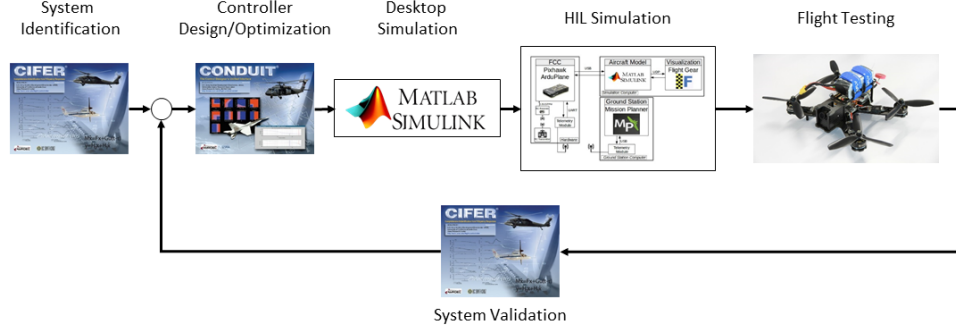


Figure 5.1 : General view of the desktop-to-flight design workflow [2].

envelope of these MAV platforms, stitched quasi-nonlinear models cover forward flight conditions within 0-10 m/s total airspeed. However, this interval is not adequate for a racer quadrotor platform which is able to perform fast forward flight and agile maneuvers. Hence, we focused on obtaining a quasi-nonlinear model and designing suitable inner/outer loop controllers which are valid for a wide range of flight envelope.

This chapter presents the application and experimental demonstration of the desktop-to-flight design workflow on a high performance agile maneuvering quadrotor platform which is capable of fast forward flight up to 32 m/s airspeed. This is the first time that this methodology is extended to such a technology demonstrator based on a racer system. Linear mathematical models for hover and forward flight are obtained by utilizing the frequency domain system identification process. Then, a quasi-nonlinear stitched mathematical model of the quadrotor is obtained for hover/low speed and forward flight conditions. To obtain an adequate trajectory tracking performance, required handling qualities are determined and some of them are modified for the proposed small scale MAV by using Froude scaling analysis. Based on these selected handling qualities, inner and outer-loop control systems of the legacy controller are modified and optimized to improve the stability and performance of the closed-loop system. Lateral reposition and longitudinal depart/abort maneuvers from ADS-33E-PRF are scaled-down according to kinematic scaling method. Then, several flight tests and Monte-Carlo simulations are performed to evaluate the closed-loop system performance. A footage and GPS position data from the actual flight tests are given in Figure 5.2.

In previous studies, system identification and controller design processes are applied for several non-agile quadrotor platforms such as 3DR Iris+. Due to the narrow flight

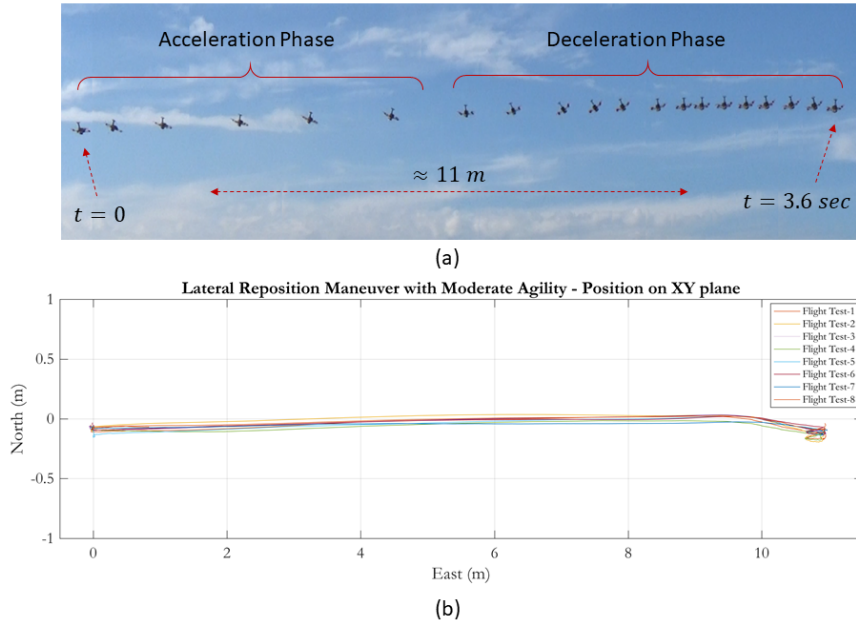


Figure 5.2 : Moderate agility lateral reposition maneuver. a) A footage from actual flight tests, b) Recorded North and East position.

envelope of these MAV platforms, stitched quasi-nonlinear models cover forward flight conditions within 0-10 m/s total airspeed. However, this interval is not adequate for a racer quadrotor platform which is able to perform fast forward flight and agile maneuvers. Hence, we focused on obtaining a quasi-nonlinear model and designing suitable inner/outer loop controllers which are valid for a wide range of flight envelope.

This chapter is organized as follows; in Section 5.1, the MAV platform and subsystems are explained. In Section 5.2, the linear model structure is given for hover and forward flight. In Section 5.3, frequency-domain system identification and time-domain verification processes for hover and forward flight are described. In Section 5.4, the simulation environment is generated based on the stitched quasi-nonlinear mathematical model. In Section 5.5, selected handling qualities are described, attitude and trajectory tracking control systems are designed. In Section 5.6, simulation and flight test results are evaluated and compared.

5.1 Experimental Platform

A high performance racer type quadrotor platform is used to track the given trajectory because of its aggressive maneuvering capability and wide airspeed range in forward flight phase between 0-32 m/s. General view of the test platform is shown in Figure 5.3. To achieve a high level of thrust-to-weight ratio, carbon fiber plates are used in

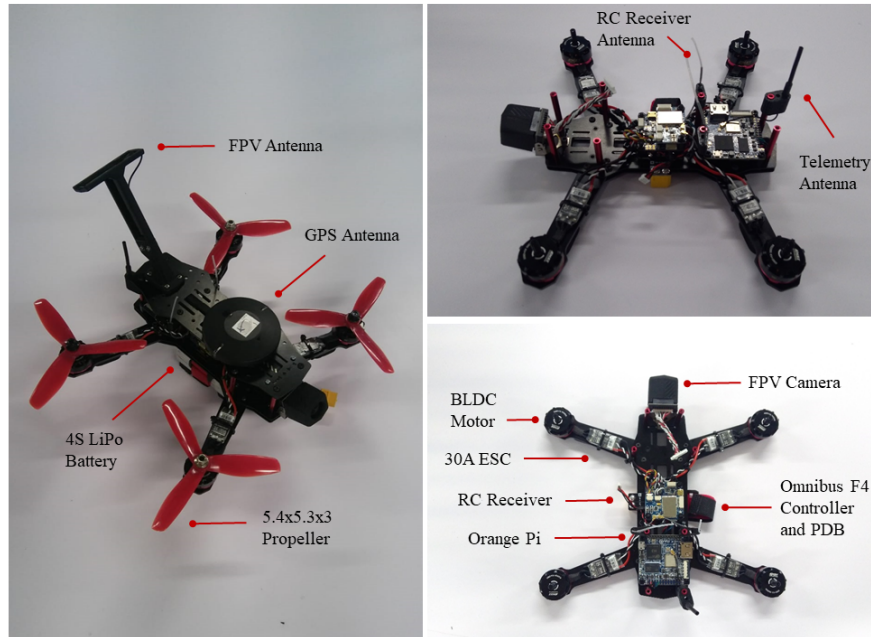


Figure 5.3 : General view of the high performance agile maneuvering drone platform.

the airframe structure. It has EMAX RS2205 2600 KV brushless DC (BLDC) motors, Hobbywing 30A Electronic speed controller (ESC), 4S LiPo battery and 5x4.5 inch tri-blade propellers.

In avionics structure, Omnibus F4Pro V3 and Arducopter are used as flight control system hardware and software, respectively. Omnibus F4Pro V3 is a small size and low weight flight control hardware and it is widely used in the racer quadrotor community. It has STM32F405 micro-controller, barometer, accelerometer, and gyroscope sensors onboard. Proficnc Here GPS receiver, which contains u-blox M8N GPS module and a magnetometer, is connected to the flight control board externally. In order to achieve high-frequency data logging, Arducopter flight control software runs on the Chibios which is a small footprint Real-Time Operating System (RTOS).

To increase telemetry range and allow high-speed communication between the UAV and ground station, Orange Pi Zero Plus2, which is a small size computer with the embedded WiFi module, is used on-board. Orange Pi and Omnibus flight control system is connected with the UART serial communication protocol. General scheme of the avionics structure is shown in Figure 5.4.

In the next section, mathematical model structure, which includes linear and angular accelerations, Euler rates and propulsion system dynamics, is introduced.

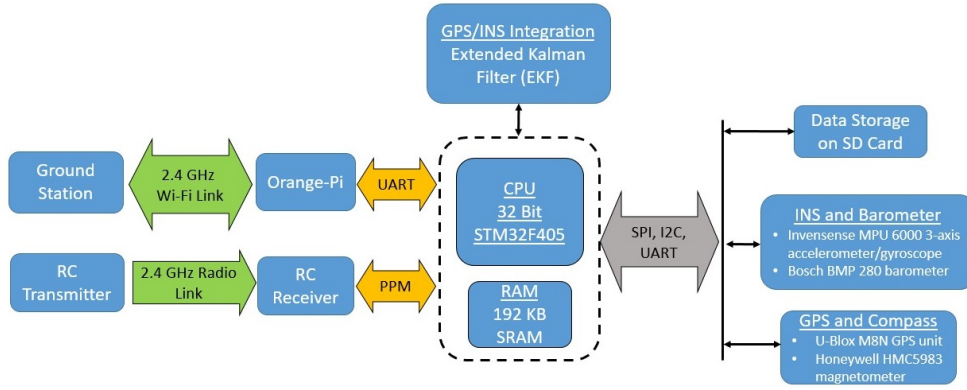


Figure 5.4 : General scheme of the Racer drone avionics architecture.

5.2 Mathematical Model Structure

As a preliminary step for the frequency-domain system identification process, it is important to define a linear mathematical model structure for hover and forward flight conditions. The general structure of the linearized 6 degree-of-freedom (DoF) equations of motion (EoM) in state-space form is given in equation 5.1.

$$\begin{aligned} \mathbf{M}\dot{\mathbf{x}} &= \mathbf{F}\mathbf{x} + \mathbf{G}\mathbf{u}(t - \tau) \\ \mathbf{y} &= \mathbf{H}_0\mathbf{x} + \mathbf{H}_1\dot{\mathbf{x}} \end{aligned} \quad (5.1)$$

where \mathbf{x} is the state vector, \mathbf{y} is the measurement vector, \mathbf{F} includes gradients to state perturbations in trim conditions, \mathbf{G} includes the gradients to control perturbations, τ is the time delay vector, \mathbf{M} includes the parameters which are depend on the rates of change of the state variables, \mathbf{H}_1 and \mathbf{H}_0 matrices are called as measurement matrices and they define the measurement vector by using the states and state derivatives. State and measurements vectors are given in equation 5.2 and equation 5.3.

$$\mathbf{x}^T = [u \quad v \quad w \quad p \quad q \quad r \quad \phi \quad \theta \quad \psi \quad \delta'_a \quad \delta'_e \quad \delta'_r] \quad (5.2)$$

$$\mathbf{y} = [\dot{u} \quad \dot{v} \quad \dot{w} \quad p \quad q \quad r \quad a_x \quad a_y \quad a_z] \quad (5.3)$$

Here, $\dot{u}, \dot{v}, \dot{w}$ cannot be measured directly. So, they should be reconstructed by using the accelerometer measurement definition as shown in equation 5.4.

$$\begin{aligned}
a_x &= \dot{u} + W_0 q - V_0 r + g \cos(\Theta_0) \theta + z_a \dot{q} - y_a \dot{r} \\
a_y &= \dot{v} + U_0 r - W_0 p - g \cos(\Theta_0) \phi - z_a \dot{p} + x_a \dot{r} \\
a_z &= \dot{w} + V_0 p - U_0 q + g \sin(\Theta_0) \theta + y_a \dot{q} - x_a \dot{q}
\end{aligned} \tag{5.4}$$

where $[x_a, y_a, z_a]$ defines the offset between the center of gravity and inertial measurement unit (IMU). In the technology demonstrator quadrotor platform, the center of gravity is quite close to the IMU location and these offsets can be neglected.

The actuation system dynamics (ESC, motor and propeller assembly) on roll and pitch axes are modelled as a first-order differential equation as shown in equation 5.5.

$$\dot{\delta}' = \omega (\delta_{cmd} - \delta') \tag{5.5}$$

where, δ_{cmd} , δ' and ω describe commanded input, actual output and propulsion system natural frequency for lateral, longitudinal and directional dynamics, respectively.

Unlike roll and pitch axis control moments, the quadrotor platform generates yaw rate by using differential drag moments of the propellers. As a result of this situation, phase of the $r(s)/\delta_r(s)$ frequency response is nearly constant in low frequency region which indicates a lead effect in this input-output pair (shown in Figure 5.9 and 5.10). To identify the lead in the yaw axis of the quadrotor, yaw rate dynamics is modeled as given in equation 5.6 [44].

$$\dot{r} + \tau_{lead} \dot{\delta}'_r = N_v v + N_p p + N_r r + N_{\delta'_a} \delta'_a + N_{\delta'_r} \delta'_r \tag{5.6}$$

Here, τ_{lead} is set as a flexible variable in the identification process and it is used to capture the dynamical effects of this extra zero on the yaw dynamics.

The propulsion system model is integrated into the linearized 6-DoF mathematical model as the last three terms in the state-space structure. The linearized 6-DoF bare-airframe dynamical model including aerodynamics, gravitational and coriolis terms can be written as shown in equation 5.7.

$$\begin{aligned}
\dot{u} &= X_u u + X_w w + (X_q - W_0) q - g \cos(\Theta_0) \theta + X_{\delta_e} \delta'_e \\
\dot{v} &= Y_v v + (Y_p + W_0) p + (Y_r - U_0) r + g \cos(\Theta_0) \phi + Y_{\delta_a} \delta'_a + Y_{\delta_r} \delta'_r \\
\dot{w} &= Z_u u + Z_w w + (Z_q + U_0) q - g \sin(\Theta_0) \theta + Z_{\delta_e} \delta'_e \\
\dot{p} &= L_v v + L_p p + L_r r + L_{\delta_a} \delta'_a \\
\dot{q} &= M_u u + M_w w + M_q q + M_{\delta_e} \delta'_e \\
\tau_{lead} \dot{\delta}'_r + \dot{r} &= N_v v + N_p p + N_r r + N_{\delta_a} \delta'_a + N_{\delta_r} \delta'_r \\
\dot{\phi} &= p + r \tan(\Theta_0) \\
\dot{\theta} &= q \\
\dot{\psi} &= r \sec(\Theta_0) \\
\dot{\delta}'_a &= -\omega_a \delta'_a + \omega_a \delta_{a_{cmd}} \\
\dot{\delta}'_e &= -\omega_e \delta'_e + \omega_e \delta_{e_{cmd}} \\
\dot{\delta}'_r &= -\omega_r \delta'_r + \omega_r \delta_{r_{cmd}}
\end{aligned} \tag{5.7}$$

In the next section, system identification and verification process is performed for the agile maneuvering quadrotor platform in hover and forward flight conditions.

5.3 System Identification and Verification

One of the most challenging task in modeling and flight control system design process is obtaining a suitable bare-airframe model of the aerial vehicle which contains airframe and propulsion system (ESC, BLDC motors, propellers and mixer) dynamics. Accuracy of the mathematical model directly affects the controller performance and reduces development costs.

The frequency-domain system identification method is a powerful tool to identify the bare-airframe dynamics of the aerial vehicle. In this process, the aerial vehicle is excited on each axis by using variable frequency sinusoidal input signal which covers a specific frequency range. After performing several flight tests, the recorded input-output dataset is used in Comprehensive Identification from Frequency Responses (CIFER) software to obtain frequency responses of the aerial vehicle on each axis. Then, a suitable linear mathematical model is fitted on the frequency responses and identified models are verified in time-domain by using doublet input

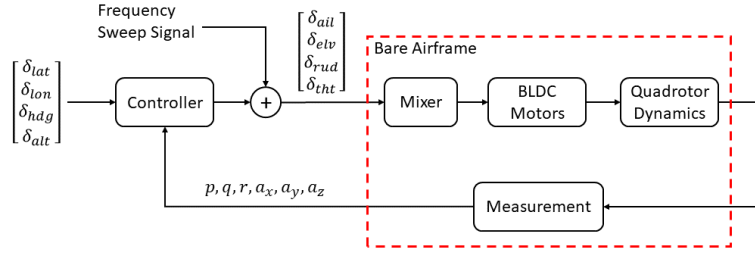


Figure 5.5 : Block diagram and input/output definitions for frequency sweep tests.

signals [3]. The system identification and verification process and results are explained in the following subsections.

5.3.1 Frequency response generation

Frequency sweep flight tests are performed to excite the interested bare-airframe dynamics of the quadrotor. One of the critical issue in designing the frequency sweep input is determining the frequency range of the test signal. Because of the unstable dynamics of the rotorcrafts, frequency range of interest is determined based on the crossover frequency of the closed-loop system as shown in equation 5.8 [3].

$$0.3 \omega_c \leq \omega \leq 3 \omega_c \quad (5.8)$$

As an initial guess, crossover frequency values of the IRIS+ quadrotor platform are used in which $\omega_c \approx 20 - 30 \text{ rad/s}$ for lateral and longitudinal axes and $\omega_c \approx 6 \text{ rad/s}$ for directional axis [99].

According to the data collecting procedure given in [3], automated sweep signal is designed to cover 1-60 rad/s frequency range. The individual sweep record length is 90 sec and duration of the additional hover flight at the beginning and at the end of the sweep tests is 5 seconds. The concatenated record length is 200 seconds, data sampling time and filter cut-off frequency are set as 250 Hz and 25 Hz, respectively.

Because of the unstable dynamics of the quadrotor platform, frequency sweep tests should be performed while the inner-loop attitude control system is engaged. So, altitude-hold mode of the ArduCopter is used while performing the frequency sweep tests. To excite the bare-airframe dynamics directly, the frequency sweep test signals are summed with the controller signal and applied into the mixer as shown in Figure 5.5.

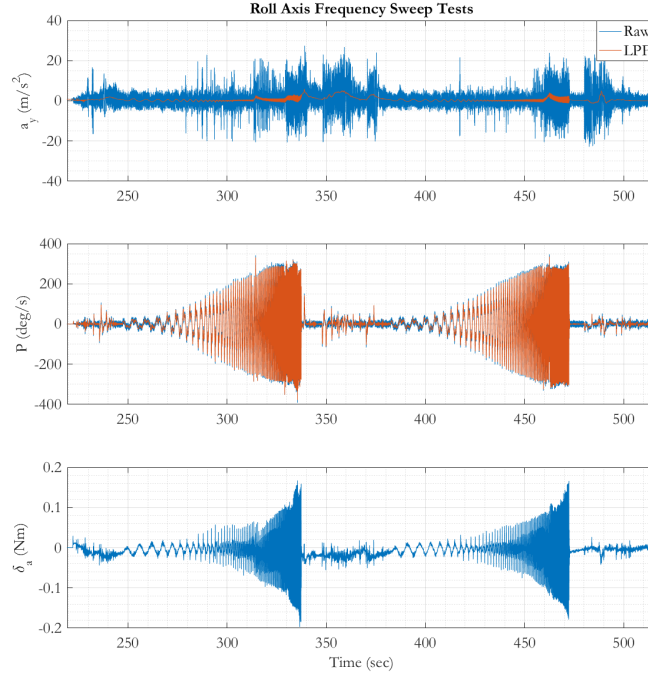


Figure 5.6 : Roll axis frequency sweep test.

After the system identification test flights, body-axis acceleration, body-axis rate and mixer inputs for lateral, longitudinal and directional axes are recorded on an SD card. A sample flight test record for the lateral axis system identification process is given in Figure 5.6.

5.3.2 Obtaining the speed derivatives for hover flight Conditions

As mentioned before, because of the unstable dynamical characteristics of the quadrotor bare-airframe, it is necessary to perform the system identification flight tests by using the inner-loop controllers of the ArduCopter. However, low frequency sweep test signal will be suppressed by the controller and this results in low coherence of the identified angular rate responses in the low frequency region. Hence, it may be difficult to identify the speed damping derivatives (X_u, Y_v) and speed stability derivatives (M_u, L_v). Although the coherence is low for the control inputs, there is good energy content in the \dot{u}, \dot{v}, θ and ϕ as a result of the kinematic consistency. So, these signals can be used to obtain the speed derivatives of the aerial platform [3]. Identified speed damping and stability derivatives are fixed in the system identification process.

For hover conditions, lateral specific force can be given as shown in equation 5.9 in simplified form.

$$\dot{v} = Y_v v + g\phi \quad (5.9)$$

After calculating the time derivative and performing the Laplace transform, transfer function of $\dot{v}(s)/\phi(s)$ is generated as shown in equation 5.10 which allows the direct identification of the lateral speed damping derivative Y_v from the roll axis sweep flight test data.

$$\frac{\dot{v}(s)}{\phi(s)} = \frac{sg}{s - Y_v} \quad (5.10)$$

Frequency response of the $\dot{v}(s)/\phi(s)$ is given in Figure 5.7. As shown in the figure, coherence value is almost 1 which indicates the linearity of the response. $\dot{v}(s)/\phi(s)$ transfer function is fitted on the frequency response between 1-5 rad/s by using NAVFIT module in the CIPHER. The cost value of this fitting process is calculated as 1.034. As a result, equation 5.11 is obtained which indicates that $Y_v = -0.26068$.

$$\frac{\dot{v}}{\phi} = \frac{9.806s}{s + 0.26068} \quad (5.11)$$

In a similar way with the lateral specific force expression, longitudinal specific force can be defined as shown in equation 5.12.

$$\dot{u} = X_u u - g\theta \quad (5.12)$$

After calculating the time derivative and performing the Laplace transform, transfer function of $\dot{u}(s)/\theta(s)$ is generated as shown in equation 5.13. The coherence is almost 1 between 1-30 rad/s frequency range.

$$\frac{\dot{u}(s)}{\theta(s)} = \frac{-sg}{s - X_u} \quad (5.13)$$

Frequency response of the $\dot{u}(s)/\theta(s)$ is given in Figure 5.7. As shown in the figure, coherence value is almost 1 which indicates the linearity of the response.

Transfer function fitting process is applied for 1-5 rad/s frequency range. The obtained transfer function is given in equation 5.14 with the fitting cost value of 3.880.

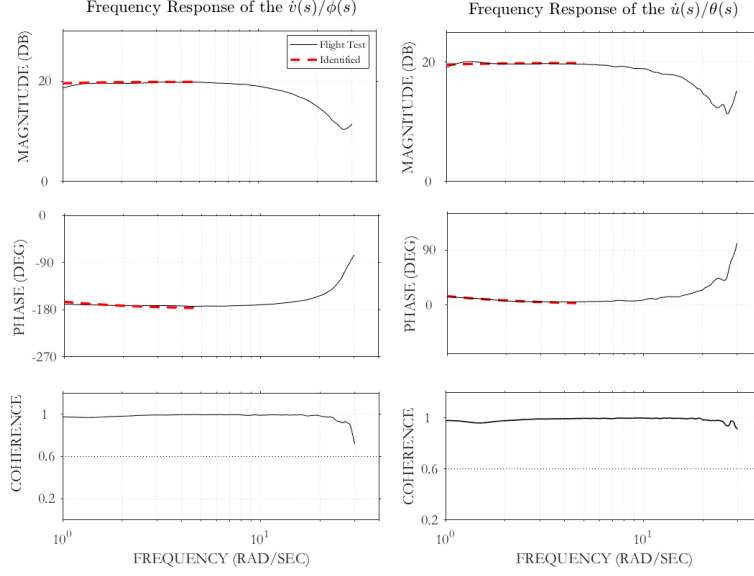


Figure 5.7 : Frequency responses of the $\dot{v}(s)/\phi(s)$ and $\dot{u}(s)/\theta(s)$.

According to this transfer function, longitudinal speed damping derivative is calculated as $X_u = -0.270617$.

$$\frac{\dot{u}}{\theta} = \frac{-9.806s}{s + 0.270617} \quad (5.14)$$

Estimation of longitudinal speed stability derivative M_u

Longitudinal static stability (LSS) tests are performed to calculate the speed stability derivative M_u which is dominant in hover and low speed forward flight phases. In trim flight conditions, the pitching angular acceleration should be zero as shown in equation 5.15.

$$\dot{q} = 0 = M_u \Delta u + M_w \Delta w + M_{\delta_e} \Delta \delta_e \quad (5.15)$$

When the equation is solved for M_u , equation 5.16 is obtained.

$$M_u = -M_{\delta_e} \frac{\Delta \delta_e}{\Delta u} + M_w \frac{Z_u}{Z_w} \quad (5.16)$$

Due to the dominant effects of the first part of the equation, the second part can be neglected. So, to calculate the longitudinal speed stability derivative in the near hover flight conditions, it is required to obtain $\Delta \delta_e / \Delta u$ relationship from the low-speed LSS flight tests.

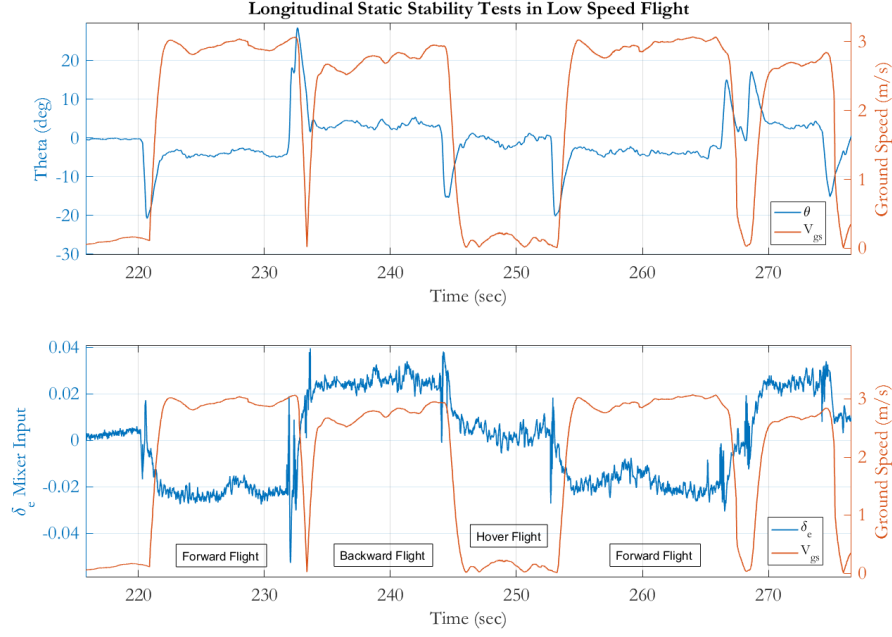


Figure 5.8 : LSS flight test in near hover conditions.

In these tests, legacy velocity tracking control system in ArduCopter is activated and 3 m/s constant ground speed reference signal is applied to the closed-loop system. It is important to perform the low-speed LSS flight tests in almost 0 m/s wind conditions to observe the input and vehicle response in the low speed regime. A sample time history of the LSS flight test is given in Figure 5.8.

After performing the LSS flight tests, pitch axis mixer input - ground velocity ($\Delta\delta_e/\Delta V_{gs}$) ratio is calculated as -0.007467. Here, it is possible to use the ground velocity (V_{gs}) instead of the X_b axis velocity u in hover/low speed flight conditions because of the small pitch angle and neglected wind. By using this relationship, M_u is calculated as shown in equation 5.17.

$$M_u = -M_{\delta_e} \frac{\Delta\delta_e}{\Delta u} = (-766.7)(-0.007467) = 5.72495 \quad (5.17)$$

5.3.3 System identification results for hover and forward flight conditions

The technology demonstrator quadrotor platform has a wide flight envelope covers hover and forward flight conditions with 32 m/s maximum total airspeed. Hence, it is important to evaluate the MAV dynamics in these phases. After performing several frequency sweep tests in hover and fast forward flight conditions, recorded data is processed to obtain the frequency responses of the open-loop quadrotor platform.

Measured acceleration and body rate data are used to obtain the non-parametric model, i.e. frequency responses, of the quadrotor roll, pitch, yaw and heave dynamics. Then, linear parametric state-space model is fitted on the obtained frequency responses of the actual system by using the DERIVID tool of the CIFER. The frequency responses of the identified and actual bare-airframe dynamics in hover and forward flight conditions are compared in Figure 5.9, 5.10 and 5.11. Here, solid line represents actual system responses and dashed line represents identified parametric model. As shown in these figures, coherence of the frequency responses are above 0.6 for a wide range of frequency which indicates the linearity of the dynamics.

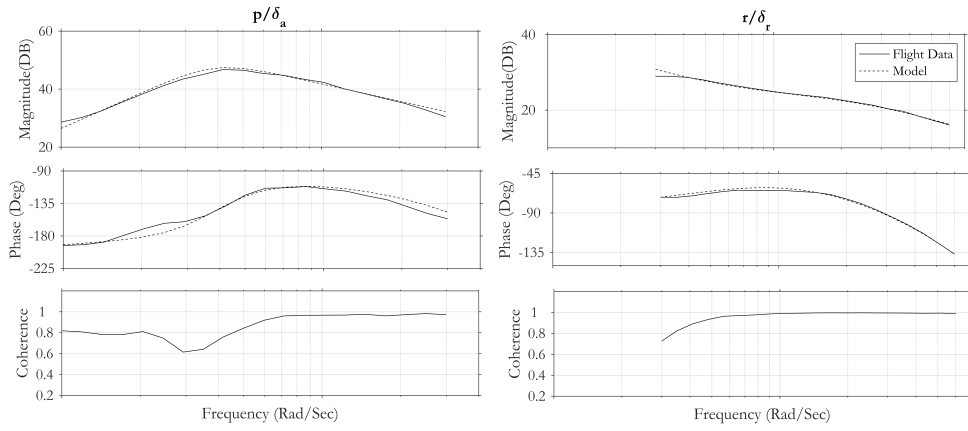


Figure 5.9 : On-Axis $p/\delta_a, r/\delta_r$ frequency responses of the actual system and identified model in hover flight conditions.

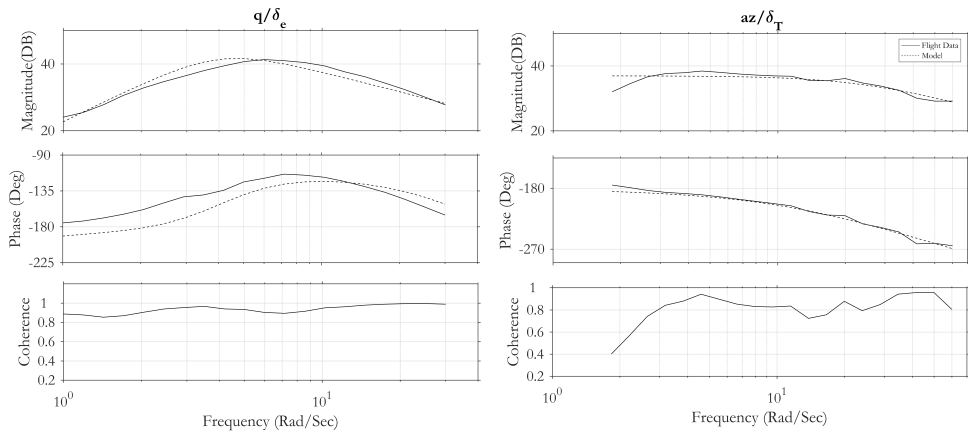


Figure 5.10 : On-Axis $q/\delta_e, a_z/\delta_T$ frequency responses of the actual system and identified model in hover flight conditions.

Identified model costs for lateral, longitudinal, directional and heave axis are given in Table 5.1. Subscripts '*hvr*' and '*ff*' are used for hover and forward flight phases. Here, it is shown that individual (J_i) and average (J_{ave}) cost values for the identification process are within or near the suggested limits given in equation 5.18 [3].

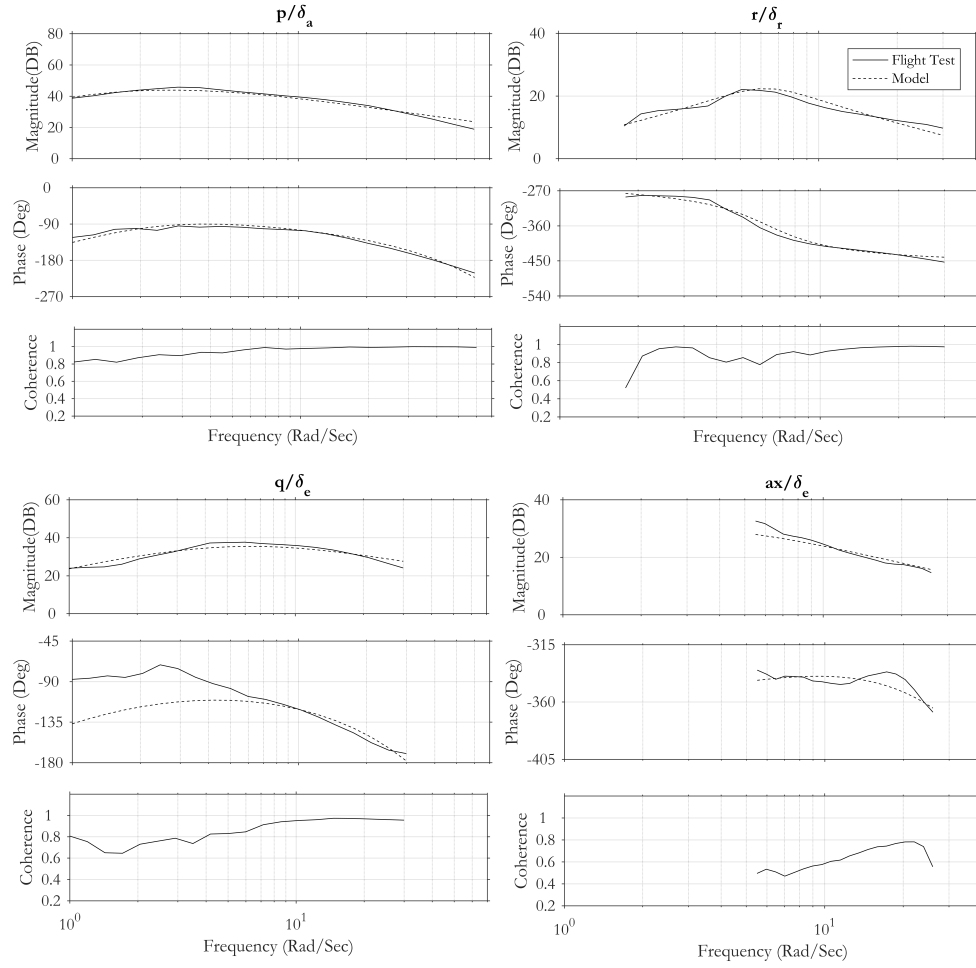


Figure 5.11 : On-Axis frequency responses of the actual system and identified model in forward flight conditions.

$$J_i \leq 150 \text{ to } 200$$

$$J_{ave} \leq 100$$
(5.18)

Identified aerodynamic parameters of the quadrotor bare-airframe dynamics for hover and forward flight phases are given in Table 5.2. Several parameters, which have high Cramer-Rao bound ($\geq 25\%$) and insensitivity ($\geq 10\%$), are neglected and set to zero in the model reduction step. These are marked with (+) superscript in the table.

As shown in Table 5.2, speed damping and stability derivatives X_u, Y_v and M_u are identified with low Cramer-Rao bound and insensitivities. These results are also verified by the given speed stability and damping analysis in Section 5.3.2.

5.3.4 Identification of the propulsion system dynamics

Because of the high natural frequency of the BLDC motors, propulsion dynamics may not be captured in the low frequency range. So, it is required to perform a high

Table 5.1 : Identification costs for each input-output pairs.

Response	J_{hvr}	J_{ff}
p/δ_a	23.453	69.997
r/δ_a	48.816	-
a_y/δ_a	31.992	48.599
\dot{v}/δ_a	71.426	68.978
\dot{u}/δ_e	118.755	141.831
q/δ_e	126.780	212.850
a_x/δ_e	53.733	34.916
r/δ_r	4.2752	50.852
\dot{v}/δ_r	-	90.682
a_z/δ_t	23.476	-
\dot{w}/δ_t	43.763	-
$J_{ave\delta_a}$	43.922	62.525
$J_{ave\delta_e}$	99.756	129.866
$J_{ave\delta_r}$	4.2752	70.767
$J_{ave\delta_t}$	33.619	-

frequency sweep test to identify the propulsion system dynamics. For this purpose, the frequency sweep flight tests are repeated for the pitch and roll axes by using the test parameters as shown in Table 5.3.

If we ignore the low-frequency hovering cubics, pitch and roll dynamics of the quadrotor bare-airframe can be modelled as second-order transfer functions in the high frequency region. So, high frequency dynamics are represented as shown in equation 5.19 and 5.20 which combine the frame and BLDC motor dynamics.

$$\frac{p(s)}{\delta_a(s)} = \frac{L_{\delta_a}(\omega_\phi)e^{-\tau_\phi s}}{s(s + \omega_\phi)} \quad (5.19)$$

$$\frac{q(s)}{\delta_e(s)} = \frac{M_{\delta_e}(\omega_\theta)e^{-\tau_\theta s}}{s(s + \omega_\theta)} \quad (5.20)$$

where, ω_θ and ω_ϕ are natural frequencies of the propulsion system, τ_θ and τ_ϕ are high frequency delays on roll and pitch axes. Then, transfer functions are fitted on the identified $p(s)/\delta_a(s)$ and $q(s)/\delta_e(s)$ frequency responses as shown in Figure 5.12.

The identified linear models for the high frequency range are given in equation 5.21 and 5.22 with the cost of 3.992 and 1.009, respectively. As shown in these

Table 5.2 : Identified parameters for hover and forward flight conditions.

		Vs = 0 m/s				Vs = 20 m/s			
	Derivative	Value	CR Bound	CR Bound (%)	Insensitivity (%)	Value	CR Bound	CR Bound (%)	Insensitivity (%)
Longitudinal Model	X_{tt}	-0.25860	0.01812	7.007	2.274	-0.1635	0.01764	10.79	4.698
	X_q	-0.07132	9.992E-03	14.01	5.033	-0.2107	0.01649	7.828	3.201
	X_{δ_e}	-9.124	0.4095	4.488	1.6	0 ⁺	—	—	—
	M_{tt}	5.688	0.3699	6.503	1.724	3.571	0.2903	8.128	2.338
	M_q	1.958	0.3935	20.09	5.825	0 ⁺	—	—	—
	M_{δ_e}	765.7	26.51	3.462	0.9258	753.0	36.58	4.858	1.242
	τ_{δ_e}	0.03368	2.680E-03	7.958	3.218	0.05124	2.292E-03	4.474	2.003
Lateral Model	Y_v	-0.2615	0.01644	6.289	2.446	-0.3413	0.01906	5.584	1.656
	Y_p	0 ⁺	—	—	—	0 ⁺	—	—	—
	Y_r	0 ⁺	—	—	—	0 ⁺	—	—	—
	L_v	-6.154	0.3272	5.317	1.783	-0.7775	0.05845	7.518	2.233
	L_p	0 ⁺	—	—	—	-1.532	0.2521	16.45	6.770
	L_r	0 ⁺	—	—	—	0 ⁺	—	—	—
	N_v	1.169	0.3145	26.91	6.279	0 ⁺	—	—	—
	N_p	0.2032	0.03175	15.62	3.464	0 ⁺	—	—	—
	N_r	0 ⁺	—	—	—	0 ⁺	—	—	—
	Y_{δ_a}	12.07	0.5377	4.456	1.747	7.036	1.365	19.41	6.580
	L_{δ_a}	1232	38.12	3.094	0.9929	913.4	30.57	3.347	1.045
	N_{δ_a}	18.50	1.361	7.357	3.545	0 ⁺	—	—	—
	τ_{δ_a}	0.03323	2.205E-03	6.637	2.976	0.03898	1.360E-03	3.489	1.651
Directional Model	N_r	0 ⁺	—	—	—	-21.44	3.234	15.08	0.2437
	Y_v	0 ⁺	—	—	—	15.11	3.107	20.56	0.2740
	Y_r	0 ⁺	—	—	—	9.188	1.249	13.59	0.1818
	N_{δ_r}	92.71	8.614	9.284	4.028	122.0	9.521	7.807	0.3676
	Y_{δ_r}	0 ⁺	—	—	—	35.67	4.724	13.24	0.4037
	N_v	0 ⁺	—	—	—	51.02	9.108	17.85	0.2593
	ω_{δ_r}	-26.04	4.708	18.06	3.468	-26 ⁺	—	—	—
	τ_{lead}	-16.13	1.608	9.978	2.193	-2.313	0.2286	9.883	2.807
Heave Model	τ_{δ_r}	0.01891	2.253E-03	11.91	4.309	0 ⁺	—	—	—
	Z_w	0 ⁺	—	—	—	—	—	—	—
	Z_{δ_z}	-70.27	2.808	3.996	1.501	—	—	—	—
	ω_{δ_z}	-25.6	2.307	9.012	2.923	—	—	—	—
	τ_{δ_z}	6.514E-03	1.730E-03	26.57	10.49	—	—	—	—

Table 5.3 : Test signal parameters for propulsion system identification in high frequency range.

Parameter	Value
Frequency Range	1-100 rad/s
Sweep Length	90 sec
Sampling Time	400 Hz
Concatenated Record Length	200 sec

identified transfer functions, natural frequency of the propulsion system is obtained as approximately 29 rad/s.

$$\frac{p(s)}{\delta_a(s)} = \frac{L_{\delta_a}(\omega_\phi)e^{-\tau_\phi s}}{s(s + \omega_\phi)} = \frac{39018.6e^{-0.0052s}}{s(s + 28.276s)} \quad (5.21)$$

$$\frac{q(s)}{\delta_e(s)} = \frac{M_{\delta_e}(\omega_\theta)e^{-\tau_\theta s}}{s(s + \omega_\theta)} = \frac{26229.3e^{-0.0060s}}{s(s + 29.695s)} \quad (5.22)$$

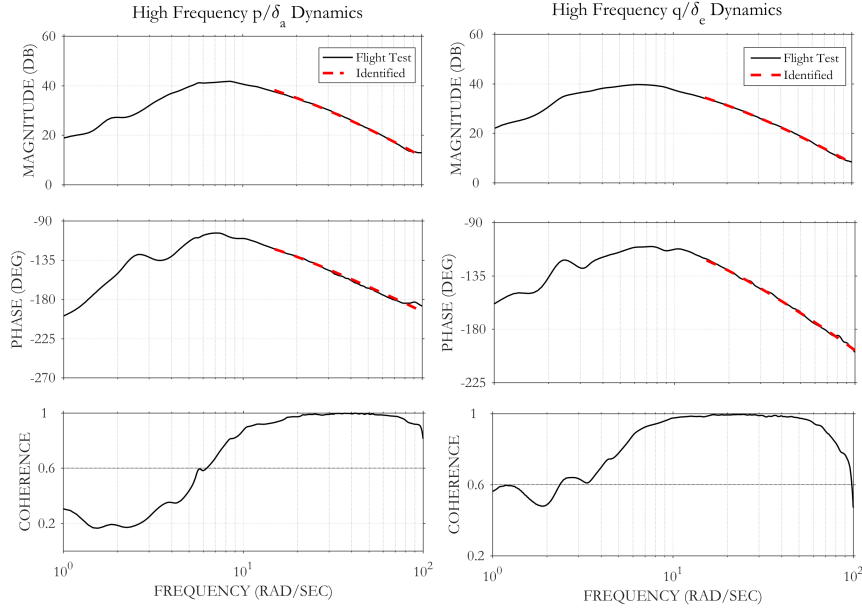


Figure 5.12 : Identification of high frequency dynamics on longitudinal and lateral axes.

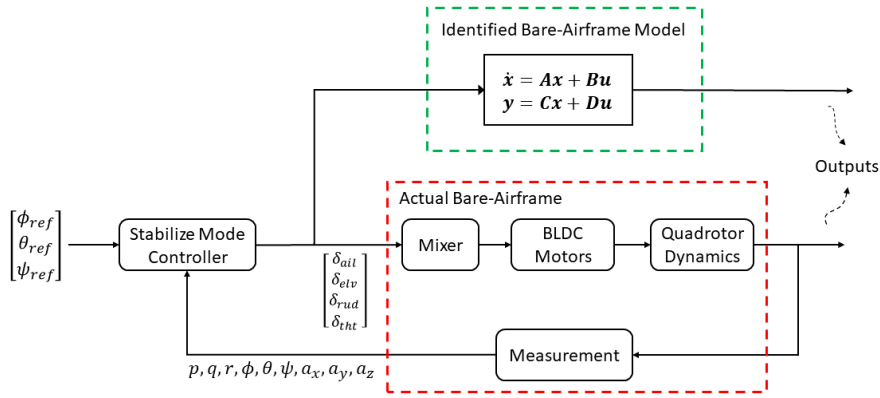


Figure 5.13 : Schematics of the bare-airframe model verification process.

5.3.5 Model verification

Identified linear models of the quadrotor platform should be verified before using in the control system design process. For this purpose, verification test procedure is utilized in the time-domain. In these tests, doublet reference attitude signals with $\simeq \pm 10\%$ amplitude of the pilot stick range are applied on each axis separately. Then, mixer input and system output data are logged on the SD card. Mixer inputs are applied into the identified linear bare-airframe models and responses are compared with the actual system outputs. The schematics of the time-domain verification process is shown in Figure 5.13.

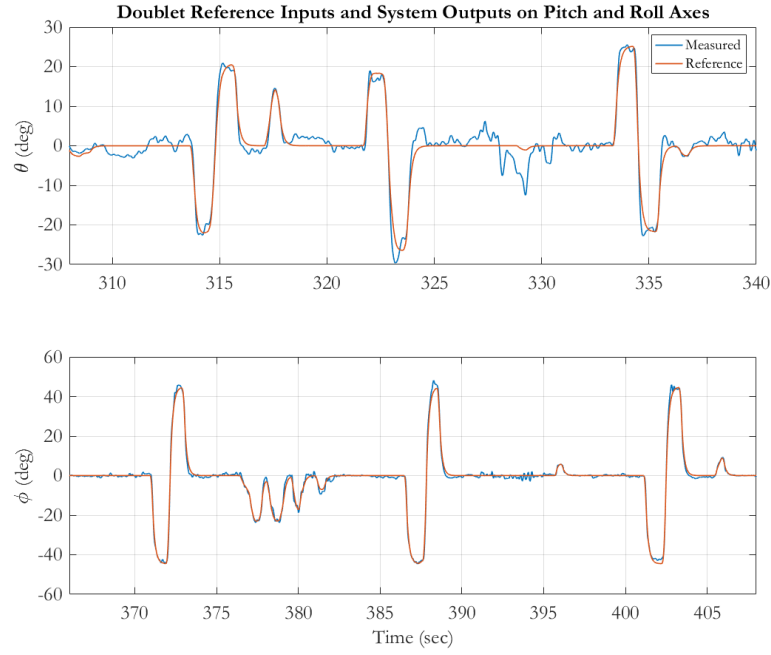


Figure 5.14 : Sample doublet reference input tests on pitch and roll axes.

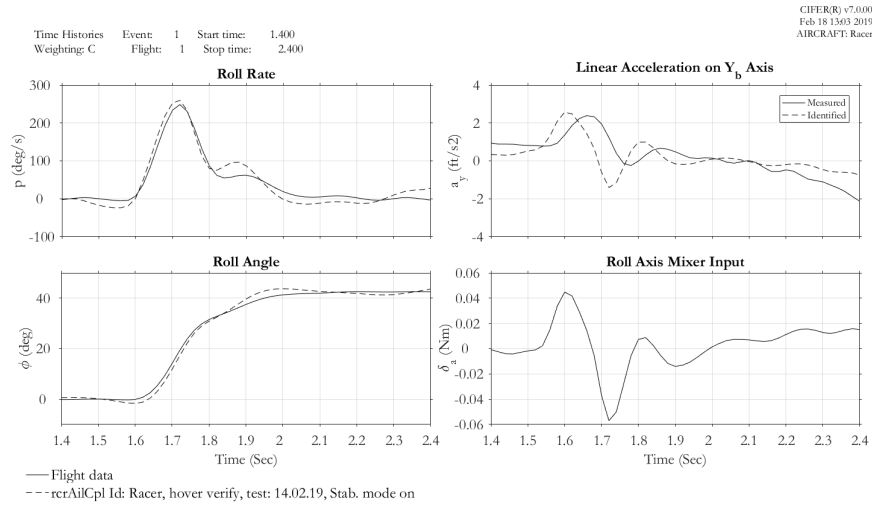


Figure 5.15 : Roll axis verification test results in hover flight.

Model verification flight tests are performed by using stabilize mode of the ArduCopter. In this mode, pilot sends attitude commands in the doublet form as shown in Figure 5.14. Then, verification test data is processed by using VERIFY tool in CIPHER. Because of the unstable bare-airframe dynamics, linear model is simulated for about 1.5-2 seconds to avoid the unstable model responses. Roll, pitch and yaw axes verification results are given in Figure 5.15, 5.16 and 5.17. As shown in these figure, actual system and linear models have similar responses which verifies the system identification results.

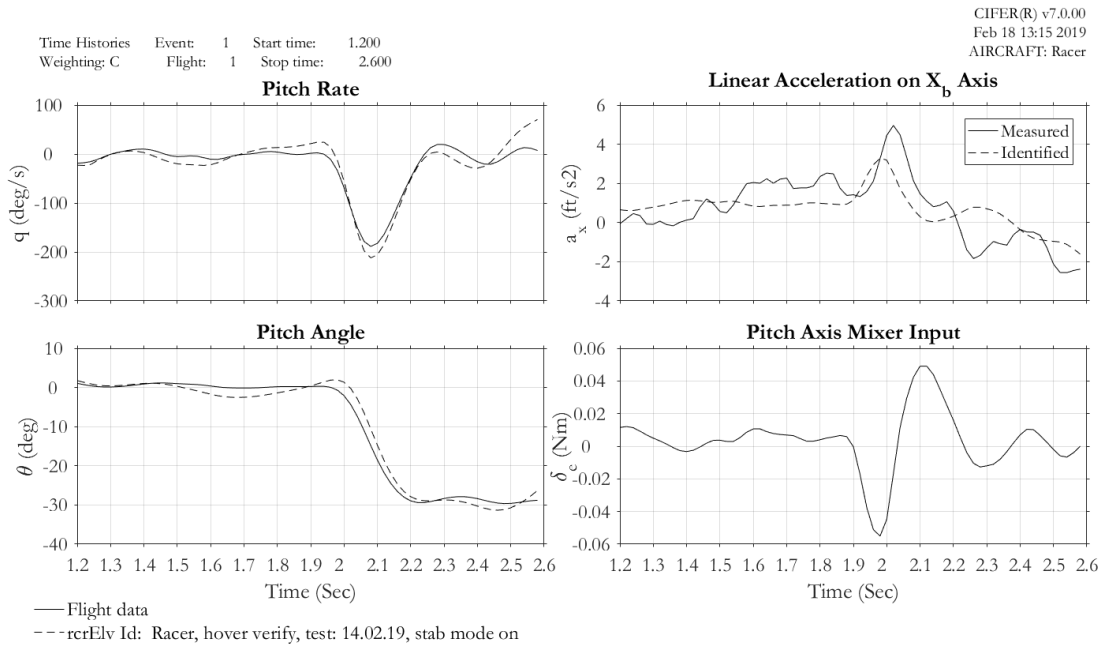


Figure 5.16 : Pitch axis verification test results.

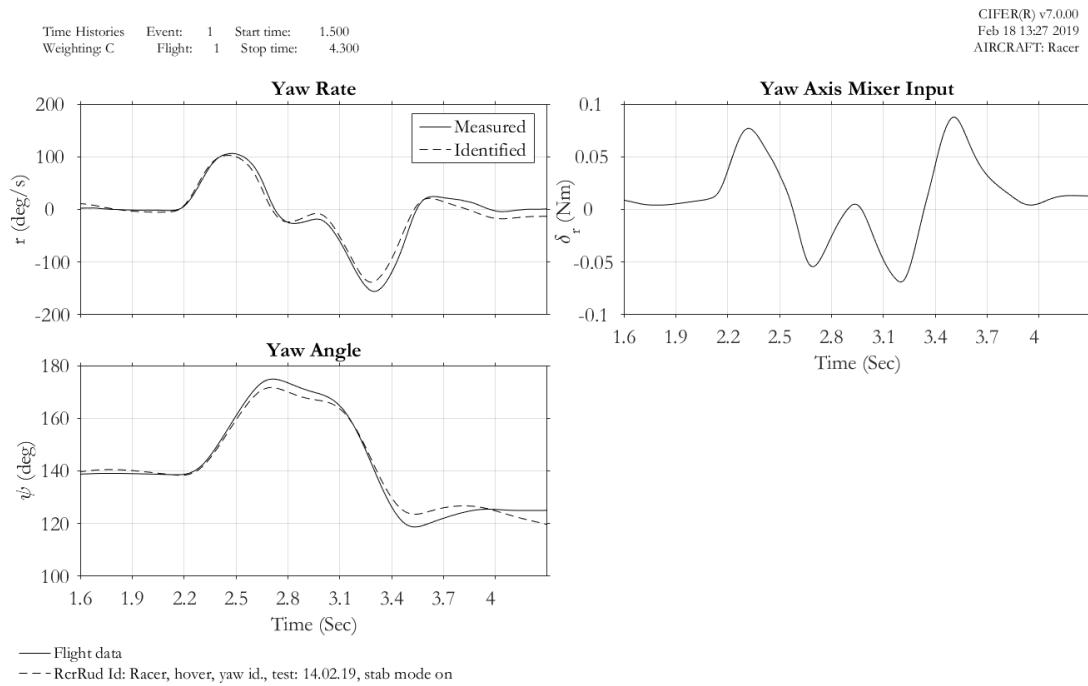


Figure 5.17 : Yaw axis verification test results.

Table 5.4 : Verification TIC and cost (J_{vrf}) values for hover and forward flight conditions.

Axis	TIC_{hvr}	$J_{vrf_{hvr}}$	TIC_{ff}	$J_{vrf_{ff}}$
Roll	0.06834	1.804	0.05307	0.723
Pitch	0.09661	1.632	0.04378	1.251
Yaw	0.06953	1.914	0.03334	0.760

In the model verification process, Theil-inequality constant (TIC) and verification cost (J_{vrf}) values are used to evaluate the similarity of the identified model and actual system responses. According to the guideline in [3], TIC and J_{vrf} values should be as given in equation 5.23 and 5.24.

$$TIC \leq 0.25 \text{ to } 0.30 \quad (5.23)$$

$$J_{vrf} \leq 1.0 \text{ to } 2.0 \quad (5.24)$$

Model verification results for hover and forward flight conditions are given in Table 5.4. As shown in this table, TIC and J_{vrf} values are below the given limits in equation 5.23 and 5.24. Here, subscripts ' hvr ' and ' ff ' are used for hover and forward flight phases, respectively.

In the next section, model stitching method is introduced which is used to generate a full-flight envelope simulation environment by using linear point models and trim dataset.

5.4 Model Stitching

Linear state-space perturbation models represent the dynamical behaviour of the aerial system and critical dynamics can be captured by using these simple mathematical models. However, linear models are valid only for a specific flight condition. If the aerial vehicle has a wide flight envelope, one linear model would be insufficient to capture the dynamical behaviour in the whole envelope. Hence, linear models should be obtained for several flight conditions and control system parameters should be scheduled based on airspeed, dynamic pressure or altitude.

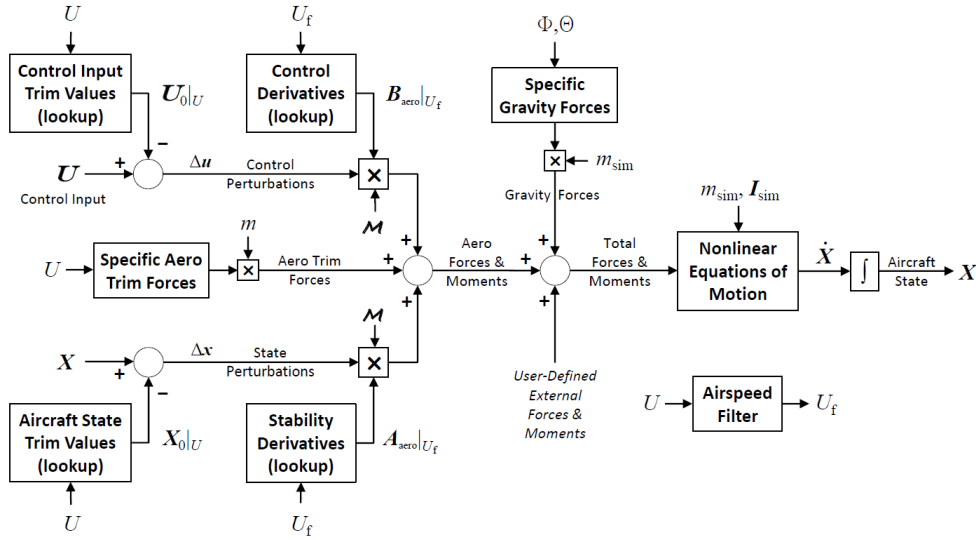


Figure 5.18 : General view of the stitch model structure [4].

As we mentioned in the previous sections, the system identification process is a powerful tool to obtain the linear mathematical model of the aerial vehicle for a specific flight condition. However, it is required to generate a full-flight envelope simulation environment to evaluate the closed-loop system behaviour. For this purpose, model stitching method is developed in which several anchor points and trim data are stitched together to cover the flight envelope of the aerial vehicle [3, 4, 43]. General structure of the stitched model is given in Figure 5.18.

5.4.1 Anchor point data

Anchor point data is defined as a specific flight condition in which the linear model and trim data are available. For the agile maneuvering quadrotor platform, two anchor point models (for hover and 20 m/s forward flight) are identified and used in the stitched model. Stability and control derivatives are linearly interpolated between these two point models as a function of U . To obtain the anchor trim point, forward flight tests are performed in several pitch attitude between 0° and -55° . Then, $W_0, \Theta_0, \delta_{e_0}$ and δ_{i_0} are calculated by using the trim flight data records as shown in Figure 5.19. This data set is used to obtain the stitched model which covers the hover/low speed and fast forward flight phases. For more information and comprehensive analysis about the model stitching method, readers may refer to [3, 4, 43].

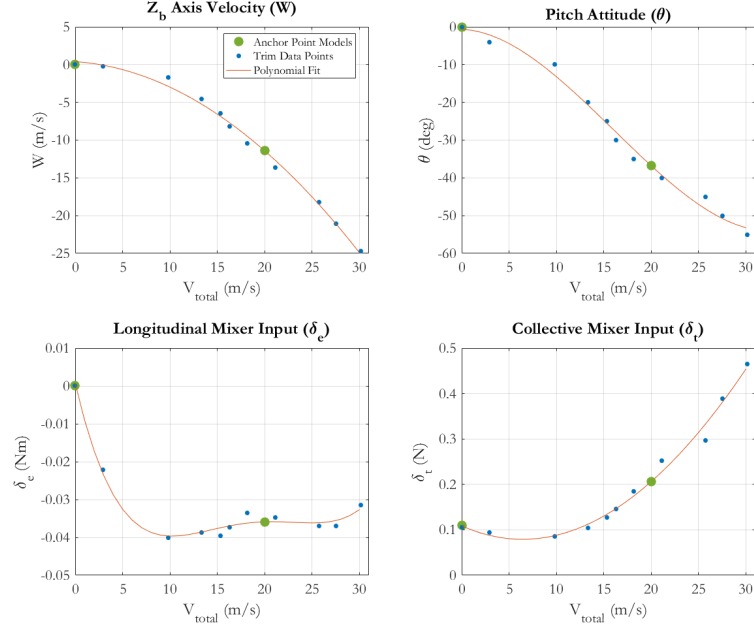


Figure 5.19 : Anchor point models and trim data obtained from the forward flight tests in trim conditions.

In the next section, trajectory tracking control system structure is given, controller parameters are optimized by using multi-objective optimization process and robustness analysis is performed.

5.5 Control System Design

Legacy ArduCopter control system has a nested-loop structure which contains attitude, velocity and position control loops. By using this legacy structure and controller parameters, it is possible to perform general purpose flights in which it is not critical to track a given reference signal precisely. However, it is not suitable for accurate trajectory tracking applications such as B-spline tracking missions. For this reason, the legacy structure is modified and controller parameters are optimized for the agile maneuvering quadrotor platform. At first, stability and performance of the legacy attitude controllers are evaluated by using the frequency domain analysis. These results are used to compare the legacy and optimized controller performances quantitatively. Then, inner and outer-loop controllers are optimized in Control Designer's Unified Interface (CONDUIT) software [2] by using selected handling qualities.

5.5.1 ArduCopter controller structure

ArduCopter controllers are used as legacy control systems which is developed based on nested-loop structure [100]. The innermost loop of the controller structure contains a PID controller which is utilized to control the body rates of the quadrotor. Output of the inner-loop rate controller is sent to the mixer to obtain the required PWM signal for the each BLDC motor. A proportional controller is used in the second loop to track the given attitude references. Also, a feed-forward element is used in this loop. The third loop of the ArduCopter position controller is in PID structure and designed to track given velocity reference signals in the NED frame. The outermost loop is designed based on a proportional control structure and utilized to track a given position reference. Block diagram of the ArduCopter position controller is shown in Figure 5.20.

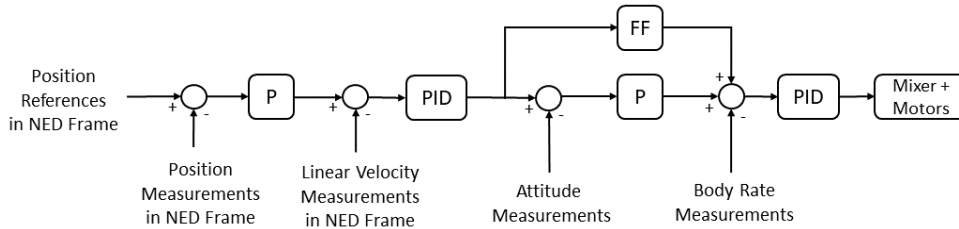


Figure 5.20 : Block diagram of the ArduCopter Position control system.

As shown in Figure 5.20, only the position reference signal can be applied into the legacy closed-loop system. It is not possible to track the given position and velocity references simultaneously. Hence, the position and velocity control loops of the legacy structure have to be modified. To simplify the overall design process, attitude control loop structure is kept same. However, it is important to evaluate the stability and performance of the legacy attitude controller as given in the following section.

5.5.2 ArduCopter inner-loop attitude controller performance Evaluation

Before improving the legacy controller performance or designing a new controller structure, it is important to obtain the broken-loop (BL), closed-loop (CL) and disturbance rejection (DR) performance of the baseline inner-loop attitude control system. This information provides a prior knowledge about the required improvement that should be performed by the control engineer. Hence, to determine the dynamical

Table 5.5 : Frequency sweep signal parameters for Arducopter performance evaluation tests.

Parameter	Broken-loop	Closed-loop	Disturbance Rejection
T_{sweep}	90 sec	90 sec	90 sec
ω_{min}	1 rad/s	1 rad/s	1 rad/s
ω_{max}	100 rad/s	90 rad/s	90 rad/s
T_s	400 Hz	400 Hz	400 Hz
Pitch Axis Test Signal Amp.	0.05 Nm	± 10 deg	± 15 deg
Roll Axis Test Signal Amp.	0.05 Nm	± 10 deg	± 15 deg
Yaw Axis Test Signal Amp.	0.1 Nm	± 20 deg/s	± 20 deg/s

characteristics of the ArduCopter, broken-loop, closed-loop and disturbance rejection flight tests are performed by using the legacy controller. The input-output pairs for these tests are given in Figure 5.21.

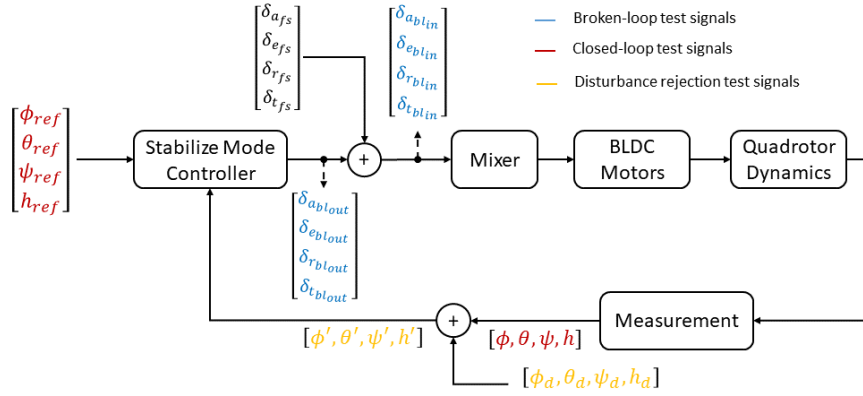


Figure 5.21 : Schematic of the closed-loop, broken-loop and disturbance rejection test input-output pairs.

where, subscripts '*ref*', '*bl*' and '*d*' refer to the reference, broken-loop and disturbance inputs, respectively. Frequency sweep flight test is designed to obtain the frequency response of BL, CL and DR dynamics. Sweep signal parameters are given in Table 5.5.

To evaluate the stability margins and crossover frequencies of the legacy attitude controllers, the broken-loop flight test data is used and the frequency responses of $\delta_{a_{blout}}/\delta_{a_{blin}}$, $\delta_{e_{blout}}/\delta_{e_{blin}}$ and $\delta_{r_{blout}}/\delta_{r_{blin}}$ input-output pairs are obtained in CIFER. In the turbulence flight conditions, the attitude control/attitude hold (ACAH) performance of the UAV has a crucial role to track the given reference signal. Hence, disturbance rejection bandwidth and disturbance rejection peak characteristics are analyzed by using the frequency responses of the ϕ'/ϕ_d , θ'/θ_d and ψ'/ψ_d input-output pairs in

the CIFER software. Another important reference signal tracking performance metric is the bandwidth of the closed-loop system. It is required to design an inner-loop system with adequate bandwidth to track given reference signal by the outer-loop, such as trajectory tracking system. Therefore, the closed-loop system performance of the legacy attitude controller is evaluated by using the frequency responses of ϕ/ϕ_c , θ/θ_c and ψ/ψ_c input-output pairs in the CIFER.

The frequency-domain stability and performance characteristics of the actual legacy controller is also used to verify the mathematical model of the closed-loop system (controller, sensor dynamics and bare-airframe) in CONDUIT environment. BL, CL and DR flight test results are given in Table 5.6. Handling quality analysis of the legacy roll attitude controller from CONDUIT is given in Figure 5.22.

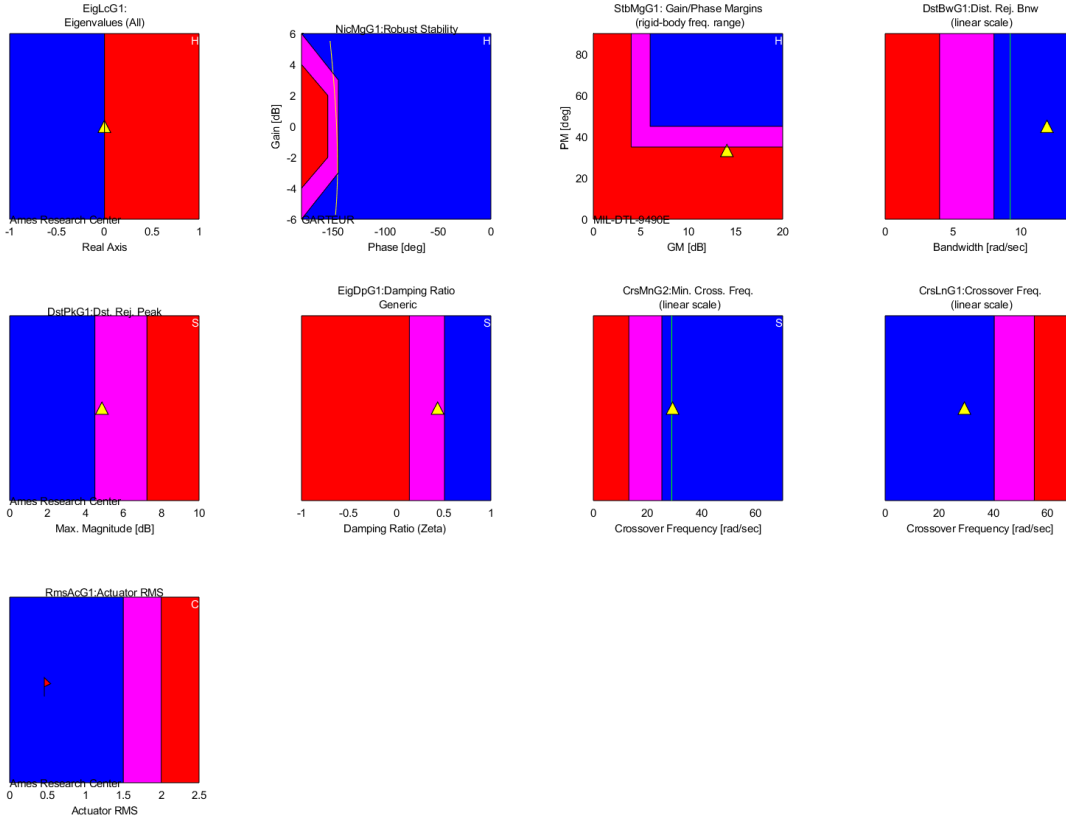


Figure 5.22 : Performance evaluation of ArduCopter roll attitude controller in CONDUIT for hover/low speed conditions.

As shown in the Table 5.6 and Figure 5.22, the legacy controllers have adequate crossover frequency and disturbance rejection bandwidth characteristics. However, they have low phase margin which results in low damping ratio of the closed-loop system. Also, the closed-loop system with legacy controller has Nichols Margin in Level-3 which indicates that the system is not robust against simultaneous changes in

Table 5.6 : Performance evaluation of the legacy control systems.

Axis		ω_c (rad/s)	PM (deg)	GM (dB)	-135 deg BW (rad/s)	-180 deg BW (rad/s)	DRB (rad/s)	DRP (dB)
Roll Attitude Controller	Flight Test	34.64	23	13.08 dB @ 5.53 rad/s	33.41	46	9.725	2.51
	CONDUIT	29.3	33.33	19.34 dB @ 7.42 rad/s	31.95	51.74	11.96	4.87
Pitch Attitude Controller	Flight Test	20.9	33.6	9.69 dB @ 5.40 rad/s	22.7	38.20	8.217	2.9
	CONDUIT	19.33	24.39	9.93 dB @ 9.49 rad/s	21.1	37.34	10.09	7.47

magnitude and phase. This situation reduces the stability of the system. In the fast forward flight tests, effect of the low stability margin characteristics of the attitude control loop is observed as low-damping oscillations in pitch and roll attitude of the quadrotor platform. This results insufficient trajectory tracking performance in the fast forward flight phase. Hence, it is required to improve the inner-loop reference tracking performance of the attitude control loop.

5.5.3 Dynamic scaling

In literature, there are several sources about handling quality requirements for manned aerial vehicles. For manned rotorcrafts and fixed-wing aircrafts, ADS-33E-PRF and MIL-STD-1797B provide a comprehensive set of handling and flying qualities. However, there is very limited information about the handling quality requirements for UAVs and MAVs. In recent years, researchers have focused on dynamic (Froude) scaling to scale down the Level-1 boundaries of the several handling quality requirements such as disturbance rejection bandwidth (DRB) and crossover frequency (ω_c). Scaling factor is calculated by using the rotor diameter (for full scale rotorcrafts) and the hub-to-hub distance (for multicopter platforms) of the aerial vehicles [1, 36].

In this study, XV-15 full-scale tilt-rotor aircraft is used to perform the Froude scaling analysis. Scaling factor N is calculated as the ratio of the rotor-to-rotor distance of the XV-15 (L_{xv15}) and the rotor-to-rotor diagonal distance of the technology demonstrator drone platform (L_{td}) as shown in equation 5.25.

$$N = \frac{L_{xv15}}{L_{td}} = \frac{17.374}{0.255} = 68.137 \quad (5.25)$$

By using the dynamical scale factor N , full-scale frequency requirements can be scaled down by using equation 5.26.

Table 5.7 : Froude scaling analysis of the agile maneuvering drone roll mode in hover flight.

Mode	XV-15	Scaled XV-15	Agile Drone	Difference (%)
$\lambda_{roll1,2}(rad/s)$	0.4668	3.8532	3.8785	0.6556
$\lambda_{roll3}(rad/s)$	0.6458	5.3308	4.0114	24.7501

$$\omega_{scaled} = \omega_{full-scale} \sqrt{N} \quad (5.26)$$

To evaluate the validity of the dynamical scaling, actual and scaled natural frequencies of the XV-15 roll mode poles are compared with the identified roll mode poles of the drone platform in Table 5.7. Here, it is shown that the difference between the natural frequencies of the scaled and identified roll axis hovering cubic poles are 0.6562% and 24.7501%, respectively. This indicates that the Froude scaling can be used to obtain the scaled handling quality requirements for the quadrotor platform.

5.5.4 Trajectory tracking control system design

A suitable control system structure is necessary to perform the trajectory tracking mission with a minimum error in velocity and position. The legacy ArduCopter position control system has a classical nested-loop structure as mentioned before. By using this structure, it is possible to track the given position reference signal. However, simultaneous tracking of the position and velocity commands, which is required for the trajectory tracking mission, is not possible with the legacy closed-loop system. Hence, a modification on the position control loop is performed and the position controller signal is used as a correction on the velocity reference signal. The general scheme of the trajectory tracking system is given in Figure 5.23.

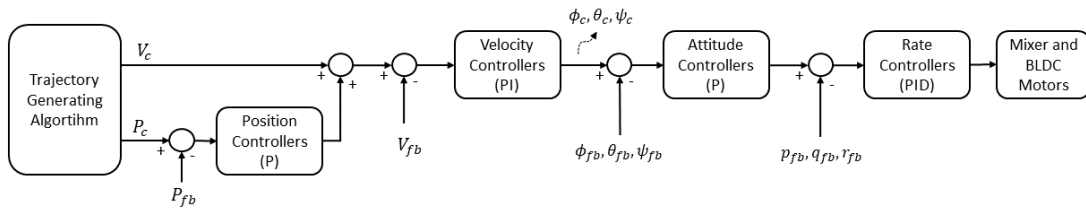


Figure 5.23 : Block diagram of the proposed trajectory tracking system.

As mentioned in the previous sections, ArduCopter is used as a legacy control system for the Racer quadrotor platform. System identification and model verification tests are performed by using the legacy controller because of the inherent unstable dynamics

of the quadrotor. Then, in Section 5.5.2, broken-loop, closed-loop and disturbance rejection characteristics are evaluated in frequency-domain. As a result of these analysis, it is shown that the legacy attitude controllers have low phase margin. Hence, it may not be possible to perform an accurate and agile trajectory tracking mission by using the legacy controllers. At this point, modifying the controller structure and optimizing its parameters become necessary to improve the reference tracking performance.

In this study, the legacy attitude controller structure (P+PID) is not changed to simplify the problem. CONDUIT is used to optimize the attitude control system parameters by using the selected stability and handling quality specifications given in Table 5.8. In CONDUIT, flight control system design problem is constrained by these selected specifications and Feasible Sequential Quadratic Programming (FSQP) solver is used to obtain the pareto-optimum solution with the minimum overdesign [2]. However, most of the design specifications, such as minimum crossover frequency and disturbance rejection bandwidth requirements, are not suitable for unmanned aerial vehicles. In the next two subsections, it is described how to modify the level-1 boundaries of these specifications according to bare-airframe dynamics and Froude scaling analysis to obtain suitable specifications for UAV and MAV platforms.

Minimum crossover frequency

One of the main characteristics of the feedback systems is its suppression ability against the variations in the system dynamics due to mass, airspeed and center of gravity location, etc. If the parameter variation has significant effects on the dynamical characteristics of the system, consistent response can be obtained by using high feedback gains. This increases the crossover frequency of the broken-loop system at the cost of increased actuator activity. Hence, it is important to select a minimum crossover boundary to avoid the overdesign. According to the guideline in [2], the minimum crossover frequency boundary should be selected at least 2 to 3 times greater than the natural frequency of the unstable modes of the bare-airframe as shown in equation 5.27.

$$\omega_c \geq (2 - 3)\omega_{unstable} \quad (5.27)$$

In the agile maneuvering quadrotor platform, identified unstable mode natural frequencies of the hovering cubics are 3.8785 rad/s for roll dynamics and 4.0881 rad/s for short-period dynamics. So, level-1 boundary of the minimum crossover frequency specification (CrsMnG2) of the attitude control loop is selected as 25 rad/s.

Velocity hold controller is wrapped around the attitude hold control system of the quadrotor platform. It generates the commanded pitch and roll attitude to track the given velocity reference signal. Here, it is important to minimize the dynamical interaction between the inner and outer loop. Only a small decrease in the stability margin of the inner loop is acceptable when the outer-loop is added into the nested-loop structure. For this purpose, crossover frequency of the velocity-hold control system is selected to provide frequency separation between the attitude control loop and velocity hold loop. According to the guidelines, crossover frequency of the outer loop is selected as 1/5 to 1/3 of the inner loop crossover frequency as shown in equation 5.28 [2].

$$\omega_{c_{vel}} = \left(\frac{1}{5} - \frac{1}{3} \right) \omega_{c_{att}} \quad (5.28)$$

In the proposed trajectory tracking structure, position controller is used as a correction loop instead of using as an outer-loop. Hence, bandwidth separation is not applied in the position correction loop and crossover frequency of the position controller is selected as 10 rad/s.

Disturbance rejection requirements

Disturbance rejection requirements consists of disturbance rejection bandwidth (DRB) and disturbance rejection peak (DRP) criteria which is used to evaluate the rejection capabilities of the aerial vehicle in a disturbed situation [2, 94]. In CONDUIT, DRB and DRP specifications are defined as DstBwG1 and DstPkG1, respectively. Although DRP specification can be used for the sub-scale aerial vehicle, DRB specification should be scaled-down by using the Froude scaling in equation 5.25. As a result, level-1 boundary of the attitude DRB specification is shifted to the 8.25 rad/s. Summary of the selected design specifications and Level-1 boundaries are given in Table 5.8. Here, H, S, J are used to define hard, soft constraints and summed objectives in the optimization problem, respectively.

Table 5.8 : Summary of the selected design specifications in control system design process.

Specifications	Nominal Level-1 Boundary	Roll and Pitch Attitude Controllers	Yaw Attitude Controller	Velocity Controller	Position Controller
EigLcG1 (H)	0	Unmodified	Unmodified	Unmodified	Unmodified
NcMgG1 (H)	-	Unmodified	Unmodified	Unmodified	Unmodified
StbMgG1 (H)	45 deg / 6 dB	Unmodified	Unmodified	Unmodified	Unmodified
DstBwG1 (S)	1 rad/s	8.25 rad/s	2 rad/s	1.61 rad/s	1.51 rad/s
DstPkG1 (S)	4.5 dB	Unmodified	Unmodified	Unmodified	Unmodified
EigDpG1 (S)	0.35	Unmodified	0.5	Unmodified	Unmodified
CrsMnG2 (S)	2 rad/s	25 rad/s	5 rad/s	5 rad/s	2.5 rad/s
CrsLnG1 (J)	10 rad/s	40 rad/s	10 rad/s	10 rad/s	10 rad/s
RmsAcG1 (J)	1.5	Unmodified	Unmodified	Unmodified	Unmodified

5.5.5 Robustness analysis of the attitude controllers

Robustness analysis is a crucial step for the control system design process to evaluate the system behavior in the presence of parametric uncertainties. So, it is important to calculate the uncertainty level of the system parameters. Each of the aerodynamic parameter identified in the system identification process has a Cramer-Rao (CR) bound which represents the uncertainty level of the related parameter as given in equation 5.29 [3].

$$(CR_i)_{cifer} \approx \sigma_i \quad (5.29)$$

where, σ_i is the standard deviation of the identified aerodynamic parameter of the aerial vehicle. This uncertainty value is used to evaluate the closed-loop system robustness against the parametric uncertainties in the mathematical model. $\pm 2CR \approx 2\sigma_i$ and $\pm 3CR \approx 3\sigma_i$ uncertainty levels in the state-space parameters account for 95.4% and 99.7% confidence interval in the mathematical model [3].

In CONDUIT, CR bounds of the identified parameters are imported from the CIFER and 100-runs Monte-Carlo simulation is performed for $3\sigma_i$ uncertainty level. Design margin in DRB and minimum crossover specifications are set as 30% to keep the closed-loop system in the Level-1 region in the presence of uncertainties. As a result of the robustness analysis, it is shown that the optimized attitude control systems have adequate robustness capability against $3\sigma_i$ parametric uncertainties. Robustness analysis results of the roll axis attitude controller is given in Figure 5.24. As shown

in Figure 5.24, most of the design point remain in level-1 region in the presence of uncertainty. In the worst cases, some of them shift slightly into the level-2 which is still acceptable. Similar results are obtained for the pitch and yaw attitude controllers.

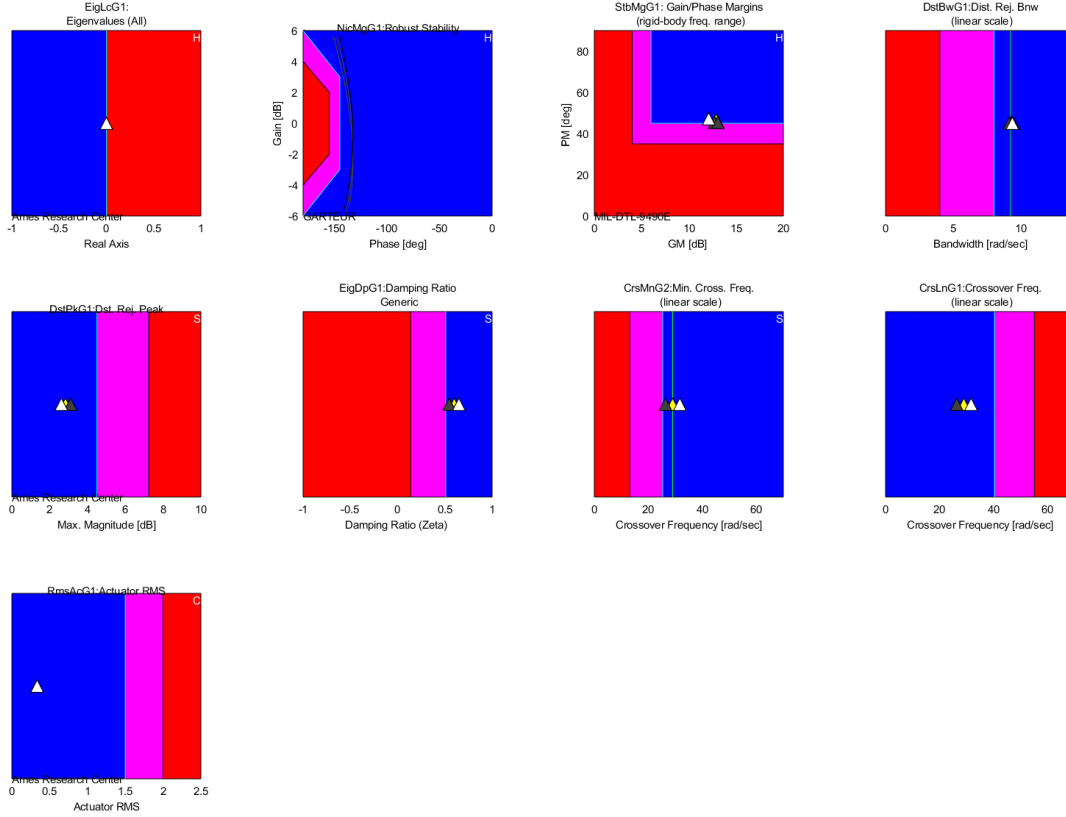


Figure 5.24 : 3σ robustness analysis of optimized roll attitude controller in CONDUIT for hover/low speed conditions.

In the next section, closed-loop system performance is evaluated in hover/low speed flight conditions by using scaled lateral reposition and longitudinal depart/abort mission task elements.

5.6 Simulation and Flight Test Results

Control system design and robustness analysis are followed by Monte-Carlo simulations and flight tests to evaluate and verify the closed-loop system performance. Required improvements could be defined and applied according to the obtained results. In ADS-33E-PRF, mission task elements (MTEs) are used to evaluate the system ability in good visual environments (GVE) and degraded visual environment (DVE). However, these MTEs are not suitable for the unmanned and micro aerial vehicles. So, they should be scaled down before applying to the unmanned systems.

In this section, kinematic scaling is applied to the lateral reposition and longitudinal depart/abort MTEs from ADS-33E-PRF. Then, hover and trajectory tracking and aggressiveness (TTA) analysis are performed on the technology demonstrator quadrotor platform to evaluate the proposed system performance.

5.6.1 Kinematic scaling

For the MTE scaling purpose, kinematic scaling is utilized successfully based on maximum forward flight speed of the aerial vehicles [1]. Maximum airspeed values of the agile maneuvering quadrotor and UH-60 are $V_{max_{uav}} = 32m/s$, $V_{max_{uh60}} = 82.31m/s$, respectively. Spatial (L_{scale}), velocity (V_{scale}) and time (t_{scale}) scale factors are given in equation 5.30, 5.31 and 5.32.

$$L_{scale} = \left(\frac{V_{max_{uav}}}{V_{max_{uh60}}} \right)^2 \quad (5.30)$$

$$V_{scale} = \alpha \frac{V_{max_{uav}}}{V_{max_{uh60}}} \quad (5.31)$$

$$t_{scale} = \alpha^{-1} \frac{V_{max_{uav}}}{V_{max_{uh60}}} \quad (5.32)$$

where, α is aggressiveness level which is selected as $\alpha = 1, 1.5, 2$ in this study. For more information about the MTE scaling, readers may refer to [1].

5.6.2 Position-hold performance evaluation in hover flight

One of the most critical missions for a rotary-wing aerial vehicle is position hold flight in which adequate disturbance rejection performance is necessary. Especially in the urban environment, it is crucial to hold the commanded position with the acceptable error and overshoot to minimize the crash risk in the airspace.

To evaluate the position hold performance of the legacy and optimized controllers, hover flight tests are performed on the quadrotor platform. In these tests, given reference velocity and position commands are set to zero to maintain the hover conditions. Wind velocity is about 2-3 m/s from North and light turbulence level is observed. Position of the quadrotor with the legacy and optimized controllers

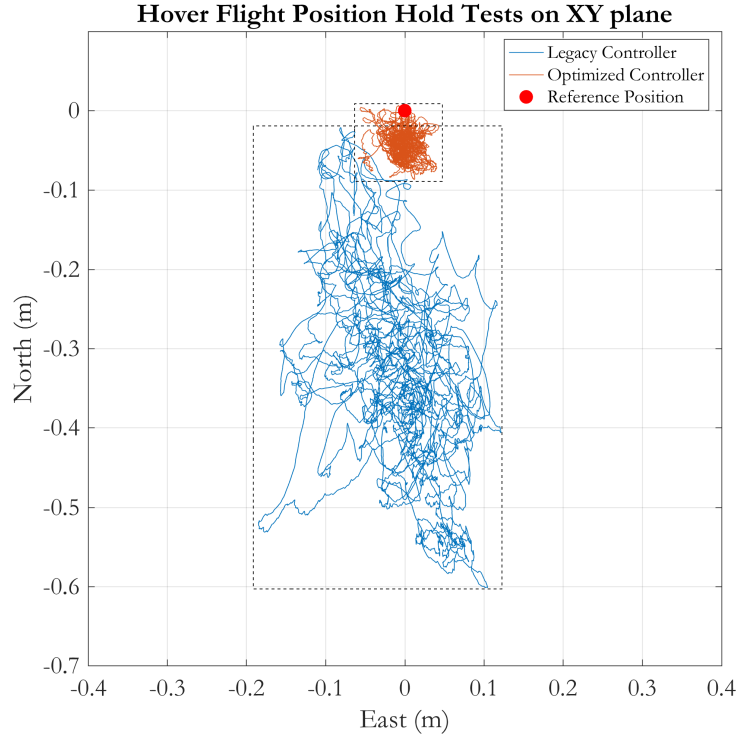


Figure 5.25 : Position-hold flight test results with the legacy and optimized controllers.

are compared in Figure 5.25. Velocity and position time histories of the legacy and optimized controllers in hover flight are given in Figure 5.26.

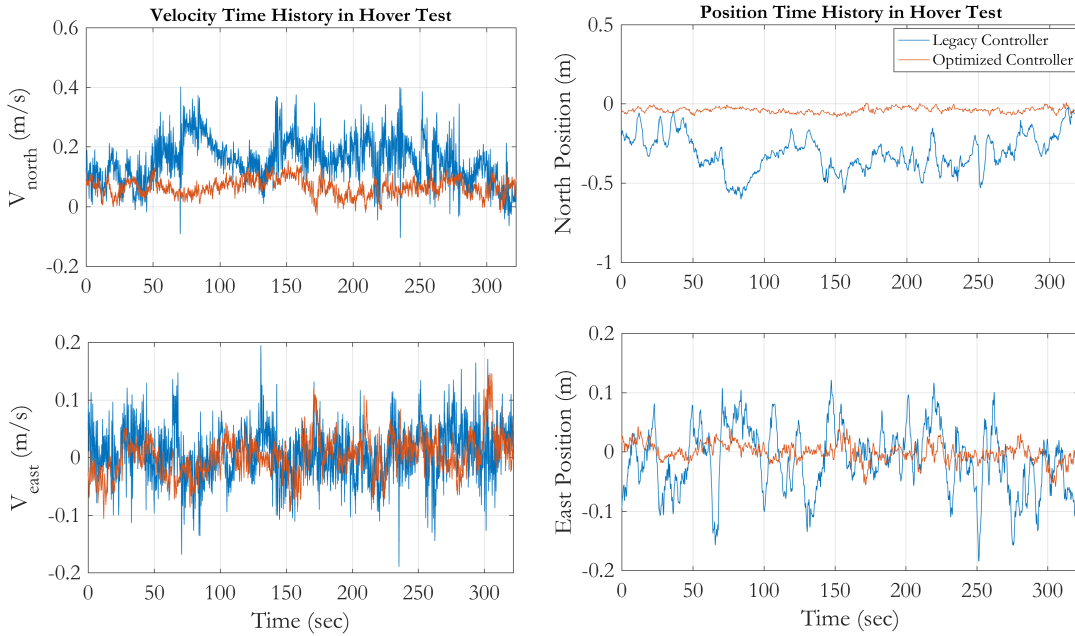


Figure 5.26 : Position and velocity time histories in hover flight test with the legacy and optimized controllers.

In these flight tests, position and velocity RMSE of the legacy and optimized controllers are given in Table 5.9. As shown from the hover flight test results,

Table 5.9 : Position and velocity RMSE for hover flight test.

Controller	Position RMSE (m)	Velocity RMSE (m/s)
Legacy	0.3364	0.1761
Optimized	0.0468	0.0791

the proposed controller has superior position-hold performance in the same wind conditions which is crucial for the urban environment missions.

5.6.3 Trajectory tracking and aggressiveness analysis

In ADS-33E-PRF, there are several moderate amplitude maneuvers to evaluate the agility of the full-scale rotorcrafts. However, direct usage of these maneuvers is not sufficient for the quadrotor platforms. Hence, in the previous subsection, kinematic scaling with three levels of aggressiveness ($a = 1, 1.5, 2$) is applied based on maximum airspeed of the quadrotor and UH-60 rotorcraft [1]. These maneuvers are performed in the stitched quasi-nonlinear model and flight tests. Velocity and position time histories are compared in Figure 5.27 and 5.28.

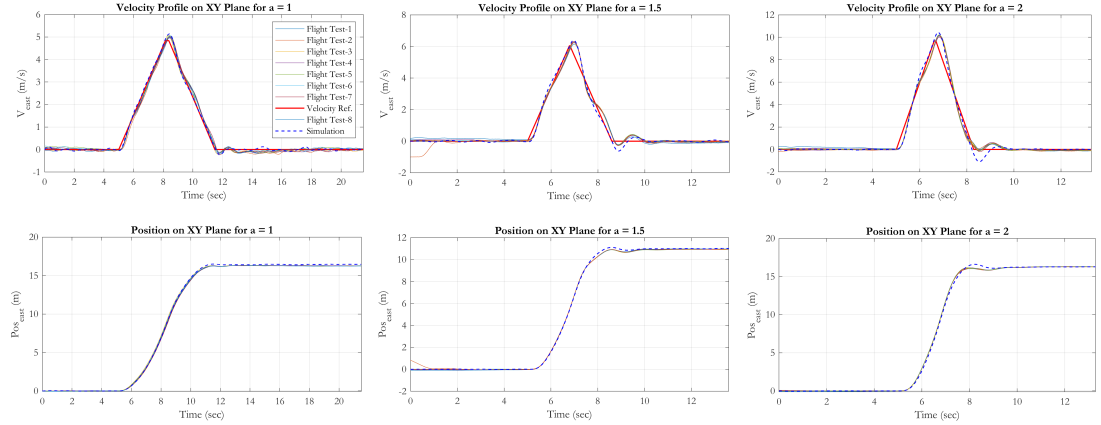


Figure 5.27 : Lateral reposition simulation and flight test results.

After performing several flight tests and simulations, TTA performance of the proposed closed-loop system should be evaluated quantitatively. Hence, it is required to define a cost function (L) and TTA performance score (ϕ_{TTA}) which includes aggressiveness level, velocity and position reference tracking RMSE [1].

$$L = w_a \frac{a - a_G}{a_B - a_G} + w_\epsilon \frac{\epsilon - \epsilon_G}{\epsilon_B - \epsilon_G} + w_R \frac{R - R_G}{R_B - R_G} \quad (5.33)$$

Here, a is aggressiveness level, ϵ is tracking error term for position and velocity and R is robustness of the closed-loop system which is a metric for the mission success.

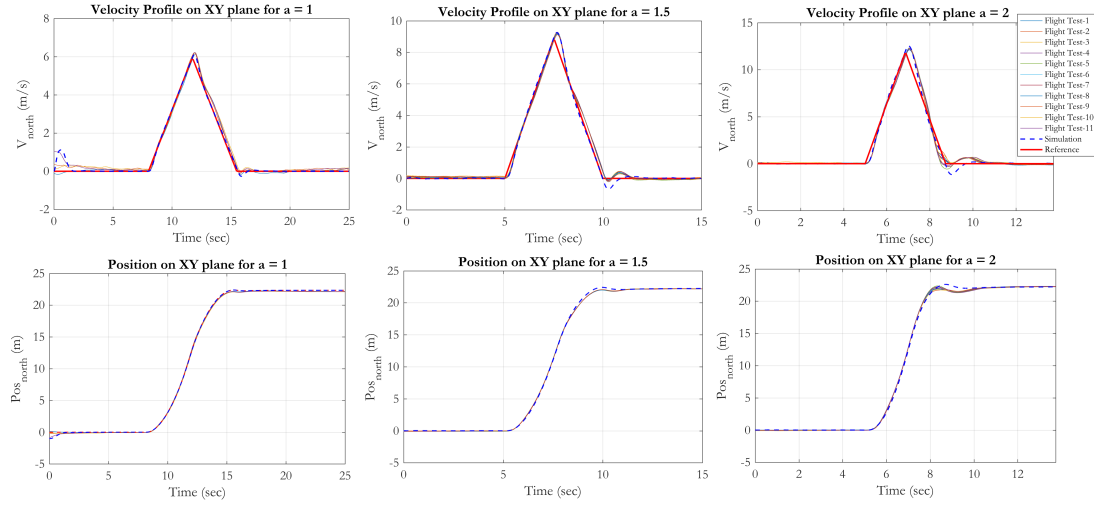


Figure 5.28 : Longitudinal depart/abort simulation and flight test results.

Subscripts ' G ' and ' B ' stand for the bad and good possible values for these metrics.

w_a, w_{ϵ}, w_R are used to define the weights of these metrics in the cost function.

The aggressiveness term a is calculated by using equation 5.34.

$$a = \frac{V_{max_{cmd}}}{V_{max_{nom}}} \quad (5.34)$$

where, $V_{max_{cmd}}$ is commanded maximum velocity and $V_{max_{nom}}$ is nominal speed of the rotorcraft which is $5.88m/s$ for the drone platform. Velocity and position tracking error term in the cost function is calculated by using equation 5.35.

$$\epsilon_1 = w_{vel} \frac{RMSE_{vel}}{V_{max_{cmd}}} + w_{pos} \frac{RMSE_{pos}}{L_{path}} \quad (5.35)$$

where, w_{vel}, w_{pos} are weights for the position and velocity tracking errors. In this definition, velocity and position RMSE are normalized by using the maximum commanded velocity and length of the commanded path L_{path} .

In the Monte-Carlo simulations and flight tests, all of the MTEs are completed successfully. Hence, as described in [1], robustness term is not used in the cost function. However, in future studies, concept of "mission success" will be defined and robustness term will be included in the TTA analysis.

In this study, the weights in the cost function are used as shown in Table 5.10.

After obtaining the cost function value, it is used in the TTA scoring step which is defined in equation 5.36. The value of the TTA score ϕ_{TTA} is in 0 – 100 interval.

Table 5.10 : Weights used in the TTA analysis.

Parameter	w_a	w_ε	w_R	a_G	a_B	ε_G	ε_B	w_{vel}	w_{pos}
Value	0.5	0.5	0	3	0	0	0.35	0.7	0.3

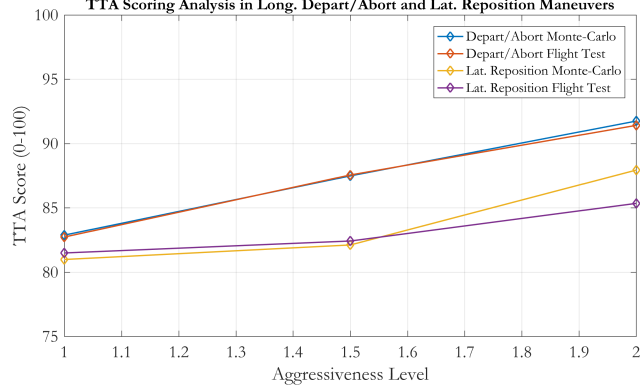


Figure 5.29 : TTA Scoring of the depart/abort and lateral reposition maneuvers with optimized controllers.

High TTA score means lower tracking error and higher aggressiveness; low TTA score means higher tracking error and lower aggressiveness.

$$\phi_{TTA} = \frac{200}{1 + e^L} \quad (5.36)$$

After several flight tests and Monte-Carlo simulations, TTA scores of the quadrotor platform are given in Figure 5.29.

Here, it is shown that the TTA scores for each aggressiveness level are above the recommended boundaries given in Table 5.11 [1]. Also, the optimized controller has similar TTA scores in Monte-Carlo simulation and flight tests which validates the simulation results.

The legacy controller parameters are not suitable for this type of trajectory tracking control system structure. Oscillatory responses are observed in flight tests in pitch and

Table 5.11 : TTA score guideline for scaled lateral reposition and depart/abort MTEs [1].

Maneuver	Desired TTA Score (Level-1)	Adequate TTA Score (Level-2)
Lateral Reposition	$\phi_{TTA} \geq 82$	$77 \leq \phi_{TTA} \geq 82$
Depart/Abort	$\phi_{TTA} \geq 82$	$77 \leq \phi_{TTA} \geq 82$

roll axes. Because of the safety considerations, TTA scoring analysis of the closed-loop system with the legacy controller is not performed.

6. IMPROVEMENT OF CRM-ADAPTIVE SYSTEM PERFORMANCE BY UTILIZING REINFORCEMENT LEARNING

Recent concepts such as urban air mobility or air cargo delivery rely heavily on technological advances in autonomy, intelligence and decentralized air traffic management solutions. As such, creating safe, sustainable, cost effective and high quality air transportation solutions are key for such urban airspace concepts. Specifically, at the air vehicle level, ability to perform precise tracking of designed trajectories or flight corridors is a crucial requirement for feasibility of such concepts. Aforementioned requirement becomes further complicated by real-life variations in properties such as mass, moment of inertia, aerodynamic properties, power system properties of the aerial vehicle due to the changes in a huge range of operating conditions and payload weights. Also, flight control systems should have a certain level of adaptation, fault tolerance and robustness to avoid catastrophic accidents in the presence of power system and/or actuation system anomalies. In this thesis, we present a new reinforcement learning based approach for closed-loop reference model adaptive flight control system design as to further enhance the adaptation transient response beyond the existing MRAC and classical CRM-adaptive systems. The proposed methodology uses reinforcement learning, through an actor-critic agent, to learn the time-varying adaptation policy using the tracking error observations from the environment.

From perspective of the control theory, uncertainties, faults, failures and changes in the mass and aerodynamic properties are the most challenging subjects that should be considered while designing a flight control system for an aerial vehicle. Adaptive control theory provides powerful solutions to handle these potentially catastrophic situations. In a general manner, two types of adaptive control structures are studied, i.e. indirect and direct adaptive control system. In indirect adaptive control systems, uncertain parameters in the system dynamics are identified and these are used to adjust the controller parameters. On the other hand, in direct adaptive control systems,

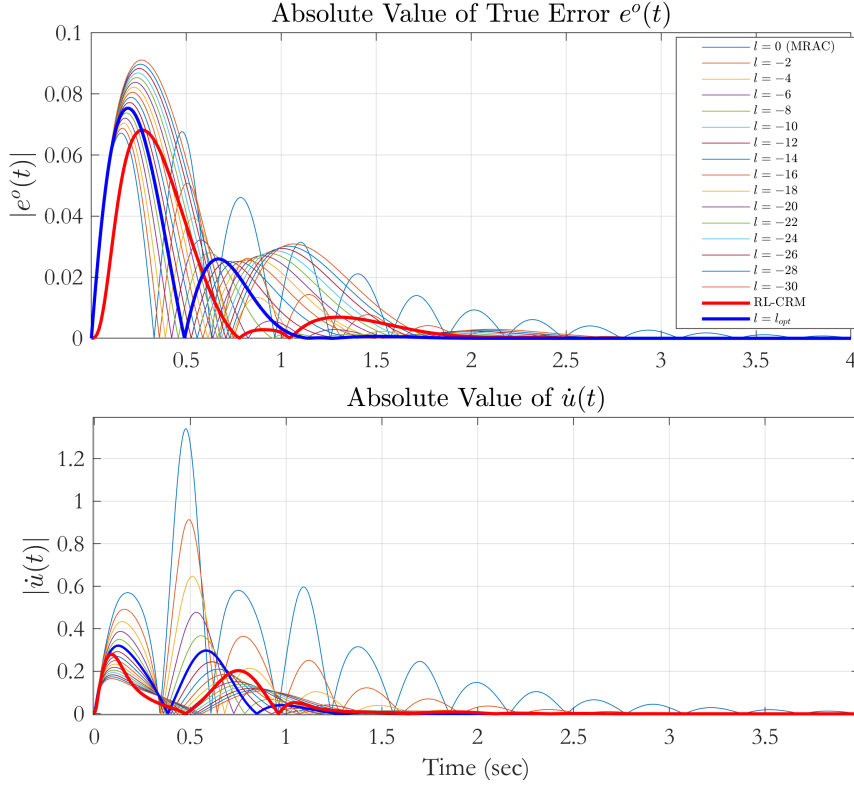


Figure 6.1 : Comparison of $|e^o(t)|$ and $|\dot{u}(t)|$ time history of the dynamic system with MRAC, CRM and RL-CRM.

parameter estimation is not performed and control system parameters are generated so that the tracking error converges to zero asymptotically [101, 102].

Model reference adaptive control (MRAC) algorithm is a classical method in adaptive control system theory in which learning rates are used to tune the system performance. While a higher value of the learning rate provides fast compensation of the uncertainties in the system dynamics, it also causes high frequency oscillation in the control signal. This situation may lead catastrophic accidents especially in aerial platforms as a result of system fault and failure [103].

Combined/composite model reference adaptive control (CMRAC) system is developed to handle with the high frequency oscillation in the transient response. In this algorithm, indirect and direct adaptive control techniques are used together and estimation error is used in adaptation law in addition to tracking error. Even though the stability of the CMRAC scheme is established in several studies, rigorous guarantees are not provided about the improved transients and it remains a conjecture [49, 50]. In addition to the combined/composite scheme, transient response of the MRAC is improved by using a closed-loop reference model instead of an open-loop one. This algorithm is called as CRM-adaptive system. Tracking error is also included in the

Table 6.1 : Comparison of performance metrics in the transient phase.

Performance Metrics	MRAC ($l = 0$)	CRM ($l = l_{opt}$)	RL-CRM
$\ \hat{\dot{k}}_q\ $	14.9183	3.6694	2.3723
$\ \hat{\dot{k}}_{q,cmd}\ $	18.1553	7.7114	5.4476
$\ \hat{\dot{\theta}}\ $	0.0873	0.0333	0.0204
$\ q_m\ _\infty$	0.2000	0.2058	0.2000
$\ e\ $	0.4539	0.1929	0.1361
$\ e^o\ $	0.4539	0.3831	0.3765
$\ \dot{u}\ $	6.4389	2.0465	1.3889

reference model and it provides an additional design freedom for tuning the control system. However, there is a trade-off between the improved transient response and convergence speed of the adaptive parameters. In the case of the slow adaptation, large tracking error is observed between the original reference model and system response. Also, a badly chosen CRM-adaptive system parameters may decrease the system performance and results in water-bed effect. Hence, an optimization process is critical to obtain a suitable observer gain in the reference model [51–53, 67].

Reinforcement learning (RL) is a class of machine learning methodologies which is developed in computer science community. RL algorithm includes an agent to interact with the environment and modify the action (i.e. control policy) based on received observations. In recent years, RL has an increasing demand in feedback control applications because of its direct relationship with optimal and adaptive control theories. The combination of these methods results in optimal adaptive controllers which converges to optimal solution in real-time by using observations from the environment [104, 105].

One of the key design parameter of the CRM-adaptive system is the observer gain used in the reference model. In classical CRM-adaptive system design, an optimal value is determined and used in the process. In this thesis, it is proposed to modify the observer gain as a time-varying parameter instead of a fixed one. Hence, a time-varying scaling factor is introduced in the observer gain to increase or decrease its magnitude according to the observations. By doing so, it is proposed to combine the fast convergence speed in MRAC and improved transient dynamics in CRM-adaptive system. The scaling factor is calculated by an actor-critic agent and trained by using deep deterministic policy gradient (DDPG) algorithm [69]. In training phase, the proposed agent uses

a reward function and observations to learn the policy for calculating the optimal scaling factor magnitude. By using the proposed algorithm, transient performance of the CRM-adaptive system is improved in terms of selected performance metrics such as L_2 and L_∞ signal norms and preliminary results are given in Table 6.1. In this table, it is obvious that the key signal norms are much lower in RL-CRM adaptive system than MRAC and CRM-adaptive systems which means that the proposed system provides improved transient response.

In addition, according to the preliminary analysis as given in Figure 6.1, the water-bed effect is suppressed in the proposed algorithm which is observed in time history of $|e^o(t)|$ and $|\dot{u}(t)|$ signals. It is important to note that peak magnitude of the $|\dot{u}(t)|$ is kept small while minimizing $|e^o(t)|$.

From the robustness point of view, it is important to compensate the variations and uncertainties in the system parameters especially in the transient phase, i.e. at the beginning of the adaptation parameter estimation process. The proposed RL-CRM algorithm is shown to compensate the potential parameter variations, uncertainties and undesired transients in the dynamical system. In addition, we have demonstrated through Monte-Carlo analysis that the RL-CRM provides a high level of robustness to parametric uncertainties of the aerial vehicle.

The remaining of this chapter is organized as follows; in Section 6.1, basic definitions about the transient response metrics and mathematical model are given. Section 6.2 investigates background for MRAC and CRM-adaptive systems and introduces the proposed RL-CRM adaptive system structure. In Section 6.3, simulation results are evaluated and system performances are compared in the presence of parametric uncertainties.

6.1 Background and Problem Definition

In this section, general definitions of scalar linear mathematical model structure and aerodynamic parameters of a transport helicopter are presented. Here, it is important to note that simplified scalar linear model is just an approximation and used to illustrate the proposed RL-CRM concept.

Mathematical model of a linear scalar plant is given in equation 6.1.

$$\dot{x}(t) = ax(t) + b(u(t) + f(x)) \quad (6.1)$$

where, $x(t)$ and $u(t)$ represent system state and control input signal, respectively. a and b are unknown constant system parameters. Here, it is assumed that the sign of b is known to provide controllability. System uncertainty is represented by a function $f(x)$ which is given in equation 6.2. It contains N known basis functions $(\phi_i(x))$ and unknown constants (θ_i) .

$$f(x) = \sum_{i=1}^N \theta_i \phi_i(x) = \theta^T \Phi(x) \quad (6.2)$$

where, $\Phi(x) \in R^N$ represents the regressor vector which contains Lipschitz-continuous components $\phi(x)$ [106].

6.1.1 Helicopter pitch dynamics in hover

Pitch dynamics of a helicopter in hover flight primarily depends on pitch rate (q) and longitudinal control input (δ_e). We assume that forward and vertical speed components of the helicopter are very small in hover flight phase. Hence, speed derivatives such as M_u and X_u are neglected to simplify the mathematical model. In this manner, pitch dynamics of the helicopter can be modeled as a scalar system which is given in equation 6.3.

$$\dot{q} = M_q q + M_{\delta_e}(\delta_e + f(q)) \quad (6.3)$$

where M_q is pitch damping derivative and M_{δ_e} is elevator effectiveness (i.e. longitudinal control power). Pitch dynamics also includes $f(q)$ (given in equation 6.4) which represents the system uncertainties as a function of pitch rate and introduces instability into the open-loop dynamics.

$$f(q) = -0.01 \tanh\left(\frac{360}{\pi} q\right) = \theta \Phi(q) \quad (6.4)$$

For a transport class helicopter, aerodynamic parameters are given as $M_q = -0.61(rad/s)$ and $M_{\delta_e} = -6.65(rad/s^2)$ [106].

6.2 Adaptive Control System Design

In this section, basics of the MRAC and CRM-adaptive systems are reviewed. Selected performance metrics are presented which are used to perform a quantitative comparison of the adaptive system performance in the transient phase. Then, proposed RL-CRM adaptive control structure is introduced and hyperparameters of the actor-critic agent are given.

6.2.1 Model reference adaptive control system design

In this subsection, model reference adaptive control system is designed to deal with the system uncertainties. First-order open-loop reference model is used in this structure as given in equation 6.5.

$$\dot{x}_m^o(t) = a_m x_m^o(t) + b_m r(t) \quad (6.5)$$

where $a_m < 0$ and b_m are reference system parameters, $x_m^o(t)$ is open-loop reference model state and $r(t)$ is command signal for the reference model.

The main goal of the MRAC system is to track the reference model state $x_m^o(t)$ asymptotically. Hence, control signal should be designed such that true state tracking error, given in equation 6.6, tends to zero as time goes to infinity.

$$e^o(t) = x(t) - x_m^o(t) \quad (6.6)$$

The control signal is generated in the form of feedback + feedforward architecture to handle with the system uncertainties as given in equation 6.7.

$$\delta_e(t) = \hat{k}_x x + \hat{k}_r r - \hat{\theta}^T \Phi(x) \quad (6.7)$$

where \hat{k}_x, \hat{k}_r and $\hat{\theta}$ are estimated feedback and feedforward gains and parameter vector. These estimations is performed to achieve global, uniform and asymptotic tracking of the reference model states.

As a result of the Lyapunov Theory, estimation of the adaptation parameters are obtained as given in equation 6.8 to enforce the closed-loop stability [106].

$$\begin{aligned}
\dot{\hat{k}}_x(t) &= -\gamma_x x(t) e^o(t) \operatorname{sgn}(b) \\
\dot{\hat{k}}_r(t) &= -\gamma_r r(t) e^o(t) \operatorname{sgn}(b) \\
\dot{\hat{\theta}}(t) &= \Gamma_\theta \Phi(x(t)) e^o(t) \operatorname{sgn}(b)
\end{aligned} \tag{6.8}$$

where, γ_x, γ_r and Γ_θ are learning rates which are selected as $\gamma_x = 200$, $\gamma_r = 200$ and $\Gamma_\theta = 0.2$.

6.2.2 CRM-adaptive control system

Unlike the MRAC structure, a closed-loop reference model is used in the CRM-adaptive system as shown in equation 6.9.

$$\dot{x}_m(t) = a_m x_m(t) + b_m r(t) - l(x(t) - x_m(t)) \tag{6.9}$$

where, a_m, b_m are reference model parameters, $x_m(t)$ is reference model state, $r(t)$ is bounded reference command signal. Also, a_m and l should be negative to obtain stable reference model and error dynamics [67].

The control law for CRM-adaptive system is the same as the MRAC which is given in (6.7). However, in parameter update laws of the CRM-adaptive system, given in equation 6.10, closed-loop reference model tracking error ($e(t)$) is used instead of the true error ($e^o(t)$).

$$\begin{aligned}
\dot{\hat{k}}_x(t) &= -\gamma_x x(t) e(t) \operatorname{sgn}(b) \\
\dot{\hat{k}}_r(t) &= -\gamma_r r(t) e(t) \operatorname{sgn}(b) \\
\dot{\hat{\theta}}(t) &= \Gamma_\theta \Phi(x(t)) e(t) \operatorname{sgn}(b)
\end{aligned} \tag{6.10}$$

In this case, the same learning rate values are used as given in the MRAC adaptation law. The closed-loop reference model tracking error is given in equation 6.11 and defined as the error between the closed-loop reference model states and actual system states.

$$e(t) = x(t) - x_m(t) \tag{6.11}$$

For detailed information about the stability properties of the CRM-adaptive systems, readers may refer to [51–53, 67, 106].

6.2.3 Transient response characteristics

Improvement of the transient response performance is the main contribution of the CRM-adaptive system. It suppresses high frequency oscillation in adaptive parameters, control signal and system responses in the transient phase. Hence, it is important to define the performance metrics for the transient response to evaluate the system performance.

In [52, 67], several performance metrics are introduced such as $\|e(t)\|$, $\|e^o(t)\|$, $\|\dot{\theta}(t)\|$, $\|\dot{u}(t)\|$ and $\|x_m(t)\|_\infty$ to characterize the transient response. Here, $e^o(t)$ is true error which is defined as the error between the system response and open-loop reference model as shown in equation 6.6.

In this study, these metrics are used to characterize the transient response performance to obtain optimal observer gain for the CRM-adaptive system. Also, quantitative evaluation of the transient response performances of MRAC, CRM and RL-CRM adaptive systems are performed based on these metrics.

6.2.3.1 Water-bed effect

As mentioned before, CRM-adaptive system introduces a trade-off between fast convergence in tracking error $e(t)$ with reduced L_2 norm of $\dot{\theta}(t)$ and true error $e^o(t)$. An optimal choice of adaptation rates and observer gain directly effects the system performance in terms of $e^o(t)$ and $\dot{u}(t)$. This is called as the water-bed effect and it should be considered to avoid transient response performance degradation. In this study, we assumed that selected adaptation rates are in their optimal values and they are fixed. We tried to find the optimal value of the observer gain (l) by using the key signal norms in an optimization process. For more information about the water-bed effect, readers may refer to [51].

6.2.3.2 Optimal design of observer gain (l) in CRM

CRM-adaptive system has superior transient performance when compared to the ORM-adaptive one. Especially, this is observed in the L_2 norm of

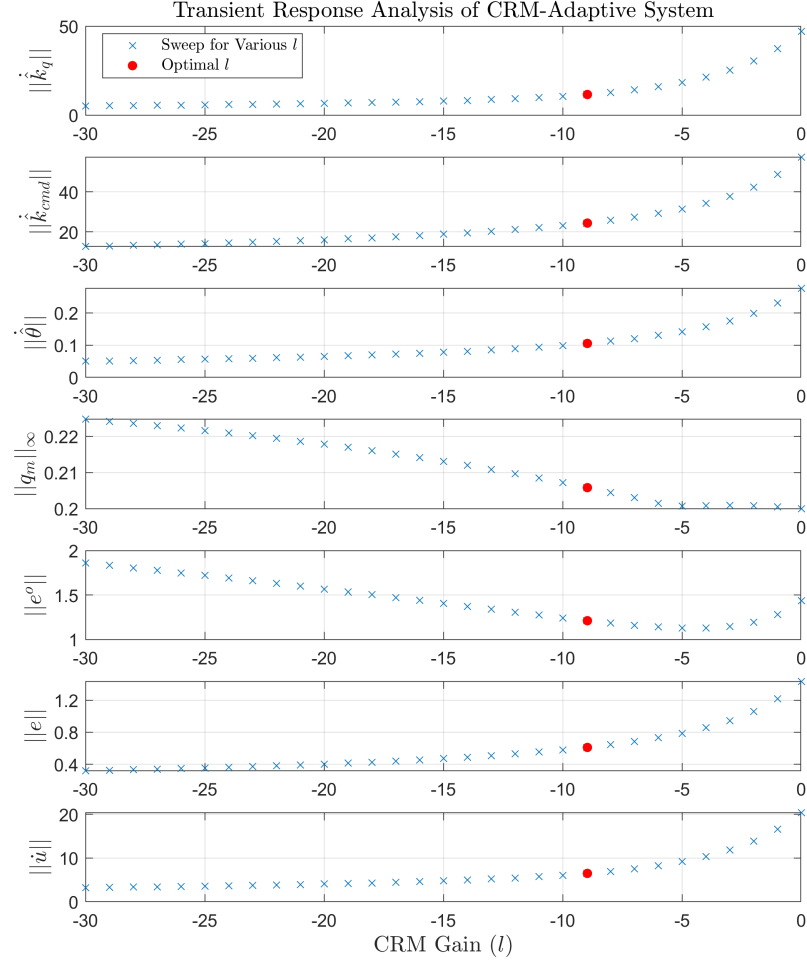


Figure 6.2 : Transient response analysis for CRM-adaptive system.

$\hat{k}_q(t)$, $\hat{k}_{cmd}(t)$, $\hat{\theta}(t)$, $e(t)$ and $\dot{u}(t)$. However, larger values of l increases L_∞ norm of $q_m(t)$ and L_2 norm of $e^o(t)$. Hence, there is a trade-off between damped oscillations and true error magnitude. To visualize this trade-off, a sweep analysis is performed for $l \in [-30, 0]$ interval and results are given in Figure 6.2. It is shown that as l decreases, most of the key signal norms decrease except $\|e^o\|$ and $\|q_m\|_\infty$. It means that as l decreases, transient oscillations are damped at the cost of increased true error and peak magnitude in the system response. Hence, an optimization problem is formulated to obtain optimal value of l by using a cost function $J(e^o, \hat{k}_q, \hat{k}_{cmd}, \hat{\theta}, \dot{u}, q_m)$ which is shown in equation 6.12.

$$J = \|e^o(t)\| + \|\hat{k}_q(t)\|/100 + \|\hat{k}_{cmd}(t)\|/100 + \|\hat{\theta}(t)\| + \|\dot{u}(t)\|/40 + \|q_m(t)\|_\infty \quad (6.12)$$

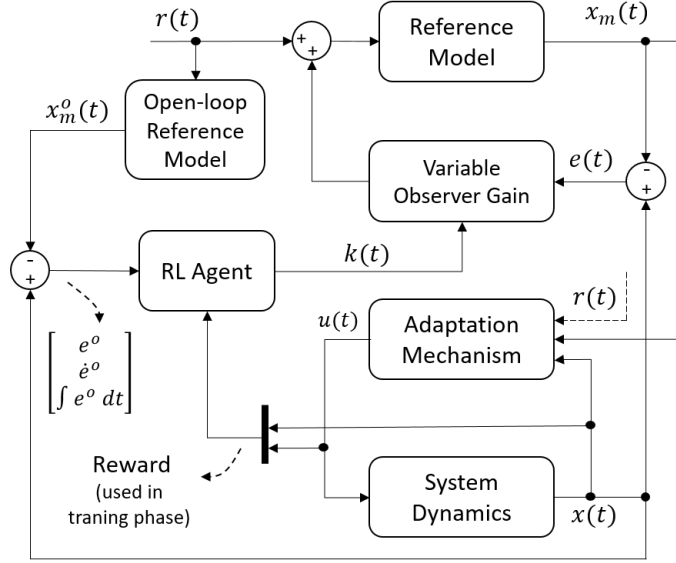


Figure 6.3 : General structure of the CRM-RL.

As a result of the optimization process, optimal observer gain is determined as $l_{opt} = -8.9648$ and it is shown in Figure 6.2.

6.2.4 RL-CRM adaptive system

As mentioned before, CRM-adaptive controllers improve the transient performance of the closed-loop system. An optimal value of the observer gain l damps high frequency oscillations in the adaptive parameters, control signal and system response in the transient phase at the cost of increased true error and peak response magnitude.

In this section, we introduce a novel CRM-adaptive system in which a variable observer gain is used to suppress high the frequency oscillations in the key signals and minimize the true error. In other words, it is aimed to combine the MRAC and CRM-adaptive algorithms by changing the observer gain.

The proposed algorithm, called as RL-CRM adaptive system, is quite similar to the classical CRM-adaptive system except its time-varying observer gain in the reference model. Variable observer gain provides flexibility in the closed-loop system and changes its dynamics according to the observed true error. At the beginning of the transient response phase, if high frequency oscillation occurs in true error $e^o(t)$, the observer gain is increased by the agent and oscillation is damped. When the oscillation in the adaptive parameters and system response disappears, the observer gain value is decreased and the control system behaves like classical model reference

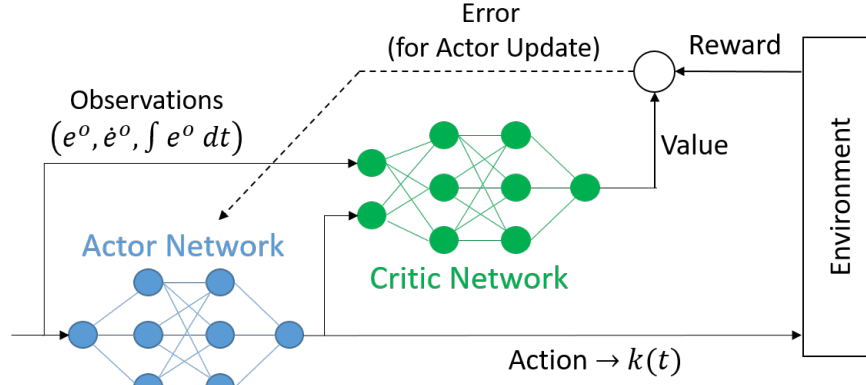


Figure 6.4 : Actor-Critic agent structure.

adaptive controller. This adaptation in the observer gain provides both fast convergence of the adaptive control parameters (as in the MRAC) and better transient response performance (as in the CRM-adaptive system).

Mathematical description of the proposed closed-loop reference model is given in equation 6.13. Here, l_{opt} is optimized observer gain and $k(t)$ is variable scaling factor determined by the RL agent.

$$\dot{x}_m(t) = a_m x_m(t) + b_m r(t) + l_{opt} k(t) e(t) \quad (6.13)$$

General structure of the proposed RL-CRM adaptive system is given in Figure 6.3. RL agent is generated based on actor-critic structure and training is preformed by using Deep Deterministic Policy Gradient (DDPG) algorithm [69].

In the actor-critic agent structure, actor component generates and action (i.e. control policy) and applies it into the system. Then, critic component compares the estimated and actual value of that action and quantifies the action optimality [105]. General structure of the actor-critic agent is given in Figure 6.4.

Hyperparameters of the actor-critic structure of the RL agent are given in Table 6.2. Training parameters of DDPG algorithm is given in Table 6.3.

In the training phase, the actor-critic agent should be trained by using a reward function which provides a metric of the system performance. The agent learns the required action that should be applied to the system to increase the reward. In this study, we used a reward function as given in equation 6.14. Here, $R_e, R_u, R_{e_{cmd}}$ are designed to bound the related signals below the specified value.

Table 6.2 : Hyperparameters of Actor-Critic agent.

Network	Parameter	Value
Actor	Number of Layers	5
	Learning Rate	0.001
	Gradient Threshold	1
Critic	Number of Hidden Layers	9
	Learning Rate	0.002
	Gradient Threshold	1

Table 6.3 : Training parameters for DDPG algorithm.

Parameter	Value
Sample Time	0.005
Target Smooth Factor	0.001
Discount Factor	0.99
Mini-Batch Size	1024
Buffer Length	1E6

$$R = R_e + R_u + R_{e_{cmd}} \quad (6.14)$$

where, R_e, R_u and $R_{e_{cmd}}$ are defined in equations 6.15, 6.16 and 6.17.

$$R_e = \begin{cases} 2, & \text{if } |e(t)| \leq 0.02 \\ 0, & \text{otherwise} \end{cases} \quad (6.15)$$

$$R_u = \begin{cases} 2, & \text{if } |\dot{u}(t)| \leq 0.3 \\ 0, & \text{otherwise} \end{cases} \quad (6.16)$$

$$R_{e_{cmd}} = \begin{cases} 2, & \text{if } |e_{cmd}(t)| \leq 0.01 \text{ and } t \geq 1.1 \text{ sec} \\ 0, & \text{otherwise} \end{cases} \quad (6.17)$$

where, R_e, R_u are used to bound the tracking error and time derivative of the control signal. $R_{e_{cmd}}$ is used to specify the settling time bound for the step response.

Observations are another input for the actor-critic agent in both training and simulation phases. In this study, observations are selected based on the true error which is the difference between the actual system and open-loop reference model responses. Observation vector \mathbf{O} is given in equation 6.18.

$$\mathbf{O} = \left[e^o(t), \dot{e}^o(t), \int e^o(t) dt \right]^T \quad (6.18)$$

To avoid the high frequency action signal ($k(t)$), a low-pass filter (LPF) is used with $\tau = 0.2 \text{ sec}$ on output path of the actor-critic agent. This LPF protects the system from high-frequency scaling factor variation which may decrease the system safety.

6.3 Simulation Results

In this section, the proposed RL-CRM adaptive system performance is compared with MRAC and fixed-gain CRM-adaptive systems. Simulations are performed on simplified pitch dynamics of a transport class helicopter which is given in Section 6.1.1. Transient response characteristics of the closed-loop systems are evaluated for pitch rate step command in $[0 - 4]$ seconds time interval.

In Figure 6.5, step responses of the MRAC, CRM and RL-CRM adaptive systems are given. In MRAC case ($l = 0$), the high frequency oscillation in the transient phase is observed which is the fundamental problem in MRAC. CRM-adaptive system is evaluated for different feedback gains in $l = [-30, -2]$ interval to observe its effect on the transient response performance. In cases with lower feedback gain, faster system response is obtained at the cost of increased oscillation. On the other hand, in cases with higher feedback gain, oscillation in the system response is damped at the cost of higher rise time and peak magnitude. Hence, an optimal observer gain l_{opt} is required and it is obtained as a result of optimization process as mentioned in Section 6.2.3. System response with the optimal observer gain is given in Figure 6.5. It is shown that the response of the CRM-adaptive system with optimal observer gain is more acceptable than the MRAC in terms of the transient dynamics.

The proposed RL-CRM adaptive system response is also given in Figure 6.5. Even though a little bit higher rise time and settling time, it has better performance than the CRM-adaptive system in damping the peak response. Time history of the variable scaling factor k is given in Figure 6.6.

As mentioned in Section 6.2.3, water-bed effect is an important phenomenon for CRM-adaptive systems due to the trade-off between fast convergence in $e(t)$ and increased $e^o(t)$. Also, a badly chosen learning rate and observer gain parameters can cause a degradation of the adaptive system performance in terms of $|e^o(t)|$ and $|\dot{u}(t)|$ [52]. In Figure 6.1, water-bed effect on MRAC, CRM and RL-CRM are compared.

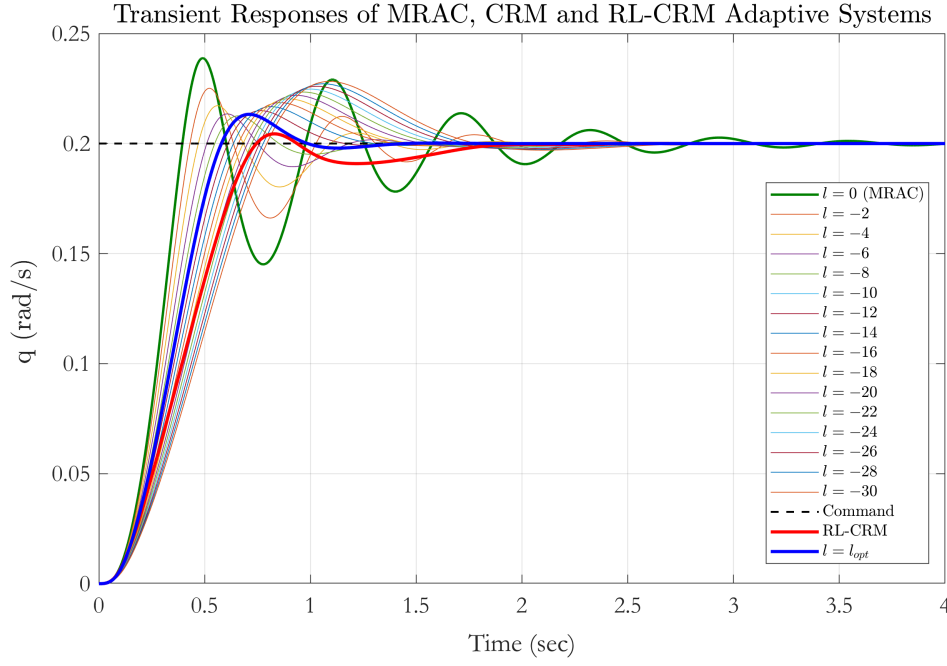


Figure 6.5 : Transient Response of the dynamic system with MRAC, CRM and RL-CRM.

Here, it is shown that RL-CRM adaptive controller provides fast convergence to zero with low magnitude peak in $|e^o(t)|$ and $|\dot{u}(t)|$.

To perform a quantitative comparison of transient response performance, L_2 and L_∞ norms of several key parameters are calculated for MRAC, CRM and RL-CRM adaptive systems and results are compared in Table 6.1. Here, it is shown that RL-CRM has better performance than CRM-adaptive system with optimal observer gain in terms of selected transient performance metrics. Also, it is important to note that by using the RL-CRM algorithm, it is possible to decrease both L_2 norm of time derivative of

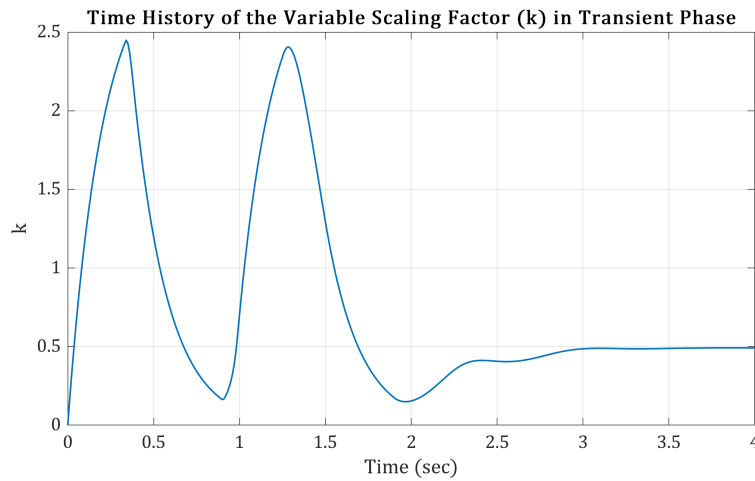


Figure 6.6 : Time history of the agent response (scaling factor, k) in the transient phase.

adaptation parameters $(\dot{\hat{k}}_q, \dot{\hat{k}}_{q_{cmd}}, \dot{\hat{\theta}})$ and true error (e^o), simultaneously. This result implies that system response with RL-CRM adaptive controller is closer to the original model response while the transient oscillations are damped. This is the main trade-off in the CRM-adaptive control theory and we have optimized this trade-off in real-time by using variable observer gain in RL-CRM-adaptive controller.

6.3.1 Uncertainty analysis

In this subsection, uncertainty analysis is performed for MRAC, CRM and RL-CRM adaptive systems. Parameter uncertainty with a $\pm 35\%$ level of nominal value is applied on the M_q and M_{δ_e} aerodynamics derivatives. Mathematical descriptions of the inserted uncertainty are given in equation 6.19.

$$\begin{aligned} M'_q &= M_q + \Delta M_q \\ M'_{\delta_e} &= M_{\delta_e} + \Delta M_{\delta_e} \end{aligned} \tag{6.19}$$

where, M'_q, M'_{δ_e} represent the aerodynamics parameter with uncertainty and $\Delta M_q, \Delta M_{\delta_e}$ represent the added uncertainty.

500-run Monte-Carlo analysis is performed for each controller and system performances are compared in terms of the mean of L_2 and L_∞ norms of the key signals given in the previous section. The result of the Monte-Carlo analysis is given in Table 6.4. Improvement percentage of the CRM and RL-CRM adaptive systems are calculated by comparing the signal norms of the MRAC. Here, $(-)$ shows mean of the 500-run simulation results. As seen from the table, the proposed RL-CRM adaptive system has higher improvement percentage when compared to the CRM-adaptive system even in the presence of parametric uncertainties.

In addition to the Monte-Carlo analysis, the worst case scenario is evaluated with -35% parametric uncertainties on both M_q and M_{δ_e} . $|e^o(t)|$ and $|\dot{u}(t)|$ responses of the CRM and RL-CRM systems are given in Figure 6.7 for this case. In this figure, it is shown that the proposed RL-CRM adaptive system has better performance than the CRM-adaptive system even in the worst case scenario with -35% parametric uncertainty. However, for -35% level of uncertainty, oscillation is observed on $|\dot{u}(t)|$ response which increases L_2 norm of the signal which is an undesirable

Table 6.4 : 500-Run Monte-Carlo analysis results of the MRAC, CRM and RL-CRM adaptive systems.

Performance Metrics	MRAC ($l = 0$)	CRM ($l = l_{opt}$)	Improvement (%)	RL-CRM	Improvement (%)
$\ \hat{\dot{k}}_q\ $	15.2114	3.7341	75.4520	2.4489	83.9008
$\ \hat{\dot{k}}_{qcmd}\ $	18.4647	7.8298	57.5958	5.5146	70.1344
$\ \hat{\dot{\theta}}\ $	0.0888	0.0338	61.9369	0.0207	76.6892
$\ q_m\ _\infty$	0.2	0.2064	-3.2	0.2	-
$\ e\ $	0.4616	0.1957	57.6039	0.1379	70.1256
$\ e^o\ $	0.4616	0.3928	14.9047	0.3886	15.8145
$\ \dot{u}\ $	6.5704	2.0811	68.3262	1.4163	78.4290

Table 6.5 : Robustness analysis results of the MRAC, CRM and RL-CRM adaptive systems in the worst case scenario.

Performance Metrics	MRAC ($l = 0$)	CRM ($l = l_{opt}$)	Improvement (%)	RL-CRM	Improvement (%)
$\ \hat{\dot{k}}_q\ $	19.7655	4.9225	75.0955	3.4801	82.3931
$\ \hat{\dot{k}}_{qcmd}\ $	22.9284	9.4137	58.9431	6.4318	71.9483
$\ \hat{\dot{\theta}}\ $	0.1103	0.0407	63.1010	0.0246	77.6972
$\ q_m\ _\infty$	0.2	0.2171	-8.5500	0.2005	-0.2500
$\ e\ $	0.5732	0.2353	58.9498	0.1608	71.9470
$\ e^o\ $	0.5732	0.5101	11.0084	0.5214	9.0370
$\ \dot{u}\ $	8.5403	2.6274	69.2353	1.8001	78.9223

situation. Beyond this uncertainty level, system performance decreases and additional precautions should be considered.

Step responses of the CRM and RL-CRM adaptive systems are compared in Figure 6.8 for the worst case scenario. In this figure, it is shown that the proposed RL-CRM system has lower peak response than the CRM-adaptive system in the worst case scenario. Also, difference between the peak responses in the nominal case and the worst case is much lower in the RL-CRM system than the difference in the CRM.

Robustness analysis of the MRAC, CRM and RL-CRM adaptive systems in the worst case scenario is performed and results are given in Table 6.5. Here, it is observed that the proposed RL-CRM adaptive system provides almost same level of improvements on the key signal norms when compared to the Monte-Carlo analysis given in Table 6.4.

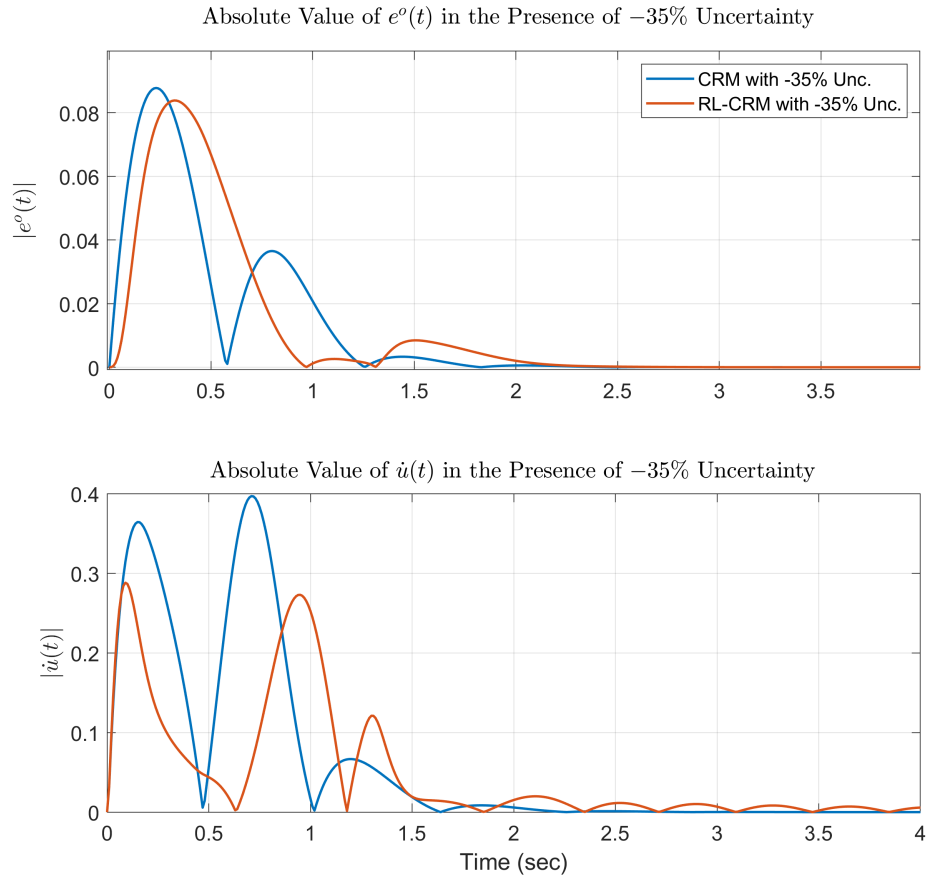


Figure 6.7 : Comparison of $|e^o(t)|$ and $|\dot{u}(t)|$ time history of the CRM and RL-CRM systems in the presence of -35% parametric uncertainty.

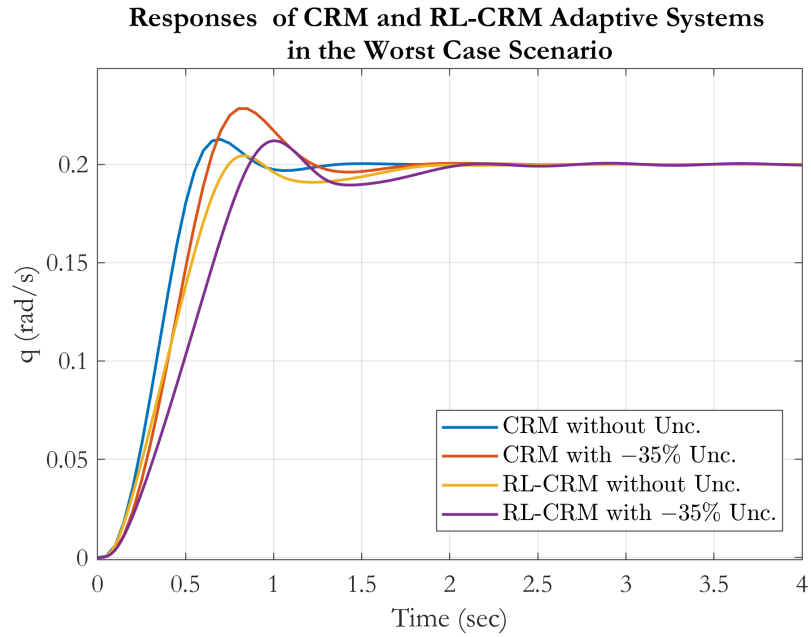


Figure 6.8 : Step responses of the CRM and RL-CRM systems in the presence of -35% parametric uncertainty.

7. CONCLUSIONS AND RECOMMENDATIONS

The urban air mobility concept consists of several key aspects such as ATM/UTM airspace integration, UAM business models, infrastructures and vehicle technologies such as power, battery, safety and autonomy. This thesis focuses on mathematical modeling and flight control system design approaches which provide fundamental requirements for the safety and autonomy. General overview of the UAM concept is given again in Figure 7.1 to enhance completeness of the study. The main focus of this thesis is mathematical modeling and flight control system design applications which are covered by "Key Vehicle Technologies" of the UAM concept in Figure 7.1.

In this thesis, we proposed modeling and control of tilt-wing, fixed-wing and rotary-wing unmanned aerial platforms. As a demonstration of the physics-based modeling approach, complete 6-DoF nonlinear mathematical model of the tilt-rotor Turac UAV, which is valid for hover, transition and forward flight regimes, is developed. This model contains propeller-induced and free-airstream effects and airspeed dependent characteristics of the propulsion system. In this approach, aerodynamic parameters are obtained by using CFD analysis. Forward-(hover-to-cruise) and back-transition (cruise-to-hover) scenarios are investigated and developed for the Turac UAV. Transition scenarios consist of a schedule for total airspeed, angle of attack and thrust levels of both the tilt-rotors and coaxial fan group. The scheduled data may be used as a pilot cue or command signal dataset for the flight control system. Transition algorithms between hover-to-cruise and cruise-to-hover are described step-by-step. Real-time 6-DoF simulations are performed for hover-to-cruise and cruise-to-hover flight by using the developed transition scenario dataset. We present the simulation results and demonstrate the successful transition of the Turac in experiment.

As the first demonstration of the desktop-to-flight design workflow, we provided a model-based flight control system design approach for a fixed-wing UAV using integrated flight testing and HIL simulation. The baseline nonlinear model is

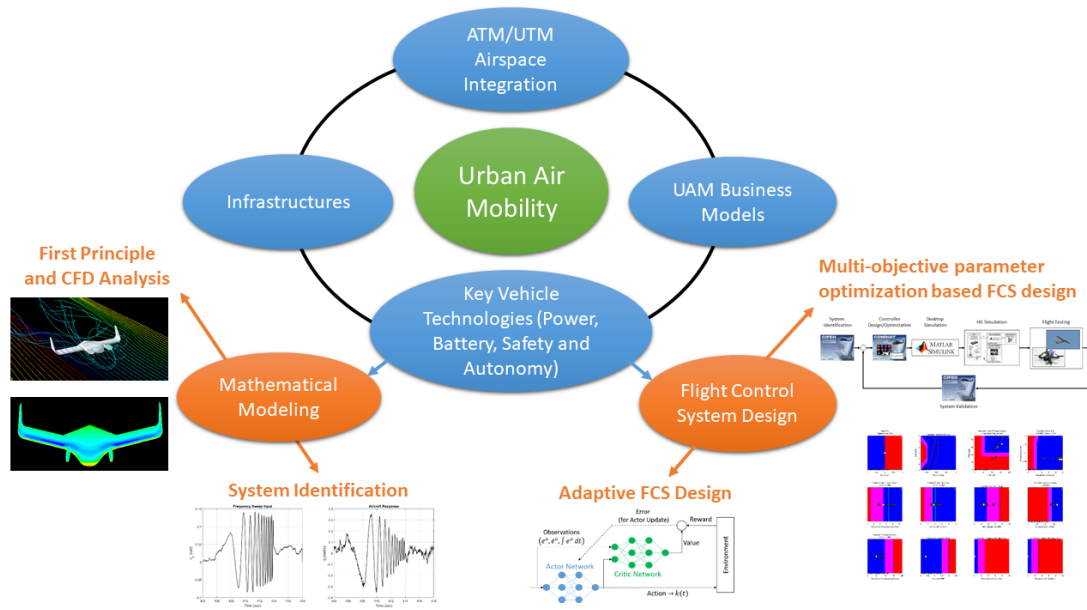


Figure 7.1 : General overview of the key aspects of urban air mobility concept.

developed by utilizing the first-principle method as a basis for the preliminary studies. Then, linear dynamical models of the UAV are identified by using the frequency-domain system identification process in CIPHER software. The aerodynamic database is updated based on the identified parameters. To track a moving ground target by a downward-facing body-fixed camera, required handling qualities are defined, some of them are scaled-down and attitude control system is designed by using the CONDUIT software. The HIL simulation system is used for the initial tests of the proposed closed-loop dynamics. Frequency responses of the legacy controller are obtained for closed-loop, broken-loop and disturbance rejection dynamics and they compared with the dynamical characteristics of the proposed controller. To evaluate the attitude-control / attitude-hold performance of the proposed and legacy controllers, level flight and doublet signal reference tracking flight tests are performed. The results demonstrate that the proposed methodology and the resulting control system provides higher performance and robust disturbance rejection in face of real-world conditions such as turbulence and winds.

As the second demonstration of the desktop-to-flight design workflow, it is applied on an highly agile quadrotor platform to obtain suitable inner- and outer-loop controllers for high precision and agile trajectory tracking missions. The frequency-domain system identification process is utilized in CIPHER for both hover/low speed and fast forward flight phases to identify the bare-airframe dynamics. Then, obtained

point models are stitched and quasi-nonlinear simulation environment is generated. Inner- and outer-loop legacy controllers are modified for the trajectory tracking mission and optimized controller parameters are determined by using multi-objective optimization based controller design process in CONDUIT. The trajectory tracking and aggressiveness of the legacy and optimized closed-loop systems are evaluated by utilizing Monte-Carlo simulations and outdoor flight tests. The results indicate that, similar to the dynamical behavior as a full-scale rotorcraft, there are significant deviations in bare-airframe dynamics of the quadrotor platform in hover and forward flight conditions. In comparison to classical control designs, the optimized controllers (across hover/low speed and high forward speed flight conditions) show significant precision, predictability and robustness. Future works may focus on further improving the reference signal tracking performance of the racer quadrotor platform in higher speed (20-32 m/s) forward flight.

In the last part of the thesis, RL-CRM adaptive system is developed to improve the transient performance of the fixed-gain CRM-adaptive system. In the proposed algorithm, a variable scaling factor is introduced to scale-up and scale-down the optimal observer gain during the transient response phase. An actor-critic agent is trained by using DDPG algorithm to learn the scaling policy of the observer gain. Simulation studies are performed on simplified pitch dynamics model of a transport helicopter with parametric uncertainties and results show that the proposed algorithm has superior transient performance than MRAC and optimal fixed-gain CRM-adaptive systems in terms of key performance metrics. In future works of the RL-CRM adaptive system, several pre-selected controller parameters such as adaptation rates and time constant of the agent LPF may be considered as free design parameters and included in the optimization process. In addition, fragility of the proposed system may be investigated and uncertainty effects can be included in the training phase to improve the robustness against parametric uncertainty. Modification of the cost function may also be considered. Several cost functions may be developed and their effects on the system performance may be evaluated. Also, the proposed algorithm may be extended for multi-input-multi-output systems and comprehensive stability and robustness analysis may be performed on a high-fidelity simulation environment of an unmanned aerial vehicle.

To sum up all of the above mentioned concluding remarks, a brief and concise comparison of the state-of-the-art and contribution of this thesis are summarized and listed in Table 7.1.

Table 7.1 : Comparison of the state-of-the-art and thesis contributions.

	State-of-Art	Thesis Contribution
Turac VTOL UAV	Aerodynamics effects in the transition phase are studied based on several simplifications and assumptions. In most of the studies, propeller-induced airflow effects in the transition phase are either neglected or modeled in a simple way such as a linear function of the tilt angle.	A detailed and new aerodynamics and trim methodology is developed including free airstream and propeller-induced airstream effects on the UAV airframe. Propeller-induced airstream effects are modeled by using 2D Vortex Lattice Method (VLM) and momentum theory. The new mathematical model and the methodology that was developed has been referenced and applied in numerous follow up studies.
Applications of Desktop-to-Flight Control System Design Workflow	Desktop-to-flight control system design workflow has been developed by US Army, Universities Space Research Association and NASA. There are lots of successfully applications on manned aerial vehicles.	Up to authors' knowledge, several local defense companies have started to use this design workflow, however the full cycle has not been demonstrated and it has not been applied on academic research realm. This thesis is the first full cycle (system identification, control system design, verification,) application of the workflow in a research laboratory in Turkey. This work has increased the maturity of the theoretical research and provided a much needed baseline controller design process to which every new is benchmarked against. Both the process and the results have provided a breakthrough in local micro UAV control system design and implementation methodology extending it beyond empiric gain tuning.
	The design workflow has also been used for unmanned aerial vehicles such as fixed-wing and non-agile rotary-wing platforms in recent years with promising results.	In this thesis, the design workflow is applied on a fixed-wing and agile quadrotor platforms. To the authors' knowledge, it is the first time that the design workflow is applied on a highly-agile multi-copter platform which has a significantly wider flight envelope and thus providing modeling challenges that need to be addressed. The model as developed has been used in designing agile flight control systems which demonstrate significant agility metrics in performance not demonstrated in previous autonomous flight designs.

Table 7.1 (continued): Comparison of the state-of-the-art and thesis contributions.

	State-of-Art	Thesis Contribution
RL-CRM Adaptive System	Closed-loop reference model (CRM) adaptive control system has been developed to increase the transient response performance of the system. Fixed feedback gain of the reference model is determined by utilizing an optimization process.	In this thesis, we introduced a new reinforcement learning (RL) based CRM-adaptive control methodology which utilizes time-varying feedback gain of the closed-loop reference model. The variation policy of this gain is determined by an RL agent which is trained by utilizing the deep deterministic policy gradient algorithm. This modification provides almost 10% improvement in the transient response performance in terms of key signal norms when compared to the optimized fixed-gain CRM-adaptive system.

REFERENCES

- [1] **Ivler, C.M. and Goerzen, C.L.** (2018). Control Design for Tracking of Scaled MTE Trajectories on an IRIS+ Quadcopter, *American Helicopter Society International 74th Annual Forum and Technology Display*, Phoenix, AZ.
- [2] **Tischler, M.B., Berger, T., Ivler, C.M., Mansur, M.H., Cheung, K.K. and Soong, J.Y.** (2017). *Practical Methods for Aircraft and Rotorcraft Flight Control Design: An Optimization-Based Approach*, AIAA Education Series.
- [3] **Tischler, M.B. and Remple, R.K.** (2012). *Aircraft and Rotorcraft System Identification*, AIAA Education Series.
- [4] **Tischler, M.B. and Tobias, E.L.** (2016). A Model Stitching Architecture for Continuous Full Flight-Envelope Simulation of Fixed-Wing Aircraft and Rotorcraft from Discrete Point Linear Models, **Technical Report**, Aviation and Missile Research, Development and Engineering Center, Redstone .
- [5] **Weingarten, N.** (2003). History of In-flight Simulation & Flying Qualities Research at Veridian, *AIAA Atmospheric Flight Mechanics Conference and Exhibit*, Austin, TX, p.5464.
- [6] **Astrom, K.J.** (1996). Adaptive Control Around 1960, *IEEE Control Systems Magazine*, 16(3), 44–49.
- [7] **Dydek, Z.T., Annaswamy, A.M. and Lavretsky, E.** (2010). Adaptive Control and the NASA X-15-3 Flight Revisited, *IEEE Control Systems Magazine*, 30(3), 32–48.
- [8] **Gupta, V.** (2005). Quad Tilt Rotor Simulations in Helicopter Mode Using Computational Fluid Dynamics, *Ph.D. thesis*, University of Maryland.
- [9] **Potsdam, M.A. and Strawn, R.C.** (2005). CFD Simulations of Tiltrotor Configurations in Hover, *Journal of the American Helicopter Society*, 50(1), 82–94.
- [10] **Young, L., Lillie, D., McCluer, M., Yamauchi, G. and Derby, M.** (2002). Insights Into Airframe Aerodynamics and Rotor-on-wing Interactions from a 0.25-scale Tilt-rotor Wind Tunnel Model, **Technical Report**, NATIONAL AERONAUTICS AND SPACE ADMINISTRATION MOFFETT FIELD CA AMES RESEARCH
- [11] **Yeo, H. and Johnson, W.** (2009). Performance and Design Investigation of Heavy Lift Tilt-rotor with Aerodynamic Interference Effects, *Journal of Aircraft*, 46(4), 1231–1239.

- [12] **Cummings, R.M., Morton, S.A. and Siegel, S.G.** (2008). Numerical Prediction and Wind Tunnel Experiment for a Pitching Unmanned Combat Air Vehicle, *Aerospace Science and Technology*, 12(5), 355–364.
- [13] **Wisnoe, W., Nasir, R.E.M., Kuntjoro, W. and Mamat, A.M.I.** (2009). Wind Tunnel Experiments and CFD Analysis of Blended Wing Body (BWB) Unmanned Aerial Vehicle (UAV) at Mach 0.1 and Mach 0.3, *13th International Conference on Aerospace Sciences & Aviation Technology*, p. 14.
- [14] **Lino, M.** (2010). Numerical Investigation of Propeller-Wing Interaction Effects for a Large Military Transport Aircraft, *Delft University of Technology*.
- [15] **Kim, C. and Chung, J.** (2006). Aerodynamic Analysis of Tilt-rotor Unmanned Aerial Vehicle with Computational Fluid Dynamics, *Journal of Mechanical Science and Technology*, 20(4), 561–568.
- [16] **Abras, J. and Narducci, R.** (2010). Analysis of CFD Modeling Techniques Over the MV-22 Tiltrotor, *American Helicopter Society 66th Annual Forum*, Phoenix, AZ, pp.11–13.
- [17] **Sweeten, B.C.** (2010). CFD Analysis of UAVs Using VORSTAB, FLUENT, and Advanced Aircraft Analysis Software, *Ph.D. thesis*, University of Kansas.
- [18] **Tekinalp, O., Unlu, T. and Yavrucuk, I.** (2009). Simulation and Flight Control of a Tilt Duct UAV, *AIAA Modeling and Simulation Technologies Conference*, Chicago, IL, p.6138.
- [19] **Flores, G.R., Escareño, J., Lozano, R. and Salazar, S.** (2012). Quad-tilting Rotor Convertible MAV: Modeling and Real-time Hover Flight Control, *Journal of Intelligent & Robotic Systems*, 65(1-4), 457–471.
- [20] **Flores, G. and Lozano, R.** (2013). Transition Flight Control of the Quad-tilting Rotor Convertible MAV, *International Conference on Unmanned Aircraft Systems (ICUAS)*, IEEE, Atlanta, GA, pp.789–794.
- [21] **Matos, C., Reddy, U. and Komerath, N.** (1999). Rotor Wake/Fixed Wing Interactions with Flap Deflection, *American Helicopter Society 55th Annual Forum*, Montreal, Quebec, Canada.
- [22] **Matos, C.A.M.** (2001). Download Reduction on a Wing-Rotor Configuration, *Ph.D. thesis*, School of Aerospace Engineering, Georgia Institute of Technology, Atlanta, GA.
- [23] **Harding, J. and Moody, S.** (2005). Identification of AH-64D Dynamics to Support Flight Control Systems Evaluations, *Annual Forum Proceedings of the American Helicopter Society*, volume 61, AHS, Grapevine, TX, p.182.
- [24] **Harding, J.W., Moody, S.J., Jeram, G.J., Mansur, H. and Tischler, M.B.** (2006). Development of Modern Control Laws for the AH-64D in Hover/Low Speed Flight, *Annual Forum Proceedings of the American Helicopter Society*, volume 62, AHS, Phoenix, AZ, p.2017.

- [25] **Theodore, C., Ivler, C., Tischler, M., Field, E., Neville, R. and Ross, H.** (2008). System Identification of Large Flexible Transport Aircraft, *AIAA Atmospheric Flight Mechanics Conference and Exhibit*, Honolulu, HI, p.6894.
- [26] **Berger, T., Tischler, M., Hagerott, S.G., Gangsaas, D. and Saeed, N.** (2012). Longitudinal Control Law Design and Handling Qualities Optimization for a Business Jet Flight Control System, *AIAA Atmospheric Flight Mechanics Conference*, Minneapolis, MN, p.4503.
- [27] **Berger, T., Tischler, M., Hagerott, S.G., Gangsaas, D. and Saeed, N.** (2013). Lateral/Directional Control Law Design and Handling Qualities Optimization for a Business Jet Flight Control System, *AIAA Atmospheric Flight Mechanics Conference*, Grapevine, TX, p.4506.
- [28] **Mettler, B.** (2003). *Identification Modeling and Characteristics of Miniature Rotorcraft*, Springer Science & Business Media.
- [29] **Cheng, R.P., Tischler, M.B. and Schulein, G.J.** (2006). R-MAX Helicopter State-Space Model Identification for Hover and Forward-Flight, *Journal of the American Helicopter Society*, 51(2), 202–210.
- [30] **Downs, J., Prentice, R., Alzell, S., Besachio, A., Ivler, C., Tischler, M.B. and Mansur, M.** (2007). Control System Development and Flight Test Experience with the MQ-8B Fire Scout Vertical Take-off Unmanned Aerial Vehicle (VTUAV), *Annual Forum Proceedings of the American Helicopter Society*, volume 63, AHS, Virginia Beach, VA, p.566.
- [31] **Wei, W., Schwartz, N. and Cohen, K.** (2014). Frequency-domain System Identification and Simulation of a Quadrotor Controller, *AIAA Modeling and Simulation Technologies Conference*, National Harbor, MD, p.1342.
- [32] **Wei, W., Cohen, K. and Tischler, M.B.** (2015). System Identification and Controller Optimization of a Quadrotor UAV, *Proceedings of the AHS International's 71st Annual Forum and Technology Display*, Virginia Beach, VA.
- [33] **Wei, W., Tischler, M.B. and Cohen, K.** (2017). System Identification and Controller Optimization of a Quadrotor Unmanned Aerial Vehicle in Hover, *Journal of the American Helicopter Society*, 62(4), 1–9.
- [34] **Niermeyer, P., Raffler, T. and Holzapfel, F.** (2015). Open-loop Quadrotor Flight Dynamics Identification in Frequency-domain via Closed-loop Flight Testing, *AIAA Guidance, Navigation and Control Conference*, Kissimmee, FL, p.1539.
- [35] **Woodrow, P., Tischler, M., Mendoza, G., Hagerott, S.G. and Hunter, J.** (2013). Low Cost Flight-Test Platform to Demonstrate Flight Dynamics Concepts Using Frequency-domain System Identification Methods, *AIAA Atmospheric Flight Mechanics Conference*, Boston, MA, p.4739.

- [36] **Sanders, F.C., Tischler, M., Berger, T., Berrios, M.G. and Gong, A.** (2018). System Identification and Multi-Objective Longitudinal Control Law Design for a Small Fixed-Wing UAV, *AIAA Atmospheric Flight Mechanics Conference*, p.0296.
- [37] **Dorobantu, A., Murch, A., Mettler, B. and Balas, G.** (2013). System Identification for Small, Low-cost, Fixed-wing Unmanned Aircraft, *Journal of Aircraft*, 50(4), 1117–1130.
- [38] **Dorobantu, A., Johnson, W., Lie, F.A., Taylor, B., Murch, A., Paw, Y.C., Gebre-Egziabher, D. and Balas, G.** (2013). An Airborne Experimental Test Platform: From Theory to Flight, *American Control Conference (ACC)*, IEEE, Washington, DC, pp.659–673.
- [39] **Juhasz, Ondrej, T.M. and Won, H.** (2018). System Identification and Control Law Optimization Applied to the AeroVironment Quantix Tail-Sitter UAS, *Proceedings of the AHS International's 74th Annual Forum and Technology Display*, Phoenix, AZ.
- [40] **Zivan, L. and Tischler, M.B.** (2010). Development of a Full Flight Envelope Helicopter Simulation Using System Identification, *Journal of the American Helicopter Society*, 55(2), 22003–22003.
- [41] **Knapp, M.E., Berger, T., Tischler, M. and Cotting, M.C.** (2018). Development of a Full Envelope Flight Identified F-16 Simulation Model, *AIAA Atmospheric Flight Mechanics Conference*, AIAA, Atlanta, GA, p.0525.
- [42] **Mansur, M.H., Tischler, M.B., Bielefield, M.D., Bacon, J.W., Cheung, K.K., Berrios, M.G. and Rothman, K.E.** (2011). Full Flight Envelope Inner Loop Control Law Development for the Unmanned K-MAX, **Technical Report**.
- [43] **Tobias, E., Sanders, F. and Tischler, M.B.** (2018). Full-Envelope Stitched Simulation Model of a Quadrotor using STITCH, *American Helicopter Society 74th Annual Forum*, Phoenix, AZ.
- [44] **Gong, A., Sanders, F.C., Hess, R.A. and Tischler, M.B.** (2019). System Identification and Full Flight-Envelope Model Stitching of a Package-Delivery Octocopter, *AIAA Scitech 2019 Forum*, San Diego, CA, p.1076.
- [45] **Whitaker, H.** (1959). An Adaptive System for Control of the Dynamics Performances of Aircraft and Spacecraft, *Inst. Aeronautical Sciences*, 59–100.
- [46] **Ioannou, P. and Fidan, B.** (2006). *Adaptive Control Tutorial*, SIAM.
- [47] **Narendra, K. and Annaswamy, A.** (1987). A New Adaptive Law for Robust Adaptation without Persistent Excitation, *IEEE Transactions on Automatic control*, 32(2), 134–145.
- [48] **Peterson, B. and Narendra, K.** (1982). Bounded Error Adaptive Control, *IEEE Transactions on Automatic Control*, 27(6), 1161–1168.

- [49] **Lavretsky, E.** (2009). Combined/Composite Model Reference Adaptive Control, *IEEE Transactions on Automatic Control*, 54(11), 2692–2697.
- [50] **Dydek, Z., Annaswamy, A. and Lavretsky, E.** (2010). Combined/Composite Adaptive Control of a Quadrotor UAV in the Presence of Actuator Uncertainty, *AIAA Guidance, Navigation, and Control Conference*, Toronto, Ontario, Canada, p.7575.
- [51] **Gibson, T., Annaswamy, A. and Lavretsky, E.** (2012). Improved Transient Response in Adaptive Control Using Projection Algorithms and Closed-loop Reference Models, *AIAA Guidance, Navigation, and Control Conference*, Minneapolis, MN, p.4775.
- [52] **Gibson, T.E., Annaswamy, A.M. and Lavretsky, E.** (2013). Adaptive Systems with Closed-loop Reference-Models, Part 1: Transient Performance, *2013 American Control Conference*, IEEE, Washington, DC, pp.3376–3383.
- [53] **Gibson, T.E.** (2014). Closed-loop Reference Model Adaptive Control: With Application to Very Flexible Aircraft, *Ph.D. thesis*, Massachusetts Institute of Technology.
- [54] **Hodgkinson, J., LaManna, W. and Heyde, J.** (1976). Handling Qualities of Aircraft with Stability and Control Augmentation Systems — A Fundamental Approach, *The Aeronautical Journal*, 80(782), 75–81.
- [55] **Maine, R.E. and Iliff, K.W.** (1981). The Theory and Practice of Estimating the Accuracy of Dynamic Flight-Determined Coefficients.
- [56] **Jategaonkar, R.V., Fischenberg, D. and Gruenhagen, W.** (2004). Aerodynamic Modeling and System Identification from Flight Data - Recent Applications at DLR, *Journal of Aircraft*, 41(4), 681–691.
- [57] **Joos, H.D.**, (1997). Multi-objective Parameter Synthesis (MOPS), *Robust Flight Control*, Springer, pp.199–217.
- [58] **Moritz, N. and Osterhuber, R.** (2006). Three-stage Gradient-based Optimization Scheme in Design of Feedback Gains within Eurofighter Primary Control Laws, *AIAA Guidance, Navigation, and Control Conference and Exhibit*, Keystone, CO, p.6311.
- [59] **Tischler, M.B., Colbourne, J.D., Morel, M.R. and Biezd, D.J.** (1999). A Multidisciplinary Flight Control Development Environment and Its Application to a Helicopter, *IEEE Control Systems Magazine*, 19(4), 22–33.
- [60] **Tischler, M.B., Blanken, C.L., Cheung, K.K., M. Swei, S.S., Sahasrabudhe, V. and Faynberg, A.** (2005). Modernized Control Laws for UH-60 BLACK HAWK Optimization and Flight-test Results, *Journal of guidance, control, and dynamics*, 28(5), 964–978.
- [61] **Christensen, K.T., Campbell, K.G., Griffith, C.D., Ivler, C.M., Tischler, M.B. and Harding, J.W.** (2007). Flight Control Development for the ARH-70 Armed Reconnaissance Helicopter Program, *Annual Forum Proceedings*

of the American Helicopter Society, volume 63, AHS, Virginia Beach, VA, p.839.

- [62] **Miller, D., White, J., McElroy, D., Taylor, J., Lukes, G., Gradle, R. and Segner, D.** (2008). HACT Program Technology Transfer, *Annual Forum Proceedings of the American Helicopter Society*, volume 64, AHS, Montreal, Quebec, Canada, p.1397.
- [63] **Duda, H.** (1997). Prediction of Pilot-in-the-loop Oscillations due to Rate Saturation, *Journal of Guidance, Control, and Dynamics*, 20(3), 581–587.
- [64] **Schittkowski, K.** (1986). QLD: A Fortran Code for Quadratic Programming, User's Guide, *Mathematisches Institut, Universit at Bayreuth, Germany*.
- [65] **Powell, M.J.D.,** (1985). On the Quadratic Programming Algorithm of Goldfarb and Idnani, *Mathematical Programming Essays in Honor of George B. Dantzig Part II*, Springer, pp.46–61.
- [66] **Gibson, T.E., Annaswamy, A.M. and Lavretsky, E.** (2013). Adaptive Systems with Closed-loop Reference Models, Part I: Transient Performance, *American Control Conference (ACC)*, IEEE, Washington, DC, pp.3376–3383.
- [67] **Gibson, T.E., Annaswamy, A.M. and Lavretsky, E.** (2013). On Adaptive Control with Closed-loop Reference Models: Transients, Oscillations and Peaking, *IEEE Access*, 1, 703–717.
- [68] **Mnih, V., Kavukcuoglu, K., Silver, D., Rusu, A.A., Veness, J., Bellemare, M.G., Graves, A., Riedmiller, M., Fidjeland, A.K., Ostrovski, G. et al.** (2015). Human-level Control Through Deep Reinforcement Learning, *Nature*, 518(7540), 529.
- [69] **Lillicrap, T.P., Hunt, J.J., Pritzel, A., Heess, N., Erez, T., Tassa, Y., Silver, D. and Wierstra, D.** (2015). Continuous Control with Deep Reinforcement Learning, *arXiv preprint arXiv:1509.02971*.
- [70] **Mnih, V., Kavukcuoglu, K., Silver, D., Graves, A., Antonoglou, I., Wierstra, D. and Riedmiller, M.** (2013). Playing Atari with Deep Reinforcement Learning, *arXiv preprint arXiv:1312.5602*.
- [71] **Silver, D., Lever, G., Heess, N., Degris, T., Wierstra, D. and Riedmiller, M.** (2014). Deterministic Policy Gradient Algorithms, *Proceedings of the 31st International Conference on Machine Learning*, Beijing, China.
- [72] **Foy, B.W.** (2005). Hover Controls for a Unique Small-scale Thrust Reversing UAV, *Ph.D. thesis*, University of Colorado at Boulder.
- [73] **Ozdemir, U., Aktas, Y.O., Vuruskan, A., Dereli, Y., Tarhan, A.F., Demirbag, K., Erdem, A., Kalaycioglu, G.D., Ozkol, I. and Inalhan, G.** (2014). Design of a Commercial Hybrid VTOL UAV System, *Journal of Intelligent & Robotic Systems*, 74(1-2), 371–393.

- [74] Aktas, Y., Ozdemir, U., Dereli, Y., Tarhan, A., Cetin, A., Vuruskan, A., Yuksek, B., Cengiz, H., Basdemir, S., Ucar, M. *et al.* (2014). A Low Cost Prototyping, Analyzing and Flight Testing for the TURAC VTOL UAV, *International Conference on Unmanned Aircraft Systems (ICUAS)*, IEEE, Orlando, FL.
- [75] Yuksek, B., Vuruskan, A., Ozdemir, U., Yukselen, M. and Inalhan, G. (2016). Transition Flight Modeling of a Fixed-wing VTOL UAV, *Journal of Intelligent & Robotic Systems*, 84(1-4), 83–105.
- [76] Blakelock, J.H. (1991). *Automatic Control of Aircraft and Missiles*, John Wiley & Sons.
- [77] Yechout, T.R. (2003). *Introduction to Aircraft Flight Mechanics*, AIAA Education Series, 1 edition.
- [78] AAA, Advanced Aircraft Analysis Software, <<https://www.darcorp.com/advanced-aircraft-analysis-software/>>, date retrieved 24.09.2019.
- [79] Colin, P. E., W.J. (1968). The Aerodynamics of V/STOL Aircraft, **Technical Report-DTIC-AD0688921**, Advisory Group for Aerospace Research and Development (AGARD).
- [80] Huang, H., Hoffmann, G.M., Waslander, S.L. and Tomlin, C.J. (2009). Aerodynamics and Control of Autonomous Quadrotor Helicopters in Aggressive Maneuvering, *International Conference on Robotics and Automation (ICRA)*, IEEE, Kobe, Japan, pp.3277–3282.
- [81] Williams, J.E. and Vukelich, S.R. (1979). The USAF stability and control digital DATCOM. Volume I. Users manual, **Technical Report**, McDonnell Douglas Astronautics CO., St. Louis, MO.
- [82] Katz, J. and Plotkin, A. (2001). *Low-Speed Aerodynamics*, Cambridge University Press.
- [83] Nelson, R.C. (1998). *Flight Stability and Automatic Control*, WCB/McGraw Hill New York, 2 edition.
- [84] APC, Propeller Performance Data, <<https://www.apcprop.com/technical-information/performance-data/>>, date retrieved 19.11.2018.
- [85] Roskam, J. and Lan, C.T.E. (1997). *Airplane Aerodynamics and Performance*, DARcorporation, Lawrence, KS.
- [86] Beard, R.W. and McLain, T.W. (2012). *Small Unmanned Aircraft: Theory and Practice*, Princeton university press.
- [87] NASA (1976). U.S. Standard Atmosphere 1976, **Technical report**, Prepared under sponsorship National Oceanic and Atmospheric Administration, National Aeronautics and Space Administration, United States Air Force.

- [88] **David J. Moorhoiuse, R.J.W.** (1982). Background Information and User Guide for MIL-F-878SC, Military Specification - Flying Qualities of Piloted Airplanes, **Technical report**, Flight Dynamics Laboratory, Air Force Wright Aeronautical Laboratories.
- [89] **Lemoine, F., Smith, D., Kunz, L., Smith, R., Pavlis, E., Pavlis, N., Klosko, S., Chinn, D., Torrence, M., Williamson, R. et al.,** (1997). The Development of the NASA GSFC and NIMA Joint Geopotential Model, Gravity, geoid and marine geodesy, Springer, pp.461–469.
- [90] **NIMA** (1997). Department of Defense World Geodetic System 1984, Its Definition and Relationships With Local Geodetic Systems, **Technical Report TR8350.2**, Flight Dynamics Laboratory, Air Force Wright Aeronautical Laboratories.
- [91] **McRuer, D.T., Ashkenas, I. and Graham, D.** (1973). *Aircraft Dynamics and Automatic Control*, Princeton University Press.
- [92] **Pixhawk**, <<https://pixhawk.org/modules/pixhawk>>, date retrieved 19.11.2018.
- [93] **Arduplane**, <<http://ardupilot.org/plane/>>, date retrieved 19.11.2018.
- [94] **Berger, T., Ivler, C.M., Berrios, M.G., Tischler, M.B. and Miller, D.** (2016). Disturbance Rejection Handling Qualities Criteria for Rotorcraft, *American Helicopter Society 72nd Annual Forum*, West Palm Beach, FL.
- [95] **MAVLink**, <<https://mavlink.io/en/>>, date retrieved 19.11.2018.
- [96] **Simulation-Pace**, <<https://www.mathworks.com/help/aeroblks/simulationpace.html>>, date retrieved 19.11.2018.
- [97] **Anon.** (2012). Military Standard, Flying Qualities of Piloted Airplanes, MIL-STD-1797B, **Technical Report**.
- [98] **Anon.** (2000). Aeronautical Design Standard, Performance Specification, Handling Qualities Requirements for Military Rotorcraft, ADS-33E-PRF, **Technical Report**, US Army Aviation and Missile Command.
- [99] **Cheung, K.K., Wagster IV, J.A., Tischler, M.B., Ivler, C.M., Berrios, M.G., Berger, T. and Lehmann, R.M.** (2017). An Overview of the US Army Aviation Development Directorate Quadrotor Guidance, Navigation, and Control Project, *Vertical Flight Society Forum*, volume 73, Fort Worth, TX.
- [100] **Arducopter**, <<http://ardupilot.org/copter/>>, date retrieved 11.06.2019.
- [101] **Åström, K.J. and Wittenmark, B.** (2013). *Adaptive Control*, Courier Corporation, 2. edition.
- [102] **Narendra, K.S. and Annaswamy, A.M.** (2012). *Stable Adaptive Systems*, Courier Corporation.

- [103] **Wise, K.A., Lavretsky, E. and Hovakimyan, N.** (2006). Adaptive Control of Flight: Theory, Applications and Open Problems, *2006 American Control Conference*, IEEE, Minneapolis, MN, pp.6–pp.
- [104] **Lewis, F.L., Vrabie, D. and Vamvoudakis, K.G.** (2012). Reinforcement Learning and Feedback Control: Using Natural Decision Methods to Design Optimal Adaptive Controllers, *IEEE Control Systems Magazine*, 32(6), 76–105.
- [105] **Lewis, F.L. and Liu, D.** (2013). *Reinforcement Learning and Approximate Dynamic Programming for Feedback Control*, volume 17, John Wiley & Sons.
- [106] **Lavretsky, E. and Wise, K.A.** (2013). *Robust and Adaptive Control*, Springer-Verlag, London.

CURRICULUM VITAE

Name Surname: Burak Yüksek

Place and Date of Birth: Sivas - 27/01/1989

E-Mail: burakyukse@gmail.com



EDUCATION:

- **B.Sc.:** 2010, Yildiz Technical University, Faculty of Mechanical Engineering, Mechanical Engineering Department
- **M.Sc.:** 2013, Istanbul Technical University, Institute of Science and Technology, Mechatronics Engineering Department

PROFESSIONAL EXPERIENCE AND REWARDS:

- 2010-2011 Enelkon Automation Systems
- 2011-2013 Istanbul Technical University at the Mechatronics Education and Research Center
- 2013-... Istanbul Technical University at the Aerospace Research Center (ARC)
- 2013-2017 TUBITAK PhD. Scholarship

PUBLICATIONS ON THE THESIS:

- **Yukse, B.**, Demirezen, U., Inalhan, G., A New Reinforcement Learning Based Approach for Closed-loop Reference Model Adaptive Flight Control System Design, Submitted for American Control Conference (ACC) 2020.
- **Yukse, B.**, Saldiran, E., Cetin, A., Yeniceri, R. and Inalhan, G., 2020. System Identification and Model-Based Flight Control System Design for an Agile Maneuvering Quadrotor Platform. Accepted for AIAA Scitech 2020 Forum, January 6-10, Orlando, FL.
- **Yukse, B.**, Saldiran, E., Cetin, A., Yeniceri, R. and Inalhan, G., 2019. A Model Based Flight Control System Design Approach for Micro Aerial Vehicle Using Integrated Flight Testing and HIL Simulation. In AIAA Scitech 2019 Forum (p. 1480), January 7-11, 2019, San Diego, CA.
- **Yukse, B.**, Vuruskan, A., Ozdemir, U., Yukselen, M.A. and Inalhan, G., 2016. Transition Flight Modeling of a Fixed-wing VTOL UAV. *Journal of Intelligent and Robotic Systems*, 84 (1-4), pp.83-105.

OTHER PUBLICATIONS:

- Herekoglu, O., Hasanzade, M., Saldiran, E., Cetin, A., Ozgur, I., Kucukoglu, A.G., Ustun, M.B., **Yuksekk, B.**, Yeniceri, R., Koyuncu, E. and Inalhan, G., 2019. Flight Testing of a Multiple UAV RF Emission and Vision Based Target Localization Method. In AIAA Scitech 2019 Forum (p. 1570), January 7-11, 2019, San Diego, CA.
- Akcakoca, M., Atici, B.M., Gever, B., Oguz, S., Demirezen, U., Demir, M., Saldiran, E., **Yuksekk, B.**, Koyuncu, E., Yeniceri, R. and Inalhan, G., 2019. A Simulation-Based Development and Verification Architecture for Micro UAV Teams and Swarms. In AIAA Scitech 2019 Forum (p. 1979), January 7-11, 2019, San Diego, CA.
- Uzun, S., Akbiyik, B., **Yuksekk, B.**, Demirezen, U. and Inalhan, G., 2019. A Simulation-Based Machine Learning Approach for Flight Control System Design of Agile Maneuvering Multicopters. AIAA Scitech 2019 Forum (p. 1978), January 7-11, 2019, San Diego, CA.
- Eroglu, B., Sahin, C., **Yuksekk, B.**, Ure, N.K. and Inalhan, G., 2018. Deep Recurrent and Convolutional Networks for Accelerated Fault Tolerant Adaptive Flight Control Under Severe Failures. In 2018 Annual American Control Conference (ACC) (pp. 6559-6565), June 27-29, Milwaukee, WI.
- **Yuksekk, B.**, Ure, N.K. and Inalhan, G., 2018. Cooperative Interception of a Highly Manoeuvrable Aerial Target. In 2018 AIAA Guidance, Navigation, and Control Conference (p. 1581), 8-12 January, Kissimmee, FL.
- **Yuksekk, B.**, Ure, N.K., Caliskan, F. and Inalhan, G., 2017. Fault Tolerant Heading Control System Design for Turac Unmanned Aerial Vehicle. Transactions of the Institute of Measurement and Control, 39(3), pp.267-276.
- Akcal, U., **Yuksekk, B.** and Ure, N.K., 2017. Modeling and Simulation of Aerobee-150A Sounding Rocket. In AIAA Modeling and Simulation Technologies Conference (p. 1557), 9-13 January, Grapevine, TX.
- Aktas, Y.O., Ozdemir, U., Dereli, Y., Tarhan, A.F., Cetin, A., Vuruskan, A., **Yuksekk, B.**, Cengiz, H., Basdemir, S., Ucar, M. and Gencdav, M., 2016. Rapid Prototyping of a Fixed-wing VTOL UAV for Design Testing. Journal of Intelligent and Robotic Systems, 84(1-4), pp.639-664.
- **Yuksekk, B.** and Ure, N.K., 2016. Optimization of Allocation and Launch Conditions of Multiple Missiles for Three-dimensional Collaborative Interception of Ballistic Targets. International Journal of Aerospace Engineering, 2016.
- **Yuksekk, B.**, Üre, N., K., Çalışkan, F., İnalhan, G., 2015, TURAÇ İnsansız Hava Aracı için Arıza Toleranslı Yönelme Açısı Kontrol Sistemi Tasarımı, Otomatik Kontrol Türk Milli Komitesi Ulusal Toplantısı (TOK), 10-12 Eylül 2015, Pamukkale, Türkiye (in Turkish).
- Vuruskan, A., **Yuksekk, B.**, Ozdemir, U., Yukselen, A. and Inalhan, G., 2014. Dynamic Modeling of a Fixed-wing VTOL UAV. In 2014 International Conference on Unmanned Aircraft Systems (ICUAS) (pp. 483-491), May 27-30, Orlando, FL.

- Aktas, Y.O., Ozdemir, U., Dereli, Y., Tarhan, A.F., Cetin, A., Vuruskan, A., **Yukse****k, B.**, Cengiz, H., Basdemir, S., Ucar, M. and Genctav, M., 2014. A Low Cost Prototyping Approach for Design Analysis and Flight Testing of the Turac VTOL UAV. In 2014 International Conference on Unmanned Aircraft Systems (ICUAS) (pp. 1029-1039), May 27-30, Orlando, FL.
- **Yukse****k, B.**, Özdemir, U., İnalhan, G., 2014, TURAÇ İnsansız Hava Aracının Yuvarlanma Hareketi için Oransal ve Uyarlamalı Denetleyici Tasarımı, V. Ulusal Havacılık ve Uzay Konferansı, 8-10 Eylül 2014, Kayseri, Türkiye (in Turkish).